

Rochester Institute of Technology

RIT Digital Institutional Repository

Theses

6-14-2021

Improvements and Analysis of Challenging Numerical Simulations of Binary Black Holes

Nicole Rosato
ncr8062@rit.edu

Follow this and additional works at: <https://repository.rit.edu/theses>

Recommended Citation

Rosato, Nicole, "Improvements and Analysis of Challenging Numerical Simulations of Binary Black Holes" (2021). Thesis. Rochester Institute of Technology. Accessed from

This Dissertation is brought to you for free and open access by the RIT Libraries. For more information, please contact repository@rit.edu.

Improvements and Analysis of Challenging Numerical Simulations of Binary Black Holes

by Nicole Rosato

A Dissertation Submitted in Partial Fulfillment of the
Requirements for the Degree of
Doctor of Philosophy in Mathematical Modeling

School of Mathematical Sciences

College of Science

Rochester Institute of Technology

Rochester, New York

June 14, 2021

MATHEMATICAL MODELING
COLLEGE OF SCIENCE
ROCHESTER INSTITUTE OF TECHNOLOGY
ROCHESTER, NEW YORK

CERTIFICATE OF APPROVAL

Ph.D. DEGREE DISSERTATION

The Ph.D. Degree Dissertation of *Nicole Rosato* has been examined and approved by the dissertation committee as satisfactory for the dissertation requirement for the Ph.D. degree in Mathematical Modeling.

Dr. Hans-Peter Bischof, Committee Chair

Dr. Yosef Zlochower, Committee Member

Dr. Lawrence Kidder, Committee Member

Dr. Carlos Lousto, Thesis Advisor

Date _____

Improvements and Analysis of Challenging Numerical Simulations of Binary Black Holes

By

Nicole Rosato

A dissertation submitted in partial fulfillment of the requirements for the degree of Ph.D. in Mathematical Modeling, in the College of Science, Rochester Institute of Technology.

June 14, 2021

Approved by

Dr. Nathan Cahill

Date

Director, Mathematical Modeling

Acknowledgements

First and foremost I would like to thank my adviser, Prof. Carlos Lousto, for journeying through “the intricate waters of relativity” with me. Without him, I could not have come as far academically, professionally, or personally and I have to express my genuine thanks and appreciation for all of his support and the knowledge he has passed on to me over the past six years.

I also must express my thanks to Dr. Jim Healy for his help with the Einstein Toolkit, running simulations, research discussions, and baby pictures during stressful times. He was always patient and helpful, and I could not have done this without all his help.

Infinite love and appreciation to my parents. Their unending and unconditional support of my academic pursuits has been absolutely vital to the success of my studies.

Finally, I must also express my gratitude and love for all of the friends I have made along the way. Your support has been invaluable, especially during the last few years. Through you, I have found the true meaning of friendship and am thankful for the lifelong bonds we will share.

Computational Acknowledgments

I also gratefully acknowledge the National Science Foundation (NSF) for financial support from Grants No. PHY-1912632, No. PHY-1707946, No. ACI-1550436, No. AST-1516150, No. ACI-1516125, No. PHY-1726215. This work used the Extreme Science and Engineering Discovery Environment (XSEDE) [allocation TG-PHY060027N], supported by NSF grant No. ACI-1548562. Computational resources were also provided by the NewHorizons, BlueSky Clusters, and Green Prairies at RIT, which were supported by NSF grants No. PHY-0722703, No. DMS-0820923, No. AST-1028087, No. PHY-1229173, and No. PHY-1726215. Computational resources were also provided by the Blue Waters sustained-petascale computing NSF projects OAC-1811228, OAC-0832606, OAC-1238993, OAC-1516247 and OAC-1515969, OAC-0725070 and by Frontera projects PHY-20010 and PHY-20007. Blue Waters is a joint effort of the University of Illinois at Urbana-Champaign and its National Center for Supercomputing Applications. Frontera is an NSF-funded petascale computing system at the Texas Advanced Computing Center

Abstract

We explore different gauge choices in the moving puncture formulation in order to improve the accuracy of a linear momentum measure evaluated on the horizon of the remnant black hole produced by the merger of a binary. In particular, motivated by the study of gauges in which the damping term in the shift $m\eta$ takes on a constant value, we design a gauge via a variable shift parameter $m\eta(\vec{r}(t))$. This parameter takes a low value asymptotically, $1/m_i$, and then takes on a value of approximately 2 at the final hole horizon. This η then follows the remnant black hole as it moves due to its net recoil velocity. We find that this choice keeps the accuracy of the binary evolution. Furthermore, if the asymptotic value of the parameter $m\eta$ is chosen about or below 1.0, it produces more accurate results for the recoil velocity than the corresponding evaluation of the radiated linear momentum at infinity, for typical numerical resolutions.

Detailed studies of an unequal mass $q = m_1/m_2 = 1/3$ nonspinning binary are provided and then verified for other mass ratios ($q = 1/2, 1/5$) and spinning ($q = 1$) binary black hole mergers. We also use a position and black hole mass dependent damping term, $\eta[\vec{x}_1(t), \vec{x}_2(t), m_1, m_2]$, in the shift evolution, rather than a constant or conformal-factor dependent choice. We have found that this substantially reduces noise generation at the start of the numerical integration and keeps the numerical grid stable around both black holes, allowing for more accuracy with lower resolutions. We test our choices for this gauge in detail in a case study of a binary with a 7:1 mass ratio, and then use 15:1 and 32:1 binaries for a convergence study. Finally, we apply our new gauge to a 64:1 binary and a 128:1 binary to well cover the comparable and small mass ratio regimes.

Finally, we perform an analytic study of two nonspinning binary systems with $q = 1$ and $q = 1/3$ that use Brill-Lindquist initial data. These spacetimes are rotated into a frame that is transverse, with two of the five Weyl scalars vanishing, and quasi-Kinnersley. We derive and evaluate an index \mathcal{D} that, when used in conjunction with the Baker-Campanelli Specialty index S , allows us to analyze and classify these spacetimes into Petrov types in the strong-field regime and between the black holes.

Also included is an appendix to be utilized in conjunction with the RIT Catalog. It provides scripts for generation of fitting coefficients for analytic formulae developed in [1], [2], and [3] for specific subsets of the full 777 waveform RIT Catalog. Finally, we use these scripts to generate fitting coefficients for all non-precessing binaries in the catalog.

Contents

| | |
|--|--------------|
| Acknowledgments | i |
| Abstract | ii |
| Contents | iv |
| List of Figures | vii |
| List of Tables | xviii |
| 1 Introduction | 1 |
| 1.1 First Detection of Gravitational Waves | 1 |
| 1.1.1 How do we detect gravitational waves? | 1 |
| 1.1.2 First Detection | 4 |
| 1.2 The importance of Numerical Relativity | 6 |
| 1.3 Brief Review of Theory | 9 |
| 1.3.1 Einstein’s Field Equations | 9 |
| 1.3.2 3+1 Formalism | 11 |
| 1.3.3 BSSNOK | 14 |
| 1.3.4 Evolution of BBH systems | 16 |
| 2 Adapted gauge to a quasi-local measure of black hole recoil | 18 |
| 2.1 Introduction | 18 |
| 2.2 Numerical Techniques | 20 |

| | | |
|--|--|------------|
| 2.2.1 | Simulation Parameters | 21 |
| 2.3 | Horizon Formulae | 22 |
| 2.4 | Results for a $q = 1/3$ nonspinning binary | 23 |
| 2.4.1 | Validation for other mass ratios ($q = 1/2, 1/5$) | 32 |
| 2.4.2 | Spinning black holes | 34 |
| 2.5 | Studies with Alternative Gauges | 36 |
| 2.5.1 | ∂_0 -gauge | 38 |
| 2.5.2 | η -variable gauge | 39 |
| 2.6 | Discussion | 44 |
| 3 | An adapted gauge for small mass ratio binaries | 46 |
| 3.1 | Introduction | 46 |
| 3.2 | Numerical Techniques | 48 |
| 3.2.1 | The Initial Gauge | 49 |
| 3.3 | Initial lapse and shift for Boosted and Spinning Black Holes | 55 |
| 3.3.1 | Lorentz-boosted black holes: | 55 |
| 3.3.2 | Spinning black holes: | 61 |
| 3.3.3 | Shift damping parameter η | 62 |
| 3.4 | Simulation Results | 66 |
| 3.4.1 | Results for a $q = 1/7$ nonspinning binary | 67 |
| 3.4.2 | Results for a $q = 1/15$ nonspinning binary | 72 |
| 3.4.3 | Results for a $q = 1/32$ nonspinning binary | 81 |
| 3.4.4 | Results for a $q = 1/64$ and $q = 1/128$ nonspinning binary | 87 |
| 3.4.5 | Noise/spurious radiation versus mass ratio | 91 |
| 3.5 | Discussion and conclusions | 92 |
| 4 | Analytic Analysis of Spacetimes in Generic Transverse Frames. | 102 |
| 4.1 | Accurate Extraction of Gravitational Waves: | |
| From the Weyl Tensor to the quasi-Kinnersley frame | | 103 |

| | | |
|----------|---|--------------|
| 4.2 | Analytic Null Rotation into the quasi-Kinnersley Frame | 107 |
| 4.2.1 | Petrov Types | 110 |
| 4.3 | Finding the Principal Eigenvalue | 111 |
| 4.4 | Calculation of Rotation Parameters \bar{a} and b | 117 |
| 4.4.1 | Reduction to Fourth Order | 118 |
| 4.5 | Analytic Classification of the Spacetime | 121 |
| 4.6 | Analytic Results for Brill-Lindquist Initial Data | 123 |
| 4.6.1 | Study of the location of the ring where $S = 1$ | 129 |
| 4.6.2 | Results: Characterization of maxima, minima, and zeros of S and \mathcal{D} . . . | 130 |
| 4.6.3 | Classification off the symmetry plane | 134 |
| 4.7 | Classification Results: Unequal Mass Binary Study | 136 |
| 4.7.1 | The Surface r_{Ring} | 136 |
| 4.7.2 | Classifying the Spacetime | 137 |
| 4.7.3 | Location of Doughnut $S = 0$ | 139 |
| 4.8 | Numerical Results: Weyl Scalars | 140 |
| 4.9 | Future Work: Extension to Full Numerical Simulation | 144 |
| 5 | Conclusion and Future Work | 145 |
| A | Remnant Fitting: A convenient method of calculating remnant fits in conjunction with the RIT catalog | A.149 |
| A.1 | Fitting Formulas | A.151 |
| A.2 | Program for Generalized Fitting Coefficients | A.154 |
| A.3 | Run on Aligned-Spin only Binaries | A.156 |
| | Appendices | A.149 |
| | Bibliography | 165 |

List of Figures

| | | |
|-----|---|----|
| 1.1 | An infographic of LIGO. Each of the Fabry-Perot cavities (arms) is 4 km long. A laser is sent through a beam splitter, down each of the arms, reflected, and then recombined in the photodetector. If a gravitational wave has passed through the detector, there will be interference that is measurable by the photodetector when the beams are recombined. Schematic taken from [4]. | 3 |
| 1.2 | Figure from [5]. The observed gravitational waves in LIGO Hanford and Livingston (top panel) versus a matching gravitational wave produced by Numerical Relativity simulations (bottom panel). | 4 |
| 1.3 | A schematic of the 3+1 split of spacetime, including the foliation of spatial hypersurface Σ a very good explanation of how the lapse and shift equations describe the coordinates. Taken from [6], page 46. | 12 |
| 2.1 | The horizon measure of the mass and spin after merger of a $q = 1/3$ nonspinning binary versus time for $m\eta = 2$ at resolutions n100, n120, n140. | 24 |

| | | |
|-----|---|----|
| 2.2 | The Hamiltonian constraint behavior versus time for $m\eta = 2$ at resolutions n100, n120, n140 in the top left panel, the (2,2)-waveform as seen by an observer at $r = 113m$ for the $q = 1/3$ nonspinning binary from an initial separation $D = 9m$ in the top right panel, the order of convergence of the Hamiltonian constraint violations in the bottom left, the phase difference (in radians), $\Delta\varphi$, and the amplitude difference between resolutions, $\Delta A/A$, with respect to the infinite resolution extrapolation (n_∞) in the bottom right panel (top and bottom respectively). | 25 |
| 2.3 | The horizon measure of the linear momentum (in km/s) after merger of a $q = 1/3$ nonspinning binary for the three resolutions n100 (dotted), n120 (dashed), and n140 (solid) for $\eta = 2/m$ (blue), $1/m$ (red), $0.5/m$ (green). The reference value of V_f (black solid line) is found by extrapolation to infinite resolution of the radiated linear momentum. | 29 |
| 2.4 | The horizon measure of the linear momentum (in km/s) after merger of a $q = 1/3$ nonspinning binary lowering values of $\eta = 2 \rightarrow 0$ at resolution n140. The reference value of V_f (black solid line) is found by extrapolation to infinite resolution of the radiated linear momentum. | 30 |
| 2.5 | Comparative results of the ∂_t -gauge (solid) and ∂_0 -gauge (dashed) for the horizon measure of the linear momentum (in km/s) after merger of a $q = 1/3$ nonspinning binary for the n140 resolution for $m\eta = 2$ (blue), 1 (green), 0.5 (red). The reference value of V_f is found by extrapolation to infinite resolution of the radiated linear momentum. | 39 |
| 2.6 | The horizon measure of the linear momentum (in km/s) after merger of a $q = 1/3$ nonspinning binary for the three resolutions labeled as n100, n120, and n140 in the ∂_0 -gauge for $\eta = 2/m$. The reference value of V_f is found by extrapolation to infinite resolution of the radiated linear momentum in this ∂_0 -gauge. | 40 |

| | | |
|-----|--|----|
| 2.7 | The horizon measure of the linear momentum after merger of a $q = 1/3$ nonspinning binary for the three resolutions labeled as n100 (dotted), n120 (dashed), and n140 (solid) for $\eta = N12$ (red) and N10 (blue), top to bottom respectively. The reference value of V_f is found by extrapolation to infinite resolution of the radiated linear momentum. | 44 |
| 3.1 | In red is shown the initial lapse $\alpha_0(\psi_0)$ and in blue is the late time lapse α_{LTL} . [This is for a case study with $m_2 = 3/4$, $m_1 = 1/4$, located at $x_1 = -6$ and $x_2 = 2$ respectively, and where we have normalized so that $m_1 + m_2 = 1$]. . . . | 54 |
| 3.2 | In red is the usual zero initial shift, and in blue is the superposition of the individual shifts showing the push away from each black hole. [This is for a case study with $m_2 = 3/4$, $m_1 = 1/4$, located at $x_1 = 2$ and $x_2 = -6$, respectively]. | 55 |
| 3.3 | For small r , β^y for an initial velocity $v = 0.1$ versus $\psi_0 = 1 + m/(2r)$. The horizon of this Schwarzschild black hole is located at $\psi_H = 2$ and spatial infinity is at $\psi_\infty = 1$. We see that the shift decays slowly, like $\psi_0 - 1$ | 57 |
| 3.4 | L2 norm of the Hamiltonian constraint violations versus time for the simulations with $q = 1/3$ and $d = 7m$ separation with initial gauge choices α_0/β_0 from Eqs.(3.2.2), the LTL/LTS choices, and the LTL/LTS + Boost (B) correction. Both of the LT simulations show an early increase in constraint violations, but then drop to acceptable levels within $t = 20m$ | 59 |
| 3.5 | Horizon mass of the small black hole m_1 (top) and the large black hole m_2 (bottom) for a binary with $q = 1/3$ and $d = 7m$ separation with initial gauge choices α_0/β_0 from Eqs.(3.2.2), the LTL/LTS choices, and the LTL/LTS + Boost (B) correction. Both of the simulations that use LT initial data show deviations from constancy of mass - the large black hole m_2 shows mass loss and the small black hole m_1 shows mass increase. | 60 |

| | | |
|------|--|----|
| 3.6 | <p>η_ψ profile for ($m = m_1 + m_2 = 1$ here) $m_2 = 3/4$, $m_1 = 1/4$; $x_1 = 2.5$, $x_2 = -7.5$; $a = 1$, $b = 2$; $A = 1$, $B = 1$. Note that this is technically different from the $\eta(W)$ used in [7] since we use the specific form (3.2.3) for ψ_0 instead of the evolved variable, which is related to the inverse of the conformal factor $W = \sqrt{\chi}$ [8].</p> | 64 |
| 3.7 | <p>η_G profile for ($m = m_1 + m_2 = 1$ here) $m_2 = 3/4$, $m_1 = 1/4$; $x_1 = 2.5$, $x_2 = -7.5$; $A = 1$, $B = 1$, $C = 1$; $\sigma_1 = 2m_1$, $\sigma_2 = 2m_2$. At large separations, $n = 0$ and $n = 2$ show good agreement.</p> | 65 |
| 3.8 | <p>η_G profile for ($m = m_1 + m_2 = 1$ here) $m_2 = 3/4$, $m_1 = 1/4$; $x_1 = 0.5$, $x_2 = -1.5$; $A = 1$, $B = 1$, $C = 1$; $\sigma_1 = 2m_1$, $\sigma_2 = 2m_2$. At small separations $n = 2$ reduces the peaks in Eq. (3.3.46) that using $n = 0$ is designed to produce.</p> | 66 |
| 3.9 | <p>Violations to the Hamiltonian constraint (top) and the x-component of the momentum constraint (bottom) for the $q = 1/7$ binary using resolution n100 with the different gauge choices: G, G+LTL, $\eta = 2/m$ and LZ in red, purple, yellow, and blue respectively. Both G and G+LTL settle to a similar gauge. All gauges produce acceptably-valued constraint violations.</p> | 70 |
| 3.10 | <p>Horizon masses for m_1 and m_2 versus time for the $q = 1/7$ n100 simulations with different choices for $m\eta = G$, LZ, and $2/m$, and the initial lapse, LTL. The $\eta = 2/m$ and LZ gauges produce continuous growth (mass-loss) over the course of the simulation in m_2 (m_1). The G and G+LTL choices maintain both horizon masses well.</p> | 71 |
| 3.11 | <p>The amplitude of the dominant (2,2)-mode of Weyl scalar Ψ_4 for the $q = 1/7$ binary as seen by an observer situated $r = 113m$ from the origin of coordinates. Higher frequency noise of the LZ gauge is apparent at $t \sim (75 - 135)m$ (in the top panel) as is its bounce at the next refinement level at $t \sim (200 - 600)m$ (in the bottom panel). The other gauge choices G, G+LTL, and $\eta = 2/m$ show no high frequency noise early on, as well as substantially reduce high frequency oscillations during inspiral (shown in the bottom panel).</p> | 73 |

| | | |
|------|--|----|
| 3.12 | Horizon masses for m_2 (top) and m_1 (bottom) versus time for the $q = 1/15$ simulation with the different choices for $m\eta$, G, LZ, and $\eta = 2/m$. The dashed, dot-dashed, and solid lines are the low n084, medium n100, and high n120 resolutions respectively. The horizon masses m_1 and m_2 deviate from constant most dramatically when the LZ gauge is used. Both the $\eta = 2/m$ and G gauges maintain the masses of the horizons well over the course of the simulation, except at the lowest resolution n084. | 76 |
| 3.13 | Radial average size of each of the horizons of the $q = 1/15$ binary versus evolution time for the different gauge choices. The three resolutions using the LZ gauge lie on top of each other, as do the three resolutions using the G gauge. In both m_1 and m_2 these gauges maintain the coordinate size of the horizons well over the full inspiral. The $\eta = 2/m$ is only shown in one resolution (n100), and the associated horizons m_1 and m_2 grow continuously throughout the simulation. | 78 |
| 3.14 | The amplitude of the dominant mode of Ψ_4 for the $q = 1/15$ binary extracted at an observer location of $r = 113m$. The waveform is shown for G and LZ in three resolutions and $\eta = 2/m$ in one. In the top panel, higher frequency noise of the LZ gauge early on at $t \sim (75 - 135)m$ and its bounce at the next refinement level in the second panel from $t \sim (200 - 600)m$ is apparent. | 80 |
| 3.15 | Horizon masses for m_2 (top) and m_1 (bottom) versus time for the $q = 1/32$ simulation with the different choices for $m\eta$, G, LZ, and $\eta = 2/m$. The dashed, dot-dashed, and solid lines are the low n084, medium n100, and high n120 resolutions respectively. The horizon masses m_1 and m_2 deviate from constant most dramatically when the LZ gauge is used. Both the $\eta = 2/m$ and G gauges maintain the mass of the horizon well over the course of the simulation, except at the lowest resolution n084. | 84 |

| | | |
|------|--|----|
| 3.16 | The amplitude of the Ψ_4 waveform of the $q = 1/32$ binary extracted at an observer located at $r = 113m$. The top panel shows the early part of the waveform from $t = (75 - 135)m$, and the bottom panel shows the inspiral period from $t = (200 - 900)m$. Higher frequency noise of the LZ gauge is apparent at $t \sim (90 - 100)m$, which is damped by the G and $\eta = 2/m$ gauges. Refinement boundary reflections of the high frequency noise are apparent in the second panel, which shows a longer inspiral. | 85 |
| 3.17 | Inspiral (top) and ringdown (bottom) periods of the gravitational wave strain $h_{2,2}$ of the mid-resolution simulations of the $q = 1/32$ binary using the G, LZ, and $\eta = 2/m$ gauges. In the inspiral, the waveform using the $\eta = 2/m$ gauge exhibits oscillatory behavior which is not present in either of the variable gauges. However, post-merger, the waveform using LZ exhibits oscillations, whereas the G and $\eta = 2/m$ waveforms do not. This suggests that a variable gauge is useful during inspiral, and a more constant gauge is most effective post-merger. . . . | 95 |
| 3.18 | Horizon masses for m_1 and m_2 versus time for the $q = 1/64$ simulation. The masses in the LZ gauge are shown in two resolutions n084 and n100, and the masses in the G gauge are shown in only n100. The masses using G are more constant than their counterparts that use the LZ gauge, especially in the case of the small black hole m_1 | 96 |
| 3.19 | Horizon masses for m_1 and m_2 versus time for the $q = 1/128$ simulation. The masses in both the LZ and G gauges are shown in only n100. The large black hole m_2 using the LZ gauge is held slightly more constant than its counterpart that uses the G gauge, however the LZ gauge simulation has significantly more noise than the G gauge one. | 97 |

| | | |
|------|---|-----|
| 3.20 | The amplitude of the Ψ_4 waveform of the $q = 1/64$ extracted at an observer located at $r = 113m$. The top panel shows the early part of the waveform from $t = (75 - 135)m$, and the bottom panel shows the inspiral period from $t = (200 - 900)m$. Higher frequency noise of the LZ gauge is apparent at $t \sim (95 - 100)m$, which is damped by the G and $\eta = 2/m$ gauges. Refinement boundary reflections of the high frequency noise are apparent in the second panel, which shows a longer inspiral. | 98 |
| 3.21 | The amplitude of the Ψ_4 waveform of the $q = 1/128$ extracted at an observer located at $r = 113m$. The top panel shows the early part of the waveform from $t = (75 - 135)m$, and the bottom panel shows the inspiral period from $t = (200 - 800)m$. Higher frequency noise of the LZ gauge is apparent at $t \sim (95 - 100)m$, which is damped by the G and $\eta = 2/m$ gauges. Refinement boundary reflections of the high frequency noise are apparent in the second panel, which shows a longer inspiral. | 99 |
| 3.22 | Inspiral (top) and ringdown (bottom) amplitudes for the $q = 1/64$ binary using the G and LZ gauges with resolutions n084 and n100. There is no clear difference between gauges in the inspiral, however, in the ringdown period, $h_{2,2}$ using the LZ gauge exhibits oscillations that are larger in amplitude and slightly higher in frequency than $h_{2,2}$ using the G gauge. | 100 |
| 3.23 | The data points show the ratio $\mathcal{N}_{peak}/\mathcal{S}_{peak}$ of $\Psi_4^{2,2}$ extracted at $r = 113m$ for each mass ratio q . The black line is a power law fit to the data $F(q) = 9.9753q^{0.8557}$. Errors are shown in Table 3.8. | 101 |
| 4.1 | Eigenvalues for a BBH system with Brill-Lindquist initial data for $q = 1$ on the equatorial plane $\theta = \pi/2$. The black holes are at $z = \pm 5$. At approximately $r = 5.2$, the principal eigenvalue must be switched from λ_1 so that it remains smooth. | 113 |
| 4.2 | The grid set up for our initial data simulation of two equal-mass black holes in a head-on collision. | 113 |

| | | |
|------|--|-----|
| 4.3 | S invariant for the $q = 1$, $d = 10$ BL initial data system. At approximately $r = 5.2$, $S = 1$. This corresponds to the location where the principal eigenvalue must be switched from λ_1 | 114 |
| 4.4 | Eigenvalues for a BBH system with Brill-Lindquist initial data for $q = 1$ at $\theta = \pi/2$, but with forced branch cuts when $J = 0$. The black holes are at $z = \pm 5$. Before determining the principal branch, here it would be necessary to force continuity in the eigenvalues except at the point $r \approx 5.2$ | 115 |
| 4.5 | Eigenvalues for a BBH system with Brill-Lindquist initial data for $q = 1$ on the symmetry plane $\theta = \pi/2$. The black holes are at $r = \pm 5$ on the z -axis. At approximately $r = 5m$, the principal eigenvalue must be switched from λ_1 so that it remains smooth. | 125 |
| 4.6 | Eigenvalues for a BBH system with Brill-Lindquist initial data for $q = 1$ at $\theta = \frac{8\pi}{15}$. The black holes are at $z = \pm 5$. On the whole spacetime, the principal eigenvalue remains λ_1 | 126 |
| 4.7 | A plot of $\log \xi = \Psi_0^{QK}\Psi_4^{QK} $ for Ψ_0 and Ψ_4 in all four transverse frames on the plane $\theta = \frac{\pi}{2}$. The scalars ξ_2 and ξ_3 are quasi-Kinnersley since $\xi \rightarrow 0$ as $S \rightarrow 1$ (equivalently, $r \rightarrow \infty$). The red point in the green curve comes from the fact that there is only one transverse frame at that point, so all four values of ξ coincide. This will be discussed in Section 4.6.1. | 127 |
| 4.8 | The value of Ψ_4 for the two roots a_2 and a_3 (left and right), where $\xi \rightarrow 0$ as $S \rightarrow 1$. For root 2, Ψ_4 has the expected behavior, heading to 0 as $r \rightarrow \infty$, for root 3, Ψ_4 diverges. | 128 |
| 4.9 | The Weyl scalars $\log \Psi_0^{QK} $, $\log \Psi_2^{QK} $, and $\log \Psi_4^{QK} $ shown on the xy -plane for the head-on, equal mass BBH case. | 128 |
| 4.10 | The radius of the ring r_{Ring} versus the initial binary separation d of the $q = 1$ Brill-Lindquist system. The ring is always on the equatorial plane, and is always approximately the same distance from the origin on the xy -plane as the singularities are on the z -axis. | 129 |

4.11 The Speciality invariant S on the xy - and xz -planes (left/right) for a $q = 1$ binary with separation $d = 10m$ located on the z -axis. Other than far from the black holes and between the black holes, the only region of algebraic speciality is located in a ring on the x -axis at $r = 5m$ 130

4.12 \mathcal{D} and S invariants in the quasi-Kinnersley frame for the $q = 1, d = 10m$, binary black hole case with Brill-Lindquist initial data on a slice through the symmetry plane $\theta = \frac{\pi}{2}$. The index \mathcal{D} associated with the quasi-Kinnersley frame goes to -2 asymptotically, intersects with \mathcal{D}_3 and then switches branches to be on the branch associated with λ_3 132

4.13 The ring of points on the xz -axis where $S = 0$ (left). This ring rotates around the z -axis, forming a hollow "doughnut" of points in space where $S = 0$ (right). As resolution increases, the points will approach a continuous ring on the xz -plane. 133

4.14 D-ality and S invariants in the quasi-Kinnersley frame for the $q = 1, D = 10m$, binary black hole case with Brill-Lindquist initial data on a slice through cone $\theta = \frac{8\pi}{15}$ 136

4.15 The radius of the ring r_{Ring} versus the initial binary separation d of the $q = 1/3$ Brill-Lindquist system. The ring always occurs near $\theta \approx 19\pi/15$ (shown here). There is a distinctly linear relationship between r_{Ring} for each binary and the binary's separation. 137

4.16 The Speciality invariant S on the xy - and xz -planes (left/right) for a $q = 1/3$ binary with separation $d = 7m$ located on the z -axis. Other than far from the black holes and between the black holes, the only region of algebraic speciality is located in a ring with radii in the centers of the "eyes" in the right hand plot. The coordinates of the ring are $(r_{Ring}, \theta_{Ring}) \approx (4.6, 19\pi/15)$ 138

4.17 D-ality and S invariants in the quasi-Kinnersley frame for the $q = 1/3, d = 7m$, binary black hole case with Brill-Lindquist initial data on the conical slice $\theta = \frac{19\pi}{15}$. 139

| | | |
|------|---|-------|
| 4.18 | The location of the doughnut $S = 0$ on the xz -plane for the $q = 1/3$, $d = 7m$ separated Brill-Lindquist system (left). Because of ϕ -symmetry, the ellipsoid shown is rotated around the z -axis forming a hollow doughnut where $S = 0$ (right). | 139 |
| 4.19 | Real part of Ψ_0 for a $q = 1$, $d = 10m$ binary with Brill Lindquist initial data in the QK frame calculated using numerical initial data generated by the TwoPunctures thorn. | 142 |
| 4.20 | Real part of Ψ_2 for a $q = 1$, $d = 10m$ binary with Brill Lindquist initial data in the QK frame calculated using numerical initial data generated by the TwoPunctures thorn. | 143 |
| 4.21 | Real part of Ψ_4 for a $q = 1$, $d = 10m$ binary with Brill Lindquist initial data in the QK frame calculated using numerical initial data generated by the TwoPunctures thorn. | 143 |
| A.1 | (Top) Known values of remnant horizon mass for all 477 aligned spin runs (blue circles) and reproduced values using the fitting formula (red cross). (Bottom) Natural log of residuals between fits and data points. | A.159 |
| A.2 | (Top) Known values of remnant horizon spin for all 477 aligned spin runs (blue circles) and reproduced values using the fitting formula (red cross). (Bottom) Natural log of residuals between fits and data points. | A.160 |
| A.3 | (Top) Known values of remnant horizon recoil velocity for all 477 aligned spin runs (blue circles) and reproduced values using the fitting formula (red cross). (Bottom) Natural log of residuals between fits and data points. | A.161 |
| A.4 | (Top) Known values of peak luminosity for all 477 aligned spin runs (blue circles) and reproduced values using the fitting formula (red cross). (Bottom) Natural log of residuals between fits and data points. | A.162 |
| A.5 | (Top) Known values of gravitational wave amplitude for all 477 aligned spin runs (blue circles) and reproduced values using the fitting formula (red cross). (Bottom) Natural log of residuals between fits and data points. | A.163 |

A.6 (Top) Known values of gravitational wave frequency for all 477 aligned spin runs (blue circles) and reproduced values using the fitting formula (red cross).
(Bottom) Natural log of residuals between fits and data points. A.164

List of Tables

2.1 The final black hole mass (m_f/m) for different η and resolutions (top table).
 Difference between final black hole and ADM masses (bottom table). Values
 for $m\eta \rightarrow 0.0$ and resolution $h_i \rightarrow 0$ are extrapolated (the latter by order n). 26

2.2 The final black hole spin (α_f/m^2) for different η and resolutions (top table).
 Difference between final black hole angular momentum α_f and initial ADM
 angular momentum J_{ADM} (bottom table). Values for $m\eta = 0.0$ are extrapolated
 as those for infinite resolution $h_i \rightarrow 0$ with order n 26

2.3 Energy radiated away in gravitational waves up to $\ell = 6$ for the $q = 1/3$
 nonspinning binary. Values for $m\eta = 0.0$ are extrapolated. Convergence order
 calculated from the three resolutions, n , and using the two highest resolutions
 and assuming the converged value is the value calculated on the horizon, $n(AH)$. 27

2.4 Angular momentum radiated away in gravitational waves up to $\ell = 6$ for the
 $q = 1/3$ nonspinning binary. Values for $m\eta = 0.0$ are extrapolated. Conver-
 gence order calculated from the three resolutions, n , and using the two highest
 resolutions and assuming the converged value is the value calculated on the
 horizon, $n(AH)$ 27

2.5 Total linear momentum radiated in gravitational waves up to $\ell = 6$ for the
 $q = 1/3$ nonspinning binary in km/s. Values for $m\eta = 0.0$ are extrapolated.
 Convergence order n is extrapolated to infinite resolution $h_i \rightarrow 0$. Bottom panel
 shows the angle (in degrees) of the net momentum with respect to the initial
 x-axis. 31

| | | |
|------|---|----|
| 2.6 | Horizon linear momentum measured at the interval $t = 950m - 1250m$ for the $q = 1/3$ nonspinning binary in km/s. The bottom panel gives the angle (in degrees) this magnitude subtends with the initial x-axis. The measured standard deviation is given by the \pm in the relevant quantities. Convergence order and extrapolations are given for $h_i \rightarrow 0$ and $\eta \rightarrow 0$ | 31 |
| 2.7 | Coordinate trajectory velocity in km/s as measured at $575m$ after merger for the $q = 1/3$ nonspinning binary. | 32 |
| 2.8 | Comparison of the computation of the recoil velocity (in km/s) of the remnant of a $q = 1/2$, nonspinning binary by traditional radiation of linear momentum and the horizon formula (2.1.1) averaged between $t = 1550m$ and $t = 1850m$ for the traditional $\eta = 2$ and for the $\eta = 0.5$ case. Extrapolation to infinite resolution and convergence order is also given for the horizon and radiative extraction. The bottom panel gives the angle (in degrees) of the recoil velocity with respect to the x-axis. Standard deviations of horizon measurements are given as \pm for each quantity. Convergence with numerical resolution is also given. | 33 |
| 2.9 | Comparison of the computation of the horizon mass and spin of the remnant of a $q = 1/2$, nonspinning binary with the radiation of the energy and angular momentum for the $\eta = 2$ and for the $\eta = 0.5$ cases. Extrapolation to infinite resolution and convergence order is also given for the horizon computation and the radiative extraction. | 34 |
| 2.10 | Comparison of the computation of the horizon mass and spin of the remnant of a $q = 1/5$, nonspinning binary with the radiation of the energy and angular momentum for the $\eta = 2$ and for the $\eta = 0.5$ cases. Extrapolation to infinite resolution $h_i \rightarrow 0$ and convergence order n is also given for the horizon computation and the radiative extraction. | 35 |

| | | |
|------|--|----|
| 2.11 | Comparison of the computation of the recoil velocity (in km/s) of the remnant of a $q = 1/5$, nonspinning binary by traditional radiation of linear momentum and the horizon formula (2.1.1) averaged between $t = 2300m$ and $t = 2500m$ for the traditional $\eta = 2$ and for the $\eta = 0.5$ case. Extrapolation to infinite resolution $h_i \rightarrow 0$ and convergence order n is also given for the horizon and radiative extraction. The bottom panel gives the angle (in degrees) of the recoil velocity with respect to the x-axis. Standard deviations of horizon measurements are given as \pm for each quantity. | 36 |
| 2.12 | Comparison of the computation of the recoil velocity (in km/s) of the remnant of a $q = 1$, $\alpha_i = \pm 0.8$ binary by traditional radiation of linear momentum and the horizon formula (2.1.1) averaged between $t = 1050m$ and $t = 1350m$ for the traditional $\eta = 2$ and the $\eta = 1$ and 0.5 cases. Extrapolation to infinite resolution $h_i \rightarrow 0$ and convergence order n is also given for the radiative extraction. The bottom panel gives the angle (in degrees) of the recoil velocity with respect to the x-axis. Standard deviations of horizon measurements are given as \pm for each quantity. In this case $m\eta = 1$ produces a better measure of recoil velocity than other choices of $m\eta$ | 37 |
| 2.13 | Comparison of the computation of the horizon mass and spin of the remnant of a $q = 1$, $\alpha_i = \pm 0.8$ binary with the radiation of the energy and angular momentum for the $m\eta = 2$ and for the $m\eta = 0.5$ cases. Extrapolation to infinite resolution $h_i \rightarrow 0$ and convergence order n is also given for the radiative extraction. | 38 |

- 2.14 Comparison of the computation of the recoil velocity (in km/s) of the remnant of a $q = 1/3$, $\alpha_i = \pm 0$ binary by traditional radiation of linear momentum and the horizon formula (2.1.1) measured $75m$ after merger. Computation uses the ∂_0 -gauge $m\eta = 2$ case for resolutions n100 n120 and n140 and ∂_0 -gauge $m\eta = 1, 0.5$ cases for resolution n140. Extrapolation to infinite resolution $h_i \rightarrow 0$ and convergence order n is also given for the radiative extraction for appropriate cases. The bottom panel gives the angle (in degrees) of the recoil velocity with respect to the x-axis. Standard deviations of horizon measurements are given as \pm for each quantity. Compare this results with those of Tables 2.5-2.6. 41
- 2.15 Top panel shows the comparison of the computation of the recoil velocity (in km/s) of the remnant of a $q = 1$, $\alpha_i = \pm 0.80$ binary by traditional radiation of linear momentum and the horizon formula (2.1.1) averaged from $t/m = 1050$ to 1350 using the ∂_0 -gauge with $m\eta = 2$ and $m\eta = 0.5$ case at resolutions n100 and n120. The bottom panel gives the angle (in degrees) of the recoil velocity with respect to the x-axis. Both panels give also the ∂_t results from Table 2.12 for comparison. Standard deviations of horizon measurements are given as \pm for each quantity. 42
- 2.16 Comparison of the computation of the recoil velocity (in km/s) of the remnant of a $q = 1/3$, $\alpha_i = 0$ binary by traditional radiation of linear momentum and the horizon formula (2.1.1) measured $75m$ after merger for the modified N12 and N10 gauges. The standard $m\eta = 1$ from Tables 2.5 and 2.6 is also provided for reference. Extrapolation to infinite resolution $h_i \rightarrow 0$ and convergence order n is also given for the radiative extraction. The bottom panel gives the angle (in degrees) of the recoil velocity with respect to the x-axis. Standard deviations of horizon measurements are given as \pm for each quantity. 43

| | | |
|------|---|----|
| 2.17 | Comparison of the computation of the recoil velocity (in km/s) of the remnant of a $q = 1$, $\alpha_i = \pm 0.80$ binary by traditional radiation of linear momentum and the horizon formula (2.1.1) measured from $t/m = 1050$ to 1350 for the modified N12 and N10 gauges using $m\eta \rightarrow 1$ asymptotically, as well as $m\eta = 1.0$ for comparison. The bottom panel gives the angle (in degrees) of the recoil velocity with respect to the x-axis. Standard deviations of horizon measurements are given as \pm for each horizon quantity. | 43 |
| 3.1 | A full of initial data parameters for the simulations performed. The smaller black hole is labeled 2 and larger black hole labeled 1. The punctures are located at $r_i = (x_i, 0, 0)$ with initial momenta $P = \pm(P_r, P_t, 0)$ and mass-ratio q . All simulations are nonspinning. A full study with 3 resolutions for all gauge choices was done on the $q = 1/15$ binary, but results are shown for simulations 5-7, 9, and 11-13 because simulation 8 could only be completed with a in increase in time resolution (CFL $1/3 \rightarrow 1/4$). The $q = 1/32$ binary has three resolutions for the LZ and G gauge choices. The smaller $q = 1/64$ and $q = 1/128$ as well as the larger $q = 1/7$ mass ratios are used for verification. All simulations use eighth order finite differencing in space. | 67 |
| 3.2 | For the $q = 1/7$ binary, the total linear momentum (km/s) calculated in two ways: (1) measured quasi-locally on the horizon averaged over $t = (2600 - 2800)m$, in column 4, and (2) measured by the amount radiated away in gravitational waves, in column 5. All simulations have resolution $n100$ as well as CFL=1/3 and 8th order finite differencing stencils. The gauges G and G+LTL allow for the most accurate measure of horizon recoil when compared against the radiated value. | 72 |

| | | |
|-----|---|----|
| 3.3 | The slopes (\mathcal{A} , columns 3 and 5) of linear fits to the horizon masses m_1 and m_2 computed over the inspiral $t = 100m$ to 1000 for the $q = 1/15$ binary using $\eta = G$, LZ, and $2/m$. Error is calculated via root mean square error over the interval, and is shown in columns 4 and 6. The time frame is chosen so a linear fit is a reasonable approximation of the mass curves. The G and LZ simulations have 3 resolutions: n084, n100, n120, and the $\eta = 2/m$ simulation has 1 resolution: n100. The G gauge produces a reliably constant value for the horizon mass, even at low resolution, whereas the mid- and low- resolution LZ simulations show large changes in mass (reflected in the slopes \mathcal{A}) as well as higher error values overall. | 75 |
| 3.4 | For the $q = 1/15$ binary, the total mass, angular, and linear momentum (1) measured by the amount radiated away in gravitational waves, in columns 3-5, and (2) measured quasi-locally on the horizon, in columns 6-8. Extrapolations to infinite resolution ($n\infty$) and convergence order (CO) are included where applicable. All simulations have resolution specified in column 3 as well as CFL=1/3 and 8th order finite differencing stencils. A dash indicates no convergence was found. | 81 |
| 3.5 | The slopes (\mathcal{A} , columns 3 and 5) of linear fits to the horizon masses m_1 and m_2 computed over the inspiral $t = (0 - 1000)m$ for the $q = 1/32$ binary using $\eta = G$, LZ, and $2/m$. Error is calculated via root mean square error over the interval, and is shown in columns 4 and 6. The time frame is chosen so a linear fit is a reasonable approximation of the mass curves. The G and LZ simulations have 3 resolutions: n084, n100, n120, and the $\eta = 2/m$ simulation has 1 resolution: n100. The G gauge provides an effective gain in resolution of a factor of 2 in the horizon mass. | 83 |

| | | |
|-----|---|-----|
| 3.6 | For the $q = 1/32$ binaries using G, LZ, and $\eta = 2/m$, the resolutions are given in column 2. The horizon quantities (energy and angular momentum) are in columns 3 and 4, and the corresponding radiated quantities are in columns 5-7. All simulations use CFL=1/4 and 8th order finite differencing stencils. The G gauge does a good job of measuring the horizon mass and spin, however, the horizon linear momentum requires high resolution to approach the radiated linear momentum. | 87 |
| 3.7 | The horizon quantities for the $q = 1/64$ binary using the G and LZ gauges and the $q = 1/128$ binary using the LZ gauge. The remnant quantities for the $q = 1/128$ binary in the G gauge are not included since that simulation was not run through merger. The resolutions are given in column 3. The horizon quantities (energy and angular momentum) are in columns 4-5, and the corresponding radiated quantities are in columns 6-8. All simulations use CFL=1/4 and 8th order finite differencing stencils. The G gauge does a good job of measuring the horizon mass and spin, however, the horizon linear momentum requires high resolution to get close to the radiated measure, and is therefore not shown. | 90 |
| 3.8 | The absolute and relative errors between $F(q)$ for all q and $\mathcal{N}_{peak}/\mathcal{S}_{peak}$ and standard deviation for $\Psi_4^{2,2}$ extracted at $r = 113m$ using resolution n100. | 92 |
| 4.1 | Special Petrov types in terms of G , H and K | 122 |
| 4.2 | Summary of the values of the scalars S and \mathcal{D} at different r -locations in different Transverse frames (QK, 2, and 3) and the associated Petrov type for the $q = 1$ Brill-Lindquist binary on $\theta = \pi/2$. We are using the transverse frame 2 for classification. When $\mathcal{D} = \pm 1.73$ and $S = 0$ the spacetime is Petrov type I, but is closer to Petrov type II than Petrov type D. When $\mathcal{D} = \pm 1.5$, the spacetime is halfway between Petrov types II and D. | 135 |

| | | |
|-----|---|-------|
| 4.3 | Summary of the values of the scalars S and \mathcal{D} at different r - locations in different Transverse frames (QK, 2, and 3) and the associated Petrov Type for the $q = 1$ Brill-Lindquist binary on $\theta = 19\pi/15$. Note that for $r \leq r_{Ring}$, frames QK and 3 flip places when $S = 1$ at r_{Ring} . | 140 |
| A.1 | Table of fitting parameters for mass and spin formulae using only aligned spin binaries. | A.157 |
| A.2 | Table of fitting parameters for recoil (in Km/s) and peak luminosity formulae using only aligned spin binaries. | A.157 |
| A.3 | Table of fitting parameters for peak amplitude and peak frequency formulae using only aligned spin binaries. | A.158 |

Chapter 1

Introduction

1.1 First Detection of Gravitational Waves

On September 14, 2015, the Laser Interferometer Gravitational Wave Observatory (LIGO) detected a gravitational wave signal from the merger of two binary black holes approximately 1.3 billion light-years away [5]. The detection of gravitational waves from this system (GW150914) was the first of its kind. This detection confirmed the existence of gravitational waves and assured of the correctness of the Theory of General Relativity, spurring newfound interest in relativistic research from both the observational and computational sides. In the years since, LIGO and its European counterpart, Virgo, have detected 50 signals from merging compact objects, including a neutron star/neutron star pair (GW170817) and suspected black hole/neutron star pairs. These detections have pushed researchers to study not only black hole binary simulations, but also mergers of compact objects containing matter.

1.1.1 How do we detect gravitational waves?

The gravitational wave detectors that are currently active are ground-based Michelson interferometers. Currently, there are three active detectors; two are part of LIGO: one in Livingston, Louisiana, and one in Hanford, Washington, and one is part of Virgo, located in Italy. More detectors are planned in Japan and India, and sensitivity upgrades to currently active detectors increase the number of compact object mergers we can observe. Many powerful detectors

placed at significant distances from each other not only help to verify that a detection is actually a gravitational wave and eliminate sources of noise, but also constrain the source sky localization [9, 10, 11, 12, 13, 14].

Also planned is a space-based detector, the Laser-Interferometer Space Antenna (LISA), developed by an international consortium of scientists [15, 16, 17, 18, 19, 20, 21]. LISA will be triangular, with three 2.5 million km long arms, and will be trailing Earth, in its orbit around the sun, by 20 degrees. LISA's proposed sensitivity falls in the low-frequency, high-gravitational wave strain region - in other words, it will be able to detect mergers of compact objects that orbit around each other for a long time before merging (referred to as long inspiral periods). These are undetectable by LIGO/Virgo because the frequency of the gravitational waveforms is too low. Typically, these types of objects are expected to be highly precessing or of very high mass-ratio (i.e. one black hole is many times the size of the other). LISA's approval has motivated the study of such pairs of binary black holes and, recently, RIT researchers have been able to simulate a binary black hole pair with mass-ratio $q = m_1/m_2 = 1/128$ [22], which is the smallest mass-ratio to ever have been simulated.

Figure 1.1 helps to illustrate exactly how a LIGO Interferometer works. This detector uses very powerful lasers to detect the Earth's stretching and squeezing due to the passage of a gravitational wave.

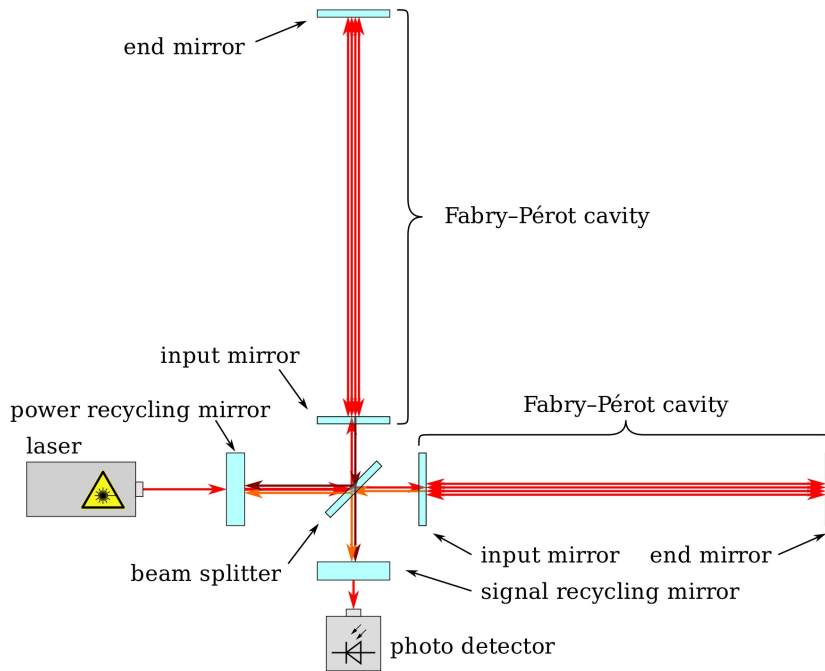


Figure 1.1: An infographic of LIGO. Each of the Fabry-Perot cavities (arms) is 4 km long. A laser is sent through a beam splitter, down each of the arms, reflected, and then recombined in the photodetector. If a gravitational wave has passed through the detector, there will be interference that is measurable by the photodetector when the beams are recombined. Schematic taken from [4].

Figure 1.1 shows cartoon of a LIGO interferometer with its components labeled. It works by shooting a laser into the beam splitter, which sends photons down each of the 4km long perpendicular arms to mirrors that reflect each laser nearly 280 times before the split lasers merge again. These reflections help increase the sensitivity of the detector by increasing the distance traveled by each beam of photons from 4 km to 1120 km. High sensitivity is vital, since gravitational waves produce a variation in arm length on the order of less than 1/10000th the size of a proton [5].

When a gravitational wave (GW) passes through the LIGO interferometer, the length of one arm will be shortened and the other lengthened by a very small amount, and as the wave passes through the detector, the sizes of the arms oscillate back and forth. This change in arm length causes the lasers in each of the arms to become slightly out of phase with each other, which is measurable when the two beams are recombined in the beam splitter and sent to the

photodetector. This interference pattern is what is detected, measured, and plotted by LIGO, and both detectors' results are compared to eliminate sources of external noise and verify that a GW source has actually passed through the detector.

1.1.2 First Detection

During the first (O1) run of LIGO, a signal was detected on September 14, 2015 and determined to be a gravitational wave with a confidence level of 5.1σ [5]. Comparison with Numerical Relativity simulations of gravitational wave strain from binary black hole mergers allowed for the determination of the total mass of the system (62_{-3}^{+4} solar masses), the mass of each black hole (36_{-4}^{+5} and 29_{-4}^{+4} solar masses), and the amount of mass radiated away in gravitational waves ($3_{-0.5}^{+0.5}$ solar masses) [5] during the inspiral and merger. Figure 1.2, from [5], shows the observed gravitational wave strain overlaid with Numerical Relativity simulations whose black holes produce gravitational waveforms matching those observed by the detector.

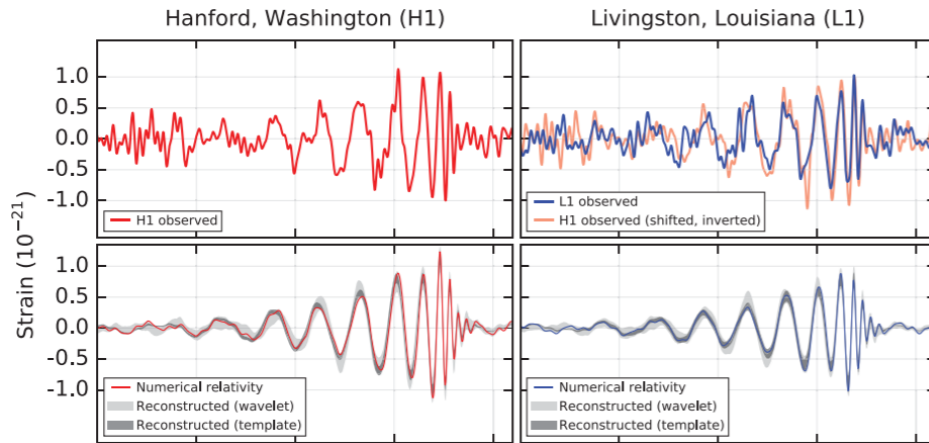


Figure 1.2: Figure from [5]. The observed gravitational waves in LIGO Hanford and Livingston (top panel) versus a matching gravitational wave produced by Numerical Relativity simulations (bottom panel).

In order to verify that what passed through LIGO's detectors on September 14, 2015 was in fact a gravitational wave, there needed to be a model with which to compare the observations. Numerical relativists produced models of gravitational waveforms (as in the bottom panel of Figure 1.2) by solving the Einstein field equations on a four dimensional spacetime grid

(3 spatial dimensions + 1 time dimension). These types of simulations are highly nontrivial and require weeks to months of supercomputer time to produce accurate results. In fact, until fairly recently, numerical relativists were unable to evolve a binary black hole system through merger. In 2005, three separate research groups [23], [8], and [24] produced three independent codes to solve the ten coupled Einstein field equations; two codes use a moving-puncture approach and adaptive mesh refinement while the third uses excision of the black hole horizons. We will discuss some of the techniques used in a more sophisticated fashion throughout the dissertation, however, an in depth comparison among the techniques is given in [25].

The radiation output of these numerical relativistic simulations is compared directly to gravitational wave data obtained by the LIGO Scientific Collaboration (LSC). The current generation of GW detectors are able to identify many coalescing BHBs per year [11, 26, 27, 28, 29, 30] over a broad range of (redshifted) masses between $20M_{\odot}$ and $200M_{\odot}$ where $1M_{\odot}$ indicates 1 solar mass. These BHBs are generally of comparable mass, are spinning and precessing, and have a short, but rich, multimodal signal. In much of this mass region, Numerical Relativity and hybrids are immediately actionable, with waveforms and frequency content comparable to relevant data. The signal brevity – relatively few cycles can be detected due to LIGO’s frequency band range – also ensures a broad posterior distribution, comparable to inter-simulation spacing. For this reason, Numerical Relativity has an extremely significant role to play in the interpretation of these kinds of events, both as synthetic signals used to validate existing search and parameter estimation algorithms, as well as parameter estimation templates, directly comparable to the data itself.

While the LIGO detectors’ sensitivities are attuned to comparable mass binary black hole pairs, with the third generation of gravitational wave detectors on the horizon, researchers will be able to detect binaries with extreme differences in size. As such, numerical simulation accuracy as well as thorough coverage of the parameter space are vitally important.

The more advanced, space-based detector, the Laser Interferometer Space Antenna (LISA), is proposed to be launched in 2034. It is meant to trail Earth’s orbit around the sun, at an

angle of 20 degrees. Instead of the traditional T shape, LISA will be triangular, with detectors at each node and 2.5 million km long arms [21]. LISA's design allows for the detection of low-frequency long inspiral gravitational waves, such as continuous waves or those produced by binaries with very small mass ratios.

For a number of reasons that will be discussed throughout this dissertation, these types of binaries are very challenging to numerically simulate. They have long inspiral periods, and require precise calculations of the binary parameters (mass, spin, and linear momentum) and radiated output in order to be accurately compared with the waveforms that will be detected by LISA. Over the next decade, advancements must be made in the numerical relativistic simulations of small mass-ratio binaries in order to verify that the detections received from next-generation gravitational wave detectors can be successfully identified as BBH mergers.

1.2 The importance of Numerical Relativity

"I have bet these numerical relativists that gravitational waves will be detected from black-hole collisions before their computations are sophisticated enough to simulate them. I expect to win, but hope to lose, because the simulation results are crucial to interpreting the observed waves."

-Reference: K.S. Thorne, "Spacetime Warps and the Quantum World: Speculations About the Future," in R.H. Price, ed., 'The Future of Spacetime' (W.W. Norton, New York, 2002).

In fact, this problem was solved in 2005 with the breakthroughs in Numerical Relativity; in particular by the first generic, long term Binary Black Hole (BBH) evolutions of [31].

Numerical Relativity uses an algorithmic, iterative approach to solve the ten coupled non-linear partial differential equations of general relativity. To do this, relativists must employ supercomputers to study the coalescence of compact binary objects. A typical simulation is carried out as follows; first the initial data of the system is calculated based on what we *want* the system to look like - particularly, the mass ratio q , the magnitudes and directions of the

spins a_1 and a_2 of the black holes, the initial momenta of the individual black holes, and the initial separation d of the binary, all in geometrized units which are scaled such that the gravitational constant and speed of light are $G = c = 1$, respectively. This initial data is then used in conjunction with the Einstein Toolkit¹, a collaborative code used specifically for solving the Einstein field equations and setting up the computational grid that is contributed to by groups across the world. RIT has its own set of initial data and evolution “thorns” in the Toolkit (HiSPID and LazEv, respectively), which are used in conjunction with the Cactus thorns to structure the four-dimensional grid.

Numerical Relativity simulations have the benefit of providing us with a solution that is both correct (often up to machine precision) and informative. It is important to have very accurate results for the physical parameters (mass, spin, momentum, etc.), as well as the gravitational waveform for accurate comparison to detector output. A large catalogue of waveforms helps to fill out the parameter space so that more extremal (in mass and spin) binaries can be studied, and analytic formulae that take in the binary’s initial parameter and return approximated quantities of the remnant can be perfected [1, 32, 33, 3].

The detriment of the high accuracy requirement of Numerical Relativity (NR) on solutions to the Einstein field equations (EFEs) is the significant computational cost. Increasing grid resolution to improve output accuracy is not always feasible. The grid itself discretizes the spacetime into millions of points on a three dimensional grid, and the Einstein field equations must be solved at each of these points as well as evolved through time. In spite of this, RIT’s catalog [2, 34, 35] consists of 777 simulations of binary pairs, all with different initial masses, spins, and separations, along with precessing and eccentric binaries. The parameter space is well covered with the exception of the extreme cases - binaries with high spin and/or small mass-ratios. Highly spinning binaries require high resolution around the black holes in order to properly capture the dynamics [36]. Small mass-ratio binaries require very high resolution around the small black hole in order for it to be resolved. RIT has been successful in evolving binaries with mass-ratios of up to $q = 1/128$ [22], but such a small mass-ratio binary can take more than 6 months on the fastest computers available today. The coming

¹<https://einstein toolkit.org/>

generations of gravitational wave detectors will be able to detect low-frequency, long-inspiral waveforms, possibly in the extreme mass-ratio regime. We would like to fill the parameter space with these types of binaries so that our catalogue is robust prior to these detections. Since computational expense will always be an issue that requires mitigation, finding methods of improving simulation accuracy, without requiring resolution increase, is vital and will be a main focus of this dissertation.

Accuracy improvements can also be done at the level of radiation extraction. RIT extracts gravitational radiation using one of the five Weyl scalars, Ψ_4 , that is representative of outgoing radiation in the system. The scalars Ψ_0 and Ψ_2 represent the ingoing radiation and the Coulomb field, respectively, but Ψ_1 and Ψ_3 do not have physical meaning in a matter-free spacetime. Theoretically, one can choose a tetrad that rotates the Weyl scalars into a frame that forces $\Psi_1 = \Psi_3 = 0$. This can be done, and has been, far from the black holes. In fact, work has been done by [37], [38], [39], and [40] on an analytical method to extract a gravitational waveform from specific vectors associated with the spacetime, and introduced a scalar that measures the total amount of ingoing and outgoing gravitational radiation in a spacetime, $\xi = \Psi_0\Psi_4$. This method can currently be applied to our own ability to extract gravitational waves by allowing us to extract at an earlier simulation time (or, equivalently, closer to the binary) without losing accuracy. We would also like to be able to do this transformation into a transverse ($\Psi_1 = \Psi_3 = 0$) frame close to the black holes, and then use the resultant Weyl scalars to analytically classify the spacetime in this strong-field region. There are expectations for what the spacetime should look like far from the black holes, but we have no a priori information about what will happen near and between them. A more technical discussion on this follows in Chapter 4.

At its most fundamental level, a BBH simulation is just a numerical computation of the two-body problem for general relativity, the solution of which has far-reaching applications. In addition to studying the merger of compact objects, improvements in NR techniques will allow us to make great strides in fields such as strong gravity and high-energy physics, higher-dimensional black holes, Trans-Planckian scattering, and alternative theories of gravity. More

information on any of these topics can be found in [41], but no further discussion will be provided here.

We seek to improve upon and contribute to the current techniques used in Numerical Relativity simulations of binary black hole systems. First, a very brief review of theory necessary for this dissertation will be provided, but the bulk of the theoretical discussion will be saved for the Chapters in which dissertation results are presented.

1.3 Brief Review of Theory

This dissertation will have two primary focuses: first, on gauge choices and their effects on horizon quantities, and second, on that of gravitational wave extraction and spacetime classification. As discussed, the first sections will be on the gauge conditions of the BBH system, both the initial data given to the gauge equations, as well as choices for the damping coefficient η during evolution. We will then study the rotation of the spacetime into a frame in which more of the physically outgoing radiation can be captured and extracted. However, before these results are discussed, it is important to contextualize this research in the broader scope of the full field of Numerical Relativity.

This section will include a brief introduction of necessary components of Einstein's Theory of Relativity and numerical relativistic techniques used to perform simulations of binary black hole mergers. Basic knowledge of the mathematical structures of the field, including metric tensors, important (pseudo-)tensors, such as Christoffel symbols, and tensor mathematics will be assumed. Then, a discussion about how these equations are actually solved in practice will proceed, which will include brief synopses of the the 3+1 and BSSN Formalisms.

1.3.1 Einstein's Field Equations

The spacetime metric $g_{\mu\nu}$ describes the interval between two events at particular points in spacetime (t, x, y, z) . The metric is symmetric, and invariant under Lorentz transformations (so observers in different reference frames will measure the same interval between events A and B). It also has a signature, which defines the signs of its eigenvalues. Relativists generally

choose $(-, +, +, +)$ instead of $(+, -, -, -)$. If a spacetime has no curvature, it can be simply described by the flat metric $g_{\mu\nu} = \eta_{\mu\nu}$, where

$$\eta_{\mu\nu} = \begin{bmatrix} -1 & 0 & 0 & 0 \\ 0 & 1 & 0 & 0 \\ 0 & 0 & 1 & 0 \\ 0 & 0 & 0 & 1 \end{bmatrix} \quad (1.3.1)$$

which describes Minkowski spacetime.

The spacetime itself is encoded in the Christoffel symbols

$$\Gamma_{\beta\mu}^{\alpha} = \frac{1}{2}g^{\alpha\gamma} (g_{\gamma\beta,\mu} + g_{\gamma\mu,\beta} - g_{\beta\mu,\gamma}) \quad (1.3.2)$$

where via an arbitrary spacetime metric $g_{\mu\nu}$.

The Riemann curvature tensor

$$R_{\beta\mu\nu}^{\alpha} = \partial_{\mu}\Gamma_{\beta\nu}^{\alpha} - \partial_{\nu}\Gamma_{\beta\mu}^{\alpha} + \Gamma_{\rho\mu}^{\alpha}\Gamma_{\beta\nu}^{\rho} - \Gamma_{\rho\nu}^{\alpha}\Gamma_{\beta\mu}^{\rho}, \quad (1.3.3)$$

where and

$$\partial_{\mu}V^{\nu} = \frac{\partial}{\partial x^{\mu}}V^{\nu}, \quad (1.3.4)$$

describes how a particular spacetime curves. In flat spacetime it is such that $R_{\alpha\beta\mu\nu} = 0$ since there is no curvature and the spacetime is described by the flat metric $\eta_{\mu\nu}$. The Riemann tensor obeys the following identities:

- Antisymmetry in its first two indices, last two indices, and symmetry between pairs of indices:

$$R_{\alpha\beta\mu\nu} = -R_{\beta\alpha\mu\nu} \quad R_{\alpha\beta\mu\nu} = -R_{\alpha\beta\nu\mu} \quad R_{\alpha\beta\mu\nu} = R_{\mu\nu\alpha\beta} \quad (1.3.5)$$

- Cyclic identity:

$$R_{\alpha\beta\mu\nu} + R_{\alpha\nu\beta\mu} + R_{\alpha\mu\nu\beta} = 0 \quad (1.3.6)$$

- Bianchi identities:

$$\nabla_\gamma R_{\alpha\beta\mu\nu} + \nabla_\nu R_{\alpha\beta\gamma\mu} + \nabla_\mu R_{\alpha\beta\nu\gamma} = 0. \quad (1.3.7)$$

Using $R_{\alpha\beta\mu\nu}$ we can find coordinates from which the Ricci tensor and Ricci scalar (respectively)

$$R_{\alpha\beta} = R^\gamma_{\alpha\gamma\beta}, \quad (1.3.8)$$

$$R = R^\alpha_{\alpha}, \quad (1.3.9)$$

can be satisfied. The Ricci tensor $R_{\alpha\beta}$ has ten independent components and is the trace of $R_{\alpha\beta\mu\nu}$ [42]. The trace-free component is known as the Weyl Tensor $C_{\alpha\beta\mu\nu}$, which will be discussed in great detail in Chapter 4.

The Einstein Field Equations

$$R^{\mu\nu} - \frac{1}{2}g^{\mu\nu}R + \Lambda g^{\mu\nu} = 8\pi T^{\mu\nu} \quad (1.3.10)$$

are a system of 10 (by symmetries) coupled, nonlinear partial differential equations [43]. In the vacuum solution, the stress energy tensor $T^{\mu\nu} = 0$ and the constant Λ is negligible when considering black hole spacetimes so we set $\Lambda = 0$ during our evolutions. The cosmological constant is relevant only when considering problems on a much larger scale, such as the expansion of the universe. Therefore, for the remainder of this thesis the reader should assume $\Lambda = 0$ in the construction of the EFEs and their subsequent numerical evolution.

Furthermore, symmetries of the Riemann tensor allow Equations (1.3.10) to be reduced in number from 16 to 10. These equations, while elegant, are not situated well for computational solutions and require a very significant rewrite in order to be solved numerically.

1.3.2 3+1 Formalism

The equations in 3+1 formalism are equivalent to the standard equations of General Relativity. Writing the EFEs in 3+1 formalism evolves 12 purely spatial quantities and forces them to satisfy specific constraints on particular time slices (spatial hypersurfaces at an instant of time

t). The development of the 3+1 formalism is motivated by the necessity of a numerical solution for the GR equations since analytic solutions are unobtainable. When studying time dependent solutions to differential equations, one considers dynamical changes in the equation system between timesteps. Equations (1.3.10) do not clearly differentiate between space and time, therefore making computational solutions to them, as written, impossible even numerically. It is then necessary to perform a “3+1 split” of the spacetime, which separates the three spatial dimensions from the singular time dimension. The spacetime is foliated into distinct spacelike hypersurfaces Σ_t separated by timesteps $t_0 = 0, t_1 = dt, t_2 = 2dt, \dots$ etc. These hypersurfaces can be seen in Figure 1.3.

Determination of the geometry between these hypersurfaces is parameterized by three things: the lapse α of proper time between adjacent hypersurfaces Σ_t and Σ_{dt} as measured by observers normal to the hypersurfaces, the shift β^i , a 3-vector that measures the relative velocity between normal observers and lines of constant spatial coordinates, and the spatial metric γ^{ij} , where i, j are purely spatial indices, on each hypersurface. Geometric depictions of the lapse and shift can be seen in Figure 1.3 The lapse and shift, known as the *gauge equations*,

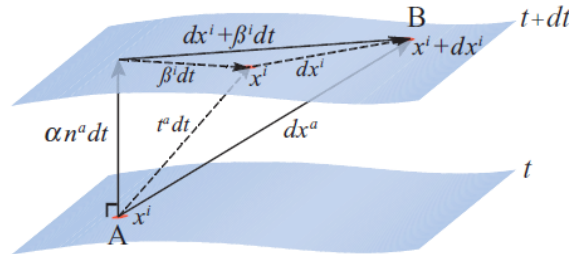


Figure 2.4 Pythagorean theorem in 3 + 1 dimensional spacetime. The normal vector αn^a and the time vector t^a connect points on two neighboring spatial slices. The shift vector β^i resides in the slice and measures their difference. The infinitesimal displacement vector dx^a connects two nearby, but otherwise arbitrary, points on neighboring slices (e.g., the point A at x^i on slice t and the point B at $x^i + dx^i$ on slice $t + dt$). The total displacement vector $dx^a = t^a dt + dx^i$, where dx^i is the spatial vector drawn in the figure, may be decomposed alternatively into two vectors that form the legs of a right-triangle, $dx^a = (\alpha n^a dt) + (dx^i + \beta^i dt)$, as shown. Using this decomposition to evaluate the invariant interval $ds^2 = dx^a dx_a$, commonly expanded as in equation (1.1), yields the Pythagorean theorem, equation (2.123).

Figure 1.3: A schematic of the 3+1 split of spacetime, including the foliation of spatial hypersurface Σ a very good explanation of how the lapse and shift equations describe the coordinates. Taken from [6], page 46.

are independent of the evolution equations, and can be freely specified, but do define the

coordinates. Different choices for these equations, known as slicings of the spacetime, vary the stability of the solutions of the field equations. Therefore, these equations can be fine-tuned to increase accuracy, but a poor choice of gauge can cause a numerical simulation to fail. For our simulations, we typically choose a 1+log slicing for the lapse and a modified Gamma-driver shift condition, ((1.3.11) and (1.3.12) respectively) [44, 8],

$$\partial_0 \alpha = (\partial_t - \beta^i \partial_i) \alpha = -2\alpha K \quad (1.3.11)$$

$$\partial_t \beta_a = \frac{3}{4} \tilde{\Gamma}^a - \eta(x^k, t) \beta^a. \quad (1.3.12)$$

where K is the trace of the extrinsic curvature, $\tilde{\Gamma}$ is a normalized Christoffel, α is the lapse and β is the shift. The initial values are defined by an initial shift vanishing and an initial lapse choice of $\alpha(t=0) = \frac{2}{1+\psi_{BL}^4}$ where ψ_{BL} is the Boyer-Lindquist conformal factor. The function $\eta(x^k, t)$ is typically chosen to be a constant $\eta = 2/m$ and should be assumed to be so unless otherwise specified. The metric can be written in terms of the lapse, shift, and spatial metric exclusively, which is known as the 3+1 split of the metric:

$$ds^2 = (-\alpha^2 + \beta_i \beta^i) dt^2 + 2\beta_i dt dx^i + \gamma_{ij} dx^i dx^j \quad (1.3.13)$$

where γ_{ij} is the spatial 3-metric. Now, the Einstein Field Equations themselves must be rewritten in terms of 3+1 language. Four of the equations specified are the Hamiltonian and momentum constraint equations. The Hamiltonian constraint equations in vacuum are defined as

$$R + K^2 - K_{\mu\nu} K^{\mu\nu} = 16\pi n^\mu n^\nu T_{\mu\nu} = 0 \quad (1.3.14)$$

where R is the three dimensional Ricci scalar, which is found by contracting twice the Riemann tensor ($R_{\alpha\mu\beta}^\mu = R_{\alpha\beta}$ and $R_\alpha^\alpha = R$), $K_{\mu\nu}$ is the extrinsic curvature

$$K_{\alpha\beta} = -\frac{1}{2} \mathcal{L}_n \gamma_{\alpha\beta} \quad (1.3.15)$$

for Lie derivative \mathcal{L} along unit normal n^μ . The momentum constraint equations in vacuum

are defined as

$$D_\mu(K^{\alpha\mu} - \gamma^{\alpha\mu}K) = -8\pi P^{\alpha\mu}n^\nu T_{\mu\nu} = 0 \quad (1.3.16)$$

where D_μ is the covariant derivative. Both (1.3.14) and (1.3.16) are vanishing only in vacuum spacetime. These are constraint equations and not evolution equations because, while all four are coupled to the other 6 field equations, neither contain time derivatives or any components of the gauge equations.

These equations must be satisfied to a high degree on each spatial hypersurface. Since we work in vacuum in a BHB system, ideally both Eqs. (1.3.14) and (1.3.16) would be identically zero. However, in practical numerical simulations, that is impossible; therefore their deviations from zero are a good measure of both the quality of the gauge choice, and how accurately the spacetime is evolving. As long as the values of these equations converge to zero as resolution increases, we assume we are in a convergence regime.

There is much more formalism that needs to be laid out in order to fully grasp the numerical 3 + 1 split of the Einstein Field Equations, such as the construction of the remaining 6 equations and the corresponding Arnowitt-Deser-Misner (ADM) evolution equations [45, 46], which recast second order derivatives as first order. In the interest of brevity, and since the results discussed in later sections of this proposal are explicitly dependent on only the Hamiltonian and momentum constraints, we will not include the full set of 3+1 equations. Instead, we will proceed to the presentation of the full BSSNOK [47, 48, 49] formalism.

1.3.3 BSSNOK

Although the 3 + 1 split provides a set of evolution equations, it can be shown that these are not unique [43] because arbitrary multiples of the constraints can be added to provide equally valid constructions of the evolution equations. Furthermore, the ADM evolution equations have been shown to be only weakly hyperbolic [50] since the system's characteristic matrix has real eigenvalues, but does not have a corresponding full set of eigenvectors [6]; the weak hyperbolicity of the equations implies that the problem, in the ADM formalism, is not well-posed. Using the fact that the constraints vanish analytically, one can add arbitrary multiples

of them to the evolution equations, therefore changing the appearance of higher-order derivatives in the characteristic matrix. Using these methodologies, the problem can be recast in such a way that is it strongly hyperbolic and therefore well-posed. The BSSN [48, 51, 52] formalism is standardly used to recast the ADM equations into a more suitable form for evolution. The theory relies on the rescaling of the spatial metric γ_{ij} by a conformal factor of the form

$$\tilde{\gamma}_{ij} = e^{-4\phi}\gamma_{ij} \quad (1.3.17)$$

with the constraint that

$$\phi = \frac{1}{12}\ln\left(\frac{\gamma}{\eta}\right) \quad (1.3.18)$$

where γ and η are the determinants of the spatial and flat metric respectively. The extrinsic curvature's trace (A_{ij}) and trace-free (K_{ij}) components are split, and the trace is rescaled by the same conformal factor as in (1.3.17)

$$\tilde{A}_{ij} = e^{-4\phi}A_{ij} \quad (1.3.19)$$

which allows us to rewrite the extrinsic curvature K_{ij} as

$$K_{ij} = e^{4\phi}\tilde{A}_{ij} + \frac{1}{3}\gamma_{ij}K. \quad (1.3.20)$$

and the Hamiltonian and momentum constrain equations as

$$\mathcal{H} = \tilde{\gamma}^{ij}\tilde{D}_i\tilde{D}_je^\phi - \frac{e^\phi}{8}\tilde{R} + \frac{e^{5\phi}}{8}\tilde{A}_{ij}\tilde{A}^{ij} - \frac{e^{5\phi}}{12}K^2 + 2\pi e^{5\phi}\rho \quad (1.3.21)$$

$$\mathcal{M}^i = \bar{D}_j(e^6\phi\tilde{A}^{ji}) - \frac{2}{3}e^{6\phi}\bar{D}^iK - 8\pi e^{6\phi}S^i \quad (1.3.22)$$

where D_j is the spatial covariant derivative, S^i is the momentum density measured by a normal observer and ρ is the total energy density. Both constraint equations should be vanishing in a matter-free spacetime. The evolution equation for the spatial metric γ_{ij} is split into two

equations:

$$\partial_t \phi = -\frac{1}{6} \alpha K + \beta^i \partial_i \phi + \frac{1}{6} \partial_t \beta^i, \quad (1.3.23)$$

$$\partial_t \bar{\gamma}_{ij} = -2\alpha \tilde{A}_{ij} + \beta^k \partial_k \bar{\gamma}_{ij} + \bar{\gamma}_{ik} \partial_j \beta^k + \bar{\gamma}_{kj} \partial_i \beta^k - \frac{2}{3} \bar{\gamma}_{ij} \partial_k \beta^k. \quad (1.3.24)$$

The extrinsic curvature K_{ij} is also split into two equations:

$$\partial_t K = -\gamma^{ij} D_j D_i \alpha + \alpha (\tilde{A}_{ij} \tilde{A}^{ij} + \frac{1}{3} K^2) + 4\pi \alpha (\rho + S) + \beta^i \partial_i K, \quad (1.3.25)$$

$$\partial_t \tilde{A}_{ij} = e^{4\phi} [-(D_i D_j \alpha)^{TF} + \alpha (R_{ij}^{TF} - 8\pi S_{ij}^{TF})] + \alpha (K \tilde{A}_{ij} - 2\tilde{A}_{il} \tilde{A}_j^l) \quad (1.3.26)$$

$$+ \beta^k \partial_k \tilde{A}_{ij} + \tilde{A}_{ik} \partial_j \beta^k + \tilde{A}_{kj} \partial_i \beta^k - \frac{2}{3} \tilde{A}_{ij} \partial_k \beta^k \quad (1.3.27)$$

where the superscript TF denotes the trace-free part of the tensor. More detail can be found in Box 11.1 in [6]. The BSSN system presented above is strongly hyperbolic. Furthermore, zero-speed modes that violate the momentum constraint can be made to have nonzero speed by adding the momentum constraint to the evolution equation $\tilde{\Gamma}^i$, and therefore these modes will propagate off the grid and encourage numerical stabilization.

All of our simulations, unless otherwise specified, use Bowen-York initial data [53], in which the momentum constraint is solved analytically, and the Hamiltonian constraint is left to be solved numerically. The form that this constraint takes is dependent on spacetime assumptions such as conformal flatness and type of slicing. It is then solved with the puncture approach, and evolved using the moving puncture method [8]. The puncture approach recasts the constraint equations so that singularities are absorbed into analytical terms, which leads to a regular equation that can then be solved numerically.

1.3.4 Evolution of BBH systems

In 2005, breakthroughs were made by Frans Pretorius, and then by the Campanelli and Baker research groups, all three of which allowed for the evolution through merger of black hole binaries [23], [8], [24]. The approach [23] uses the fact that the interior and exterior of the black hole, separated by the event horizon, are causally disconnected, which means that the

interior of the black hole can be excised from the computational grid without sacrificing any of the physics occurring outside of the horizon. The other codes, [8] and [24] use puncture initial data; these initial data absorb singularities within the black hole into an analytical expression and then solve the EFEs. The gauge conditions used in these approaches are known as the "1+log" slicing condition for the lapse and the "gamma-driver" shift condition, equations (1.3.11) and (1.3.12). These allow for stable evolutions of the BHBs through merger and damp large, potentially catastrophic, oscillations in the gauge. Our code employs the "moving puncture method" [8]. In brief, this method decomposes the metric as a sum of one analytic term that contains the singularity, and a numerical correction. Since the singularity has been factored out, this numerical correction is regular and can be evolved.

These systems are evolved using Adaptive Mesh Refinement, which has nested square grids, with three or four levels, surrounding both compact objects, and then, closer to the black holes, into two grids surrounding each individual horizon that follow their trajectories during evolution. Typically, each grid level increases in resolution by a factor of two, with the coarsest level being located farthest from the horizons. We maintain a constant Courant factor of $1/3$ or $1/4$ depending on the parameters of the binary. Specifics of the individual simulations performed will be outlined in Chapters 2, 3, and 4. Chapters 2 and 3 present methods of improving the results of physical parameters associated with the system via a parameter η that damps oscillations in the gauge, first using a constant η and then a variable η specifically tuned to small mass-ratio binaries. In Chapter 4 a discussion will be presented of a method which should, in principle, improve accuracy of the gravitational wave extraction. We will then use the techniques of that method to study the strong-field region of the binary in an analytic way. Finally, Chapter 5 will conclude the thesis and provide some ideas for extending the results of these projects in the future. The Appendix A presents updated coefficients for remnant fitting formulae developed in [1, 3] that use the full RIT simulations catalog of 777 waveforms, as well as a code that allows fitting coefficients to be calculated for different subsets of the catalog data.

Chapter 2

Adapted gauge to a quasi-local measure of black hole recoil

2.1 Introduction

Over the past several years, theoretical explorations have begun to evaluate the possibility of directly detecting the effects of recoil on gravitational waves observed by LIGO [54] and LISA [55, 56]. Numerical relativistic waveforms used for direct comparison with observations of gravitational waves require accurate modeling and good coverage of the parameter space [9]. There are already successful descriptions for the GW150914 [25, 34] and GW170104[57] events and the analysis of the rest of the O1/O2 events [13] is well underway [58].

The accurate modeling of the final remnant of the merger of binary black holes is of high interest for applications to gravitational wave modeling and tests of gravity [59, 14]. The computation of the final remnant mass and spin can be performed in three independent ways; first, by a fit to the quasinormal modes of the final remnant Kerr black hole [60, 61, 62]. Second, by a computation of the energy and angular momentum carried away by the gravitational radiation to evaluate the deficit from the initial to final mass and spins. Finally, by doing a quasilocal computation of the mass and spin directly on the horizons themselves using the isolated horizon formulas [63]. Comparison of the three methods has been carried out

in [64, 54], with the conclusion that at the typical resolutions used in production numerical relativity simulations the horizon quasilocal measures are an order of magnitude more accurate than the radiation or quasinormal modes fittings.

Of interest to numerical relativists is the ability to accurately infer quantities of the remnant (mass, spin, recoil) from the parameters of the initial binary. Using the isolated horizon formulae leads to very accurate modeling of the final mass and spins from the initial binary configuration. In particular for nonprecessing binaries, the modeling [3] warrants errors typically 0.03% for the mass and 0.16% for the spin. Meanwhile, the modeling of the remnant recoil uses the radiated linear momentum for fittings and this leads to errors on the order of 5%. A similarly accurate modeling of the recoil could be attempted by the use of a horizon quasilocal measure instead of the corresponding radiated quantity.

In reference [65] a quasi-local formula for the linear momentum of black-hole horizons was proposed, inspired by the formalism of quasi-local horizons. The formula is based on the coordinate rotation and translation vectors

$$P_{[i]} = \frac{1}{8\pi} \oint_{AH} \xi_{[i]}^a R^b (K_{ab} - K \gamma_{ab}) d^2V, \quad (2.1.1)$$

where K_{ab} is the extrinsic curvature of the 3D-slice, d^2V is the natural volume element intrinsic to the horizon, R^a is the outward pointing unit vector normal to the horizon on the 3D-slice, and $\xi_{[i]}^i = \delta_{\ell}^i$.

This formula was tested using two complementary configurations: (i) by calculating the large orbital linear momentum of the two black holes in an orbiting, unequal-mass, zero-spin, quasi-circular binary and (ii) by calculating the very small recoil momentum imparted to the remnant of the head-on collision of an equal-mass, anti-aligned-spin binary. The results obtained were consistent with the horizon trajectory in the orbiting case, and consistent with the radiated linear momentum for the much smaller head-on recoil velocity. A key observation we will explore in this study is the dependence of the accuracy on a gauge parameter, η used in our simulations to damp oscillations in the shift.

This Chapter is organized as follows: in Section 2.2 we discuss the numerical techniques

used to evolve the BBH systems, including the gauge and the evolution thorns. In Section 2.3, we summarize the methods used to study in detail the effects of choosing different (constant) values of η , the damping parameter in the shift evolution equation, on the accuracy of the quasilocal measure of the horizon linear momentum proposed in [65]. Section 2.4 discusses, in detail, a prototype case of a nonspinning $q = 1/3$ binary. Other unequal mass cases and one spinning case are verified as well. In Section 2.5, we perform additional studies of the shift evolution equation for the alternative ∂_0 -gauge, variable η , and apply what we learned in the previous section to develop a variable shift parameter η and to more extreme unequal mass binary black hole mergers. In Section 2.6 we discuss the benefits of the use of values of η different from our standard $m\eta = 2$ (see also [66]) for generic simulations, in particular for those that involve an accurate computation of the remnant recoil and we also conclude by noting the advantage of keeping the ∂_t -gauge for evolutions over the ∂_0 -gauge. The results of this study can be found in [67].

2.2 Numerical Techniques

Thanks to the 2005 breakthrough work [8] we are able to obtain accurate, convergent waveforms and horizon parameters by evolving the BSSNOK [47, 48, 49] system in conjunction with a modified 1+log lapse and a modified Gamma-driver shift condition [44, 8],

$$\partial_0\alpha = (\partial_t - \beta^i\partial_i)\alpha = -2\alpha K, \quad (2.2.2)$$

$$\partial_t\beta^a = \frac{3}{4}\tilde{\Gamma}^a - \eta(x^k, t)\beta^a. \quad (2.2.3)$$

with an initial vanishing shift β and lapse $\alpha(t = 0) = 2/(1 + \psi_{BL}^4)$. The parameter K is extrinsic curvature and $\tilde{\Gamma}^a$ is a connection coefficient composed with the spatial metric γ^{ij} . In the subsequent text, we will refer to this set of equations (2.2.3) as the ∂_t -gauge. Here, and for the remainder of the dissertation, latin indices cover the spatial range $i = 1, \dots, 3$.

An alternative moving puncture evolution can be achieved [24] by choosing [66]

$$\partial_0\alpha = (\partial_t - \beta^i\partial_i)\alpha = -2\alpha K, \quad (2.2.4)$$

$$\partial_0\beta^a = (\partial_t - \beta^i\partial_i)\beta^a = \frac{3}{4}\tilde{\Gamma}^a - \eta(x^k, t)\beta^a. \quad (2.2.5)$$

These (2.2.5) will be referred to as the ∂_0 -gauge. Unless otherwise stated, all binary black hole simulations in this paper use the ∂_t gauge.

The parameter η (with dimension of one-over-mass: $1/m$) in the shift equation regulates the damping of gauge oscillations and is commonly chosen to be of order unity (we use $\eta = 2/m$) as a compromise between the accuracy and stability of binary black hole evolutions. It was found in [68] that coordinate dependent measurements, such as spin and linear momentum direction, become more accurate as η is reduced (and resolution $h \rightarrow 0$). However, if η is too small ($\eta \ll 1/m$), the runs may become unstable. Similarly, if η is too large ($\eta \gg 10/m$), then grid stretching effects can cause the remnant horizon to continuously grow, eventually leading to an unacceptable loss in accuracy at late times.

2.2.1 Simulation Parameters

To compute initial data for our binary system, we use the `TWOPUNCTURES` [69] thorn. We evolve these black-hole-binary data-sets using the `LAZE` [70] implementation of the moving puncture formalism [8]. We use the `Carpet` [71, 72] mesh refinement driver to provide a ‘moving boxes’ style mesh refinement and we use `AHFINDERDIRECT` [73] to locate apparent horizons. We compute the magnitude of the horizon spin using the *isolated horizon* (IH) algorithm detailed in Ref. [74] (as implemented in Ref. [75]). Once we have the horizon spin, we can calculate the horizon mass via the Christodoulou formula $m_H = \sqrt{m_{\text{irr}}^2 + S_H^2/(4m_{\text{irr}}^2)}$, where $m_{\text{irr}} = \sqrt{A/(16\pi)}$ and A is the surface area of the horizon. We measure radiated energy, linear momentum, and angular momentum, in terms of Ψ_4 , using the formulae provided in Refs. [76, 77] and extrapolation to \mathcal{S}^+ is performed with the formulas given in Ref. [78].

Convergence studies of our simulations have been performed in Appendix A of Ref. [1], in Appendix B of Ref. [33], and for nonspinning binaries are reported in Ref. [79]. For very

highly spinning black holes ($s/m^2 = 0.99$) convergence of evolutions was studied in Ref. [80], for precessing $s/m^2 = 0.97$ in Ref. [54], and for ($s/m^2 = 0.95$) in Ref. [81] for unequal mass binaries. These studies allow us to assess that the simulations presented in the following sections, with similar grid structures, are well resolved by the adopted resolutions and are in a convergence regime.

2.3 Horizon Formulae

Reference [65] introduced an alternative quasi-local measurement of the linear momentum P of the individual (and final) black holes of the binary

$$P_\xi^{(S)} = \frac{1}{8\pi} \oint_S (K_{ij} - K\gamma_{ij})\xi^i d^2S^b \quad (2.3.6)$$

where S is apparent horizon surface, K_{ij} is the extrinsic curvature and K is its trace, and ξ^i is a killing vector. The right hand side of this equation should be interpreted as the “flux” of linear momentum between the horizon and infinity [65].

This formula was tested using two complementary configurations: (i) by calculating the large orbital linear momentum of the two unequal-mass ($q = 1/3$), nonspinning, black holes in a quasi-circular orbit and (ii) by calculating the very small recoil momentum imparted to the remnant of the head-on collision of an equal-mass, anti-aligned-spin binary. When the gauge parameter $m\eta$ was reduced from 2 to 1 in the orbiting case, results consistent with the horizon trajectory measure were obtained. Similarly for the head-on case, results consistent with the net radiated linear momentum were found, however the remainder of the paper will focus on a more detailed study of the orbiting case only.

Here, we expand upon these initial results, allowing for even smaller values of η and assessing convergence of the results with both numerical resolution and extrapolation of $\eta \rightarrow 0$. This will allow us to assess when the quasilocal measure of linear momentum (2.1.1) can be considered more accurate than the measure of radiated linear momentum at \mathcal{I}^+ .

In our simulations, we normalize data such that the sum of the horizon masses, after

spurious radiation of initial data, is set to unity, i.e. $m_{H1} + m_{H2} = 1$. In the tables below, we also introduce the difference of the ADM mass and angular momentum minus the final black hole mass and spins, as $\Delta m = M_{ADM} - m_f$ and $\Delta J = J_{ADM} - \alpha_f$.

2.4 Results for a $q = 1/3$ nonspinning binary

As a prototypical case of study we will consider a binary with mass ratio $q = m_1/m_2 = 1/3$ and spinless black holes starting at an initial coordinate separation $d = 9m$, with $m = m_1 + m_2$ the total mass of the system. From this separation the binary performs about 6 orbits before the merger into a single final black hole at around $t = 725m$.

The final mass and final spin are measured very accurately by the horizon quasilocal formulas [63, 75]; Figs. 2.1 provide a visualization of their respective values after merger into the final settling black hole remnant. They display smaller variations versus time with increasing resolutions.

In Figs. 2.2 the convergence of the Hamiltonian constraint (the momentum constraints show a very similar convergent behavior) and the $(\ell, m) = (2, 2)$ -mode of the gravitational waveform around merger are displayed. The constraints show convergent behavior and small relative error, as do the gravitational waveforms, therefore we can be confident that we are resolving the binary system accurately. Figure ?? shows the quadratic convergence of the Hamiltonian constraints from Figure 2.2 to provide a quantitative measure of their convergence.

As shown in the Tables 2.1 and 2.2 the computed final mass and spin of the remnant black hole are well in the convergence regime at typical computation resolutions [2, 34]. We calculate convergence order n using the formulas for a 3 point extrapolation to infinity, and

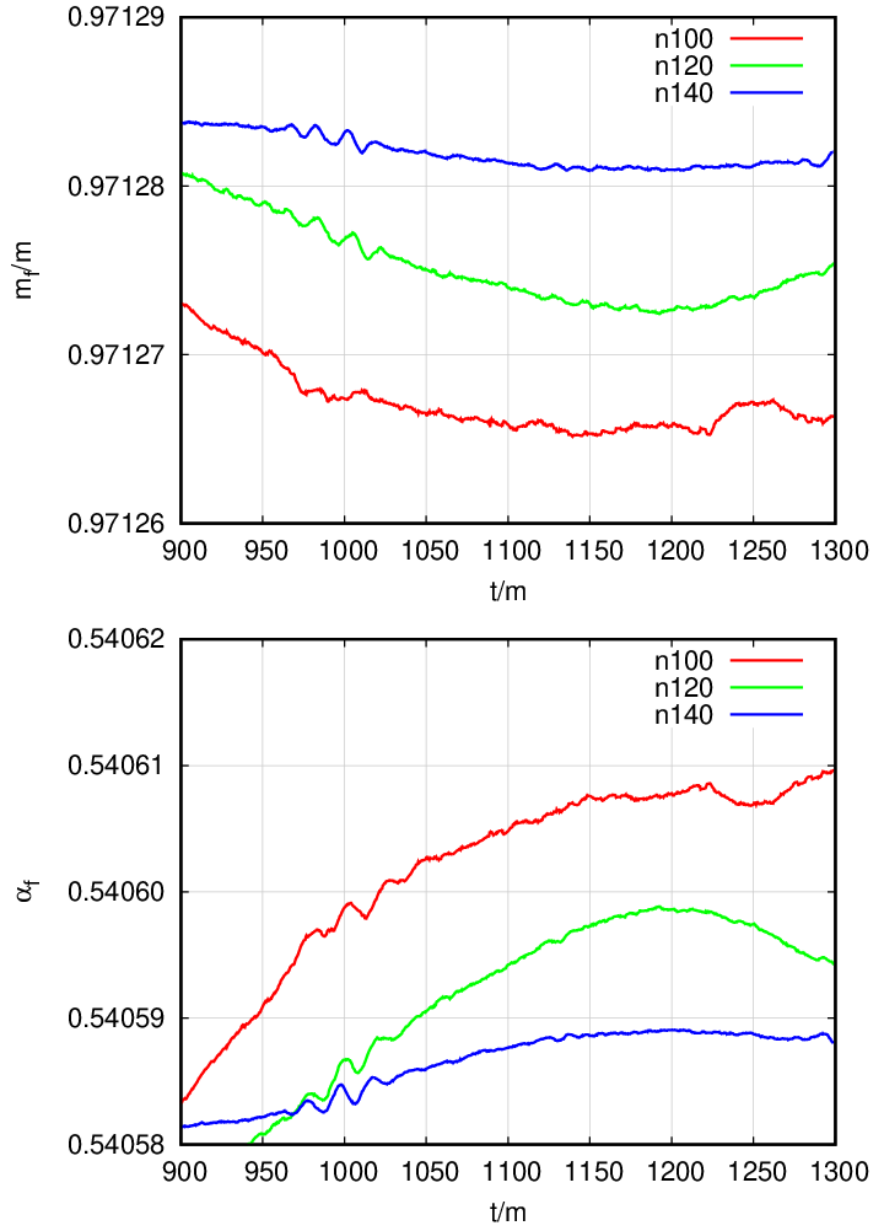


Figure 2.1: The horizon measure of the mass and spin after merger of a $q = 1/3$ nonspinning binary versus time for $m\eta = 2$ at resolutions n100, n120, n140.

solve a system of equations of the form:

$$y_1 = A + Bh1^n \quad (2.4.7)$$

$$y_2 = A + Bh2^n \quad (2.4.8)$$

$$y_3 = A + Bh3^n \quad (2.4.9)$$

2.4. Results for a $q = 1/3$ nonspinning binary

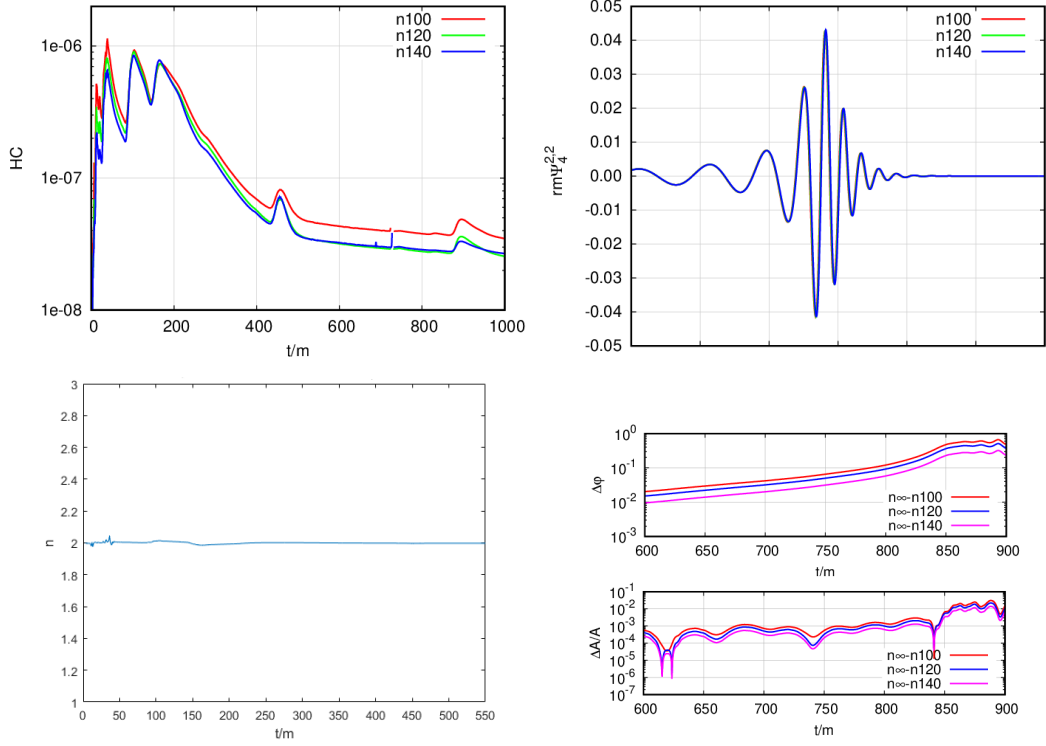


Figure 2.2: The Hamiltonian constraint behavior versus time for $m\eta = 2$ at resolutions n100, n120, n140 in the top left panel, the (2,2)-waveform as seen by an observer at $r = 113m$ for the $q = 1/3$ nonspinning binary from an initial separation $D = 9m$ in the top right panel, the order of convergence of the Hamiltonian constraint violations in the bottom left, the phase difference (in radians), $\Delta\varphi$, and the amplitude difference between resolutions, $\Delta A/A$, with respect to the infinite resolution extrapolation (n_∞) in the bottom right panel (top and bottom respectively).

for parameters A, B , and n using known data points y_1, y_2, y_3 , and resolutions h_1, h_2, h_3 . A is the extrapolation to infinite resolution and n is the convergence order. The parameter B is the leading order approximant of the error. For our purposes, we take B to be the same for all resolutions, but in reality is dependent on the h_i chosen.

The convergence order $n(AH)$ is measured assuming that A is known from the horizon measure of a specific parameter. Then, the two highest resolution simulations are used to solve for the convergence order. From these results, we get an $n(AH)$ and $B(AH)$.

Table 2.1 displays the difference between the initial total ADM mass and final horizon mass and Table 2.2 displays the loss of ADM angular momentum from its initial value to the final horizon spin for different resolutions and different (η -values) gauges. The computations

2.4. Results for a $q = 1/3$ nonspinning binary

| h_i/m | $m\eta = 2.0$ | $m\eta = 1.0$ | $m\eta = 0.5$ | $m\eta \rightarrow 0.0$ |
|-----------------|---------------|---------------|---------------|-------------------------|
| 1/100 | 0.97127 | 0.97127 | 0.97128 | 0.97127 |
| 1/120 | 0.97128 | 0.97129 | 0.97126 | 0.97128 |
| 1/140 | 0.97128 | 0.97128 | 0.97128 | 0.97128 |
| $\rightarrow 0$ | 0.97131 | 0.97135 | 0.97135 | 0.97132 |
| n | 1.59 | 2.24 | 1.95 | 2.29 |
| 1/100 | 0.02046 | 0.02046 | 0.02047 | 0.02046 |
| 1/120 | 0.02046 | 0.02045 | 0.02045 | 0.02044 |
| 1/140 | 0.02045 | 0.02045 | 0.02045 | 0.02045 |

Table 2.1: The final black hole mass (m_f/m) for different η and resolutions (top table). Difference between final black hole and ADM masses (bottom table). Values for $m\eta \rightarrow 0.0$ and resolution $h_i \rightarrow 0$ are extrapolated (the latter by order n).

give consistent values to 5-decimal places for each resolution, showing we are deep in the convergence regime and also versus η , showing (as expected) that those computations are gauge-invariant.

| h_i/m | $m\eta = 2.0$ | $m\eta = 1.0$ | $m\eta = 0.5$ | $m\eta = 0.0$ |
|-----------------|---------------|---------------|---------------|---------------|
| 1/100 | 0.54060 | 0.54046 | 0.54060 | 0.54094 |
| 1/120 | 0.54059 | 0.54051 | 0.54060 | 0.54080 |
| 1/140 | 0.54059 | 0.54056 | 0.54059 | 0.54061 |
| $\rightarrow 0$ | 0.54058 | — | — | — |
| n | 3.56 | — | — | — |
| 1/100 | -0.19185 | -0.19187 | -0.19183 | -0.19186 |
| 1/120 | -0.19184 | -0.19185 | -0.19184 | -0.19185 |
| 1/140 | -0.19183 | -0.19184 | -0.19184 | -0.19184 |

Table 2.2: The final black hole spin (α_f/m^2) for different η and resolutions (top table). Difference between final black hole angular momentum α_f and initial ADM angular momentum J_{ADM} (bottom table). Values for $m\eta = 0.0$ are extrapolated as those for infinite resolution $h_i \rightarrow 0$ with order n .

To evaluate the convergence rate with three resolutions h_i with $i = 1, 2, 3$ we model the errors of a measured quantity $M_i = M(h_i)$ as $A_i h_i^n$ in such a way that the extrapolated to infinite resolution quantity $M_\infty = M(0)$ can be written as $M_\infty = M_i + \langle A \rangle h_i^n$, where $\langle A \rangle$ is an averaged value of the A_i . Thus for the three resolutions we have a system of three equations for the three unknowns, M_∞ , n , and $\langle A \rangle$, n representing the convergence rate and M_∞ the extrapolation to infinite resolution given in all tables in this chapter.

The corresponding computation of radiated energy and angular momentum from the wave-

2.4. Results for a $q = 1/3$ nonspinning binary

forms extrapolated to an observer at infinity (from an extraction at $r = 113m$) and summed over all (ℓ, m) -modes up to $\ell = 6$ are displayed in Tables 2.3 and 2.4 showing consistent approximate 3rd order convergence for the three resolutions n100, n120, and n140. When using the extrapolated to infinite resolution horizon values as exact, the convergence order increases, and is over 4th order for the radiated angular momentum. In all cases, the computations are consistent in the first 3 digits. While taking as the exact reference the extrapolated to infinite resolution horizon values, the convergence is over 4th order. Consistent first 4-digits are computed in all cases. Note that in all radiative computations we do not remove the initial data (spurious) radiation content to allow direct comparison with the corresponding horizon quantities. In particular, very weak dependence on η is found, again as expected on the ground of gauge invariance of the gravitational waveform extrapolated to an observer at infinite location.

| h_i/m | $m\eta = 2.0$ | $m\eta = 1.0$ | $m\eta = 0.5$ | $m\eta = 0.0$ |
|-----------------|---------------|---------------|---------------|---------------|
| 1/100 | 0.02017 | 0.02017 | 0.02017 | 0.02017 |
| 1/120 | 0.02030 | 0.02030 | 0.02029 | 0.02030 |
| 1/140 | 0.02036 | 0.02036 | 0.02036 | 0.02036 |
| $\rightarrow 0$ | 0.02047 | 0.02045 | 0.02046 | 0.02046 |
| n | 3.03 | 3.23 | 3.08 | 3.10 |
| $n(AH)$ | 3.31 | 3.23 | 3.18 | — |

Table 2.3: Energy radiated away in gravitational waves up to $\ell = 6$ for the $q = 1/3$ nonspinning binary. Values for $m\eta = 0.0$ are extrapolated. Convergence order calculated from the three resolutions, n , and using the two highest resolutions and assuming the converged value is the value calculated on the horizon, $n(AH)$.

| h_i/m | $m\eta = 2.0$ | $m\eta = 1.0$ | $m\eta = 0.5$ | $m\eta = 0.0$ |
|-----------------|---------------|---------------|---------------|---------------|
| 1/100 | -0.19075 | -0.19073 | -0.19070 | -0.19076 |
| 1/120 | -0.19128 | -0.19130 | -0.19125 | -0.19128 |
| 1/140 | -0.19157 | -0.19157 | -0.19154 | -0.19157 |
| $\rightarrow 0$ | -0.19217 | -0.19196 | -0.19215 | -0.19216 |
| n | 2.56 | 3.38 | 2.62 | 2.55 |
| $n(AH)$ | 4.78 | 4.50 | 4.62 | — |

Table 2.4: Angular momentum radiated away in gravitational waves up to $\ell = 6$ for the $q = 1/3$ nonspinning binary. Values for $m\eta = 0.0$ are extrapolated. Convergence order calculated from the three resolutions, n , and using the two highest resolutions and assuming the converged value is the value calculated on the horizon, $n(AH)$.

Tables 2.3 and 2.4 also show that both radiative quantities, energy and angular momentum show very small variations with respect to the extrapolated $\eta \rightarrow 0$ values, as expected from gauge invariant quantities.

Since the formula (2.1.1) is not gauge invariant when applied to the horizon of the final black hole we expect to find stronger variation with η when we use it to evaluate the linear momentum of the remnant. We will pursue this exploration in more detail next in order to assess what values of η allow us to compute the recoil velocity of the final black hole with good accuracy. We are interested in particular, for our typical numerical simulation resolutions, what values of η can produce more accurate values of the recoil from the horizon by use of (2.1.1) than from the evaluation of the radiated linear momentum at infinity.

Our starting point is the gauge choices that we have been using regularly in our systematic studies of binary black hole mergers ($m\eta = 2$ and Eqs. (2.2.3)) and numerical resolutions labeled by the resolution at the extraction level of radiation as n100, n120, n140, corresponding to wavezone resolutions of $h = 1/1.00m, 1/1.20m, 1/1.40m$, respectively [2, 34]. We use 10 levels of refinement with an outer boundary at 400m. For each of these three resolutions we add a set of simulations by decreasing η by factor of two, i.e. $\eta = 1/m, 1/2m$. The results of those nine simulations are displayed in Fig. 2.3. For $\eta = 2/m$, the curves are very flat versus time after the merger with the highest resolution run, n140, being notably so. However their values for the evaluation of the recoil fall short compared to the estimate coming from the extrapolation of the radiative linear momentum to infinite resolution, represented by the solid black lines at about 177km/s.

The progression towards smaller η shows closer agreement with that extrapolated value. The time dependence shows variations as we approach the smaller η but still converging with resolution towards the expected 177km/s value and flatter for n140, but clearly the limit $\eta \rightarrow 0$ requires much higher resolutions, as shown in Fig. 2.4. In our regime, reaching $\eta = 1/m$ or $\eta = 0.5/m$ seems a good compromise of accuracy versus cost of the simulation.

Fig. 2.4 shows the progression of $m\eta = 2.0, 1.5, 1.0, 0.5, 0.25$ for simulations with resolution n140. Notably they lie in a roughly linear convergence towards the expected higher recoil

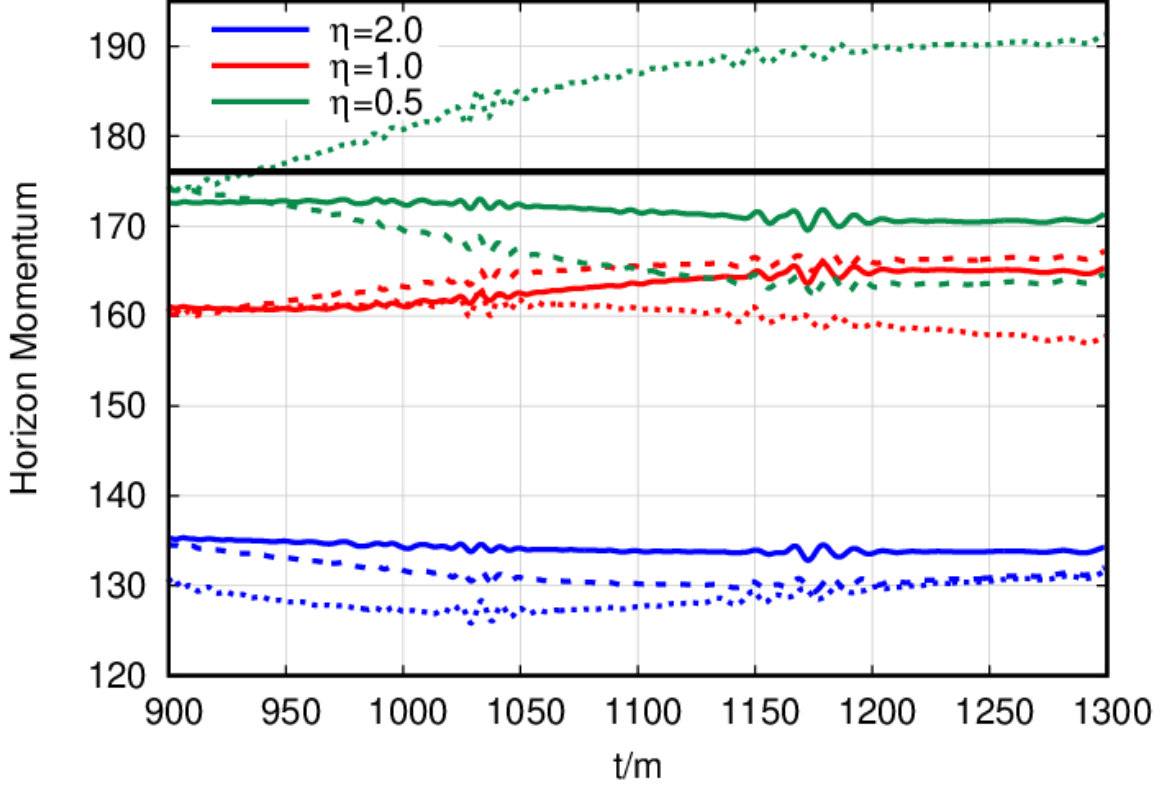


Figure 2.3: The horizon measure of the linear momentum (in km/s) after merger of a $q = 1/3$ nonspinning binary for the three resolutions n100 (dotted), n120 (dashed), and n140 (solid) for $\eta = 2/m$ (blue), $1/m$ (red), $0.5/m$ (green). The reference value of V_f (black solid line) is found by extrapolation to infinite resolution of the radiated linear momentum.

velocity value 177km/s, but as we reach the smaller $m\eta = 0.25$ value it overshoots slightly, an effect of the required higher resolution needed to resolve accurately smaller values of η . In what follows we will restrict ourselves to values of $m\eta = 2.0, 1.0, 0.5$ to make sure we are in a convergence regime for our standard resolutions n100, n120, n140. Note that we have verified that the simulation with n140 and $\eta = 0$ does not crash, but leads to inaccurate results.

The radiation of linear momentum in terms of the Weyl scalar Ψ_4 , as given by the formulas in [82], can be computed in a similar fashion as we compute the energy and angular momentum radiated. For this study, we do not remove the initial burst of spurious radiation from the linear momentum calculation since we are interested in comparing to the final velocity of the merged BH. The burst will impart a (usually) small kick to the center of mass of the

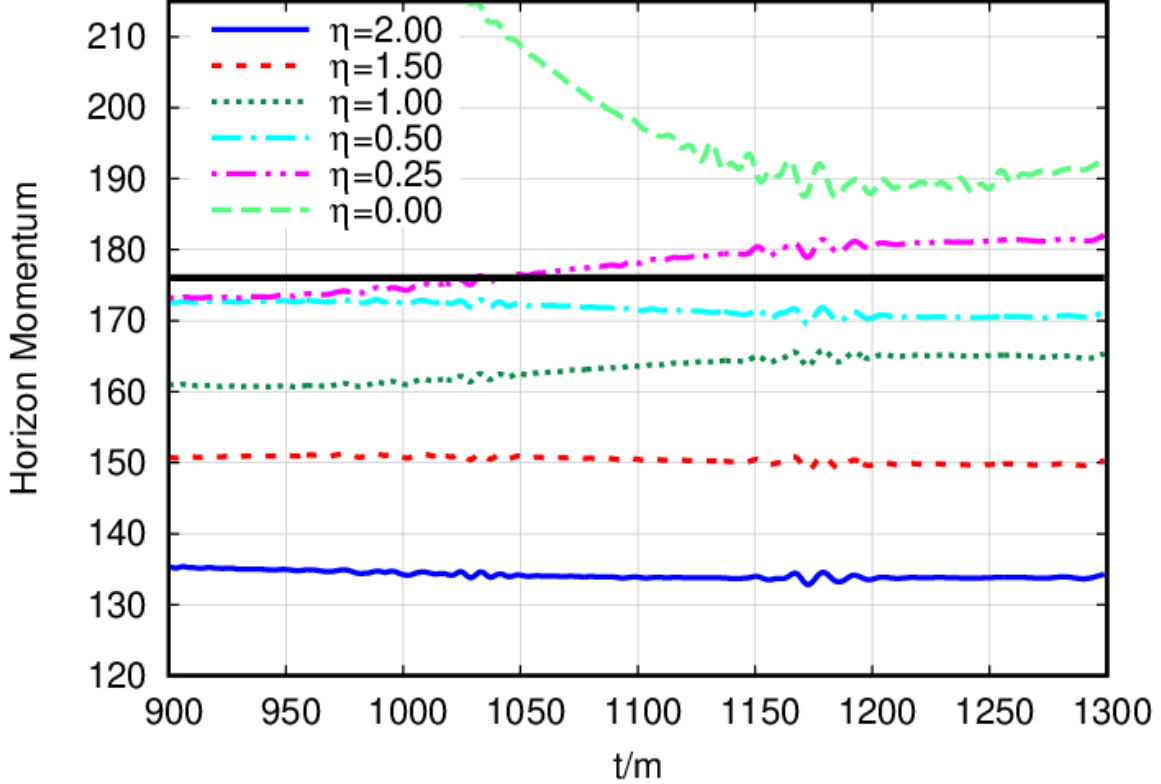


Figure 2.4: The horizon measure of the linear momentum (in km/s) after merger of a $q = 1/3$ nonspinning binary lowering values of $\eta = 2 \rightarrow 0$ at resolution n140. The reference value of V_f (black solid line) is found by extrapolation to infinite resolution of the radiated linear momentum.

system. This allows direct comparison with horizon quantities in this paper. For astrophysical applications the removal of the initial burst of radiation is done in the waveform time domain and can be applied to remove their contributions to the final mass, spin and recoil velocity.

Table 2.5 shows that the radiation of linear momentum converges with resolution (at an approximate 2.6-2.7th order) at similar rates than the radiated energy and momentum (roughly 3rd order), and still varies little with η , again this result is expected due to the gauge invariance of radiated quantities.

The values extrapolated to infinite resolution lie in the 176-177km/s range, consistently for all three values of $m\eta = 2, 1, 0.5$. Extrapolations of the recoil velocities to $\eta \rightarrow 0$ are very close to their values at $m\eta = 2, 1, 0.5$ for all three resolutions, again confirming the gauge

2.4. Results for a $q = 1/3$ nonspinning binary

| h_i/m | $m\eta = 2.0$ | $m\eta = 1.0$ | $m\eta = 0.5$ | $m\eta = 0.0$ |
|-----------------|---------------|---------------|---------------|---------------|
| 1/100 | 163.648 | 163.753 | 163.759 | 163.760 |
| 1/120 | 168.569 | 168.678 | 168.660 | 168.662 |
| 1/140 | 171.256 | 171.314 | 171.324 | 171.326 |
| $\rightarrow 0$ | 176.750 | 176.422 | 176.708 | 176.702 |
| n | 2.582 | 2.699 | 2.608 | 2.611 |
| 1/100 | 375.01° | 374.67° | 373.61° | — |
| 1/120 | 374.93° | 375.09° | 374.54° | — |
| 1/140 | 375.50° | 375.59° | 375.78° | — |
| $\rightarrow 0$ | 375.15° | 375.12° | — | — |
| n | 1.99 | 2.00 | — | — |

Table 2.5: Total linear momentum radiated in gravitational waves up to $\ell = 6$ for the $q = 1/3$ nonspinning binary in km/s. Values for $m\eta = 0.0$ are extrapolated. Convergence order n is extrapolated to infinite resolution $h_i \rightarrow 0$. Bottom panel shows the angle (in degrees) of the net momentum with respect to the initial x-axis.

| h_i/m | $m\eta = 2.0$ | $m\eta = 1.0$ | $m\eta = 0.5$ | $m\eta = 0.0$ | order |
|-----------------|-------------------------------|-------------------------------|-------------------------------|---------------|-------|
| 1/100 | 137.515 ± 1.12 | 160.507 ± 1.14 | 171.977 ± 3.99 | 183.397 | 1.00 |
| 1/120 | 139.543 ± 0.86 | 161.615 ± 1.36 | 174.703 ± 2.80 | 193.765 | 0.75 |
| 1/140 | 139.194 ± 0.40 | 165.014 ± 1.55 | 174.948 ± 0.87 | 181.161 | 1.38 |
| 1/100 | $373.83^\circ \pm 0.27^\circ$ | $370.26^\circ \pm 0.29^\circ$ | $367.52^\circ \pm 0.86^\circ$ | 358.475° | 0.38 |
| 1/120 | $373.87^\circ \pm 0.48^\circ$ | $371.83^\circ \pm 0.27^\circ$ | $373.64^\circ \pm 0.36^\circ$ | 372.909° | 25.41 |
| 1/140 | $374.63^\circ \pm 0.58^\circ$ | $371.98^\circ \pm 0.09^\circ$ | $374.37^\circ \pm 0.16^\circ$ | 373.389° | 27.46 |
| $\rightarrow 0$ | 374.11° | 372.36° | 375.81° | 373.418° | — |
| n | 2.00 | 6.07 | 6.11 | 18.53 | — |

Table 2.6: Horizon linear momentum measured at the interval $t = 950m - 1250m$ for the $q = 1/3$ nonspinning binary in km/s. The bottom panel gives the angle (in degrees) this magnitude subtends with the initial x-axis. The measured standard deviation is given by the \pm in the relevant quantities. Convergence order and extrapolations are given for $h_i \rightarrow 0$ and $\eta \rightarrow 0$.

independence of the results. In addition we display the angle (in degrees, reversed sign) the net radiated momentum has with respect to the x-axis (line joining the black hole initially).

Table 2.6 displays the crucial result of recoil velocities very close to their desired values for low resolutions when $m\eta = 0.5$. They do not vary so much with resolution, as expected for horizon quantities, when compared to the variations with respect to the gauge choices. We observe close to a linear dependence on η of the recoil values. Their extrapolation to $\eta \rightarrow 0$ overshoots the expected value by a few percent, but the values at $m\eta = 0.5$ are nearly within 1%. This provides an effective way to compute recoils, since the corresponding radiative

2.4. Results for a $q = 1/3$ nonspinning binary

quantities are 3% away for n140. The horizon evaluations lie closer to the expected values by a factor 3 over the radiative ones for all three resolutions. In addition we display the angle the recoil velocity subtends with respect to the x-axis (line joining the black holes initially) showing a notable agreement of this sensitive quantity with the results in Table 2.5.

The coordinate velocities do not benefit systematically from the small η gauges, but still provide a good bulk value as shown in Table 2.7. This shows the benefits of having a quasilocal measure of the momentum of the hole over its horizon compared to the local coordinate velocity of the puncture.

| h_i/m | $m\eta = 2.0$ | $m\eta = 1.0$ | $m\eta = 0.5$ | $m\eta = 0.0$ |
|---------|---------------|---------------|---------------|---------------|
| 1/100 | 154.448 | 158.513 | 184.809 | 153.705 |
| 1/120 | 155.051 | 167.205 | 159.472 | 162.479 |
| 1/140 | 158.123 | 165.702 | 165.957 | 165.966 |

Table 2.7: Coordinate trajectory velocity in km/s as measured at $575m$ after merger for the $q = 1/3$ nonspinning binary.

2.4.1 Validation for other mass ratios ($q = 1/2, 1/5$)

In order to first validate our technique to extract the recoil velocity of the remnant black hole from spinning binaries, we have considered another unequal mass ($q = 1/2$) binary with initial separation $d = 11m$. The resulting recoil will be along the orbital plane and due entirely to the asymmetry produced by the unequal masses. The results are presented in Table 2.8. Assuming the extrapolation to infinite resolution of the radiative linear momentum computations is the most accurate one leads to a recoil of 154.3 ± 0.1 km/s. Even for the lowest computed resolution, n100, the horizon evaluation for $m\eta = 0.5$ at 159.6 km/s is a better approximation to that value than any radiative evolution at the same resolution (145.9 km/s), with errors of the order of 3%. This is also true for the other two resolutions n120, and n140. Although, as we have seen before, the improvement of those horizon values are obtained by lowering the value of $m\eta \rightarrow 0$, rather than by higher resolution, as the horizon quasilocal measure has essentially already converged at those resolutions.

Here we also provide the computation of the horizon evaluations for the mass and spin of

2.4. Results for a $q = 1/3$ nonspinning binary

| h_i/m | Radiation | Horizon | Radiation | Horizon |
|-----------------|----------------|-------------------------------|----------------|-------------------------------|
| | $m\eta = 2.0$ | $m\eta = 2.0$ | $m\eta = 0.5$ | $m\eta = 0.5$ |
| 1/100 | 145.45 | 127.80 ± 0.65 | 145.91 | 159.57 ± 1.05 |
| 1/120 | 149.45 | 121.02 ± 0.79 | 149.64 | 152.48 ± 0.31 |
| 1/140 | 151.38 | 118.77 ± 0.65 | 151.48 | 152.92 ± 0.41 |
| $\rightarrow 0$ | 154.28 | 117.08 | 154.39 | 150.98 |
| n | 3.31 | 5.49 | 3.18 | 6.20 |
| 1/100 | 384.43° | $379.73^\circ \pm 1.35^\circ$ | 390.60° | $388.57^\circ \pm 0.55^\circ$ |
| 1/120 | 392.74° | $387.84^\circ \pm 1.48^\circ$ | 391.04° | $388.75^\circ \pm 0.24^\circ$ |
| 1/140 | 392.54° | $388.54^\circ \pm 1.41^\circ$ | 391.74° | $389.80^\circ \pm 0.11^\circ$ |
| $\rightarrow 0$ | 394.75° | 390.48° | — | — |
| n | 6.17 | 6.14 | — | — |

Table 2.8: Comparison of the computation of the recoil velocity (in km/s) of the remnant of a $q = 1/2$, nonspinning binary by traditional radiation of linear momentum and the horizon formula (2.1.1) averaged between $t = 1550m$ and $t = 1850m$ for the traditional $\eta = 2$ and for the $\eta = 0.5$ case. Extrapolation to infinite resolution and convergence order is also given for the horizon and radiative extraction. The bottom panel gives the angle (in degrees) of the recoil velocity with respect to the x-axis. Standard deviations of horizon measurements are given as \pm for each quantity. Convergence with numerical resolution is also given.

the remnant black hole in Table 2.9. Those tables display the excellent agreement between the horizon and radiative computation of the energy and angular momentum (with convergence rates of the 3-4th order). It also displays the agreement of those radiative computations for the $m\eta = 2$ and the $m\eta = 0.5$ cases, as expected on the ground of gauge invariance at the extrapolated infinite observer location. The Table also shows the robustness of the horizon computations at any of the used resolutions (generally 5 digits) and an overconvergence due to those small differences.

We complete our nonspinning studies by simulating a smaller mass ratio ($q = 1/5$) binary with initial separation $d = 10.75m$. The recoil from radiation of linear momentum extrapolates to about 139km/s as shown in Table 2.11. The horizon evaluation for $m\eta = 2$ underevaluates this by about 30%, while for $m\eta = 0.5$ the horizon formula is about 5% this value for the medium and high resolution runs. Given the smaller mass ratio, the low resolution run is not as accurate.

We also provide as a reference the computation of the of the horizon evaluations for the mass and spin of the remnant black hole in Table 2.10. Those Tables display the excel-

| $m\eta = 2.0$ | | | | | | |
|-----------------|-------------|---------------|---------|----------------|--------------|-----------------|
| h_i/m | E_{rad}/m | J_{rad}/m^2 | m_f/m | α_f/m^2 | $\Delta m/m$ | $-\Delta J/m^2$ |
| 1/100 | 0.02999 | -0.30497 | 0.96126 | 0.62344 | 0.03029 | -0.30617 |
| 1/120 | 0.03016 | -0.30600 | 0.96125 | 0.62345 | 0.03030 | -0.30617 |
| 1/140 | 0.03024 | -0.30629 | 0.96125 | 0.62346 | 0.03030 | -0.30617 |
| $\rightarrow 0$ | 0.030337 | -0.30646 | 0.96125 | 0.62346 | | |
| n | 3.70 | 6.36 | 13.36 | 6.09 | | |
| $m\eta = 0.5$ | | | | | | |
| 1/100 | 0.02998 | -0.30516 | 0.96124 | 0.62343 | 0.03031 | -0.30620 |
| 1/120 | 0.03014 | -0.30583 | 0.96125 | 0.62345 | 0.03030 | -0.30617 |
| 1/140 | 0.03022 | -0.30615 | 0.96126 | 0.62345 | 0.03030 | -0.30617 |
| $\rightarrow 0$ | 0.03033 | -0.30662 | 0.96126 | 0.62345 | | |
| n | 3.42 | 3.39 | 7.20 | 8.62 | | |

Table 2.9: Comparison of the computation of the horizon mass and spin of the remnant of a $q = 1/2$, nonspinning binary with the radiation of the energy and angular momentum for the $\eta = 2$ and for the $\eta = 0.5$ cases. Extrapolation to infinite resolution and convergence order is also given for the horizon computation and the radiative extraction.

lent agreement between the horizon and radiative computation of the energy and angular momentum (with high convergence orders). We find excellent agreement of those radiative computations for the $m\eta = 2$ and the $m\eta = 0.5$ cases, as expected from the gauge invariance of the waveforms extrapolated to an infinite observer location. The Table also shows the robustness of the horizon computations at medium and high resolutions (generally 3 digits) and an overconvergence due to those small differences.

2.4.2 Spinning black holes

In order to further verify our technique and to extend our results, we study the recoil velocity of the remnant black hole of a pair of spinning binaries. Consider an equal mass ($q = 1$) binary with spins ($\alpha_{1,2} = \pm 0.8$) (anti)aligned with the orbital angular momentum. This system has an initial separation of $d = 10m$. The resulting recoil will be along the orbital plane and due entirely to the asymmetry produced by the opposing spins. The results are presented in Table 2.12, showing that the horizon evaluation for $m\eta = 0.5$ at 420km/s is as good to that value than any radiative evolution at the same resolution (388km/s), with errors of the order of 4%, even for the lowest computed resolution, n100. Here, we have assumed that the radiated

2.4. Results for a $q = 1/3$ nonspinning binary

| $m\eta = 2.0$ | | | | | | |
|-----------------|-------------|---------------|---------|----------------|--------------|-----------------|
| h_i/m | E_{rad}/m | J_{rad}/m^2 | m_f/m | α_f/m^2 | $\Delta m/m$ | $-\Delta J/m^2$ |
| 1/100 | 0.01237 | -0.15454 | 0.98217 | 0.41667 | 0.01253 | -0.14804 |
| 1/120 | 0.01225 | -0.14872 | 0.98235 | 0.41667 | 0.01235 | -0.14790 |
| 1/140 | 0.01226 | -0.14803 | 0.98237 | 0.41660 | 0.01232 | -0.14796 |
| $\rightarrow 0$ | 0.01227 | -0.14788 | 0.98238 | 0.41667 | | |
| n | 11.59 | 11.41 | 10.78 | -15.49 | | |
| $m\eta = 0.5$ | | | | | | |
| 1/100 | 0.01310 | -0.16762 | 0.98158 | 0.41572 | 0.01320 | -0.14944 |
| 1/120 | 0.01241 | -0.15479 | 0.98221 | 0.41670 | 0.01249 | -0.14800 |
| 1/140 | 0.01227 | -0.14859 | 0.98236 | 0.41663 | 0.01234 | -0.14795 |
| $\rightarrow 0$ | 0.01221 | -0.13922 | 0.98242 | 0.41662 | | |
| n | 8.12 | 3.30 | 7.59 | 14.39 | | |

Table 2.10: Comparison of the computation of the horizon mass and spin of the remnant of a $q = 1/5$, nonspinning binary with the radiation of the energy and angular momentum for the $\eta = 2$ and for the $\eta = 0.5$ cases. Extrapolation to infinite resolution $h_i \rightarrow 0$ and convergence order n is also given for the horizon computation and the radiative extraction.

linear momentum extrapolated to infinite resolution is the most accurate measure, leading to a recoil of 403 ± 1 km/s. As we have seen before, the improvement of those horizon values are obtained by lowering the value of $m\eta \rightarrow 0$, rather than by higher resolution, as the horizon quasilocal measure has essentially already converged at those resolutions.

For the sake of completeness, and to verify the accuracy of the horizon evaluations for the mass and spin of the remnant black hole, we provide their computation in Tables 2.13. Those tables display the excellent agreement between the horizon and radiative computation of the energy and angular momentum (with convergence rates of the 3rd-4th order). They also show the agreement of radiative computations for the $m\eta = 2$ and the $m\eta = 0.5$ cases, as is expected on the ground of gauge invariance at the extrapolated infinite observer location. Further, the tables show the robustness of the horizon computations (generally accurate to 5 digits) at any of the chosen resolutions.

A final note on the convergence studies carried out in this section is that we observe a good convergence rate of 3rd to 4th order for radiative quantities, while for horizon quantities, we observe a wider range of values, sometimes even overconvergence. This is due to the fact that the horizon evaluations (particularly for the mass and spin) lead to very accurate values,

| | Radiation | Horizon | Radiation | Horizon |
|-----------------|----------------|-------------------------------|----------------|-------------------------------|
| h_i/m | $m\eta = 2.0$ | $m\eta = 2.0$ | $m\eta = 0.5$ | $m\eta = 0.5$ |
| 1/100 | 129.40 | 98.67 ± 0.60 | 130.21 | 209.00 ± 2.16 |
| 1/120 | 133.91 | 102.53 ± 0.16 | 133.19 | 131.93 ± 1.22 |
| 1/140 | 135.94 | 101.62 ± 0.13 | 136.70 | 143.28 ± 0.17 |
| $\rightarrow 0$ | 138.57 | — | — | — |
| n | 3.72 | — | — | — |
| 1/100 | 318.79° | $317.09^\circ \pm 0.91^\circ$ | 333.20° | $366.32^\circ \pm 0.56^\circ$ |
| 1/120 | 374.99° | $376.95^\circ \pm 0.33^\circ$ | 345.29° | $293.68^\circ \pm 0.04^\circ$ |
| 1/140 | 332.13° | $329.04^\circ \pm 0.33^\circ$ | 385.40° | $384.90^\circ \pm 0.11^\circ$ |

Table 2.11: Comparison of the computation of the recoil velocity (in km/s) of the remnant of a $q = 1/5$, nonspinning binary by traditional radiation of linear momentum and the horizon formula (2.1.1) averaged between $t = 2300m$ and $t = 2500m$ for the traditional $\eta = 2$ and for the $\eta = 0.5$ case. Extrapolation to infinite resolution $h_i \rightarrow 0$ and convergence order n is also given for the horizon and radiative extraction. The bottom panel gives the angle (in degrees) of the recoil velocity with respect to the x-axis. Standard deviations of horizon measurements are given as \pm for each quantity.

and hence small differences between the three resolutions chosen for the simulations (n100, n120, and n140). In order to seek very significant differences between resolutions, factors larger than our chosen 1.2 would be necessary. Such a study would require significantly more computational resources. Nevertheless, we have been able to prove that horizon quantities can be evaluated very accurately at any of the resolutions quoted above.

2.5 Studies with Alternative Gauges

Right after the breakthrough that allowed for the evolution of binary black holes with the moving puncture formalism [8, 24], several papers analyzed extensions of the basic gauges (2.2.3) - (2.2.5). In Refs. [83] and [66] several parametrizations of the shift conditions were studied, and displayed some (slight) preference for the ∂_0 -gauge over the ∂_t -gauge (See Table I of Ref. [83] and Fig. 10 of Ref. [66]).

The sensitivity of the computed recoil on the gauge give us an opportunity to quantify the relative accuracy of the ∂_0 -gauge versus the ∂_t -gauge.

We will also exploit the possibility of using a variable $\eta(x^k(t))$ to obtain both the benefits of accuracy around the black holes and a good coordinate behavior connecting the horizon

2.5. Studies with Alternative Gauges

| h_i/m | Radiation | Horizon | Radiation | Horizon | Radiation | Horizon |
|-----------------|----------------|-------------------------------|----------------|-------------------------------|----------------|-------------------------------|
| | $m\eta = 2.0$ | $m\eta = 2.0$ | $m\eta = 1.0$ | $m\eta = 1.0$ | $m\eta = 0.5$ | $m\eta = 0.5$ |
| 1/100 | 387.92 | 331.98 ± 1.50 | - | - | 388.13 | 419.89 ± 0.30 |
| 1/120 | 394.16 | 331.84 ± 1.41 | 394.13 | 396.41 ± 0.22 | 394.16 | 421.02 ± 0.38 |
| 1/140 | 397.43 | 331.75 ± 1.49 | - | - | 397.16 | 419.67 ± 0.86 |
| $\rightarrow 0$ | 403.42 | 331.40 | - | - | 402.00 | - |
| n | 2.82 | 1.46 | - | - | 3.12 | - |
| 1/100 | 135.51° | $135.81^\circ \pm 0.93^\circ$ | - | - | 135.70° | $137.25^\circ \pm 0.27^\circ$ |
| 1/120 | 136.70° | $135.72^\circ \pm 0.92^\circ$ | 136.65° | $135.51^\circ \pm 0.27^\circ$ | 136.72° | $136.65^\circ \pm 0.14^\circ$ |
| 1/140 | 137.39° | $135.80^\circ \pm 0.94^\circ$ | - | - | 137.15° | $136.61^\circ \pm 0.13^\circ$ |
| $\rightarrow 0$ | 139.07° | 135.78° | - | - | 137.60° | 136.83° |
| n | 2.23 | 4.26 | - | - | 4.23 | 4.29 |

Table 2.12: Comparison of the computation of the recoil velocity (in km/s) of the remnant of a $q = 1$, $\alpha_i = \pm 0.8$ binary by traditional radiation of linear momentum and the horizon formula (2.1.1) averaged between $t = 1050m$ and $t = 1350m$ for the traditional $\eta = 2$ and the $\eta = 1$ and 0.5 cases. Extrapolation to infinite resolution $h_i \rightarrow 0$ and convergence order n is also given for the radiative extraction. The bottom panel gives the angle (in degrees) of the recoil velocity with respect to the x-axis. Standard deviations of horizon measurements are given as \pm for each quantity. In this case $m\eta = 1$ produces a better measure of recoil velocity than other choices of $m\eta$.

results with asymptotia.

In Fig. 2.5 we draw a comparative analysis of the final black hole horizon recoil as computed in the ∂_0 and ∂_t gauges, at our highest resolution n140. In all three cases, $m\eta = 2, 1, 0.5$, the computation in the ∂_t -gauge is notably and systematically closer to the expected ($V_f \sim 177\text{km/s}$) recoil velocity. This also provides a scale of the accuracy of the evaluation of the recoil for our new preferred value, $m\eta = 0.5$.

Convergence with resolution does not resolve the discrepancies in favor of the ∂_t -gauge as displayed in Fig. 2.6 for $m\eta = 2$ in in the ∂_0 -gauge at n100, n120, and n140 resolutions. The limit $\eta \rightarrow 0$ is even harder to resolve in the ∂_0 -gauge than in the ∂_t -gauge case.

The results for the evolutions in the ∂_0 -gauge are summarized in Table 2.14. These results should be compared with those in Tables 2.4-2.5, which are in the ∂_t -gauge. While the individual computations of the extracted radiation are comparable and convergent to essentially the same values, i.e. a recoil magnitude of about 177km/s and an angle with the x -axis of 375° , the closeness to those values in the ∂_t -gauge is apparent for all values of η . A second control case is studied in Table 2.15, where we consider the spinning binary system described

| $m\eta = 2.0$ | | | | | | |
|-----------------|-------------|---------------|---------|----------------|--------------|---------------|
| h_i/m | E_{rad}/m | J_{rad}/m^2 | m_f/m | α_f/m^2 | $\Delta m/m$ | $-\Delta J/m$ |
| 1/100 | 0.03872 | -0.34232 | 0.95071 | 0.68413 | 0.03936 | -0.34403 |
| 1/120 | 0.03898 | -0.34320 | 0.95071 | 0.68413 | 0.03936 | -0.34403 |
| 1/140 | 0.03911 | -0.34362 | 0.95071 | 0.68413 | 0.03936 | -0.34404 |
| $\rightarrow 0$ | 0.03930 | -0.34421 | 0.95071 | 0.68413 | - | - |
| n | 3.28 | 3.45 | - | - | - | - |
| $m\eta = 1.0$ | | | | | | |
| 1/120 | 0.038979 | -0.34318 | 0.95071 | 0.68413 | 0.03936 | 0.34404 |
| $m\eta = 0.5$ | | | | | | |
| 1/100 | 0.03872 | -0.34232 | 0.95071 | 0.68413 | 0.03935 | -0.34405 |
| 1/120 | 0.03898 | -0.34318 | 0.95071 | 0.68413 | 0.03936 | -0.34403 |
| 1/140 | 0.03911 | -0.34358 | 0.95071 | 0.68413 | 0.03935 | -0.34404 |
| $\rightarrow 0$ | 0.03930 | -0.34411 | 0.95071 | 0.68413 | - | - |
| n | 3.30 | 3.58 | - | - | - | - |

Table 2.13: Comparison of the computation of the horizon mass and spin of the remnant of a $q = 1$, $\alpha_i = \pm 0.8$ binary with the radiation of the energy and angular momentum for the $m\eta = 2$ and for the $m\eta = 0.5$ cases. Extrapolation to infinite resolution $h_i \rightarrow 0$ and convergence order n is also given for the radiative extraction.

in Section 2.4.2. We directly compare the ∂_0 -gauge new simulations with the ∂_t -gauge simulations reported in Table 2.12. Based on those results we expect recoil magnitudes in the 402-403km/s and angles in the $138^\circ - 139^\circ$ ranges. The results for $m\eta = 2$ confirms the closer to the expected recoils in the ∂_t -gauge, and those of $\eta = 0.5$ bracket it, with preference for the ∂_t -gauge. We also observe again that the horizon values are much more sensitive to the values of η than to resolutions (at least for increases in resolution by a factor of 1.2).

2.5.1 ∂_0 -gauge

In conclusion, we have observed the advantage of working in the ∂_t -gauge over the ∂_0 -gauge regarding computation of recoil velocities from the horizon formula (2.1.1). This is in agreement with our generic experience for binary black hole simulations being more accurate in our standard ∂_t -gauge at the same resolutions and same values of η , but now we have quantified it in the recoil computations example. As we converge to higher resolutions, both gauges lead to consistent and accurate solution in all studied quantities.

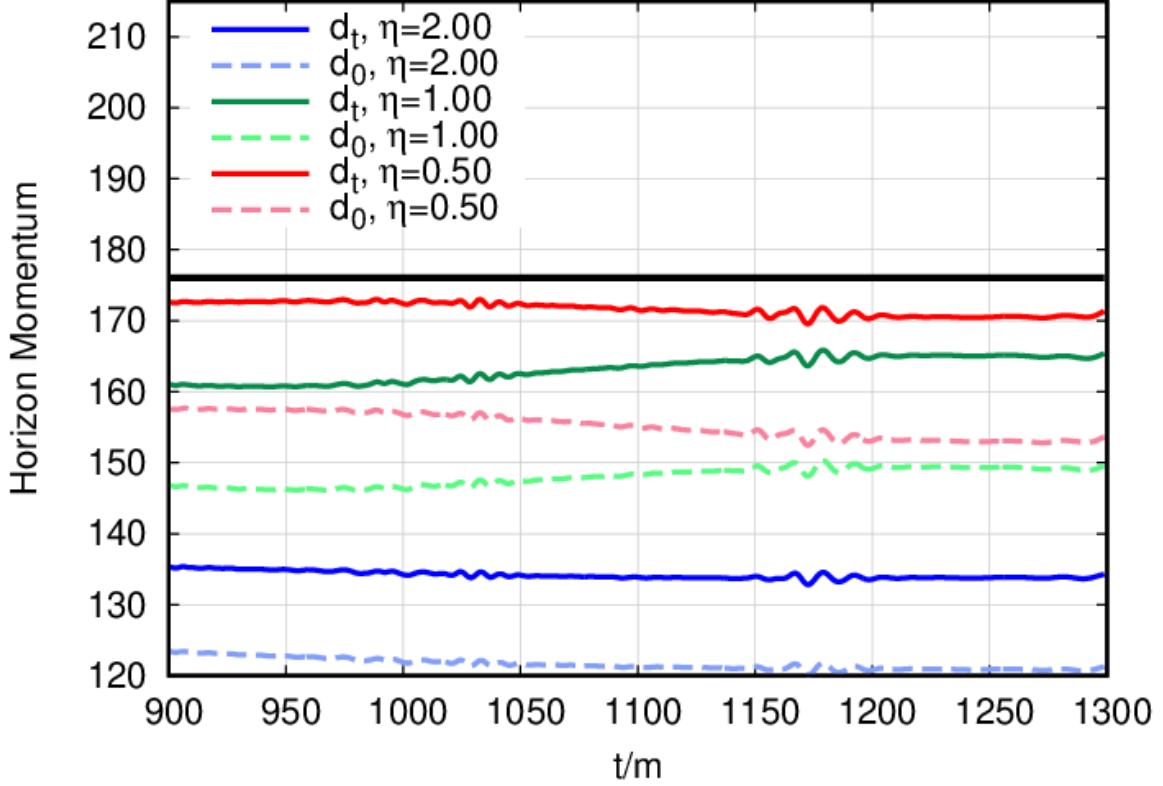


Figure 2.5: Comparative results of the ∂_t -gauge (solid) and ∂_0 -gauge (dashed) for the horizon measure of the linear momentum (in km/s) after merger of a $q = 1/3$ nonspinning binary for the n140 resolution for $m\eta = 2$ (blue), 1 (green), 0.5 (red). The reference value of V_f is found by extrapolation to infinite resolution of the radiated linear momentum.

2.5.2 η -variable gauge

In addition to the changes in the (constant) values of η , different functional dependences for $\eta(x^k, t)$ have been proposed in [70, 84, 85, 86, 87, 7].

Here we use a modified form motivated by the results of [65] and this paper that the recoil velocities (of a merged binary) are more accurately computed when using the quasilocal horizon measure of the momentum with smaller η and that the generic evolution is more accurate and convergent for larger values of η .

We hence propose a simple variant for comparable masses binary

$$m\eta(x^k, t) = m\eta_\infty - A e^{-r^2/s^2} \quad (2.5.11)$$

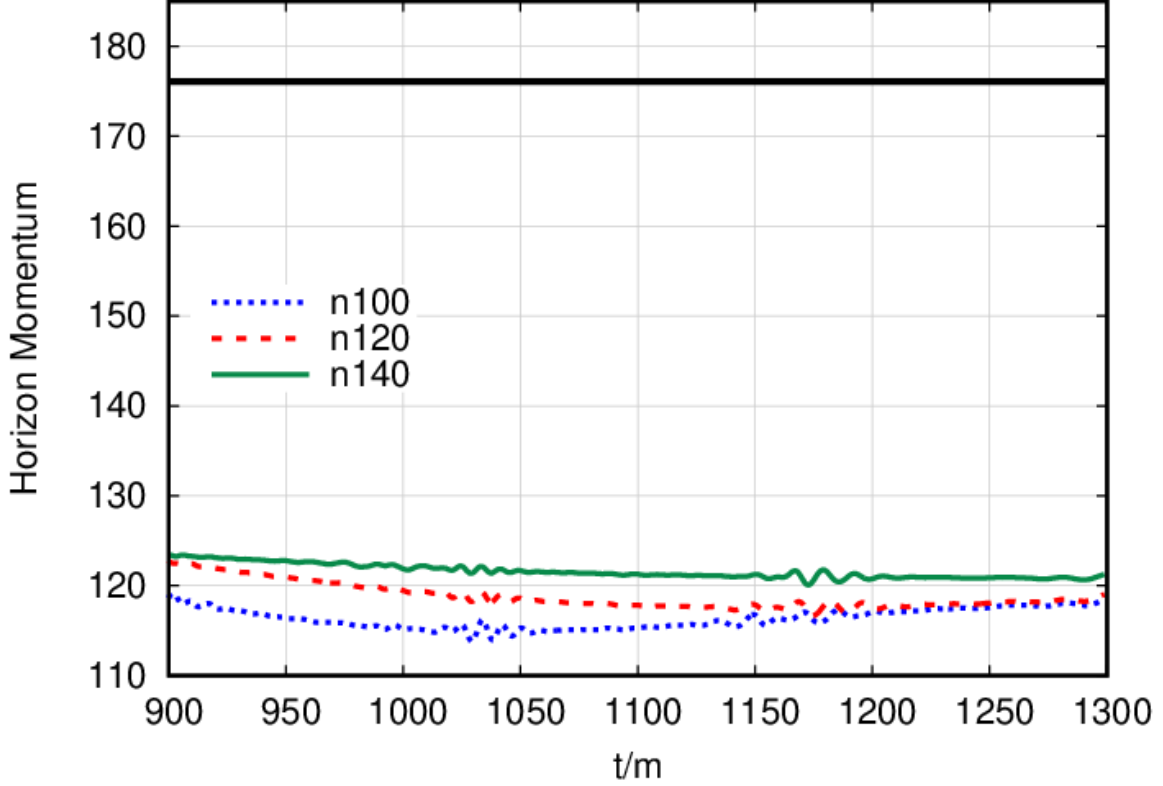


Figure 2.6: The horizon measure of the linear momentum (in km/s) after merger of a $q = 1/3$ nonspinning binary for the three resolutions labeled as n100, n120, and n140 in the ∂_0 -gauge for $\eta = 2/m$. The reference value of V_f is found by extrapolation to infinite resolution of the radiated linear momentum in this ∂_0 -gauge.

where $m = m_1 + m_2$ and $r = |\vec{r} - \vec{r}_{com}|$ is the distance from the (Newtonian) center of mass of the system [PN corrections could be added if needed [88]],

$$\vec{r}_{com} = (m_1 \vec{x}_1 + m_2 \vec{x}_2)/m \quad (2.5.12)$$

where $\vec{x}_1(t)$ and $\vec{x}_2(t)$ are the punctures location, and s is a width of the Gaussian that can be conveniently chosen, for instance, $s = 2m$. Typically for our simulations normalization is chosen such that $m \sim 1$ (and $M_{ADM} < 1$).

The choice to center the Gaussian correction to the η_∞ at the center of mass is to provide a simple way of following the final black hole after merger, even if acquired a large recoil velocity. The motivation to set different values around the black hole is to provide enough accuracy

| h_i/m | Radiation | Horizon | Radiation | Horizon | Radiation | Horizon |
|-----------------|----------------|-------------------------------|----------------|-------------------------------|----------------|-------------------------------|
| | $m\eta = 2.0$ | $m\eta = 2.0$ | $m\eta = 1.0$ | $m\eta = 1.0$ | $m\eta = 0.5$ | $m\eta = 0.5$ |
| 1/100 | 163.67 | 127.11 ± 0.87 | — | — | — | — |
| 1/120 | 168.57 | 129.10 ± 0.98 | — | — | — | — |
| 1/140 | 171.24 | 128.84 ± 0.57 | 171.30 | 152.11 ± 1.92 | 171.33 | 160.9 ± 1.55 |
| $\rightarrow 0$ | 176.65 | 129.43 | — | — | — | — |
| n | 2.60 | 6.12 | — | — | — | — |
| 1/100 | 375.82° | $369.58^\circ \pm 0.29^\circ$ | — | — | — | — |
| 1/120 | 375.17° | $368.99^\circ \pm 0.53^\circ$ | — | — | — | — |
| 1/140 | 375.63° | $369.14^\circ \pm 0.63^\circ$ | 375.67° | $371.55^\circ \pm 0.09^\circ$ | 375.88° | $373.93^\circ \pm 0.10^\circ$ |
| $\rightarrow 0$ | — | 369.24° | — | — | — | — |
| n | — | 4.14 | — | — | — | — |

Table 2.14: Comparison of the computation of the recoil velocity (in km/s) of the remnant of a $q = 1/3$, $\alpha_i = \pm 0$ binary by traditional radiation of linear momentum and the horizon formula (2.1.1) measured $75m$ after merger. Computation uses the ∂_0 -gauge $m\eta = 2$ case for resolutions n100 n120 and n140 and ∂_0 -gauge $m\eta = 1, 0.5$ cases for resolution n140. Extrapolation to infinite resolution $h_i \rightarrow 0$ and convergence order n is also given for the radiative extraction for appropriate cases. The bottom panel gives the angle (in degrees) of the recoil velocity with respect to the x-axis. Standard deviations of horizon measurements are given as \pm for each quantity. Compare this results with those of Tables 2.5-2.6.

and convergence in the strong field regime, while preserving the benefits of the coordinates adapted to recoil measurements away from the remnant hole.

In order to assess those statements we have considered two cases labeled as N10 and N12, respectively determined by the $-$ and $+$ in

$$m\eta(x^k, t) = 1 \mp e^{-r^2/(2m)^2} \quad (2.5.13)$$

with the same reference asymptotic value of 1 at infinity and vanishing or taking the standard value of 2 at the (final) hole location.

The simulations (in the standard ∂_t -gauge) make use of this (2.5.13) dependence during the whole run, not only during the post-merger phase, but the horizon of the final black hole is only found and evaluated for linear momentum after the merger occurs (about $t \sim 725m$).

The results of the two cases are displayed in Fig. 2.7. Each case has been studied at our standard n100, n120, n140 resolutions to convey an idea of the convergence. The upper panel displays a very good agreement with the expected recoil, particularly for the medium and

| h_i/m | Gauge | Radiation | Horizon | Radiation | Horizon |
|---------|--------------------------|----------------|-------------------------------|----------------|-------------------------------|
| | ∂_0, ∂_t | $m\eta = 2.0$ | $m\eta = 2.0$ | $m\eta = 0.5$ | $m\eta = 0.5$ |
| 1/100 | ∂_0 | 387.94 | 294.93 ± 2.43 | 388.01 | 377.37 ± 1.56 |
| 1/100 | ∂_t | 387.92 | 331.98 ± 1.50 | 388.13 | 419.89 ± 0.30 |
| 1/120 | ∂_0 | 394.18 | 294.82 ± 2.41 | 394.13 | 376.89 ± 0.94 |
| 1/120 | ∂_t | 394.16 | 331.84 ± 1.41 | 394.16 | 421.02 ± 0.38 |
| 1/100 | ∂_0 | 135.53° | $135.71^\circ \pm 1.00^\circ$ | 135.78° | $137.31^\circ \pm 0.27^\circ$ |
| 1/100 | ∂_t | 135.51° | $135.81^\circ \pm 0.93^\circ$ | 135.70° | $137.25^\circ \pm 0.27^\circ$ |
| 1/120 | ∂_0 | 136.71° | $135.62^\circ \pm 1.00^\circ$ | 136.69° | $136.65^\circ \pm 0.18^\circ$ |
| 1/120 | ∂_t | 136.70° | $135.72^\circ \pm 0.92^\circ$ | 136.72° | $136.65^\circ \pm 0.14^\circ$ |

Table 2.15: Top panel shows the comparison of the computation of the recoil velocity (in km/s) of the remnant of a $q = 1$, $\alpha_i = \pm 0.80$ binary by traditional radiation of linear momentum and the horizon formula (2.1.1) averaged from $t/m = 1050$ to 1350 using the ∂_0 -gauge with $m\eta = 2$ and $m\eta = 0.5$ case at resolutions n100 and n120. The bottom panel gives the angle (in degrees) of the recoil velocity with respect to the x-axis. Both panels give also the ∂_t results from Table 2.12 for comparison. Standard deviations of horizon measurements are given as \pm for each quantity.

high resolutions. The agreement is even better than the constant $m\eta = 1$ case, displayed in the central panel of Fig. 2.3, which lies in between the N12 and N10 cases. To confirm the improvements reached by this variable- η gauge, the case N10, where the asymptotic value is the same, equal to 1, but where the η is reduced near the black hole, notably reduces the accuracy necessary to compute the linear momentum of the horizon and convergence is still more challenging than in the previous N12 case.

Those results for the variable η -gauge, as in (2.5.13), are summarized in Table 2.16 where we compare results with those in Tables 2.4-2.5 in the $\eta = 1$ -gauge. While the computation of the extracted radiation are comparable and convergent to essentially the same values, i.e. a recoil magnitude of about 176-7km/s and an angle with the x -axis of $375-6^\circ$, the closeness to those values in the N12-gauge is apparent followed by the $m\eta = 1$ (the reference value) and lagged by the N10-gauge, indicating that while the same asymptotic $m\eta = 1$ value is shared by the three gauges, that with $m\eta \rightarrow 2$ near the horizon of the black hole produces the most accurate results for the recoil computed via the horizon formula (2.1.1).

A second control case is studied in Table 2.17, where we consider the spinning binary system described in Section 2.4.2. We directly compare the N12-N10-gauge new simulations

2.5. Studies with Alternative Gauges

| h_i/m | Rad. | Horizon | Rad. | Horizon | Rad. | Horizon |
|-----------------|----------------|-------------------------------|----------------|-------------------------------|----------------|-------------------------------|
| | N12 | N12 | N10 | N10 | $m\eta = 1$ | $m\eta = 1$ |
| 1/100 | 163.65 | 169.88 ± 1.29 | 163.71 | 150.54 ± 1.18 | 163.75 | 160.51 ± 1.14 |
| 1/120 | 168.59 | 172.56 ± 0.75 | 168.61 | 153.52 ± 0.86 | 168.66 | 161.62 ± 1.36 |
| 1/140 | 171.20 | 177.64 ± 1.78 | 171.26 | 155.31 ± 1.75 | 171.31 | 165.01 ± 1.55 |
| $\rightarrow 0$ | 176.09 | — | 176.52 | 160.14 | 176.42 | — |
| n | 2.78 | — | 2.64 | 2.04 | 2.70 | — |
| 1/100 | 373.01° | $371.21^\circ \pm 0.93^\circ$ | 374.39° | $364.97^\circ \pm 0.27^\circ$ | 374.67° | $370.26^\circ \pm 0.29^\circ$ |
| 1/120 | 374.02° | $373.17^\circ \pm 0.92^\circ$ | 374.85° | $366.81^\circ \pm 0.14^\circ$ | 375.09° | $371.83^\circ \pm 0.27^\circ$ |
| 1/140 | 374.72° | $377.24^\circ \pm 0.94^\circ$ | 375.57° | $367.90^\circ \pm 0.13^\circ$ | 375.59° | $371.98^\circ \pm 0.09^\circ$ |
| $\rightarrow 0$ | 378.40° | — | — | — | 375.12° | 372.36° |
| n | 1.13 | — | — | — | 2.00 | 6.07 |

Table 2.16: Comparison of the computation of the recoil velocity (in km/s) of the remnant of a $q = 1/3$, $\alpha_i = 0$ binary by traditional radiation of linear momentum and the horizon formula (2.1.1) measured $75m$ after merger for the modified N12 and N10 gauges. The standard $m\eta = 1$ from Tables 2.5 and 2.6 is also provided for reference. Extrapolation to infinite resolution $h_i \rightarrow 0$ and convergence order n is also given for the radiative extraction. The bottom panel gives the angle (in degrees) of the recoil velocity with respect to the x-axis. Standard deviations of horizon measurements are given as \pm for each quantity.

| h_i/m | Radiation | Horizon | Radiation | Horizon | Radiation | Horizon |
|---------|----------------|-------------------------------|----------------|-------------------------------|----------------|-------------------------------|
| | N12 | N12 | N10 | N10 | $m\eta = 1.0$ | $m\eta = 1.0$ |
| 1/120 | 394.88 | 379.66 ± 0.80 | 393.87 | 335.74 ± 1.10 | 394.13 | 396.41 ± 0.22 |
| 1/120 | 137.44° | $141.54^\circ \pm 0.46^\circ$ | 136.38° | $128.90^\circ \pm 0.08^\circ$ | 136.65° | $135.51^\circ \pm 0.27^\circ$ |

Table 2.17: Comparison of the computation of the recoil velocity (in km/s) of the remnant of a $q = 1$, $\alpha_i = \pm 0.80$ binary by traditional radiation of linear momentum and the horizon formula (2.1.1) measured from $t/m = 1050$ to 1350 for the modified N12 and N10 gauges using $m\eta \rightarrow 1$ asymptotically, as well as $m\eta = 1.0$ for comparison. The bottom panel gives the angle (in degrees) of the recoil velocity with respect to the x-axis. Standard deviations of horizon measurements are given as \pm for each horizon quantity.

with each other using the radiation values as the more accurate references, and again find confirmation that the N12 results are much closer to the expected results than the N10 ones.

In conclusion, a first exploration of an η -variable leads to immediate benefits and opens the possibilities for further parameter refinement to include improvements to both accuracy and precision in numerical simulations of merging binary black holes. A more in-depth study of these variable gauges will be presented, specifically for small mass-ratio binaries, in Chapter 3.

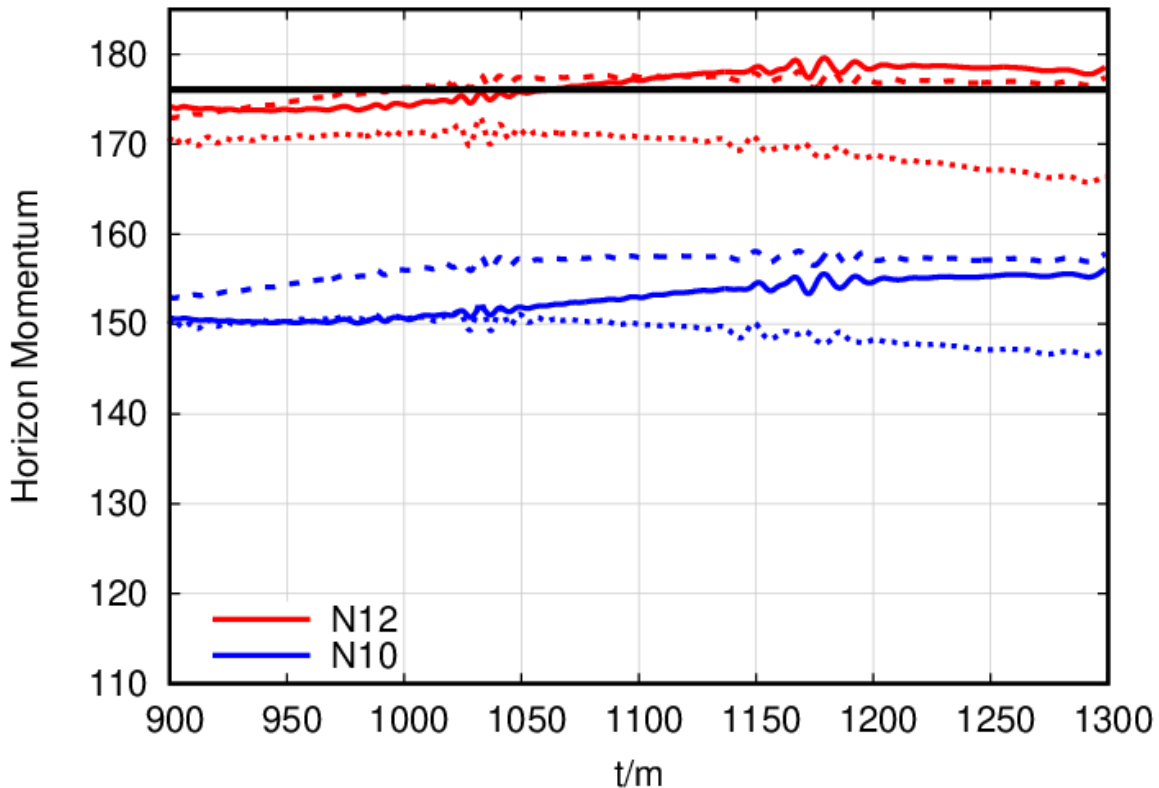


Figure 2.7: The horizon measure of the linear momentum after merger of a $q = 1/3$ nonspinning binary for the three resolutions labeled as n100 (dotted), n120 (dashed), and n140 (solid) for $\eta = N12$ (red) and N10 (blue), top to bottom respectively. The reference value of V_f is found by extrapolation to infinite resolution of the radiated linear momentum.

2.6 Discussion

The purpose of this study was to assess which choices of η lead to accurate measures of the linear momentum on the horizon with the non-gauge-independent formula (2.1.1), and we found that for small values $0.25 \leq m\eta \leq 0.5$ this is a reliable measure and can compete with the measurement at \mathcal{S}^+ of the radiated momentum carried by the gravitational waves. As with the computations of the mass and angular momentum of the remnant via the horizon measure and at infinity, it is important to have two concurrent methods to assess errors of those measures. Further accuracy could be achieved by the use of a variable η (See Eq. (2.5.11)). Our results indicate that the choice of $m\eta = 2$ at the horizon, with lower values at asymptotically far distances from the source(s), produce the best results for evaluation of the recoil).

Since these different gauges were studied in detail for a nonspinning $q = 1/3$ binary and verified with $q = 1/2$ and $q = 1/5$ as control cases, as well as for a $q = 1$ spinning case, we expect these conclusions to be general and plan to apply the findings to simulations where the computation of recoil is important, including precessing binaries. Cross checking with radiated linear momentum, extrapolated to infinity, will provide a method of evaluating these gauges' applicability and can be carried out concurrently in each simulation.

Finally, we assessed the relative accuracy of the two original moving puncture choices for the shift, the ∂_t and ∂_0 gauges, to evaluate the recoil, and found the ∂_t -gauge superior at the current typical numerical resolutions.

Chapter 3

An adapted gauge for small mass ratio binaries

3.1 Introduction

The 2005 breakthrough in numerical relativity techniques [23, 8, 24] has allowed for the production of thousands of binary black hole simulations (see for instance the catalogs [89, 90, 34, 35]). Improvements in hardware and numerical techniques contribute by speeding up simulations, however, some corners of the binary's parameter space remain relatively unexplored. Binaries in the small mass-ratio regime are challenging to simulate; they can take months of supercomputer time and require substantial computational resources to run accurate, long term numerical evolutions. These types of binaries are of particular interest for third generation gravitational wave detectors [91] and for the space-based mission LISA [92] since they have long, low frequency inspiral periods. Prototype small mass ratio simulations reaching $q = m_1/m_2 = 1/100$ have been achieved with the moving puncture approach [7, 93] and numerical convergence has been proven. Recently, another sequence of nonspinning binaries with mass ratios $q = 1/32, 1/64, 1/128$ has been studied in [22]. Such simulations should be considered proof of principle, but in order to become practical for production purposes, we need improvements in both computational efficiency and accuracy of the numerical techniques.

Of particular interest in this Chapter is to explore the choice for the numerical gauge, as well as the initial values for the lapse and shift equations, as a means to achieve improvements in accuracy without requiring more highly resolved (and hence more expensive) simulations.

One of the fundamental breakthroughs in 2005 was the optimization of the choice of the gauge equations. The gauge was originally developed to force successful evolutions without numerical simulations crashing. The moving puncture approach proved robust and produced accurate waveforms, even allowing the evolution of multi-black hole systems [94]. However, when studied in detail, subtleties appear with the convergence [95], and some gauge amplified initial noise has been observed [96]. This is particularly relevant for binaries with small mass ratios, as the amplitude of gravitational radiation scales like $\sim q$. The initial noise then reflects at the boundaries of the mesh refinement levels, which are necessary to efficiently describe the different scales of the binary system, causing high frequency oscillations when those reflections reach the observers.

In this Chapter we present work that has been accepted for publication by Physical Review D and will appear in 2021.¹ We will show that choices of the initial lapse and shift damping parameter η in the gauge can cure those initial inaccuracies, and lead to a much cleaner evolution of the binary black holes. We explore different choices of the initial lapse and shift in Section 3.2.1 to improve the accuracy of the simulations. In [67] as well as in Chapter 2 we studied the effect of different, constant shift damping parameters η on the extraction of recoil velocities from the horizon of the final remnant black hole of comparable mass ($q = 1/2, 1/3, 1/5$) binaries, we then began an exploration of a variable $m\eta$ and saw that it also provides a very good measure of quasi-local recoil. In Section 3.3.3 we will extend the analysis to adapt $\eta(\vec{x}_1(t), \vec{x}_2(t))$ to small mass ratio binaries. The results using these numerical techniques on the simulation of a prototypical nonspinning binary with mass ratio $q = 1/7$ is studied in detail in Section 3.4.1 with different choices for η and the initial lapse, as well as control convergence studies of binaries with mass ratio $q = 1/15$ and then $q = 1/32$ in Sections 3.4.2 and 3.4.3 respectively. In Section 3.4.4, we provide results for the extremal $q = 1/64$ binary as well as the $q = 1/128$ binary using the gauge choice we determined to be optimal

¹The manuscript can be found on the arxiv at <https://arxiv.org/pdf/2103.09326.pdf>.

from the previous sections.

We conclude in Section 3.5 with an optimal selection of initial lapse and shift damping parameter η that is simple to implement and numerically efficient, while still improves the accuracy of the simulations in the small mass ratio regime.

3.2 Numerical Techniques

Recall from Chapter 2, that for standard BBH evolutions we choose a gauge with a modified 1+log lapse and a modified Gamma-driver shift condition [44, 8],

$$\partial_0\alpha = (\partial_t - \beta^i\partial_i)\alpha = -2\alpha K, \quad (3.2.1)$$

$$\partial_t\beta^a = \frac{3}{4}\tilde{\Gamma}^a - \eta(x^k, t)\beta^a. \quad (3.2.2)$$

with the initial shift vanishing and the initial lapse $\alpha_0 = 2/(1 + \psi_0^4)$, where the conformal factor is defined as

$$\psi_0 = 1 + \frac{m_1}{2|\vec{r} - \vec{r}_1|} + \frac{m_2}{2|\vec{r} - \vec{r}_2|}. \quad (3.2.3)$$

The parameter η (dimensions one-over-mass: $1/m$) in the shift equation regulates the damping of the gauge oscillations. We have found in [68, 67] that coordinate dependent measurements, such as spin and linear momentum direction, become more accurate as η is reduced and the grid resolution is extrapolated to infinite ($h \rightarrow 0$). However, if η becomes too small ($\eta \ll 1/m$), the runs may become unstable. Similarly, if η is too large ($\eta \gg 10/m$), then grid stretching effects can cause the remnant horizon to continuously grow, eventually leading to an unacceptable loss in accuracy at late times. Therefore, η is commonly chosen to be of order unity as a compromise between the accuracy and stability of binary black hole evolutions; for comparable-mass binaries, our standard choice is $\eta = 2/m$.

To compute the initial data for the lapse and shift equations, we use the TWOPUNCTURES [69] thorn. These black-hole-binary (BHB) data-sets are then evolved using the LAZEV [70] implementation of the moving puncture formalism [8]. The Carpet [71] mesh refinement driver provides a ‘moving boxes’ style mesh refinement and we use AHFINDERDIRECT [73] to lo-

cate apparent horizons. The magnitude of the horizon mass, spin, and linear momentum are computed using the *isolated horizon* (IH) algorithm detailed in Ref. [74] (as implemented in Ref. [75]). Once we have the horizon spin, we can calculate the horizon mass via the Christodoulou formula $m_H = \sqrt{m_{\text{irr}}^2 + S_H^2/(4m_{\text{irr}}^2)}$, where $m_{\text{irr}} = \sqrt{A/(16\pi)}$ and A is the surface area of the horizon. The radiated energy, linear momentum, and angular momentum are all measured in terms of the Newman-Penrose Weyl scalar Ψ_4 , using the formulae provided in Refs. [76, 77], and extrapolation to \mathcal{I}^+ is performed with the formulas given in Refs. [67, 78, 65].

Convergence studies of our simulations have been performed in Appendix A of Ref. [1], in Appendix B of Ref. [33], and for nonspinning binaries are reported in Ref. [79]. For very highly spinning black holes ($s/m^2 = 0.99$) convergence of evolutions was studied in Ref. [80], for precessing $s/m^2 = 0.97$ in Ref. [54], and for ($s/m^2 = 0.95$) in Ref. [81] for unequal mass binaries. These studies allow us to assess that the simulations presented here, with similar grid structures, are well resolved by the adopted resolutions and are well within in a convergence regime.

3.2.1 The Initial Gauge

In this section we will derive the form of a new set of equations for the initial lapse and shift. The goal is to approximate those of the trumpet slice in quasi-isotropic coordinates r [97], both near the puncture $r = 0$ and far from source as powers of $1/r$. We expect that these ‘‘Trumpet-sliced’’ initial data will better match the evolved shape of the lapse and shift, therefore hopefully reducing the time necessary for the gauge to settle to its final, evolved shape. We will first construct these initial data for a single Schwarzschild black hole, then show how it is adapted for a binary. Our goal is to have this initial data take into account the full set of initial parameters of the binary, so we will then include terms that encode the initial linear and angular momenta in the expressions for the initial lapse and shift.

3.2.1.1 Initial Lapse

To construct the trumpet-like Late Time initial Lapse (LTL), we begin by proposing the following form:

$$\alpha_{LTL} = \alpha_0(\psi_0) = \frac{a}{1 + b\psi_0^n + c\psi_0^{n+1} + d\psi_0^{n-1}} \quad (3.2.4)$$

where a, b, c and d are constants to be determined by matching to trumpet data in isotropic coordinates close to the punctures, and to the behavior of the lapse far away $\alpha \sim (1 - m/r)/(1 + m/r)$. The value n is a function of an unknown constant γ , which is to be determined later.

The initial lapse is chosen to be a function of the conformal factor ψ_0 , defined in Eq. (3.2.3), as an extension of our original standard form for the lapse

$$\alpha_0 = 2/(1 + \psi_0^4). \quad (3.2.5)$$

We have the option of superposing the individual initial lapses for each puncture, so that $\alpha = \sum_{i=1,2} \alpha_{LTL}(\psi_i) - 1$ where

$$\psi_i = 1 + \frac{m_i}{2|\vec{r} - \vec{r}_i|}, \quad (3.2.6)$$

which would make our new initial lapse

$$\alpha_{LTL} = \alpha_1 + \alpha_2 - 1 \quad (3.2.7)$$

but this leads to negative values near the punctures. Instead, we would like value of the lapse to be 0 at the punctures, and approaching 1 as $r \rightarrow \infty$.

To obtain the desired behavior in Eq. (3.2.4), we begin by expanding the Schwarzschild lapse in isotropic coordinates in powers of $\frac{1}{r}$ to obtain

$$\alpha_{Sch} = (1 - m/2r)/(1 + m/2r) = 1 - 1/r + 1/2r^2 + \mathcal{O}(1/r^3). \quad (3.2.8)$$

Near the puncture, the expected trumpet-like behavior is

$$\alpha \sim Ar^{1/\gamma} \quad (3.2.9)$$

where (by Eq. (48) of [98])

$$\gamma = (2 - R_0)/(6 - 4R_0) = 0.9163407461; \quad (3.2.10)$$

$$R_0 = 1.312408290 \quad (3.2.11)$$

and according to numerical computations of [99], $A = 0.54$. Using this value will allow us to match the numerical behavior rather than strictly the isotropic coordinates, as in [98], where an alternative computation of A is done. In tests, we found that using $A = 0.54$ provides the best approximation of the settled shape of the lapse.

Choosing $n + 1 = 1/\gamma$ in Eq. (3.2.4) above and taking the limit as $r \rightarrow 0$, we obtain that

$$2.131254761(c/a) = A = 0.54 \quad (3.2.12)$$

which is approximated to be $a/c = 1/4$. Setting the other constants b, c, d to match the three orders of the expansion in Eq. (3.2.8), we find

$$a = \frac{2\gamma - 1}{6\gamma - 1}, b = -10 \frac{2\gamma - 1}{6\gamma - 1}, \quad (3.2.13)$$

$$c = 4 \frac{2\gamma - 1}{6\gamma - 1}, d = 2 \frac{4\gamma - 3}{6\gamma - 1}, \quad (3.2.14)$$

$$n = -\frac{\gamma - 1}{\gamma}$$

These expressions are finally inserted into Eq. (3.2.4) to construct this new choice for initial lapse.

For a visual representation of the differences between the typical initial lapse $\alpha_0 = 2/(1 + \psi_0^4)$ and α_{LTL} , refer to Fig. 3.1, which shows the two choices for lapse in red and blue (respectively) and their effects on a $q = 1/3$ binary with initial separation $d = 8m$. Here, we can see

that α_{LTL} (in blue) is tighter around the punctures than its counterpart in red α_0 , therefore mimicking the shape of the settled lapse slightly more accurately.

3.2.1.2 Initial Shift

We would also like to find a formula to model the late-time behavior of the initial shift β analogous to Eq. (3.2.4). From [98] [Eqs. (7) and (18)] we have analytic expressions for the shift at distances close to the black hole

$$\beta^r = r\beta/R \tag{3.2.15}$$

and at large r , the shift magnitude,

$$\beta^2 = C \exp(\alpha)/R^6, \tag{3.2.16}$$

where r denotes isotropic coordinates and R denotes Schwarzschild ones and, $C = 1.554309591$. Equating the equations (3.2.15) and (3.2.16),

$$\beta^r/r = \sqrt{C} \exp(\alpha/2)/R^3 \tag{3.2.17}$$

$$\rightarrow \sqrt{C}/R_0^3 = 0.5515207650, \tag{3.2.18}$$

for $R \rightarrow 0$ where from Eqs. (23) and (28) of [98] we have

$$\begin{aligned} C &= e^{3-\sqrt{10}}(3 + \sqrt{10})^3/128 \\ &= 1.554309591R_0^4 - 2R_0^3 + C = 0, \end{aligned} \tag{3.2.19}$$

$$R_0 = 1.312408290 \tag{3.2.20}$$

This agrees well with the estimates derived from the numerical fittings (6) and (7) in [99]. From these, define

$$K \approx 0.30 - 0.92\alpha; \quad \text{where } K = \beta\alpha'(R)/2. \tag{3.2.21}$$

From which we can find that the leading order term of the shift should be

$$\beta^r/r = \beta/R = 2K/R\alpha'(R) \quad (3.2.22)$$

$$\rightarrow 0.60/R_0\alpha'(R_0) \approx 0.55, \quad (3.2.23)$$

for $r \rightarrow 0$. With the use of Eq. (31) in [98] we have

$$\alpha'(R_0) = (6 - 4R_0)/(2 - R_0)R_0. \quad (3.2.24)$$

On the other hand, to study the shift behavior at large distances from the BH we have in the expansion of the eq. (3.2.17)

$$\frac{\sqrt{C}e^{1/2}}{r^2} - 7/2 \frac{\sqrt{C}e^{1/2}}{r^3} + \frac{57}{8} \frac{\sqrt{C}e^{1/2}}{r^4} + O(r^{-5}) \quad (3.2.25)$$

where we have used that in isotropic coordinates,

$$\alpha_{iso} = (1 - m/2r)/(1 + m/2r) \quad (3.2.26)$$

far from the center of coordinates.

In a similar fashion as for the lapse, we propose the following representation for the initial shift

$$\beta_0^r(\psi_0) = \frac{a(\psi_0 - 1)^2}{1 + b\psi_0 + c\psi_0^2 + d\psi_0^3} \quad (3.2.27)$$

Matching expansions (3.2.22) and (3.2.25) with (3.2.27), we get

$$\begin{aligned} a &= -0.5368350604, b = -3.620281004, \\ c &= 4.501732957, d = -1.946744690. \end{aligned} \quad (3.2.28)$$

3.2.1.3 Two black holes

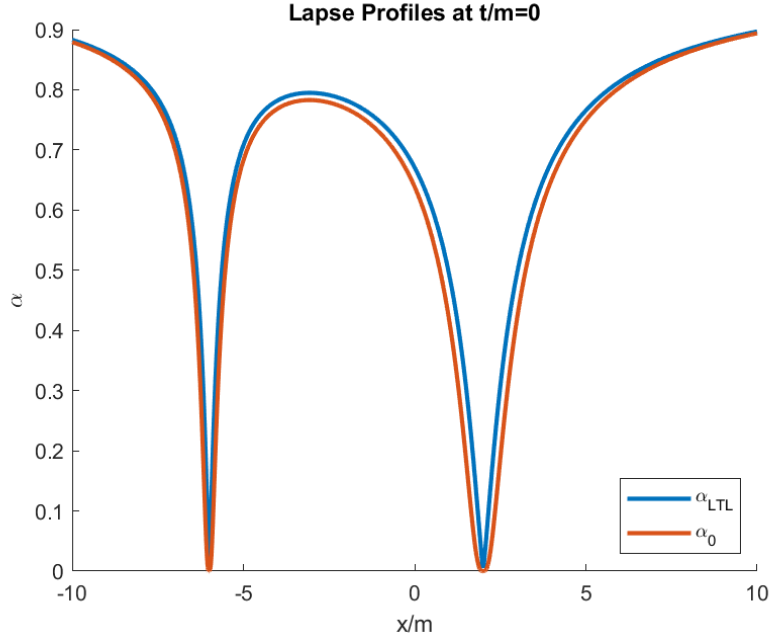


Figure 3.1: In red is shown the initial lapse $\alpha_0(\psi_0)$ and in blue is the late time lapse α_{LTL} . [This is for a case study with $m_2 = 3/4$, $m_1 = 1/4$, located at $x_1 = -6$ and $x_2 = 2$ respectively, and where we have normalized so that $m_1 + m_2 = 1$].

When constructing this initial data for two black holes, we do not assume that the lapse for each black hole adds linearly, but instead include the information about the binary in the conformal factor ψ_0 . For an arbitrary binary, the ψ_0 in Eq. (3.2.4) matches that in Eq. (3.2.3). The resulting shape of the initial lapse is shown in Fig. 3.1 for a binary with $m_1 = 1/4$, $m_2 = 3/4$, located at $x_1 = +6$ and $x_2 = -2$, respectively and normalized by $m_1 + m_2 = 1$.

In the case of the trumpet Late Time initial Shift (LTS), we do in fact assume it adds linearly for the two black holes as this matches the settled shape of the evolved shift best:

$$\beta_{LTS} = \beta_1^r(\vec{r} - \vec{r}_1)/|\vec{r} - \vec{r}_1| + \beta_2^r(\vec{r} - \vec{r}_2)/|\vec{r} - \vec{r}_2|. \quad (3.2.29)$$

Fig. 3.2 displays the behaviors of the initial shifts (zero-shift in red, and LTS in blue) for the same case study as above. The LTS initial data pushes the shift away from the black holes at the punctures and damps to zero far away, whereas our original β_0 was vanishing everywhere.

3.3. Initial lapse and shift for Boosted and Spinning Black Holes

We have chosen to not superpose the lapse and to superpose the shifts because, while testing different configurations, we found that those choices best matched the late-time behavior of the lapse and shift. Since these initial values for the gauge are ours to choose, we have this freedom. The construction presented in this section ignores the motion of the black holes. The

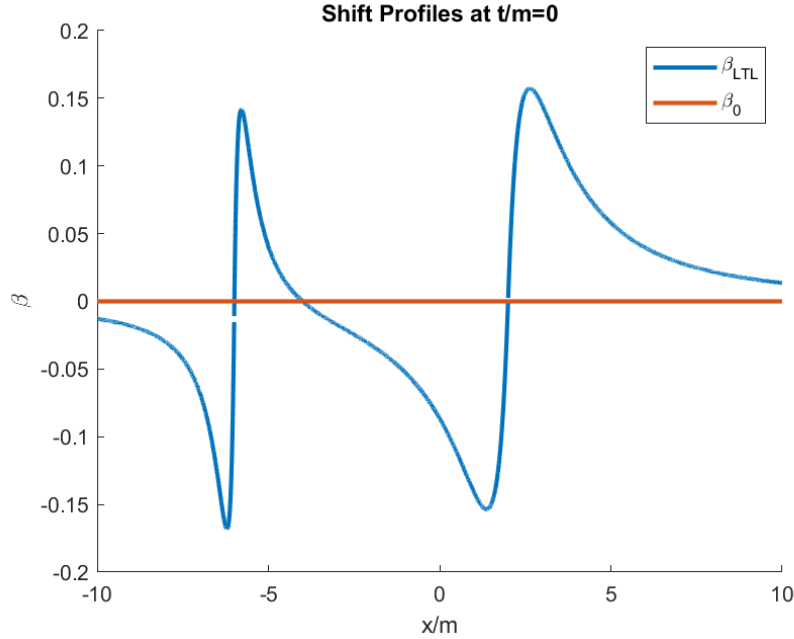


Figure 3.2: In red is the usual zero initial shift, and in blue is the superposition of the individual shifts showing the push away from each black hole. [This is for a case study with $m_2 = 3/4$, $m_1 = 1/4$, located at $x_1 = 2$ and $x_2 = -6$, respectively].

inclusion of initial linear and angular momentum of the holes into the analytic expressions for the initial lapse and shift can be done in terms of a Lorentz boost and a Kerr shift. We provide explicit expressions in Section 3.3.

3.3 Initial lapse and shift for Boosted and Spinning Black Holes

3.3.1 Lorentz-boosted black holes:

Since we are considering binaries with initial orbital momentum, it is of interest to include corrections in the configurations of the initial lapse and shift that account for this. To construct initial lapse data for a black hole system with boost, the conformal factor ψ_0 is modified so

3.3. Initial lapse and shift for Boosted and Spinning Black Holes

that its order $\frac{1}{r}$ term is multiplied by the boost

$$\gamma = \frac{1}{\sqrt{1 - |v|^2}}$$

where $|v|$ is the magnitude of the boost velocity. The conformal factor becomes

$$\psi_0 = 1 + \frac{\gamma m}{2r}.$$

It is then used in Eq. (3.2.4) to calculate the initial boosted lapse.

To construct initial shift data for a black hole system with boost, we must calculate the shift term from a boosted Schwarzschild black hole metric in Cartesian coordinates. Then, β^i terms can be added linearly onto the unboosted terms in Eq. (3.2.27). First, take the unboosted Schwarzschild metric

$$g_{\mu\nu} = \begin{bmatrix} -(\alpha)^2 & 0 & 0 & 0 \\ 0 & \psi_0^4 & 0 & 0 \\ 0 & 0 & \psi_0^4 & 0 \\ 0 & 0 & 0 & \psi_0^4 \end{bmatrix} \quad (3.3.30)$$

then apply a general boost transformation Λ_ν^μ on the metric $g_{\mu\nu}$

$$\tilde{g}_{\mu\nu} = \Lambda_\mu^\sigma \Lambda_\nu^\xi g_{\sigma\xi} \quad (3.3.31)$$

where

$$\Lambda_\mu^\nu = \begin{bmatrix} \gamma & -v_1\gamma & -v_2\gamma & -v_3\gamma \\ -v_1\gamma & 1 + \frac{(\gamma-1)v_1^2}{|v|^2} & \frac{(\gamma-1)v_1v_2}{|v|^2} & \frac{(\gamma-1)v_1v_3}{|v|^2} \\ -v_2\gamma & \frac{(\gamma-1)v_2v_1}{|v|^2} & 1 + \frac{(\gamma-1)v_2^2}{|v|^2} & \frac{(\gamma-1)v_2v_3}{|v|^2} \\ -v_3\gamma & \frac{(\gamma-1)v_3v_1}{|v|^2} & \frac{(\gamma-1)v_3v_2}{|v|^2} & 1 + \frac{(\gamma-1)v_3^2}{|v|^2} \end{bmatrix}. \quad (3.3.32)$$

3.3. Initial lapse and shift for Boosted and Spinning Black Holes

Then, the shift can be read off from the inverse spatial metric $\tilde{\gamma}^{ij}$ as

$$\beta^i = \frac{v^i(-\eta^2 + \psi_0^2)}{|v|\eta^2 - \psi_0^4} \quad (3.3.33)$$

for $\psi_0(m, r) = 1 + \frac{m}{2r}$, $\eta(m, r) = \frac{1 - \frac{m}{2r}}{\psi_0} = \alpha_{sch}$, and

$$v^i \approx \frac{P^i}{m}$$

where P^i are the momentum components of the boost. The terms β^i are added linearly onto the corresponding terms in Eq. (3.2.27) to construct an analytic representation for a boosted, nonspinning BBH system.

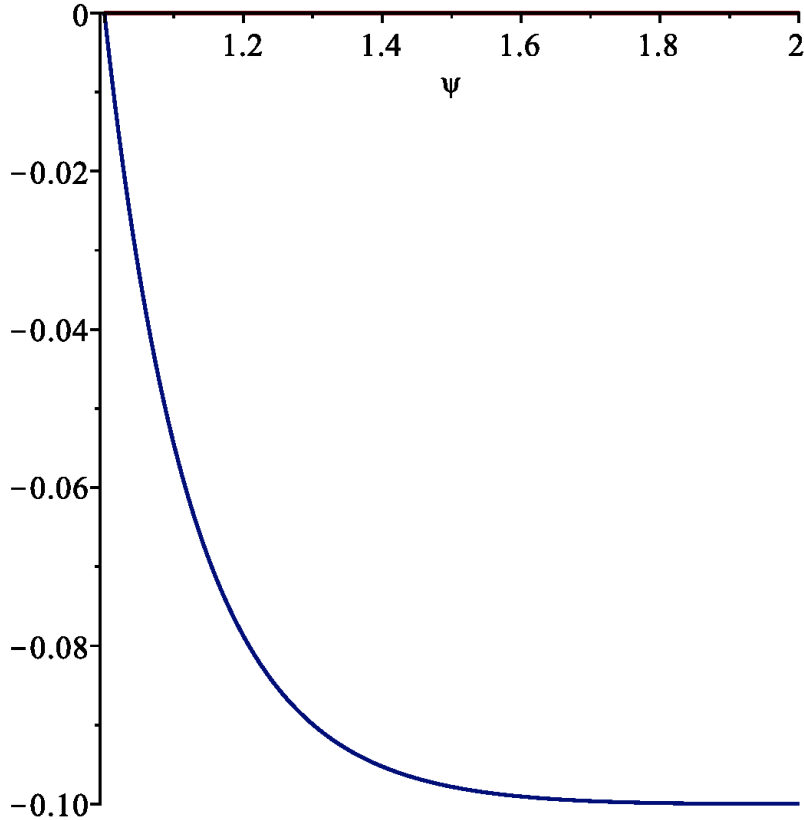


Figure 3.3: For small r , β^y for an initial velocity $v = 0.1$ versus $\psi_0 = 1 + m/(2r)$. The horizon of this Schwarzschild black hole is located at $\psi_H = 2$ and spatial infinity is at $\psi_\infty = 1$. We see that the shift decays slowly, like $\psi_0 - 1$.

We can try to force a stronger fall-off via asymptotic matching or an attenuation function. Another alternative is to directly consider the trumpet Initial Data for Boosted Black Holes: See details in Ref. [100]. For trumpet Slices in Kerr Spacetimes, see details in Ref. [101].

3.3.1.1 Results

We would like to be able to use the Late-Time Lapse, Late-Time Shift, and Lorentz boost correction to improve the early part of the binary’s inspiral. To this end, we have tested the Late-Time Lapse and Shift initial data as well as the Lorentz boost correction configuration on a binary with mass ratio $q = 1/3$, beginning at $d = 7m$ separation with no spin. This will be compared with the typical vanishing shift and $\alpha_0 = 2/(1 + \psi_0^4)$ choice for initial gauge. We use a grid resolution of n100 at the waveform extraction observer on the third coarsest level, which is somewhat over-resolved for such a simple case, but should still give a good idea of the effectiveness of these new initial data. These simulations use the 1+log lapse with Gamma-driver shift conditions for the gauge (in Eqs. (3.2.2)) and $m\eta = 2$ with merger occurring at $t/m = 725$. For consistency with the rest of this work, they also use the Lousto-Zlochower (LZ) gauge that Ref. [7] introduced, where $\eta(W)$ ($W = \sqrt{\chi} = \exp(-2\phi)$ with $\phi = \phi(\frac{1}{\psi_0})$, and the conformal factor suggested by [102]).

To evaluate the results, we will look at the constraint violations, the horizon masses and the dominant mode of Weyl scalar $\Psi_4^{2,2}$, which we use for gravitational wave extraction. We are hoping to see improvements between the early parts of simulations with the original initial gauge α_0 and β_0 and the Late-time Lapse/Shift additions and also the LTL/LTS additions and the boost-corrected versions. To that end, we expect that the simulations should settle to the same gauge and therefore will focus our study on the first $200m$ of simulation time.

Figure 3.4 shows the L2 norm of violations to the Hamiltonian constraint versus time for the initial data choices α_0/β_0 from Eqs.(3.2.2), the LTL/LTS (LTLS) choices, and the LTL/LTS + Boost (B) (LTLS + B) correction. All simulations that use LT initial data show an early spike in constraint violations, but then within $t = 20m$ they drop to acceptable levels. The LT+B initial gauge choice produces constraint violations that are slightly higher than the

3.3. Initial lapse and shift for Boosted and Spinning Black Holes

Original (O) initial gauge choice, whereas the LT-only simulation does reduce violations to the constraints. Since the simulations exist in different gauges, the constraint violations could be rescaled, and they therefore may not necessarily be reflective of the differences between gauges.

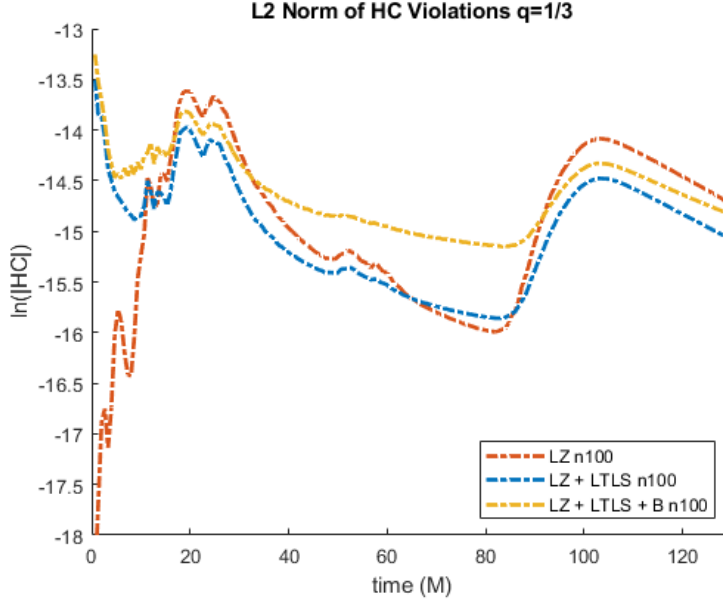


Figure 3.4: L2 norm of the Hamiltonian constraint violations versus time for the simulations with $q = 1/3$ and $d = 7m$ separation with initial gauge choices α_0/β_0 from Eqs.(3.2.2), the LTL/LTS choices, and the LTL/LTS + Boost (B) correction. Both of the LT simulations show an early increase in constraint violations, but then drop to acceptable levels within $t = 20m$.

To get an accurate idea of how the LTLS/LTLS+B initial gauges affect our simulation, we must instead look to gauge invariant measures such as physical parameters. Figure 3.5 shows the horizon masses of both black holes using the three different choices for initial gauge. The LTLS and LTLS+B initial gauge choices (blue and yellow curves, respectively), cause mass loss in m_2 and mass accumulation in m_1 , whereas the simulation with the original initial data choice remains relatively constant. We also looked at the gravitational waveform for all simulations, and saw no substantial differences between the three different gauges. To assess the origin of the issues in the masses, we then moved on to performing some further tests that studied LTL and LTS individually. In these, we found that the inclusion of the Late-Time Shift is the cause of mass-loss in the large black hole m_2 and mass increase in the small black

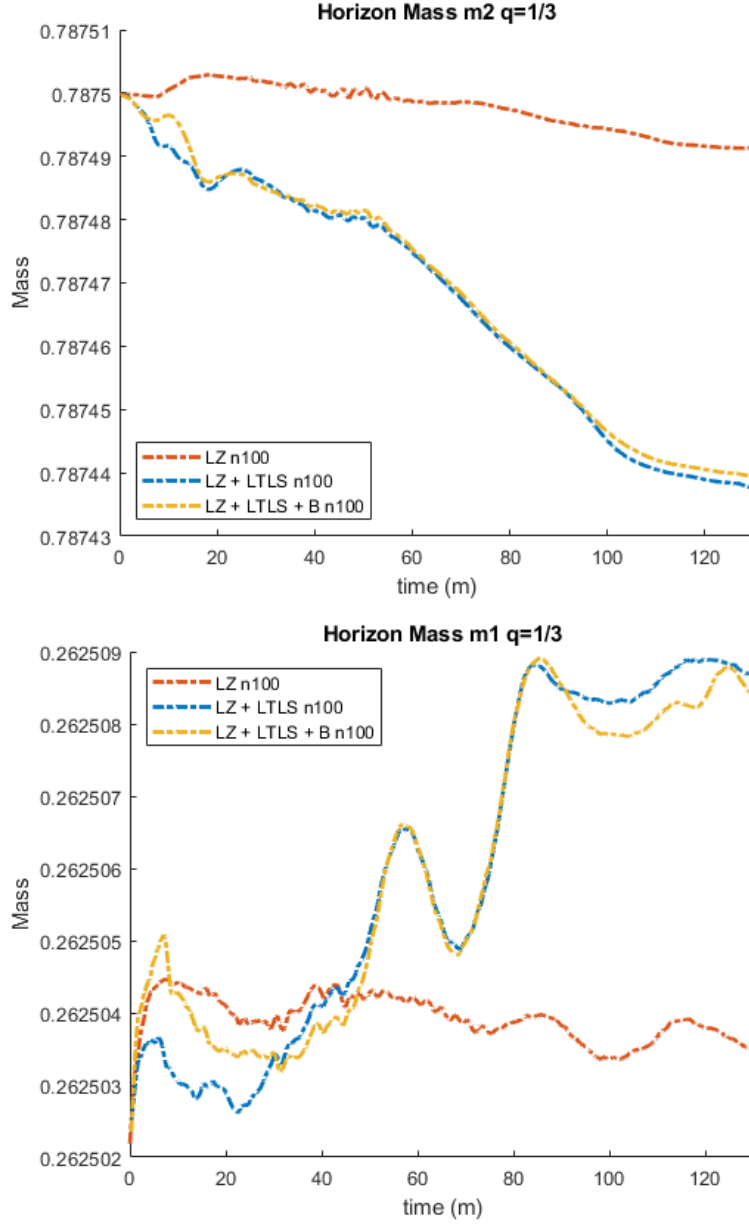


Figure 3.5: Horizon mass of the small black hole m_1 (top) and the large black hole m_2 (bottom) for a binary with $q = 1/3$ and $d = 7m$ separation with initial gauge choices α_0/β_0 from Eqs.(3.2.2), the LTL/LTS choices, and the LTL/LTS + Boost (B) correction. Both of the simulations that use LT initial data show deviations from constancy of mass - the large black hole m_2 shows mass loss and the small black hole m_1 shows mass increase.

hole m_1 as shown in the top and bottom panels of Figure 3.5 respectively. For a well-resolved system like $q = 1/3$ this is not prohibitive, but if applied to small mass-ratio binaries, this could lead to inaccuracies in the results. If we include only the Late-Time Lapse, the mass-loss

is mitigated. This is the configuration we will use in Section 3.4.1 when we study a $q = 1/7$ binary in-depth. Since the boost-correction to the lapse is very small in these cases, we have chosen not to include it in further studies here, however, its inclusion could be extremely useful for head-on collision black hole configurations.

3.3.2 Spinning black holes:

To construct initial lapse data for a black hole system with spin, the conformal factor ψ_0 is modified so that its leading order term includes the magnitude of the spin $a = S_z/m^2$.

$$\psi_0 = 1 + \frac{\gamma\sqrt{m^2 + a^2}}{2r}.$$

It is then used in Eq. (3.2.4) to calculate the initial boosted lapse.

To construct a spinning initial model for the shift, as in the boosted case, the spin terms are added linearly onto the boosted initial model for the shift. They are calculated from the conformal Kerr metric in Cartesian spacetime

$$g_{\mu\nu} = \begin{bmatrix} (\sigma - 1)r^2/\rho^2 & a\sigma y/\rho^2 & -a\sigma x/\rho^2 & 0 \\ a\sigma y/\rho^2 & 1 + a^2 h y^2 & -a^2 h x y & 0 \\ -a\sigma x/\rho^2 & -a^2 h x y & 1 + a^2 h x^2 & 0 \\ 0 & 0 & 0 & 1 \end{bmatrix} \quad (3.3.34)$$

with coordinates $x^\mu = (t, x, y, z)$ and

$$r = \sqrt{x^2 + y^2 + z^2}, \quad (3.3.35)$$

$$\bar{r} = r \left(1 + \frac{m+a}{2r} \right) \left(1 + \frac{m-a}{2r} \right), \quad (3.3.36)$$

$$\rho^2 = \bar{r}^2 + \left(\frac{az}{r} \right)^2, \quad (3.3.37)$$

$$\sigma = \frac{2m\bar{r}}{\rho^2}, \quad (3.3.38)$$

$$h = \frac{1 + \sigma}{\rho^2} r^2, \quad (3.3.39)$$

3.3. Initial lapse and shift for Boosted and Spinning Black Holes

where r is the quasi-isotropic radial coordinate, \bar{r} is the Boyer-Lindquist radial coordinate, and the spin $a = S_z/m^2$. The shift can be read off as

$$\beta_i = g_{0i} \tag{3.3.40}$$

for i spatial. In practice,

$$\beta^i = \gamma^{ij} \beta_j \tag{3.3.41}$$

is used. The shift components also must be rotated so that they are valid for arbitrary spin orientations, not just spins along the z -axis. To do this, we must perform three rotations of the shift vector

$$\begin{array}{lll} z \rightarrow z & z \rightarrow x & z \rightarrow y \\ y \rightarrow y & y \rightarrow y & y \rightarrow -z \\ x \rightarrow x & x \rightarrow -z & x \rightarrow x \end{array}$$

and then sum up the results. This produces

$$\beta^x = \frac{a_x a_z^2 x y z \rho_y^2 \sigma_x (1 + \sigma_z) - \rho_x^2 (-a_z r^2 y \rho_y^2 \sigma_z + a_y z \sigma_y (r^2 \rho_z^2 + (a_z x)^2 (1 + \sigma_z)))}{(\rho_x \rho_y)^2 ((r \rho_y)^2 + a_z^2 (x^2 + y^2) (1 + \sigma_z))}, \tag{3.3.42}$$

$$\beta^y = \frac{a_x z \rho_y^2 \sigma_x (r^2 \rho_z^2 + a_z^2 y^2 (1 + \sigma_z)) - a_z x \rho_x^2 (r^2 \rho_y^2 \sigma_z + a_y a_z y z \sigma_y (1 + \sigma_z))}{(\rho_x \rho_y)^2 ((r \rho_y)^2 + a_z^2 (x^2 + y^2) (1 + \sigma_z))}, \tag{3.3.43}$$

$$\beta^z = \frac{-a_x y \sigma_x}{\rho_x^2} + \frac{a_y x \sigma_y}{\rho_y^2} \tag{3.3.44}$$

as the spin-corrected terms for the Kerr initial shift.

3.3.3 Shift damping parameter η

The principal purpose of this study is to investigate whether the accuracy of small mass ratio binaries can be improved by modifications to the gauge equations Eq. (3.2.2). In this Section, we seek to develop a superposed Gaussian model for the shift damping parameter η . For comparable mass $q > 1/10$ binary evolutions, our simulations typically use a constant η ; in general we choose $\eta = 2/m$, but recent studies have shown that $\eta = 1/m$ may provide a better measure of recoil velocity at the horizon of the remnant black hole [65] (as in [67], in which

we studied binaries as small as $q = 1/5$).

For mass ratios smaller than $q = 1/10$, a non-constant η is required for simulation stability, especially at lower grid resolutions. Ref. [7] introduced $\eta(W)$ ($W = \sqrt{\chi} = \exp(-2\phi)$ where $\phi = \phi(\frac{1}{\psi_0})$, with the conformal factor suggested by [102]), or modified (as below in equations (3.2.3)-(3.3.46)). The modification we use is based on the superposition of weighted Gaussians with peaks at the punctures. Alternatives for the conformal factor have been suggested by Refs. [84, 103, 104, 87, 86], but they were not investigated with respect to small-mass ratio binaries.

Here we bring back some of those ideas, where we evaluate $\eta(\vec{r}_1(t), \vec{r}_2(t))$ parameterized by the black holes' punctures trajectories $(\vec{r}_1(t), \vec{r}_2(t))$. The (initial form of the) conformal factor evaluated at every time step is given by Eq. (3.2.3) and we can define, analogously to $\eta(W)$,

$$m\eta_\psi = \mathcal{A} + \mathcal{B} \frac{\sqrt{|\vec{\nabla}_r \psi_0|^2}}{(1 - \psi_0^a)^b}. \quad (3.3.45)$$

An example of this η_ψ is plotted in Fig. 3.6. At the i^{th} -puncture $m_i\eta = 1$ and at the center of mass $m\eta = 1$, but Eq. (3.3.45) goes through a minimum $m\eta = 0$ in between the holes and at this point, as well as at the punctures, η is C^0 . Since the gauge condition Eq. (3.2.2) involves an integration not a derivative, this does not affect numerical evolutions.

A second alternative for smoother behavior is the superposition of Gaussians (See similarly [104])

$$\eta_G = \frac{\mathcal{A}}{m} + \frac{\mathcal{B}}{m_1} \left(\frac{\vec{r}_1(t)^2}{\vec{r}_1(t)^2 + \sigma_2^2} \right)^n e^{-|\vec{r} - \vec{r}_1(t)|^2/\sigma_1^2} + \frac{\mathcal{C}}{m_2} \left(\frac{\vec{r}_2(t)^2}{\vec{r}_2(t)^2 + \sigma_1^2} \right)^n e^{-|\vec{r} - \vec{r}_2(t)|^2/\sigma_2^2}, \quad (3.3.46)$$

which, for the punctures of the previous example, is displayed in Fig. 3.7 (with $n = 0$), and behaves like $m_2\eta_G = 1.25$ at the first puncture, and as $m_1\eta_G = 1.75$ at the second puncture, and it goes to 1 in between and far away from the binary. In [104], the authors present a function similar to Eq. (3.3.46) and study its effects, as well as the effects of another position-

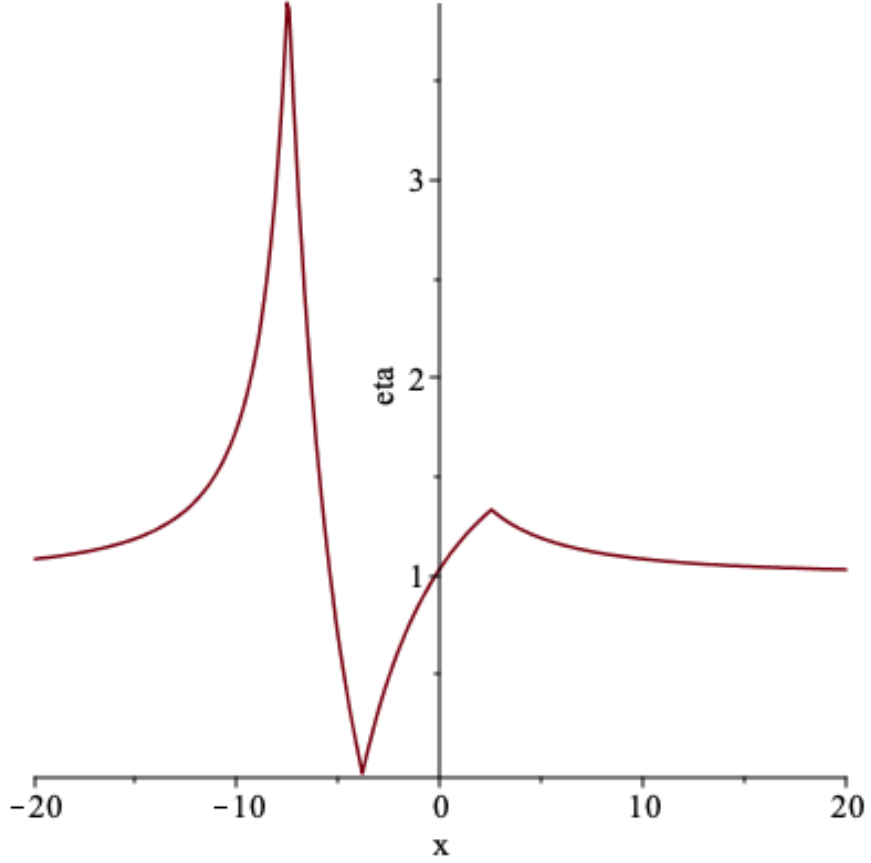


Figure 3.6: η_ψ profile for ($m = m_1 + m_2 = 1$ here) $m_2 = 3/4$, $m_1 = 1/4$; $x_1 = 2.5$, $x_2 = -7.5$; $a = 1$, $b = 2$; $A = 1$, $B = 1$. Note that this is technically different from the $\eta(W)$ used in [7] since we use the specific form (3.2.3) for ψ_0 instead of the evolved variable, which is related to the inverse of the conformal factor $W = \sqrt{\chi}$ [8].

dependent form of η , on the shift equations using a $q = 1$, $d = 10m$ separated binary and a $q = 1/4$, $d = 5m$ separated binary. They use $\mathcal{A} = 2/m$ whereas we use $\mathcal{A} = 1/m$. Even so, we find good agreement with their results; they find reduced noise in the dominant gravitational waveform mode, as well as reduced coordinate size of the horizons when compared to a constant value of η . We include factors of

$$\left(\frac{\vec{r}_i(t)^2}{\vec{r}_i(t)^2 + \sigma_j^2} \right)^n \quad (3.3.47)$$

for $i = \{1, 2\}$ and $j = \{2, 1\}$ respectively with $n \in \mathbb{N}$. The authors of [104] expect their results to hold for small mass ratio binaries and show good agreement with the results that

are presented in this paper.

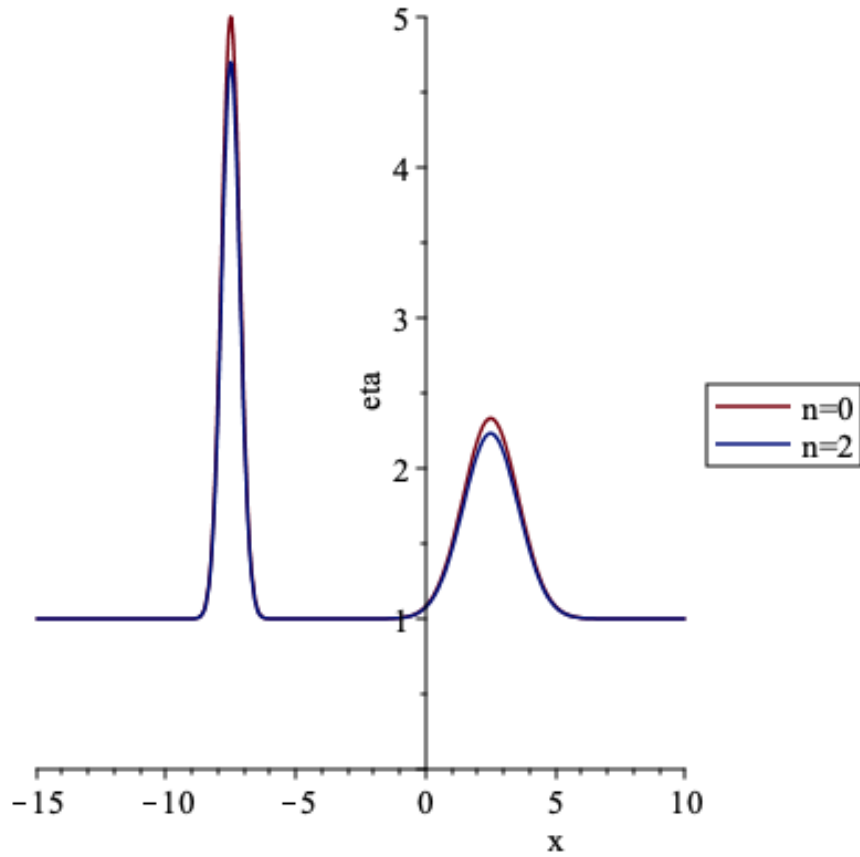


Figure 3.7: η_G profile for ($m = m_1 + m_2 = 1$ here) $m_2 = 3/4$, $m_1 = 1/4$; $x_1 = 2.5$, $x_2 = -7.5$; $A = 1$, $B = 1$, $C = 1$; $\sigma_1 = 2m_1$, $\sigma_2 = 2m_2$. At large separations, $n = 0$ and $n = 2$ show good agreement.

We have applied Eq. (3.3.46) (labelled $n = 0$) to simulations of small-mass ratio binaries (as η_G or G), and compared the physical output to both the constant $\eta = 2/m$ as well as the $\eta(W)$ gauges. The results are forthcoming in the following sections. The introduction of the $n = 2$ case is to model smaller effective spikes once the black holes are merged as shown in Fig. 3.8. For larger separation $n = 0$ and $n = 2$ essentially agree with each other as shown in Fig. 3.7.

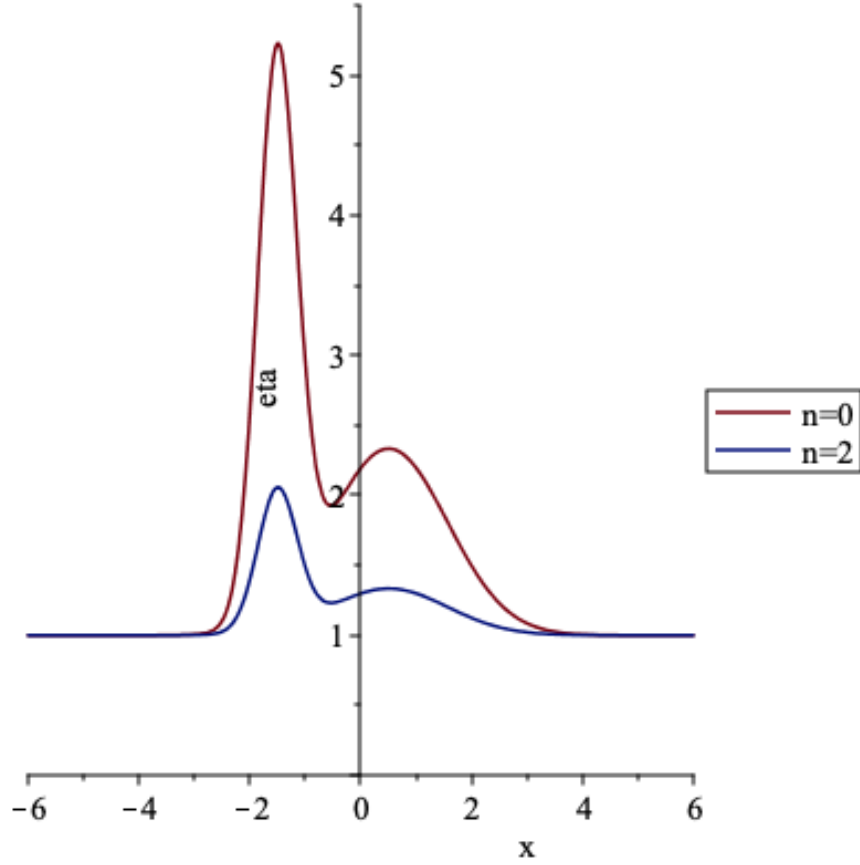


Figure 3.8: η_G profile for ($m = m_1 + m_2 = 1$ here) $m_2 = 3/4$, $m_1 = 1/4$; $x_1 = 0.5$, $x_2 = -1.5$; $A = 1$, $B = 1$, $C = 1$; $\sigma_1 = 2m_1$, $\sigma_2 = 2m_2$. At small separations $n = 2$ reduces the peaks in Eq. (3.3.46) that using $n = 0$ is designed to produce.

3.4 Simulation Results

Here we present the results of our simulations using different choices of initial lapse and choices for η . We proceed in a descendent mass ratio, from the $q = 1/7$ and $q = 1/15$, and then onto the more challenging $q = 1/32$ to find the best gauge choices and apply them to the most challenging cases, with mass ratio $q = 1/64$ and $q = 1/128$. For the rest of this work, the following notation will be used: ‘LZ’ denotes the Lousto-Zlochower $\eta = \eta(W)$ gauge, ‘2’ denotes the constant $\eta = 2/m$, ‘G’ denotes the Gaussian in Eq. (3.3.46) with $n = 0$, and the ‘+ LTL’ denotes the addition of the Late Time Lapse choice for initial data. Table 3.1 shows a full list of all the simulations performed for this Chapter and their initial parameters. All simulations use 8th order finite differencing in space.

| Run | q | D | x1/m | x2/m | P_r/m | P_t/m | $m\eta$ | CFL | Resolution |
|-------|-------|-------|--------|---------|----------|---------|---------|-----|----------------|
| 1 | 1/7 | 11m | 1.375 | -9.625 | -1.42e-4 | 0.0396 | LZ | 1/3 | n100 |
| 2 | 1/7 | 11m | 1.375 | -9.625 | -1.42e-4 | 0.0396 | 2/m | 1/3 | n100 |
| 3 | 1/7 | 11m | 1.375 | -9.625 | -1.42e-4 | 0.0396 | G | 1/3 | n100 |
| 4 | 1/7 | 11m | 1.375 | -9.625 | -1.42e-4 | 0.0396 | LTL+G | 1/3 | n100 |
| 5-7 | 1/15 | 8.5m | 0.5378 | -7.9622 | -1.04e-4 | 0.0256 | LZ | 1/3 | n084,n100,n120 |
| 8 | 1/15 | 8.5m | 0.5378 | -7.9622 | -1.04e-4 | 0.0256 | 2/m | 1/4 | n084 |
| 9,10 | 1/15 | 8.5m | 0.5378 | -7.9622 | -1.04e-4 | 0.0256 | 2/m | 1/3 | n100,n120 |
| 11-13 | 1/15 | 8.5m | 0.5378 | -7.9622 | -1.04e-4 | 0.0256 | G | 1/3 | n084,n100,n120 |
| 14-16 | 1/32 | 8.00m | 0.2424 | -7.7576 | -3.32e-5 | 0.0135 | LZ | 1/4 | n084,n100,n120 |
| 17 | 1/32 | 8.00m | 0.2424 | -7.7576 | -3.32e-5 | 0.0135 | 2/m | 1/4 | n100 |
| 18-20 | 1/32 | 8.00m | 0.2424 | -7.7576 | -3.32e-5 | 0.0135 | G | 1/4 | n084,n100,n120 |
| 21,22 | 1/64 | 7.00m | 0.1077 | -6.8923 | -1.49e-5 | 0.0077 | LZ | 1/4 | n084,n100 |
| 23 | 1/64 | 7.00m | 0.1077 | -6.8923 | -1.49e-5 | 0.0077 | G | 1/4 | n100 |
| 24 | 1/128 | 7.00m | 0.0543 | -6.9457 | -3.85e-6 | 0.0039 | LZ | 1/4 | n100 |
| 25 | 1/128 | 7.00m | 0.0543 | -6.9457 | -3.85e-6 | 0.0039 | G | 1/4 | n100 |

Table 3.1: A full of initial data parameters for the simulations performed. The smaller black hole is labeled 2 and larger black hole labeled 1. The punctures are located at $r_i = (x_i, 0, 0)$ with initial momenta $P = \pm(P_r, P_t, 0)$ and mass-ratio q . All simulations are nonspinning. A full study with 3 resolutions for all gauge choices was done on the $q = 1/15$ binary, but results are shown for simulations 5-7, 9, and 11-13 because simulation 8 could only be completed with a in increase in time resolution (CFL $1/3 \rightarrow 1/4$). The $q = 1/32$ binary has three resolutions for the LZ and G gauge choices. The smaller $q = 1/64$ and $q = 1/128$ as well as the larger $q = 1/7$ mass ratios are used for verification. All simulations use eighth order finite differencing in space.

The resolutions in Table 3.1 are listed in the form nXXX where XXX is the number of gridpoints on the coarsest level (i.e. n100 has 100 points on the coarsest grid level). This notation translates directly to the resolution in the wavezone dx ; for n100 $\rightarrow dx = m/1.00$ and in general, nXXX $\rightarrow dx = m/X.XX$. The mesh increases by a factor of two in resolution per refinement level, with the most refined levels surrounding the individual punctures.

3.4.1 Results for a $q = 1/7$ nonspinning binary

In this section we will begin our analysis by studying the effects of different gauge modifications on the physical parameters of a binary system. We will first verify it works on a comparable mass binary, with mass ratio $q = m_1/m_2 = 1/7$ and binary separation $d = 11m$. This system, while not as computationally intensive as the smaller mass ratio binaries studied later on,

is still fairly nontrivial, and will serve to help generalize our results for the other mass-ratio systems.

For this system we did four runs with four different choices for the gauge all at our typical production resolution n100. The first uses the choice LZ, and does not modify initial lapse and shift from the standard $\alpha_0 = 2/(1 + \psi_0^4)$ and $\beta_0 = 0$. This is our reference choice for η for small mass ratio runs. The second simulation uses G, the third run uses the constant choice $\eta = 2/m$ and, finally, the fourth run uses G + LTL. All use eighth order spatial finite differencing stencils and fourth order Runge-Kutta in time, with a Courant Factor of 1/3.

The Hamiltonian and momentum constraint equations are integrated over a masked volume \mathcal{V} and their norms are given by

$$\|\mathcal{H}\| = \sqrt{\int_{\mathcal{V}} \mathcal{H}^2 d^3x}, \quad (3.4.48)$$

$$\|\mathcal{M}^i\| = \sqrt{\int_{\mathcal{V}} (\mathcal{M}^i)^2 d^3x} \quad (3.4.49)$$

and should be non increasing [96]. Conservation of these constraints is not imposed. Error is accumulated in a small way, but should be kept under control and not left to grow exponentially. The evolution equations are not corrected such that constraints are forced to zero because this would lead to numerical instability. Even so, measures of the constraints' deviations from zero are commonly used as way to assess convergence with respect to numerical resolution. However, these simulations are all run in different gauges which makes it difficult to draw definitive conclusions based solely on violations to the constraints, since different gauges can change the scales of these violations. The constraint violations can still give us an idea of performance as well as allow us to compare different resolutions of the same gauge to ensure convergence. In Figure 3.9 the violations to the Hamiltonian constraint (top panel) as well as the x -component of the momentum constraint (bottom panel) are shown for the $q = 1/7$ simulations with $\eta = 2/m$ in yellow, G in red, G+LTL in purple, and LZ in blue.

The set up for the simulation in this subsection with $\eta = 2/m$ resembles that which was used to build up the RIT Catalog [2, 34, 35], with CFL=1/3 to achieve production speed. However, here we use eighth order finite differencing stencils instead of sixth order to simulate

smaller mass-ratios, as opposed to the RIT Catalog simulations, which are mainly comparable mass.

It is pertinent to reiterate that the comparison of constraint violations cannot be used as an accurate measure of simulation performance between simulations with different values for η . These simulations exist in different gauges and therefore may rescale the constraint violations, making comparisons between them an inaccurate method of ranking gauge performance. Notwithstanding, we would like to mention that the pair of simulations with initial data G and G+LTL seem to settle to approximately the same gauge, as only in the early part of the simulation we see a slight reduction of the violation of the constraints. The constant choice, $\eta = 2/m$ (in yellow) performs well throughout the course of the simulation. The LZ gauge has Hamiltonian constraint violations that are about one order of magnitude larger than the simulations with $\eta = 2/m$, G, or G+LTL, however, this may be due to a rescaling of the constraints. In general, all four simulations produce constraint violations within an acceptable range and, therefore, are considered viable candidates for production-level runs.

In order to quantitatively compare the different choices for the gauge damping parameter η , it is pertinent to assess the different gauges' effects on physical quantities such as horizon mass, spin, and gravitational waveforms. Fig. 3.10 shows the mass of each black hole m_1 and m_2 measured at the horizon using LZ, G, G+LTL and $\eta = 2/m$ gauges. The figures are generated using a 200-point running average to smooth fluctuations in the data and to better present a general trend without the distraction of numerical noise. In the masses, we are looking for constancy over the course of the inspiral from $t = (0 - 1000)$.

The top panel of Fig. 3.10 shows the horizon mass of the large black hole m_2 versus simulation time. The G and G+LTL gauges both are able to maintain the horizon measure of mass well until the simulation approaches merger, when we see some growth in the masses. The constant gauge $\eta = 2/m$ shows continuous growth over the course of the simulation; although the scale on which this growth occurs is small, $O(10^{-5})$, this may be indicative of an issue as the mass ratio decreases. The mass m_2 in the LZ gauge has relatively large oscillations over the duration of the inspiral as well as growth that is on the order of that seen in the $\eta = 2/m$

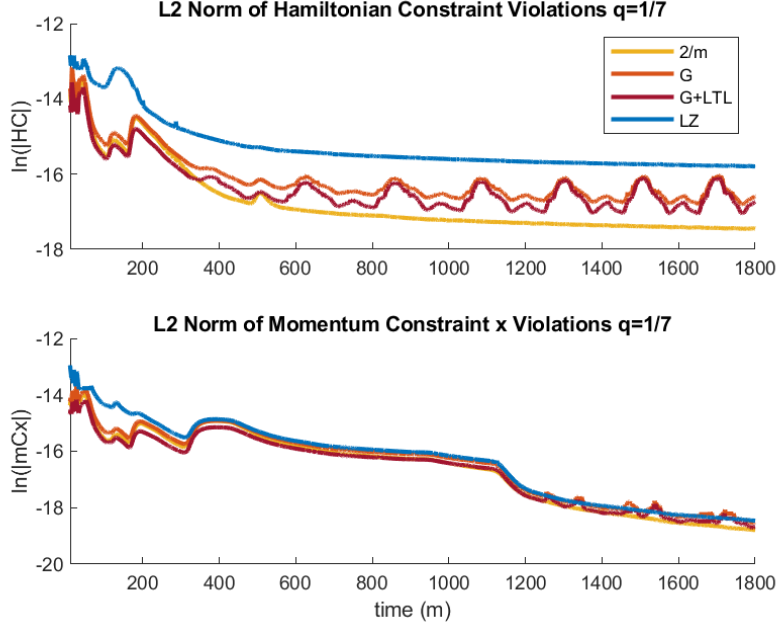


Figure 3.9: Violations to the Hamiltonian constraint (top) and the x -component of the momentum constraint (bottom) for the $q = 1/7$ binary using resolution $n100$ with the different gauge choices: G, G+LTL, $\eta = 2/m$ and LZ in red, purple, yellow, and blue respectively. Both G and G+LTL settle to a similar gauge. All gauges produce acceptably-valued constraint violations.

simulation.

The second panel of Fig. 3.10 shows the mass of the smaller black hole, m_1 , measured at the horizon. The G and G+LTL gauges both are able to maintain the horizon measure of mass well over the course of the simulation. In fact, they seem to behave the same way with G+LTL being shifted by a constant factor, indicating that the G and G+LTL settle to similar gauges since they differ only in initial data. The $\eta = 2/m$ and LZ runs show continuous declines in their respective horizon masses of m_1 over the inspiral period. As we will see in the next section, this may be the symptom of a resolution issue, especially at smaller mass ratios. Although not as vital as in smaller mass ratio systems, such as the $q = 1/15$ or $q = 1/32$ binaries studied in Sections 3.4.2 and 3.4.3, here constancy in m_1 is strongly desired.

It is of interest to investigate the gauges' effects on the dominant $(2, 2)$ -mode of the Newman Penrose Weyl scalar Ψ_4 since this scalar is what we use to calculate outgoing gravitational radiation. The top panel of Figure 3.11 shows the early part of the amplitude of $\Psi_4^{2,2}$ with

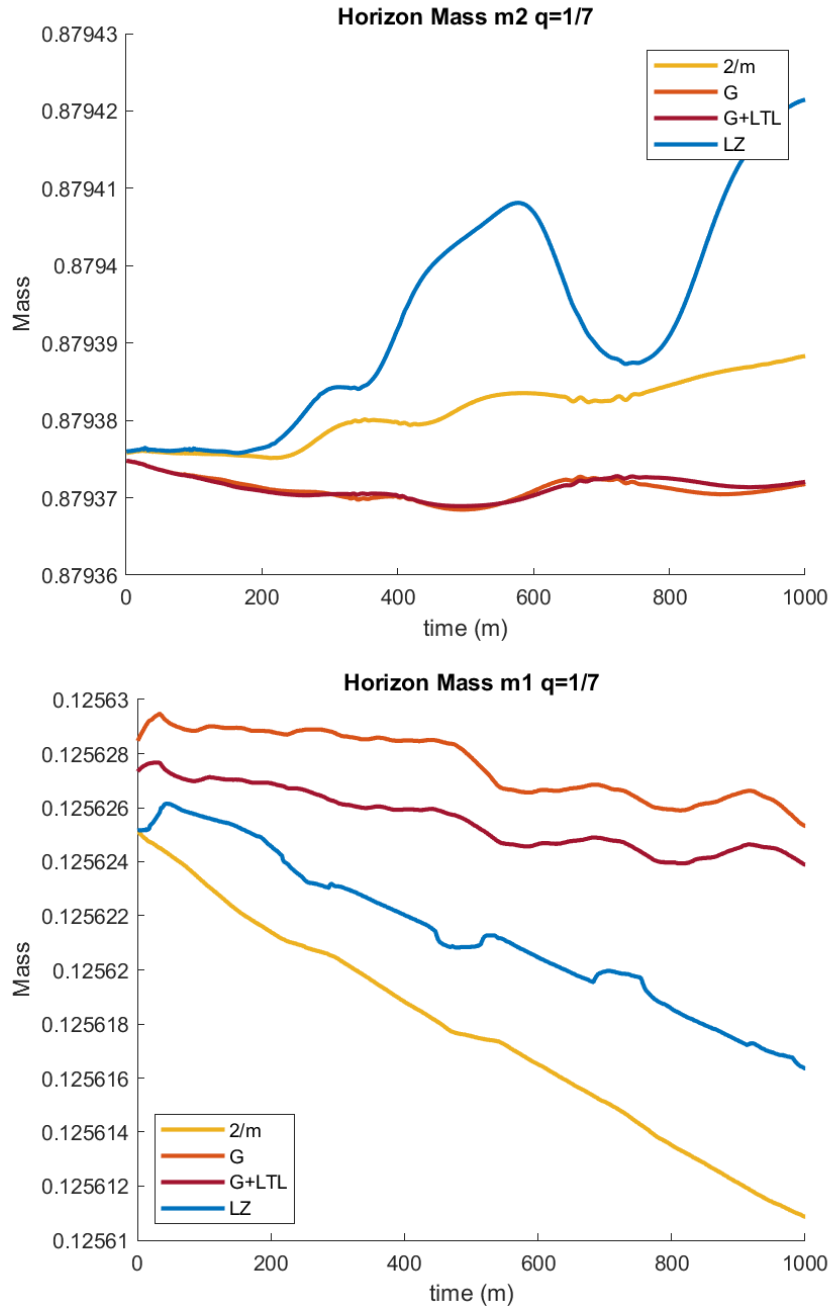


Figure 3.10: Horizon masses for m_1 and m_2 versus time for the $q = 1/7$ n_{100} simulations with different choices for $m\eta = G, LZ,$ and $2/m$, and the initial lapse, LTL. The $\eta = 2/m$ and LZ gauges produce continuous growth (mass-loss) over the course of the simulation in m_2 (m_1). The G and G+LTL choices maintain both horizon masses well.

respect to time. The observer sits at $113m$ from the origin of coordinates. In the early part, there is a clear initial burst of noise present in the simulation that uses the LZ gauge which

is damped by the use of G, G+LTL or $\eta = 2/m$. The second panel shows the amplitude of $\Psi_4^{2,2}$ over the timescale $t = (200 - 800)m$ with reflections at refinement boundaries visible between $(400 - 450)m$ and $(550 - 600)m$. This result holds and was verified for modes $(l, m) = (2, 0), (2, 1), (3, 0), (3, 1), (3, 2), (3, 3)$ as well.

As a final test of the efficiency of each of the gauge choices, one can consider their individual effects on the quasi-local computation of remnant recoil velocity, which is measured on the horizon of the remnant (in column 4 of Table 3.2). This is compared to the total amount of linear momentum radiated away via gravitational waves (column 5). Using the modified gauge G improves the horizon measure of recoil velocity over the $\eta = 2/m$ and LZ gauges by about 17% and 15% respectively. This is likely due to the fact that the G gauge damps to 1 far from the remnant, and we have already shown in [67] that this leads to a more accurate measure of quasi-local linear momentum.

| $m\eta$ | CFL | Resolution | Horizon | Radiated |
|---------|-----|------------|----------|----------|
| LZ | 1/3 | n100 | 111.2450 | 92.6987 |
| 2 | 1/3 | n100 | 80.8354 | 94.3036 |
| G | 1/3 | n100 | 95.1882 | 94.1923 |
| G+LTL | 1/3 | n100 | 95.8015 | 94.2094 |

Table 3.2: For the $q = 1/7$ binary, the total linear momentum (km/s) calculated in two ways: (1) measured quasi-locally on the horizon averaged over $t = (2600 - 2800)m$, in column 4, and (2) measured by the amount radiated away in gravitational waves, in column 5. All simulations have resolution $n100$ as well as CFL=1/3 and 8th order finite differencing stencils. The gauges G and G+LTL allow for the most accurate measure of horizon recoil when compared against the radiated value.

3.4.2 Results for a $q = 1/15$ nonspinning binary

Since the purpose of the G gauge is to improve simulations with mass ratios $q < 1/10$, next we investigate a nonspinning system with mass ratio $q = m_1/m_2 = 1/15$ starting at an initial coordinate separation $d = 8.5m$. The simulation was run through merger so that we can also investigate the gauges' effects on the remnant's recoil velocity as well as the ringdown phase of merger.

All these simulations have CFL=1/3, except the lowest resolution (n084) simulation with

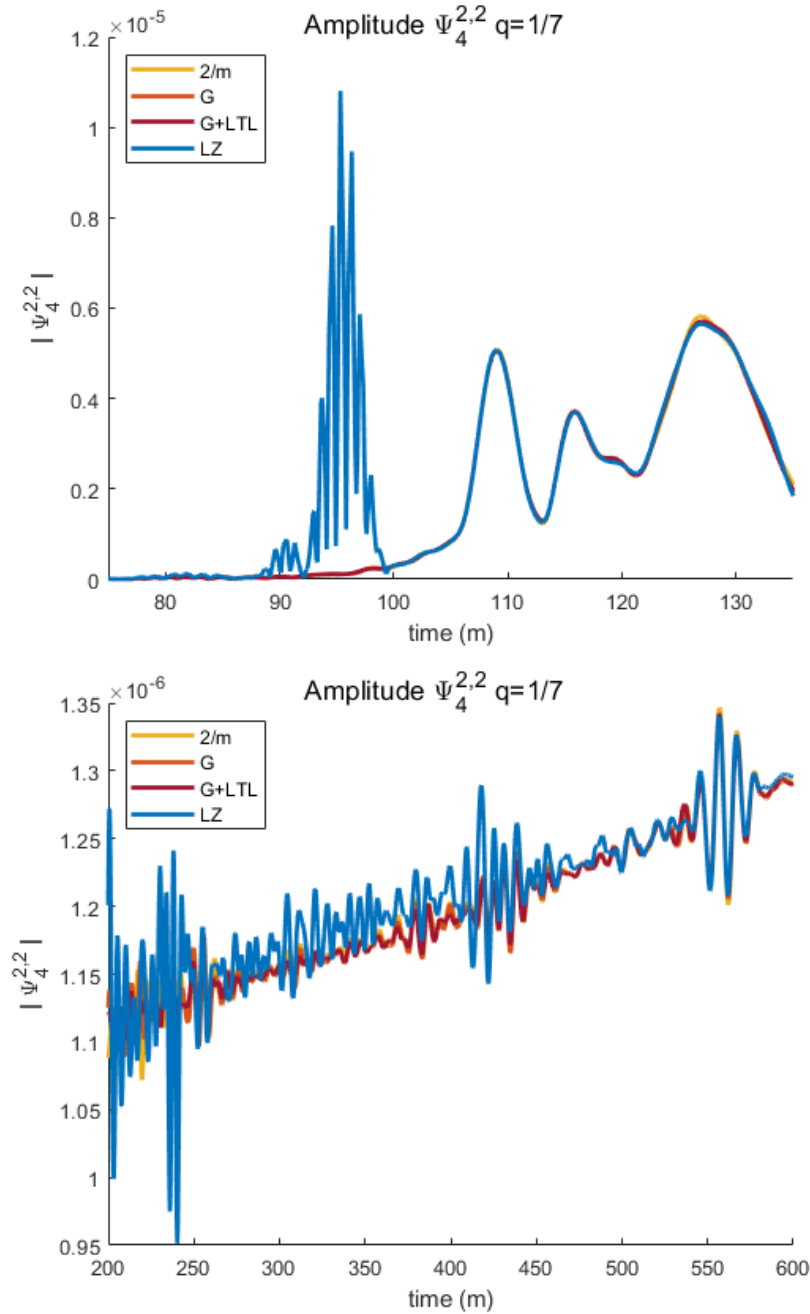


Figure 3.11: The amplitude of the dominant (2,2)-mode of Weyl scalar Ψ_4 for the $q = 1/7$ binary as seen by an observer situated $r = 113m$ from the origin of coordinates. Higher frequency noise of the LZ gauge is apparent at $t \sim (75 - 135)m$ (in the top panel) as is its bounce at the next refinement level at $t \sim (200 - 600)m$ (in the bottom panel). The other gauge choices G, G+LTL, and $\eta = 2/m$ show no high frequency noise early on, as well as substantially reduce high frequency oscillations during inspiral (shown in the bottom panel).

constant $\eta = 2/m$ which dies at about $100m$ with this configuration. This particular simulation runs successfully with CFL=1/4, but only with increased resolution in time. All $q = 1/15$ simulations use eighth order finite-differencing stencils in space.

As with the $q = 1/7$ binary, our results for the smaller mass ratio systems will be focused on analysis of the physical quantities of the system such as masses, spins, and gravitational waveforms. These quantities are invariant with respect to the gauge, and therefore can be used to measure differences in results using each gauge. Once the remnant is settled, we can compare the kicks calculated at the horizon by the isolated horizon formulae [63] to those extracted from the radiated linear momentum at infinity.

The top panel of Fig. 3.12 shows the evolution of the horizon mass of the large black hole m_2 for seven simulations: G and LZ with resolutions n084, n100, and n120, and $\eta = 2/m$ for n100. For the remainder of this work, the low resolution n084 will be a dashed line, n100 will be dot-dashed, and n120 will be solid.

In Fig. 3.12, we can see that all gauges maintain the mass to at least $O(1e-4)$, but the $\eta = 2/m$ n100 and G n100 and n120 simulations show the best constancy in mass. The figures are generated using a 20-point running average to smooth fluctuations in the data and to better present a general trend. Table 3.3 can be used in conjunction with Fig. 3.12. It shows the slopes of a linear fit to the data for each simulation over the inspiral period $t = (100 - 1000)m$. The results of this fit are given in columns 3 and 5 of Table 3.3 with the root mean square error

$$\epsilon_i = err = \sqrt{\frac{\sum_{k=1}^N (m_i^k - \hat{m}_i^k)^2}{N}} \quad (3.4.50)$$

where m_i^k are the actual mass values for black holes labeled $i = 1, 2$, measured at time points t and $\hat{m}_i^k = At + b$.

Initially, the black holes grow due to an influx of radiation from the initial data, but then are expected to settle to a value that remains almost constant until merger. The top panel shows the horizon mass of the larger black hole; in the simulation using the LZ gauge there are low frequency oscillations later on in the inspiral, in the n084 simulation, which is reflected in the increase in ϵ_1 between the linear fits of G and LZ ($\epsilon_1 = 0.0215 \cdot 10^{-6}$ vs. $\epsilon_1 = 0.0397 \cdot 10^{-6}$

respectively).

The bottom panel shows the horizon mass of the smaller black hole; in the n084 LZ gauge, the mass, after the settling of the initial data, declines fairly steadily, with $A_1 = -0.3482 \cdot 10^{-7}$ and $\epsilon_1 = 0.7943 \cdot 10^{-6}$. This occurs in the G gauge as well, although its slope is $A_1 = -0.2810 \cdot 10^{-7}$ with error $\epsilon_1 = 0.5177 \cdot 10^{-6}$. Although neither gauge maintains m_1 very well at this resolution, m_1 in the G gauge has a much shallower decline than the m_1 in the LZ gauge, as well as smaller error overall.

In the n100 simulations, $\eta = 2/m$ outperforms G in terms of linearity by $< 5\%$ in m_1 and by $> 200\%$ in m_2 , although in each case $\eta = 2/m$ has higher error than G. In LZ n100 and n120, there occurs a substantial dip in the mass of m_2 between $t = (800 - 1200)m$ that is reflected in an increase in the error of the linear fits.

| Gauge | Res. | m_1 | | m_2 | |
|-------|------|-----------------------------|----------------------|-----------------------------|----------------------|
| | | $\mathcal{A} \cdot 10^{-7}$ | err. $\cdot 10^{-6}$ | $\mathcal{A} \cdot 10^{-7}$ | err. $\cdot 10^{-4}$ |
| G | n084 | -0.2810 | 0.5177 | 0.6613 | 0.0215 |
| LZ | n084 | -0.3482 | 0.7943 | 0.6462 | 0.0397 |
| 2/m | n100 | -0.0258 | 0.3551 | 0.2564 | 0.0131 |
| G | n100 | -0.0683 | 0.2546 | 0.2655 | 0.0079 |
| LZ | n100 | -0.0641 | 0.5688 | -0.6248 | 0.1543 |
| G | n120 | -0.0463 | 0.3206 | 0.1620 | 0.0082 |
| LZ | n120 | -0.0245 | 0.2238 | -0.2601 | 0.0467 |

Table 3.3: The slopes (\mathcal{A} , columns 3 and 5) of linear fits to the horizon masses m_1 and m_2 computed over the inspiral $t = 100m$ to 1000 for the $q = 1/15$ binary using $\eta = \text{G, LZ, and } 2/m$. Error is calculated via root mean square error over the interval, and is shown in columns 4 and 6. The time frame is chosen so a linear fit is a reasonable approximation of the mass curves. The G and LZ simulations have 3 resolutions: n084, n100, n120, and the $\eta = 2/m$ simulation has 1 resolution: n100. The G gauge produces a reliably constant value for the horizon mass, even at low resolution, whereas the mid- and low- resolution LZ simulations show large changes in mass (reflected in the slopes \mathcal{A}) as well as higher error values overall.

It is informative to study the growth of the apparent horizon of each black hole in numerical (radial) coordinates for each different gauge. An extended horizon requires a large number of grid points to evaluate quantities over its surface, but the numerical evolution “loses” those points in the interior of the black hole. These are points that could be used to otherwise resolve the dynamics of the system.

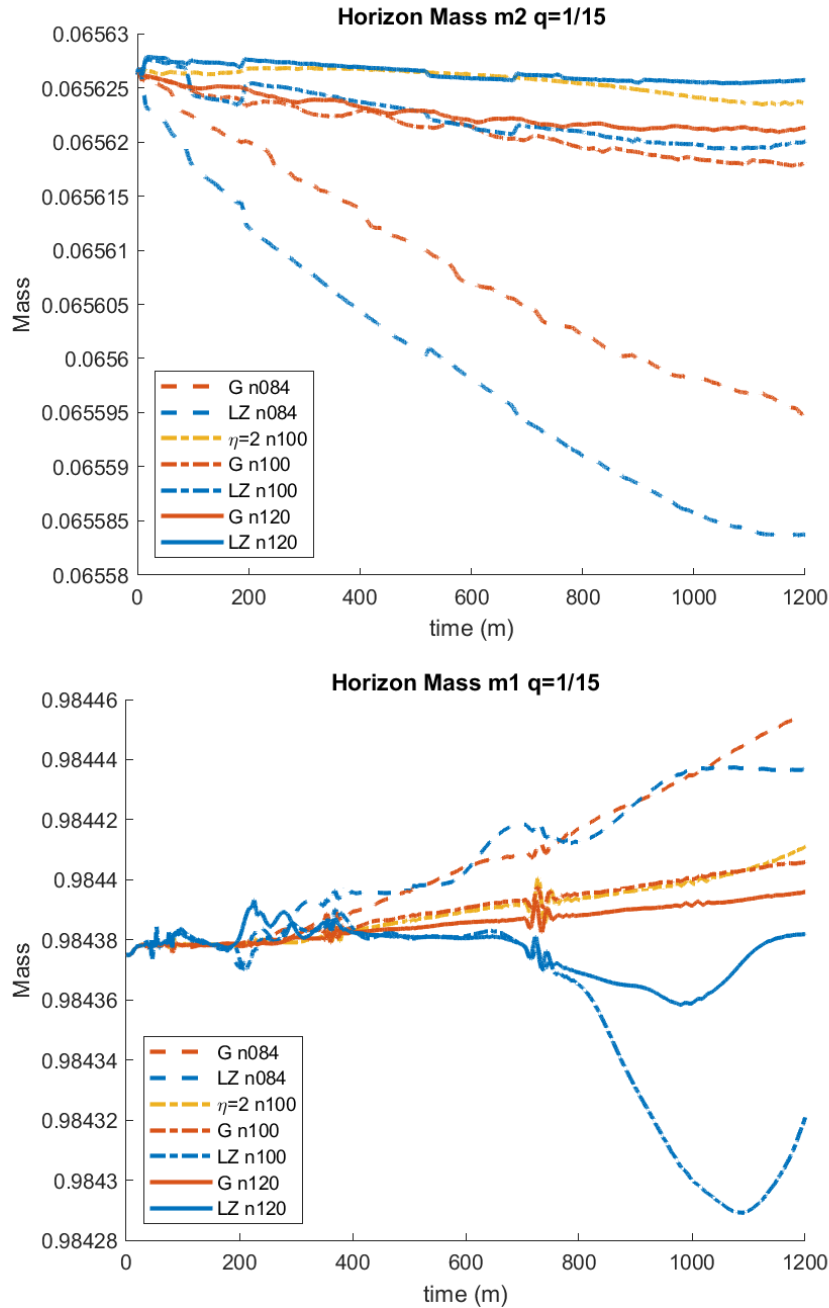


Figure 3.12: Horizon masses for m_2 (top) and m_1 (bottom) versus time for the $q = 1/15$ simulation with the different choices for $m\eta$, G, LZ, and $\eta = 2/m$. The dashed, dot-dashed, and solid lines are the low n084, medium n100, and high n120 resolutions respectively. The horizon masses m_1 and m_2 deviate from constant most dramatically when the LZ gauge is used. Both the $\eta = 2/m$ and G gauges maintain the masses of the horizons well over the course of the simulation, except at the lowest resolution n084.

The top panel of Fig. 3.13 shows the the initial growth of the larger black hole m_2 , which grows from $t = (0 - 25)m$ using all three gauge choices. This growth is due to an influx of radiation content from the initial data, and is expected. The growth in the small black hole (bottom panel), m_1 , happens within the first few iterations and then immediately stabilizes. To minimize the loss of gridpoints in the simulation, ideally the horizon will grow quickly and then settle down to maintain its coordinate size, so this rapid stabilization is critical.

The horizon coordinate sizes for the low, medium, and high resolutions of G lie directly on top of each other in both panels of Fig. 3.13. The same is true for all resolutions of LZ. Furthermore, the gauges G and LZ, regardless of resolution, maintain a constant coordinate size of the apparent horizons of m_1 and m_2 well over the course of the run. However, the $\eta = 2/m$ simulation, shown in yellow, exhibits continuous growth of both horizons. This means that gridpoints are constantly being lost inside the black hole horizons, and, in the case of m_2 , it is possible that the horizon grows so large it crosses a refinement level boundary, reducing computational accuracy and wasting resources. While this growth does not prohibit completion of the $q = 1/15$ binary at n100, further investigations should be done on its effects on more extreme mass-ratio pairs. This growth also may be related to the fact that when using $\eta = 2/m$, the low resolution $q = 1/15$ (n084) requires a CFL decrease from $1/3 \rightarrow 1/4$ in order for the simulation to be successful, whereas the other gauges G and LZ can be run at n084 with CFL of $1/3$. Therefore, using a well-chosen gauge allows for an increase in computational efficiency at lower resolutions, and using a poorly chosen gauge may cause issues at low resolutions.

An important and physically relevant method of assessing the accuracy and effectiveness of different gauges is to look at the early behavior of gravitational waveforms as seen by an observer far from the binary orbit. In our case, we will consider an observer sitting at $r = 113m$ from the origin of coordinates. Fig. 3.14 displays the amplitude of the leading waveform mode $\ell = 2, m = 2$ of the Weyl scalar Ψ_4 . In the top panel the amplitude of the waveform from $t = (75 - 135)m$ is shown. One can observe high frequency noise at $t \sim (90 - 100)m$ produced by the LZ gauge choice, in blue, that was also present in the $q = 1/7$ waveform (as shown

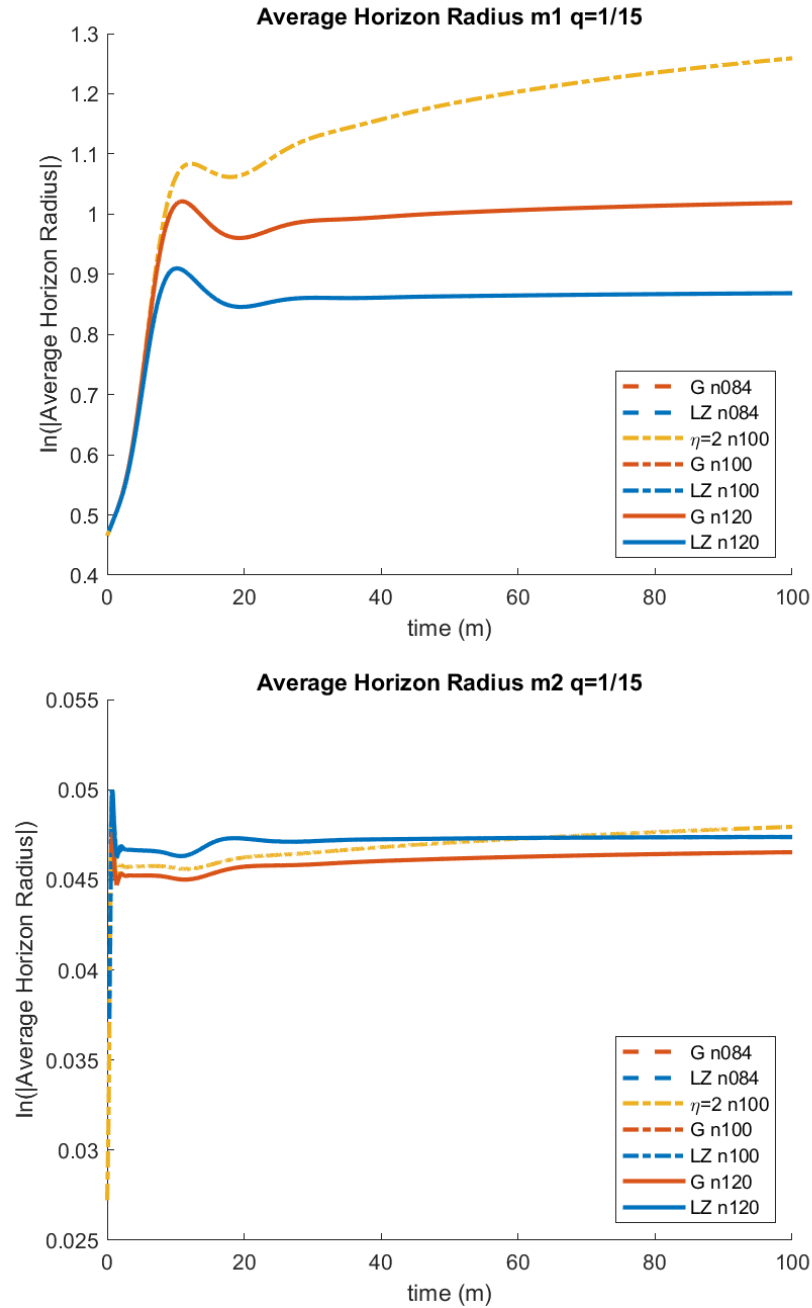


Figure 3.13: Radial average size of each of the horizons of the $q = 1/15$ binary versus evolution time for the different gauge choices. The three resolutions using the LZ gauge lie on top of each other, as do the three resolutions using the G gauge. In both m_1 and m_2 these gauges maintain the coordinate size of the horizons well over the full inspiral. The $\eta = 2/m$ is only shown in one resolution (n100), and the associated horizons m_1 and m_2 grow continuously throughout the simulation.

in Fig. 3.11). The noise has higher amplitude in the n100 (dot-dash) LZ simulation than the n084 (dash) LZ simulation. This is not indicative of improvement with decreasing resolution, but is instead due to the n084 resolution under-resolving the grid. This noise is eradicated solely by choosing either G or $\eta = 2/m$ for the gauge, which is also consistent with what was found in Fig. 3.11.

The second panel of Fig. 3.14 shows a later time in the binary’s evolution (from $t \sim (200 - 600)m$). High frequency noise during this period of the inspiral, present even in the highest resolution (n120) simulation using the LZ gauge, is significantly damped when using the G or $2/m$ choice for η instead of the typical LZ. At $t \sim (500m - 550)m$, there is an increase in the amplitude of these oscillations across all simulations. This corresponds to the bounce of noise over a grid refinement level back to the observer’s location. This effect is also damped when G or $\eta = 2/m$ are chosen, thus confirming the benefits of the introduction of the new gauges. We verified that similar features appear in other next to leading order modes $(\ell, m) = (2, 1), (2, 0), (3, 0), (3, 1), (3, 2), (3, 3)$, etc.

Table 3.4 contains the remnant quantities (energy, angular momentum, and linear momentum) of the $q = 1/15$ binary including a three-point extrapolation to infinity (n_∞) as well as convergence order in the cases where we use three resolutions and have convergence. Columns 3-5 show the mass, and angular and linear momentum measured on the horizon of the black hole using the isolated horizon formulae (See Ref. [65] and Eq. (2.3.6)). Columns 6-8 are the same quantities but calculated from the energy, angular, and linear momentum carried away by gravitational waves off to an observer located at infinity. Excellent agreement is observed between radiation and horizon measurements for the final mass and spin. In general, the horizon linear momenta are measured well at the typical production resolutions of n100 and n120 using the G gauge, coming within 12% of the radiated measure for n100 and 28% for n120. Compare this with the LZ gauge, which is off wildly (by 716% using n100) or the $\eta = 2/m$ gauge which is off by 35% using n100.

Since $\eta = 1/m$ gives a more accurate measure of recoil velocity than $\eta = 2/m$ [67], and G damps to 1 far from the center of coordinates, we expected improvement between $\eta = 2/m$ and

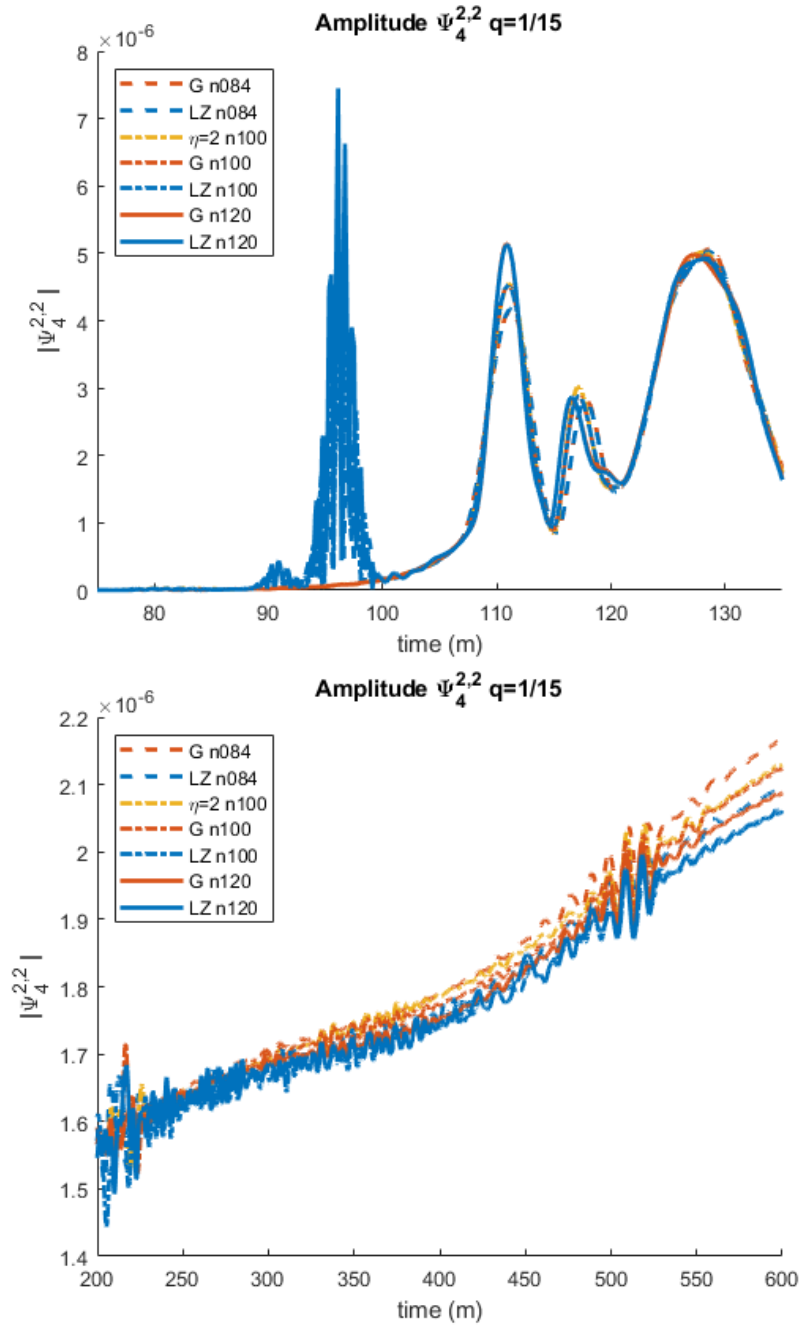


Figure 3.14: The amplitude of the dominant mode of Ψ_4 for the $q = 1/15$ binary extracted at an observer location of $r = 113m$. The waveform is shown for G and LZ in three resolutions and $\eta = 2/m$ in one. In the top panel, higher frequency noise of the LZ gauge early on at $t \sim (75 - 135)m$ and its bounce at the next refinement level in the second panel from $t \sim (200 - 600)m$ is apparent.

G. Additionally, the strong improvement between G and LZ may prove critical in measuring the horizon quantities accurately when considering extremely small mass ratios, such as the $q = 1/32$ or $q = 1/64$ binaries considered here.

| Gauge | Resolution | Horizon | | | Radiated | | |
|-------|------------|---------|---------|------------------|----------|---------|------------------|
| | | E/m | J/m^2 | $L(\text{km/s})$ | E/m | J/m^2 | $L(\text{km/s})$ |
| G | n084 | 0.9949 | 0.1863 | 178.7939 | 0.9950 | 0.1889 | 31.5722 |
| | n100 | 0.9949 | 0.1870 | 36.3859 | 0.9950 | 0.1880 | 32.9681 |
| | n120 | 0.9949 | 0.1870 | 44.79436 | 0.9949 | 0.1877 | 35.0123 |
| | $n\infty$ | 0.9950 | 0.1870 | 44.3255 | 0.9949 | 0.1874 | - |
| | CO | 4.64 | 15.50 | 15.52 | 3.51 | 5.05 | - |
| LZ | n084 | 0.9949 | 0.1865 | 232.3947 | 0.9950 | 0.1881 | 31.0327 |
| | n100 | 0.9948 | 0.1862 | 241.2582 | 0.9949 | 0.1876 | 34.3328 |
| | n120 | 0.9949 | 0.1872 | 43.4521 | 0.9949 | 0.1874 | 35.0915 |
| | $n\infty$ | 0.9948 | - | - | 0.9949 | 0.1874 | 35.3179 |
| | CO | 3.11 | - | - | 5.88 | 7.12 | 8.06 |
| $2/m$ | n100 | 0.9949 | 0.1870 | 21.1410 | 0.9950 | 0.1884 | 32.7075 |

Table 3.4: For the $q = 1/15$ binary, the total mass, angular, and linear momentum (1) measured by the amount radiated away in gravitational waves, in columns 3-5, and (2) measured quasi-locally on the horizon, in columns 6-8. Extrapolations to infinite resolution ($n\infty$) and convergence order (CO) are included where applicable. All simulations have resolution specified in column 3 as well as CFL=1/3 and 8th order finite differencing stencils. A dash indicates no convergence was found.

3.4.3 Results for a $q = 1/32$ nonspinning binary

We also performed an in-depth study on a smaller nonspinning binary with a mass-ratio of $q = 1/32$ and an initial binary separation of $d = 8m$. It uses a Courant factor of 1/4 as well as 8th order finite differencing stencils in space, and was run using three resolutions (n084, n100, n120), with both the G and LZ gauges as well as one resolution (n100) of $\eta = 2/m$.

Fig. 3.15 shows the horizon masses for the seven $q = 1/32$ simulations during inspiral from $t = 0m$ through $t = 1200m$, which is just before merger. In these figures, we are again looking for the masses to be held constant (after settling down initially) for the duration of the inspiral, as this will indicate a more accurate computation of horizon masses. The lowest resolution (n084) simulations using the G and LZ gauges show the most growth in m_2 (top panel) or mass-loss in m_1 (bottom panel), while the G n120 simulation holds both masses

most constant over time. The n100 LZ gauge shows a relatively large dip in m_2 mass between $t = (800 - 1200)m$, which is consistent with our findings for the $q = 1/15$ binary. The $\eta = 2/m$ n100 simulation holds m_2 constant until $t = 800m$ and then begins to grow at the same rate as the LZ n084 simulation. In m_1 , $\eta = 2/m$ begins with mass loss from $t = (0 - 200)m$ then stays relatively constant until $t = 1100m$ where it begins to lose mass again. While not prohibitive to the completion of this particular simulation, this mass loss in the small black hole might pose issues at lower resolutions or mass ratios.

To assess continuity of the horizon mass parameters quantitatively, we performed a linear fit to the data for each simulation over the inspiral period $t = (100 - 1000)m$. The results of this fit are given in columns 3 and 5 of Table 3.5 with the root mean square error as in Eq. (3.4.50).

The LZ n084 m_1 and m_2 have slopes of $A_1 = -0.2529 \cdot 10^{-7}$ and $A_2 = 0.2332 \cdot 10^{-7}$ (respectively), whereas G has slopes $A_1 = 0.1354 \cdot 10^{-7}$ and $A_2 = 0.6370 \cdot 10^{-7}$. The slope of m_2 is most constant using LZ, as well as has the lower error. However, the more difficult to resolve black hole is the smaller horizon, whose mass is better computed using the G gauge.

As resolution increases, so does the stability of the masses of each black hole; using G at n100 provides horizon mass measurements that are closer to constant as well as using $\eta = 2/m$, however, because of the dip using LZ at $t = (800 - 1200)m$, the slopes for LZ n100 are similar to those of n084. The G n100 gauge matches the G n120 gauge well throughout most of the inspiral period. However, $\eta = 2/m$ exhibits growth in the mass that is superlinear and is reflected in the increase in root mean squared error between the horizon masses in G and $\eta = 2/m$ (n100), respectively at $\epsilon_1^G = 0.1507 \cdot 10^{-6}$ and $\epsilon_2^G = 0.0402 \cdot 10^{-4}$ and $\eta = 2/m$ at $\epsilon_1^{2/m} = 0.4051 \cdot 10^{-6}$ and $\epsilon_2^{2/m} = 0.0407 \cdot 10^{-4}$. A full list of the mean slopes of the horizon masses and their corresponding errors can be found in Table 3.5.

In Fig. 3.16, the amplitude of the gravitational wave scalar $\Psi_4^{2,2}$ is plotted versus time for all seven simulations. The top panel shows the early part of the waveform, from $t = 75 - 135m$. Between $t = 90 - 100m$, there is noise in the LZ simulations that is damped by the G and $\eta = 2/m$ simulations across all resolutions which is consistent with our findings for the $q = 1/15$

| Gauge | Res. | m_1 | | m_2 | |
|-------|------|-----------------------------|----------------------|-----------------------------|----------------------|
| | | $\mathcal{A} \cdot 10^{-7}$ | err. $\cdot 10^{-6}$ | $\mathcal{A} \cdot 10^{-7}$ | err. $\cdot 10^{-4}$ |
| G | n084 | -0.1354 | 0.0977 | 0.6370 | 0.0222 |
| LZ | n084 | -0.2529 | 0.5638 | 0.2332 | 0.0275 |
| 2/m | n100 | -0.0410 | 0.4051 | 0.2620 | 0.0407 |
| G | n100 | -0.0231 | 0.1507 | 0.1739 | 0.0402 |
| LZ | n100 | -0.0310 | 0.2049 | -0.5344 | 0.1673 |
| G | n120 | -0.0163 | 0.1054 | 0.0659 | 0.0171 |

Table 3.5: The slopes (\mathcal{A} , columns 3 and 5) of linear fits to the horizon masses m_1 and m_2 computed over the inspiral $t = (0 - 1000)m$ for the $q = 1/32$ binary using $\eta = \text{G}$, LZ, and $2/m$. Error is calculated via root mean square error over the interval, and is shown in columns 4 and 6. The time frame is chosen so a linear fit is a reasonable approximation of the mass curves. The G and LZ simulations have 3 resolutions: n084, n100, n120, and the $\eta = 2/m$ simulation has 1 resolution: n100. The G gauge provides an effective gain in resolution of a factor of 2 in the horizon mass.

and $q = 1/7$ binaries. This means that smaller mass-ratios benefit significantly from the use of an adaptive gauge like G or a constant choice like $\eta = 2/m$. However, recall that lower resolutions of $\eta = 2/m$ may require at least increases in time resolution (via CFL) which are not necessarily computationally practical, especially as mass-ratios decrease.

The bottom panel of Fig. 3.16 shows the inspiral period of $\Psi_4^{2,2}$ from $t = (200 - 900)m$. Compare the low resolution G (n084, red dashed) and the n100 (blue, dot dashed) resolution of the same gauge between 400m and 450m. The n100 curve shows noise reflected at the mesh refinement boundary, but the G n084 curve seems to damp this noise. This is due to n084 under-resolving the grid, which is also the cause of the increase in initial noise between LZ n084 and n100. The high-frequency oscillations occurring from the subsequent reflection between $t = (500 - 600)m$ also do not appear in the G n084 simulation, whereas they do in the G n100 and G n120 simulations, which supports the hypothesis that n084 has too few gridpoints to properly resolve the system.

The LZ gauge in n084 (blue, dashed) shows high frequency oscillations over the course of the inspiral, which are somewhat damped by increasing the resolution to n100 (blue, dot-dashed). The G n100 simulation (red, dot-dashed) exhibits less oscillatory behavior when compared to the waveform in the other gauges, $\eta = 2/m$ and LZ, at resolution n100.

For smaller mass ratios, comparing the waveforms in the near-merger inspiral and ringdown

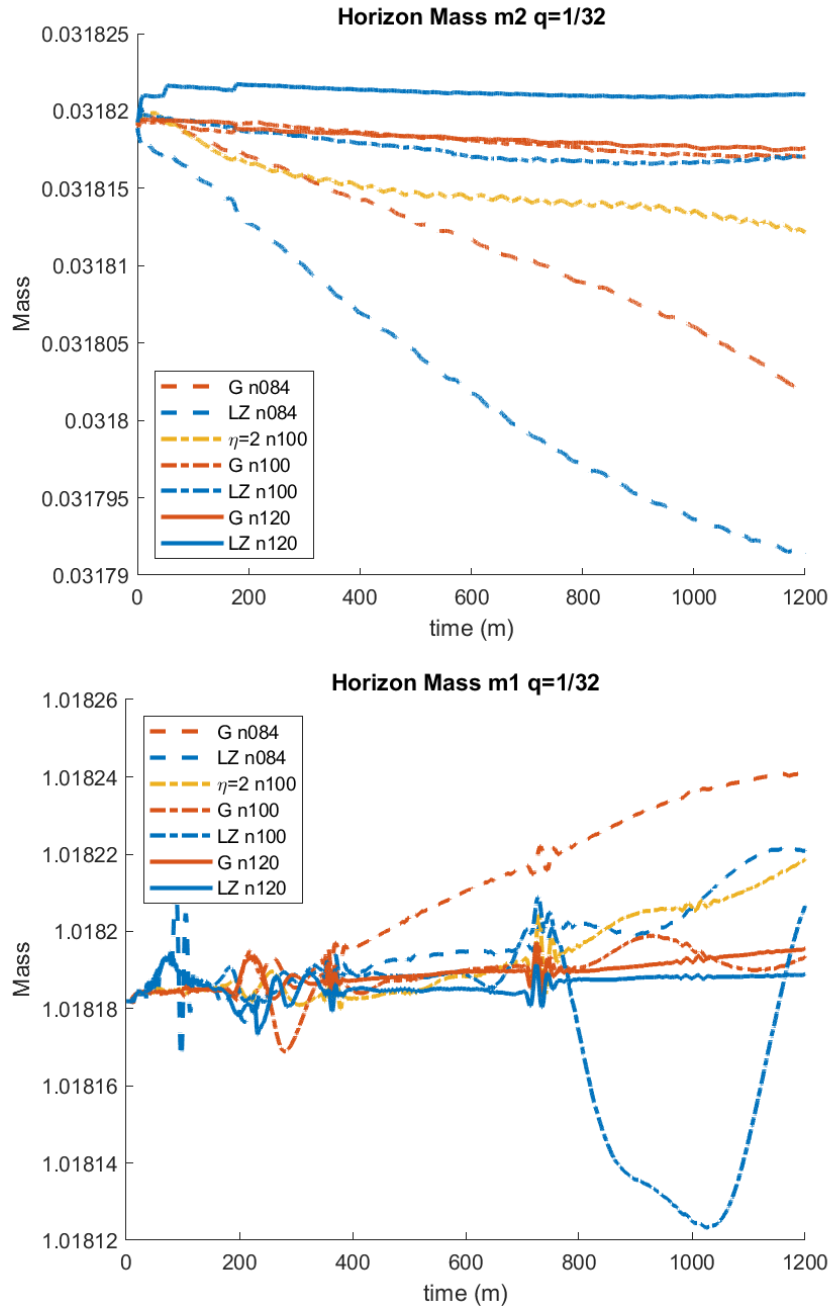


Figure 3.15: Horizon masses for m_2 (top) and m_1 (bottom) versus time for the $q = 1/32$ simulation with the different choices for $m\eta$, G, LZ, and $\eta = 2/m$. The dashed, dot-dashed, and solid lines are the low n084, medium n100, and high n120 resolutions respectively. The horizon masses m_1 and m_2 deviate from constant most dramatically when the LZ gauge is used. Both the $\eta = 2/m$ and G gauges maintain the mass of the horizon well over the course of the simulation, except at the lowest resolution n084.

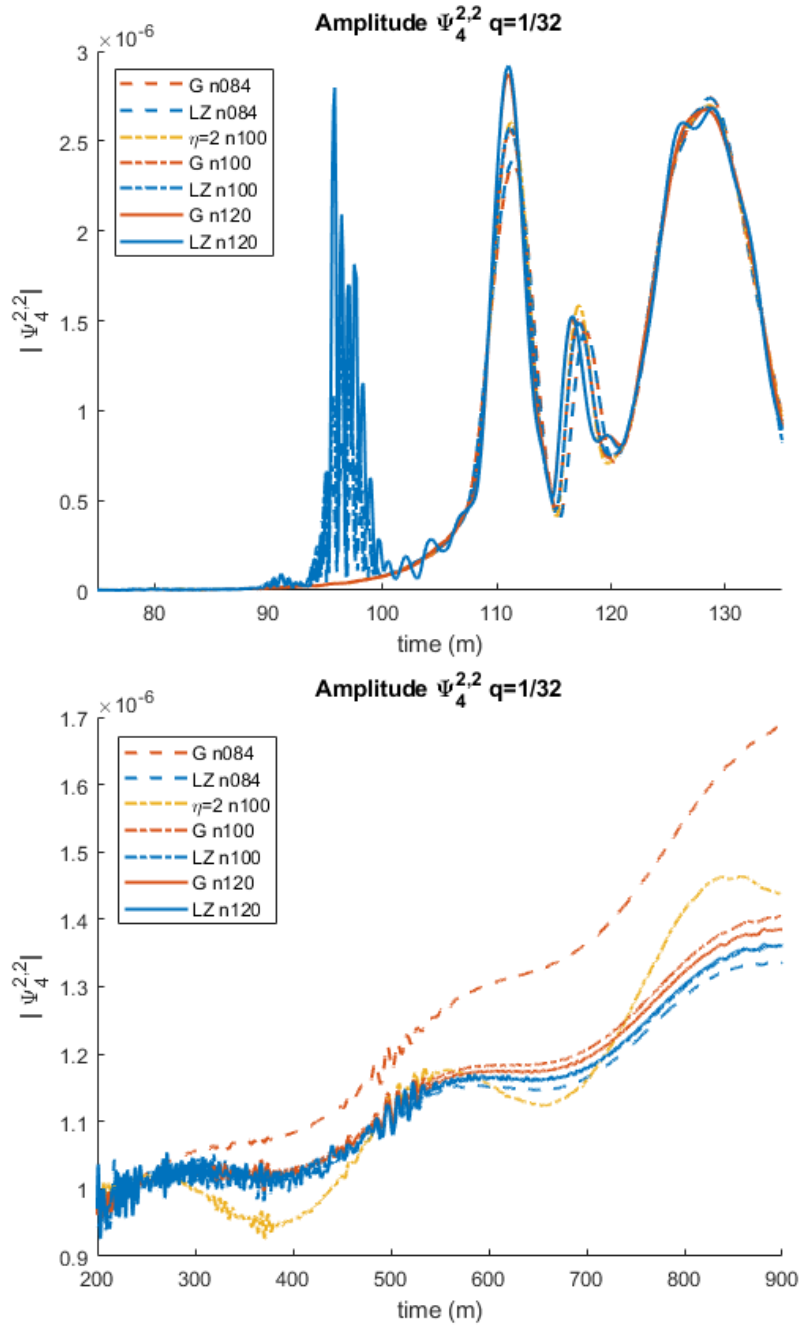


Figure 3.16: The amplitude of the Ψ_4 waveform of the $q = 1/32$ binary extracted at an observer located at $r = 113m$. The top panel shows the early part of the waveform from $t = (75 - 135)m$, and the bottom panel shows the inspiral period from $t = (200 - 900)m$. Higher frequency noise of the LZ gauge is apparent at $t \sim (90 - 100)m$, which is damped by the G and $\eta = 2/m$ gauges. Refinement boundary reflections of the high frequency noise are apparent in the second panel, which shows a longer inspiral.

phases is also a good method of quantifying gauge performance. Fig. 3.17 shows two different sections of the amplitude of the dominant mode of the gravitational wave strain $h_{2,2}$ for the $q = 1/32$ binary, using the G, LZ and $\eta = 2/m$ gauges at resolution n100, extrapolated to an observer at ∞ . The merger times for all simulations are matched for easy comparison. The top panel of Fig. 3.17 shows the inspiral portion of the waveform, from $t = (300 - 1300)m$ and the bottom panel shows the ringdown period post-merger from $t = (1500 - 1530)m$.

In Fig. 3.17, we are interested in comparing the effects of the different gauges on low frequency oscillations before and after merger. Using the constant choice $\eta = 2/m$ introduces low frequency oscillations in the inspiral portion (top panel) of the strain $h_{2,2}$ that are damped by choosing an alternative, variable gauge such as G or LZ. This suggests that using a gauge with peaks at the black holes resolves the binary's dynamics well in the strong field region, effectively damping oscillations in the gauge that propagate from the black holes. The ringdown phase (bottom panel) shows significant oscillations in gravitational waveforms that use the LZ gauge. Using $\eta = 2/m$ or G produces waveforms without these oscillations, which suggest that the low frequency oscillations come from the choice of gauge itself. We are currently investigating a gauge that uses G for the inspiral and then flattens to a near-constant $\eta = 1/m$ post-merger, i.e. Eq. (3.3.46) with $n = 2$.

As a follow up to [67], we would like to investigate the effects of different gauge choices on the horizon quantities of small mass ratio binaries as well. Table 3.6 shows the results of this study. It includes all 7 runs with mass ratio $q = 1/32$ (3 resolutions for G and LZ, and one for $\eta = 2/m$) as well as a 3-point extrapolation to infinity in the row labeled $n\infty$ and the order of convergence (CO) where they exist. The Horizon columns show the results of the energy and angular momentum calculated using the isolated horizon formulae, and the Radiated columns show the results of calculating the same three quantities as carried away by gravitational waves.

Our new gauge G does a good job of measuring mass and angular momentum on the horizon when compared to its radiated counterpart. The horizon energy and radiated energy converge to the same value (within 10^{-4}), as do the horizon and radiated angular momentum.

However, at the resolutions we used for these simulations, G, and our typical variable gauge, LZ, do a very poor job of measuring kick on the horizon when compared to the linear momentum carried away by gravitational waves. For this reason, we have chosen to omit these results from Table 3.6. It is worth mentioning that G performs slightly better, at least reaching the correct order by the highest resolution - 20.85 km/s measured on the horizon vs. 9.94 km/s measured at infinity, where LZ estimates 219.96 km/s instead of 9.73 km/s. For both G and LZ, the approximation does improve with resolution, however for an accurate measurement of horizon linear momentum we need to increase the resolution again to n144. The constant gauge $\eta = 2/m$, was only simulated for one resolution, n100, of $q = 1/32$; because of the increase in CFL that was required for the lowest resolution $q = 1/15$, we have discounted $\eta = 2/m$ as a viable option.

| Gauge | Resolution | Horizon | | Radiated | | |
|-------|------------|---------|---------|----------|---------|------------|
| | | E/m | J/m^2 | E/m | J/m^2 | L (km/s) |
| G | n084 | 0.9979 | 0.0985 | 0.9979 | 0.0982 | 8.4673 |
| | n100 | 0.9979 | 0.0972 | 0.9979 | 0.0979 | 9.7856 |
| | n120 | 0.9979 | 0.0977 | 0.9979 | 0.0978 | 9.9423 |
| | $n\infty$ | 0.9978 | 0.0976 | 0.9979 | 0.0977 | 9.9634 |
| | CO | 2.00 | 4.42 | 4.82 | 6.04 | 11.68 |
| LZ | n084 | 0.9979 | 0.0974 | 0.9979 | 0.0978 | 7.3265 |
| | n100 | 0.9979 | 0.1002 | 0.9979 | 0.0978 | 9.5137 |
| | n120 | 0.9979 | 0.0967 | 0.9979 | 0.0976 | 9.7311 |
| | $n\infty$ | 0.9979 | - | 0.9980 | 0.0971 | 9.7551 |
| | CO | 4.23 | - | 0.90 | 0.06 | 12.66 |
| $2/m$ | n100 | 0.9979 | 0.0976 | 0.9979 | 0.0978 | 9.3891 |

Table 3.6: For the $q = 1/32$ binaries using G, LZ, and $\eta = 2/m$, the resolutions are given in column 2. The horizon quantities (energy and angular momentum) are in columns 3 and 4, and the corresponding radiated quantities are in columns 5-7. All simulations use CFL=1/4 and 8th order finite differencing stencils. The G gauge does a good job of measuring the horizon mass and spin, however, the horizon linear momentum requires high resolution to approach the radiated linear momentum.

3.4.4 Results for a $q = 1/64$ and $q = 1/128$ nonspinning binary

We also performed a study on extremely small mass ratio, nonspinning binaries with $q = 1/64$ and $q = 1/128$ and initial binary separation of $d = 7m$. The simulations use a Courant

factor of 1/4 as well as 8th order finite differencing stencils. The $q = 1/64$ was run with two resolutions (n084, n100) in the LZ gauge and one resolution (n100) in the G gauge. As a follow up to [22], the $q = 1/128$ n100 simulation in the LZ gauge generated for that work is included here to compare with preliminary results for the n100 G gauge.

In Fig. 3.18, the masses measured on the horizon of the black holes (top: m_2 , bottom: m_1) are shown for $q = 1/64$. The LZ gauge is in blue and the G gauge is in red with different resolutions denoted by different line types. In m_2 , both gauges produce masses that are similarly constant at our typical production resolution of n100. The resolution n084 is quite a bit under-resolved for this extremal simulation, and therefore the LZ gauge does not do a good job of maintaining constancy in either m_1 or m_2 . However, the smaller black hole m_1 is more difficult to resolve, and using the G gauge at n100, its mass is held more constant than using the LZ gauge at the same resolution.

For the more extreme mass ratio binary, $q = 1/128$, we will consider only the early part (through $t/m = 1000$ of the n100 simulation in the G gauge; the simulation was not run through merger. This will be compared to a full simulation of the binary in the LZ gauge since it was completed for [22]. These runs are very computationally difficult to do, but comparing the results of the early part of the simulations will give us a good idea of the benefits of using G instead of LZ here. Fig. 3.19 shows both horizon masses versus simulation time in the G and LZ gauges in one resolution (n100). Since n100 is still under-resolved for the $q = 1/128$ binary, neither m_1 nor m_2 is held constant. However, m_2 in the LZ gauge has slightly less mass-gain than in the G gauge, whereas the G gauge has a significant reduction in noise over the LZ gauge. Neither gauge prevents mass loss/gain in m_1 - in order to see benefits of the G gauge it is likely we would need to increase resolution by at least a factor of 1.2 (to n120).

Fig. 3.20 shows the amplitude of the gravitational wave scalar $\Psi_4^{2,2}$ versus simulation time for the three different runs with mass ratio $q = 1/64$. The top panel shows the early part of the inspiral, and the numerical noise present when the LZ gauge is chosen is visible again between $t = (95 - 100)m$, however it has decreased substantially in amplitude. Using the

G gauge damps this noise completely, as well as reduces other oscillations present in the LZ gauge simulation with n100 resolution (blue, dot-dashed) at $t = 150m$.

The bottom panel shows the inspiral period of $\Psi_4^{2,2}$ from $t = (200 - 800)m$. The simulation with the LZ gauge in resolution n100 has high frequency oscillations between $t = (200 - 500)m$ which are nonphysical. These are damped away almost completely by making the choice of G for $m\eta$. There are reflections of noise at the grid refinement boundaries visible between $t = (300 - 400)m$ and $t = (500 - 600)m$.

Similarly, we can consider the effects of the different gauges on the inspiral period of the $q = 1/128$ binary. In contrast to the horizon masses, when the gravitational waveform is considered, the G gauge shows obvious improvement over LZ. Fig. 3.21 shows the inspiral from $t = (75 - 135)m$ in the top panel and $t = (200 - 800)m$ in the bottom panel using both G and LZ in resolution n100. In the top panel, between $t = (95 - 100)m$, we can see an initial burst of nonphysical noise that is consistent with our results for all other mass-ratios. This is damped by choosing the G gauge, which is hugely beneficial for such a demanding simulation.

The bottom panel of Fig. 3.21 shows the inspiral period of $\Psi_4^{2,2}$ up to just before merger. In the LZ gauge, there is a substantial amount of high frequency noise present in the waveform until about $t = 600m$. Using the G gauge, this noise is almost completely damped, producing a cleaner and more accurate gravitational waveform for no increase in computational expense.

As the mass-ratio of the binary decreases, the inspiral and ringdown oscillations in the dominant mode of the gravitational wave strain increase in amplitude. Consider Fig. 3.22. The top panel shows the inspiral, $t = (250 - 950)m$ of $h_{2,2}$ for $q = 1/64$ using gauges G and LZ in resolutions n084 and n100. Both G and LZ produce low-frequency oscillations in the inspiral. As shown in the dot-dashed curves, these oscillations are comparable, but small, in amplitude at the production resolution n100. This is consistent with our findings for the $q = 1/32$ binary, and is further evidence of the benefit of using a variable gauge during inspiral.

The bottom panel of Fig. 3.22 shows the ringdown phase of the evolution from $t = (1020 - 1070)m$. The oscillations in the ringdown of the simulation with the lowest resolution in the

LZ gauge are fairly severe, however they damp away with an increase in resolution to n100. With the use of the new G gauge, the oscillations in the ringdown of $h_{2,2}$ are decreased in both frequency and amplitude when compared to the corresponding ringdown in $h_{2,2}$ using the LZ gauge. We expect further improvements could be made with a gauge that has a near constant value post-merger, or an increase in resolution up to n144.

For such computationally demanding simulations as $q = 1/64$ and $q = 1/128$, the ability to accurately measure horizon quantities at lower resolution has substantial benefits in terms of computational expense. Table 3.7 shows the energy and angular momentum as measured on the horizon (columns 4 and 5), as well as the same quantities calculated from the amount of each carried away by gravitational waves (columns 6 and 7). It also includes the kicks for these simulations, but only measured by the amount of linear momentum carried away by gravitational waves (column 8). This measurement of linear momentum is significantly more consistent than using the measurement on the horizon, so the horizon results are not included since they are not the main focus of this work. An improvement in the horizon measure of linear momentum would require an increase in resolution to n120 or even n144 which is not necessarily practical for such a small mass-ratio binary.

| q | Gauge | Resolution | Horizon | | Radiated | | |
|-------|-------|------------|---------|---------|----------|---------|------------------|
| | | | E/m | J/m^2 | E/m | J/m^2 | $L(\text{km/s})$ |
| 1/64 | G | n100 | 0.9990 | 0.0529 | 0.9990 | 0.0516 | 2.8065 |
| 1/64 | LZ | n084 | 0.9990 | 0.0457 | 0.9990 | 0.0516 | 2.7216 |
| 1/64 | LZ | n100 | 0.9990 | 0.0519 | 0.9990 | 0.0516 | 2.4303 |
| 1/128 | LZ | n100 | 0.9996 | 0.0239 | 0.9995 | 0.0267 | 0.9703 |

Table 3.7: The horizon quantities for the $q = 1/64$ binary using the G and LZ gauges and the $q = 1/128$ binary using the LZ gauge. The remnant quantities for the $q = 1/128$ binary in the G gauge are not included since that simulation was not run through merger. The resolutions are given in column 3. The horizon quantities (energy and angular momentum) are in columns 4-5, and the corresponding radiated quantities are in columns 6-8. All simulations use CFL=1/4 and 8th order finite differencing stencils. The G gauge does a good job of measuring the horizon mass and spin, however, the horizon linear momentum requires high resolution to get close to the radiated measure, and is therefore not shown.

This is consistent with our findings in for the $q = 1/32$ binary, where the use of G and LZ to compute horizon linear momentum does improve with resolution but requires higher

resolution simulations than those performed here. This can be combined with our findings in [67], in which a low-value constant η , such as 1 or 0.5, was able to very accurately measure recoil velocity on the horizon even at low resolutions, to construct a variable gauge that damps to a constant η post-merger.

However, the other horizon quantities (mass and angular momentum) are measured very accurately in both the G and LZ gauge. The exception, of course, is when resolution is too low (n084) to properly resolve the grid. There is an obvious improvement with respect to resolution, and an increase to n120 would likely produce horizon quantities that are on par with their radiated counterparts.

3.4.5 Noise/spurious radiation versus mass ratio

The study of waveform amplitudes and phases can also provide an invariant measure of accuracy of the full numerical simulations. It has already been mentioned that this new gauge G completely damps the initial burst of noise at the beginning of the gravitational waveform, present when the LZ gauge is used, as well as its subsequent reflections at the refinement boundaries. In fact, this noise can be shown to be inversely proportional to the size of the peak in the spurious radiation generated at the beginning of the waveform due to initial data. Fig. 3.23 shows the peak amplitude of the noise in $\Psi_4^{2,2}$, \mathcal{N}_{peak} , over the peak amplitude of the spurious radiation in $\Psi_4^{2,2}$, \mathcal{S}_{peak} , for each mass ratio $q = 1/7, 1/15, 1/32, 1/64$, and $1/128$ extracted at $r = 113m$. This figure uses the n100 simulations since we have those for every mass ratio. We can generate a power-law fit that is a function of the mass-ratio q , which takes the form

$$F(q) = \mathcal{P}q^m \tag{3.4.51}$$

where $m = 0.8557 \pm 0.0448$ and $P = 9.5739 \pm 0.0463$ are dimensionless constants. The fit has errors at each data point shown in Table 3.8. Although the absolute difference between the fit and data points scale with q , the relative error increases as q gets smaller. If we had higher resolution simulations for the smaller mass ratios, likely they would show that $\mathcal{N}_{peak}/\mathcal{S}_{peak}$ does in fact follow a power law. This means that the noise is in fact reduced significantly in

| q | $ F(q) - \mathcal{N}_{peak}/\mathcal{S}_{peak} $ | $\frac{ F(q) - \mathcal{N}/\mathcal{S}_{peak} }{ \mathcal{N}_{peak}/\mathcal{S}_{peak} }$ |
|-------|---|--|
| 1/7 | 0.1012 | 0.0529 |
| 1/15 | 0.0367 | 0.0405 |
| 1/32 | 0.0260 | 0.0500 |
| 1/64 | 0.0511 | 0.2308 |
| 1/128 | 0.0229 | 0.1321 |

Table 3.8: The absolute and relative errors between $F(q)$ for all q and $\mathcal{N}_{peak}/\mathcal{S}_{peak}$ and standard deviation for $\Psi_4^{2,2}$ extracted at $r = 113m$ using resolution n100.

amplitude in the small q -regime.

3.5 Discussion and conclusions

The gauge choices were crucial to the moving punctures breakthrough formalism that allowed numerical relativists to successfully evolve binary black holes [8, 24]. Here we explored choices of the initial lapse, α_0 , and shift, β_0 , as well as the damping parameter η in the Equations (3.2.2).

In the construction of the waveform catalogs [2, 34, 35] we used a Courant factor of 1/3 and sixth order spatial finite differencing for non-highly spinning and comparable masses binaries evolutions. This prioritized speed of the creation and therefore population of the initial catalogs to evaluate gravitational waves events observed by LIGO and Virgo [58]. For highly spinning binaries [36, 80, 81] and the small mass ratio systems we study here ($q \leq 1/32$) require a reduction of the Courant factor to 1/4 and the use of 8th order finite differencing stencils to achieve good accuracy [95].

In our study of the improved choices of the initial lapse and shift inspired by their late time behavior we found some benefits in introducing the initial lapse as described in Section 3.4.1. In some preliminary studies we did on nonspinning binaries using an initial shift different from zero, we found the shift damped quickly to zero and then oscillated around zero during the binary’s evolution before settling to the proposed initial form, without any obvious improvements to the system’s physical parameters.

For comparable mass binaries of $q \geq 1/15$, the damping parameter η is chosen to be a small,

but constant value of order unity. Reduction of the mass ratio of the binary to $q = 1/15$ and beyond benefits from η variable in order to counteract the so called grid-stretching produced by the growth of the horizon in the numerical coordinates (See Fig. 3.13) and thus depleting those gridpoints to resolve the fields in the exterior of the black holes. Of course, one can compensate by introducing more points via higher resolutions, but this comes at an increased computational cost.

The form of this damping parameter $\eta = G$ given in Eq. (3.3.46) provides a good general form valid for a wide range of mass ratios q . In addition to better maintaining of the physical parameters such as mass and spin, this choice of η also removes unwanted initial noise in the waveforms, as well as its corresponding reflection on the mesh refinement levels when compared the alternative original choice [7, 22] (See also Eq. (3.3.45)) as displayed in Figs. 3.14 and 3.16. We have also found that the computational cost of introducing a variable η is negligible compared to the whole evolution system of equations; the change is within 5% of the speed of the $\eta = 2/m$ and is about 10% faster than choosing LZ.

The constraint violation studies we performed are a useful measure of convergence with numerical resolution within a given gauge, but are not so useful when comparing different gauges. We chose then to turn to analysis of physical parameters to determine the benefits of using different gauges. The conservation of the horizon masses and spins (as shown in Figs. 3.10 and 3.12) are a gauge independent measures of the accuracy of the simulations (Since absorption is an order of magnitude smaller of an effect during inspiral and merger). The evaluation of the horizon recoils also benefits from the property that $G \rightarrow 1$ far from the black holes, as shown in Table 3.4.

Additionally, we have looked in particular to the amplitude's behavior pre- and post- merger (see Figs. 3.17 and 3.22). To this end we have also introduced the $n = 2$ in the η_G choices in Eq. (3.3.46) and Fig. 3.8 that smooths the values of η around the smaller horizon, once the binary forms a common horizon (from when we normally drop the innermost refinement level).

In conclusion we recommend the use of the choices $(\alpha_0, \beta_0 = 0, \eta_G)$ parameters for the

moving puncture evolutions due to its reasonable computational cost as well as the simplicity of its implementation. This gauge choice shows a wide range of improvements when dealing with essentially all possible mass ratios, $q \leq 1$.

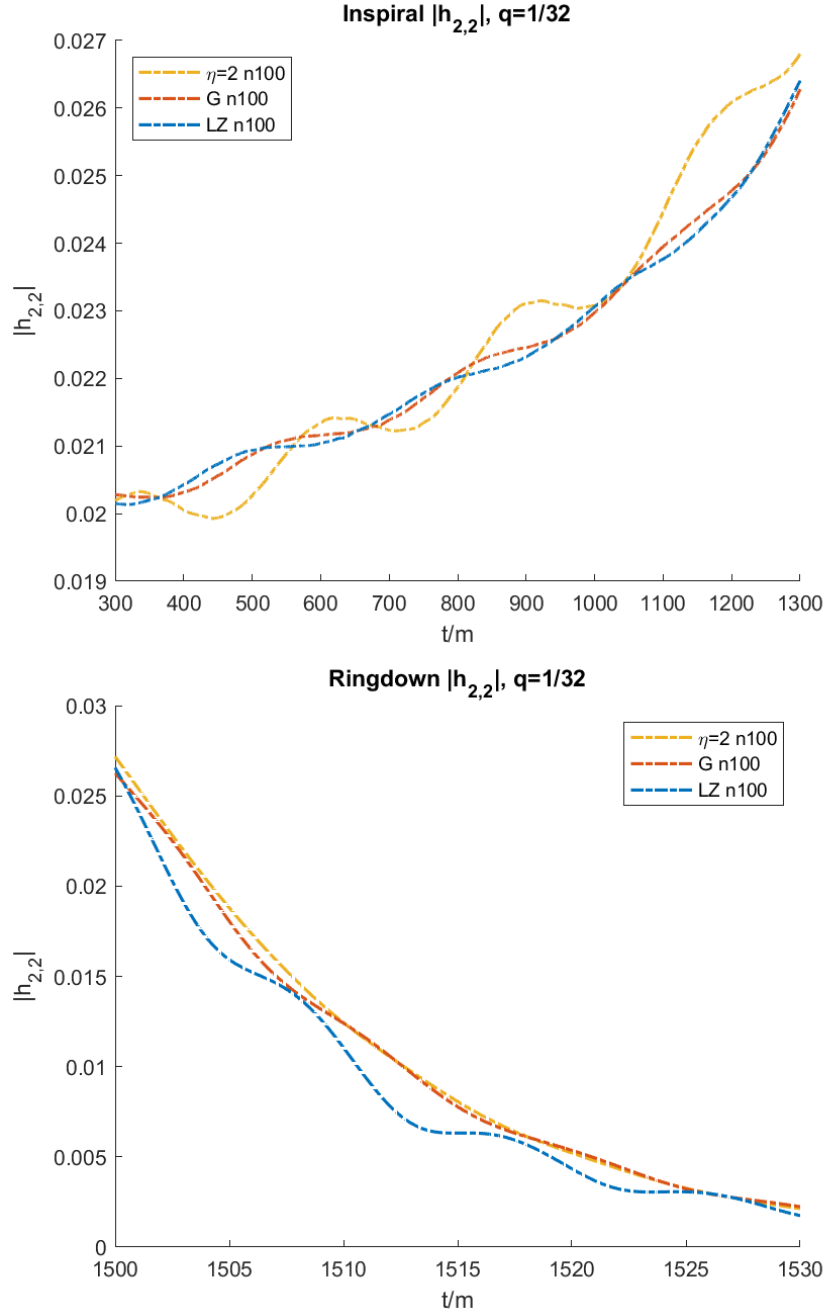


Figure 3.17: Inspiral (top) and ringdown (bottom) periods of the gravitational wave strain $h_{2,2}$ of the mid-resolution simulations of the $q = 1/32$ binary using the G, LZ, and $\eta = 2/m$ gauges. In the inspiral, the waveform using the $\eta = 2/m$ gauge exhibits oscillatory behavior which is not present in either of the variable gauges. However, post-merger, the waveform using LZ exhibits oscillations, whereas the G and $\eta = 2/m$ waveforms do not. This suggests that a variable gauge is useful during inspiral, and a more constant gauge is most effective post-merger.

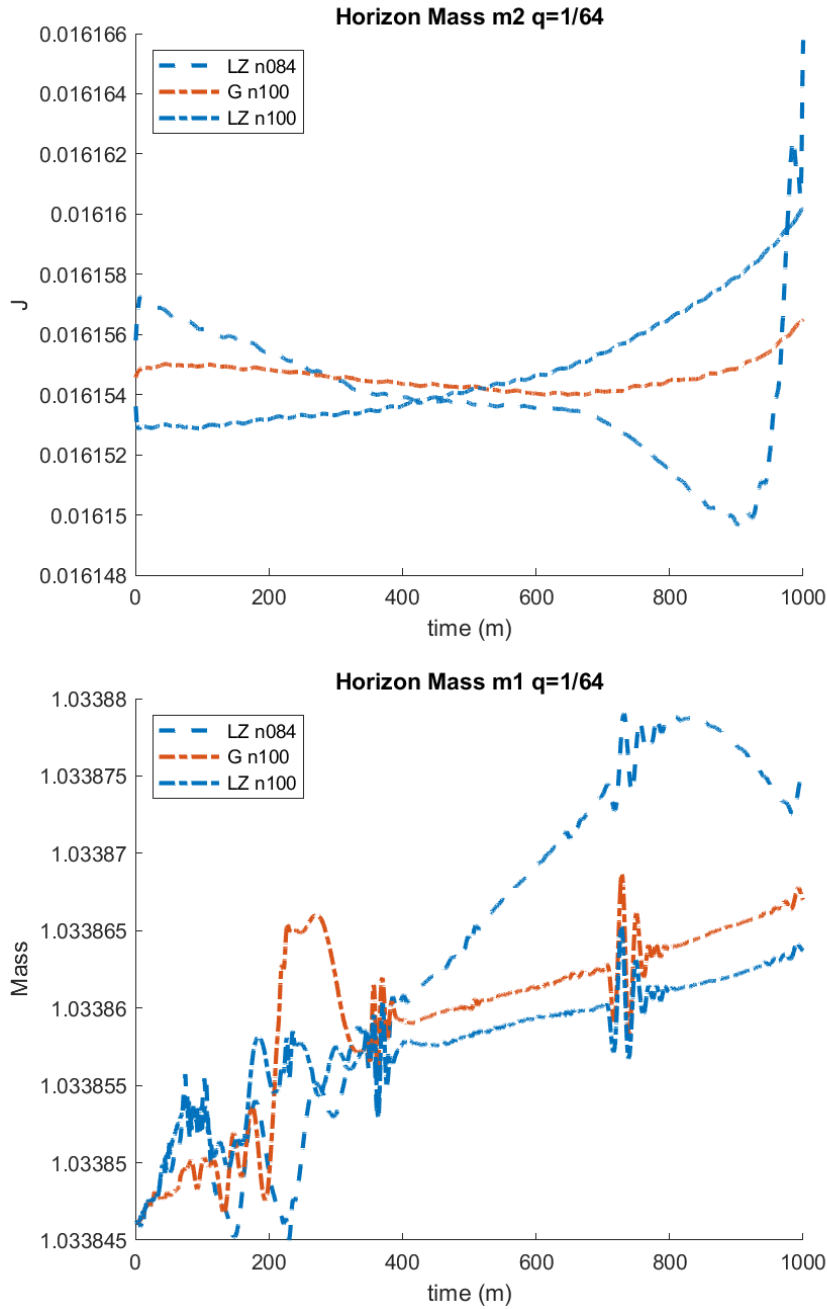


Figure 3.18: Horizon masses for m_1 and m_2 versus time for the $q = 1/64$ simulation. The masses in the LZ gauge are shown in two resolutions n084 and n100, and the masses in the G gauge are shown in only n100. The masses using G are more constant than their counterparts that use the LZ gauge, especially in the case of the small black hole m_1 .

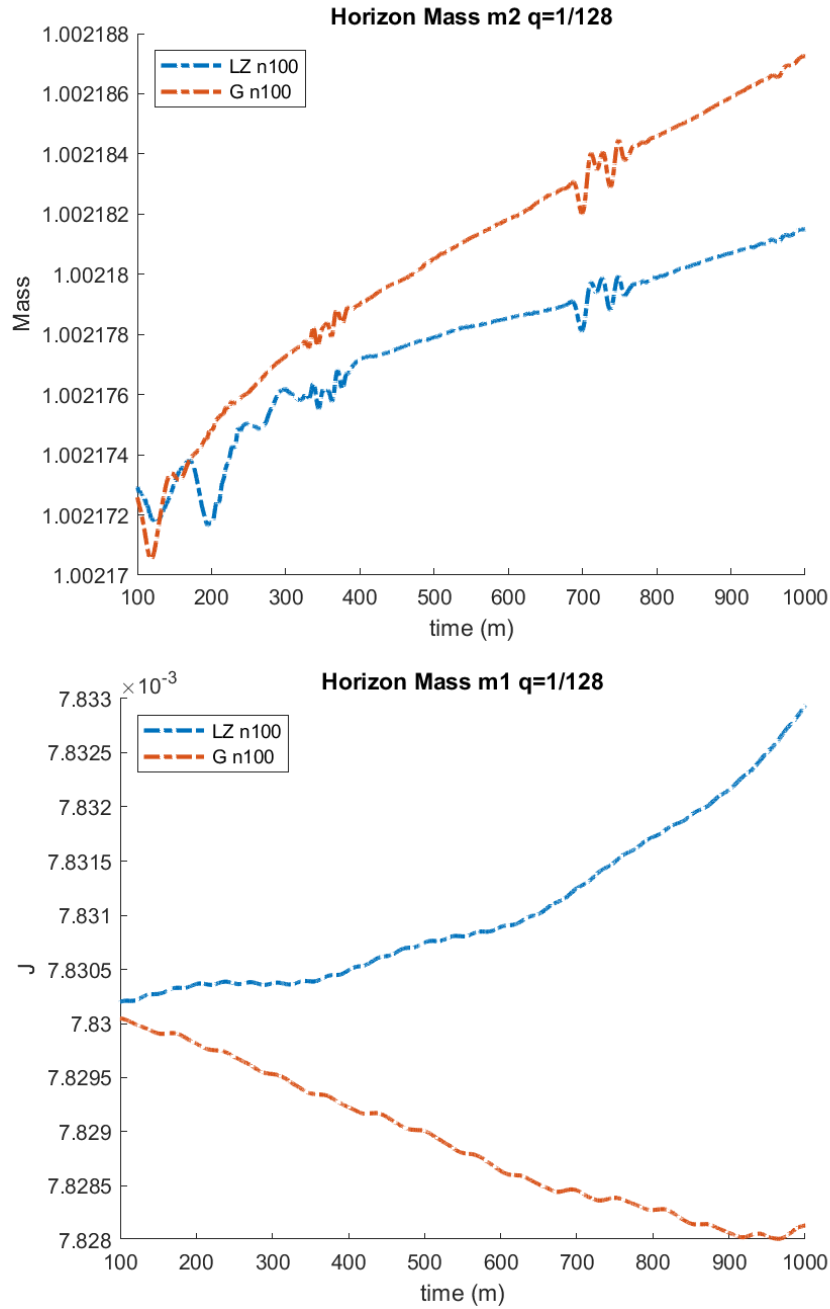


Figure 3.19: Horizon masses for m_1 and m_2 versus time for the $q = 1/128$ simulation. The masses in both the LZ and G gauges are shown in only n100. The large black hole m_2 using the LZ gauge is held slightly more constant than its counterpart that uses the G gauge, however the LZ gauge simulation has significantly more noise than the G gauge one.

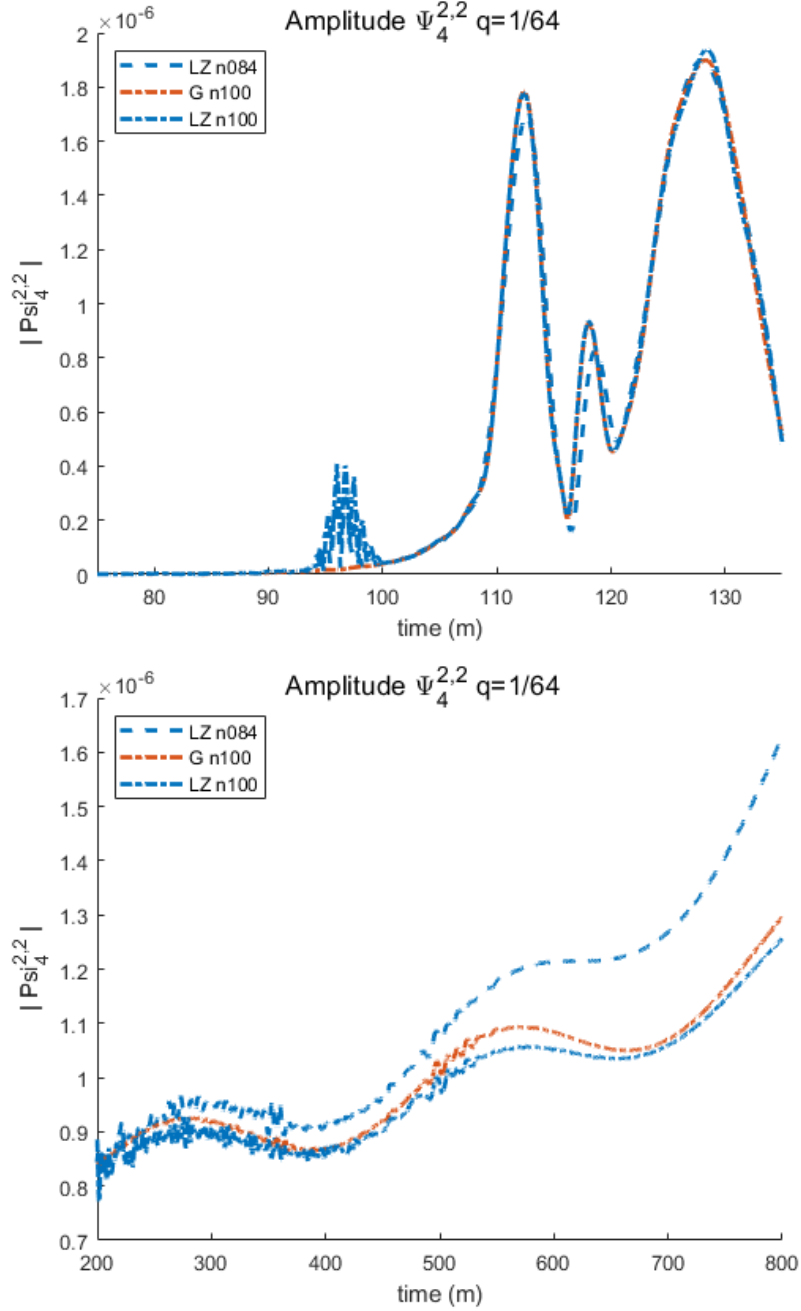


Figure 3.20: The amplitude of the Ψ_4 waveform of the $q = 1/64$ extracted at an observer located at $r = 113m$. The top panel shows the early part of the waveform from $t = (75-135)m$, and the bottom panel shows the inspiral period from $t = (200-900)m$. Higher frequency noise of the LZ gauge is apparent at $t \sim (95-100)m$, which is damped by the G and $\eta = 2/m$ gauges. Refinement boundary reflections of the high frequency noise are apparent in the second panel, which shows a longer inspiral.

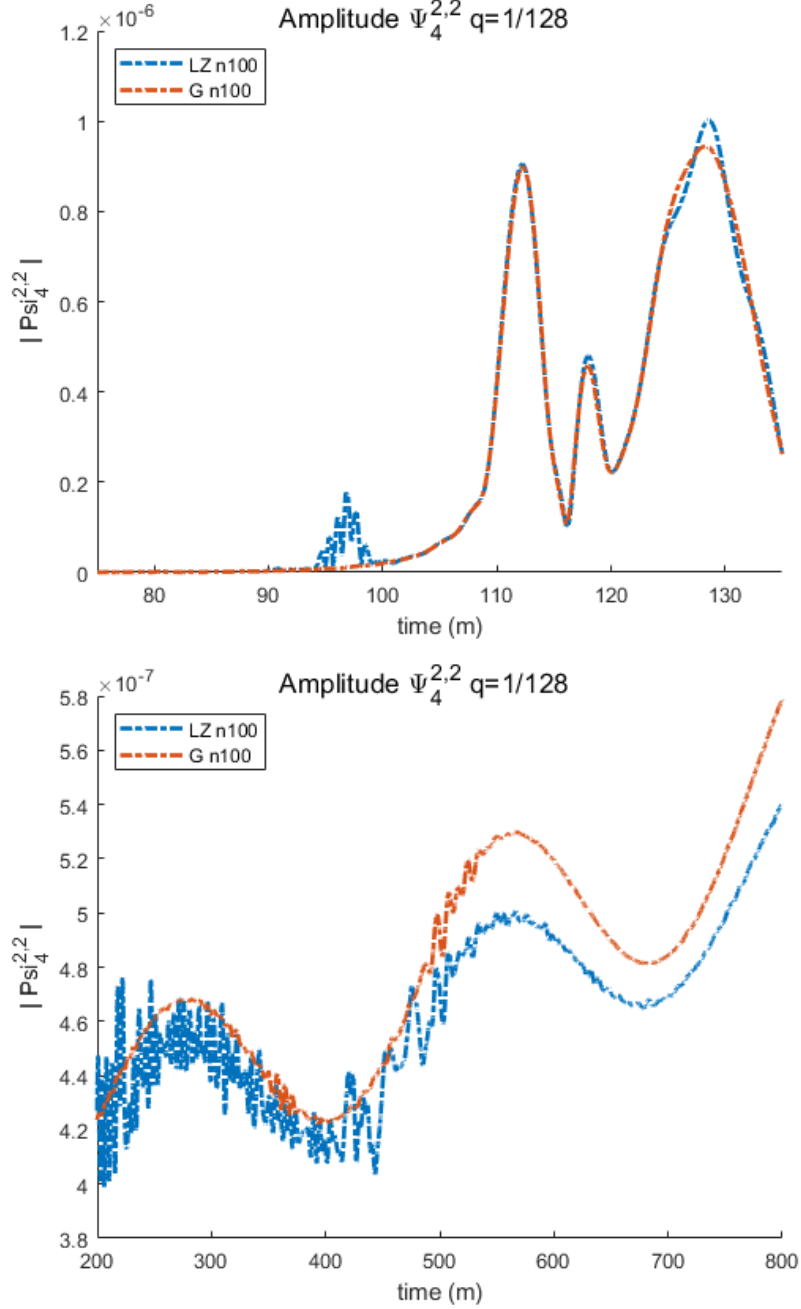


Figure 3.21: The amplitude of the Ψ_4 waveform of the $q = 1/128$ extracted at an observer located at $r = 113m$. The top panel shows the early part of the waveform from $t = (75-135)m$, and the bottom panel shows the inspiral period from $t = (200-800)m$. Higher frequency noise of the LZ gauge is apparent at $t \sim (95-100)m$, which is damped by the G and $\eta = 2/m$ gauges. Refinement boundary reflections of the high frequency noise are apparent in the second panel, which shows a longer inspiral.

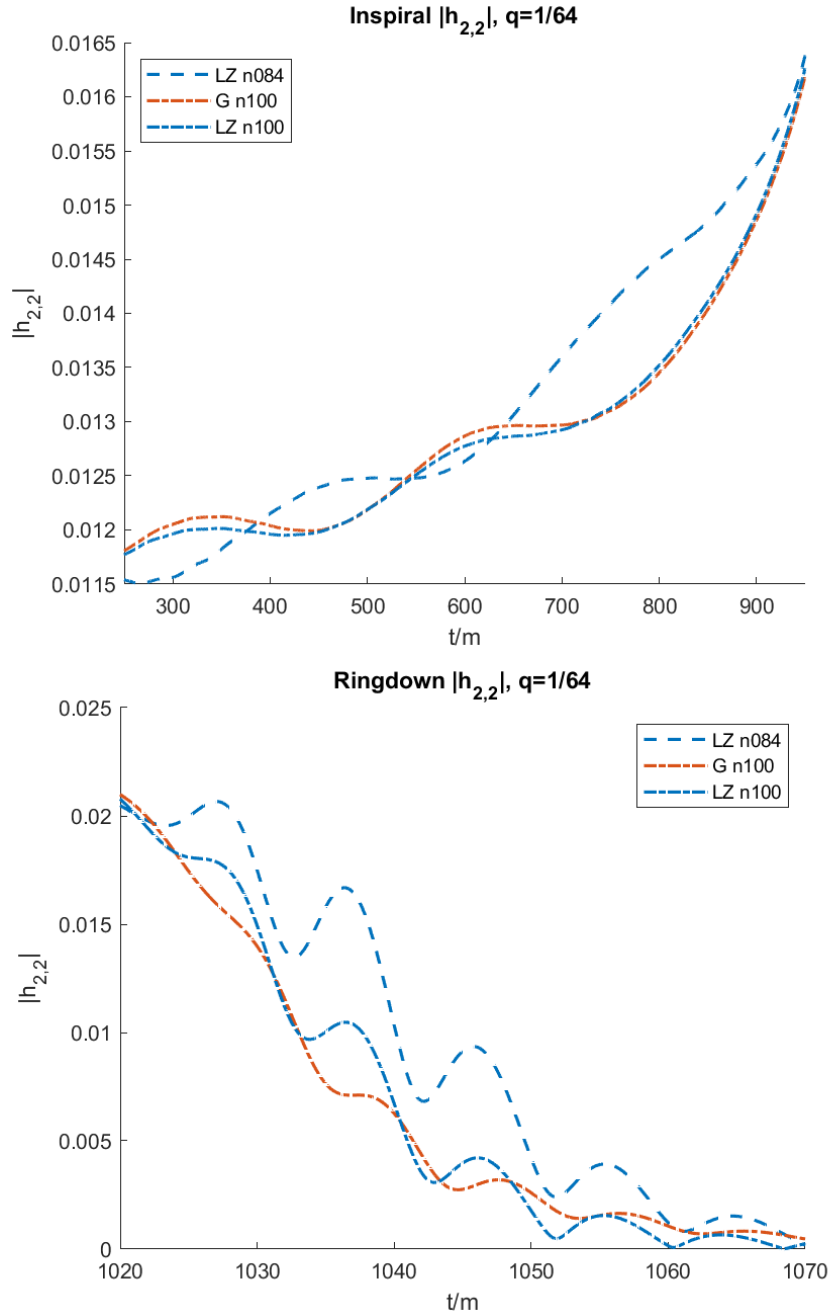


Figure 3.22: Inspiral (top) and ringdown (bottom) amplitudes for the $q = 1/64$ binary using the G and LZ gauges with resolutions n084 and n100. There is no clear difference between gauges in the inspiral, however, in the ringdown period, $h_{2,2}$ using the LZ gauge exhibits oscillations that are larger in amplitude and slightly higher in frequency than $h_{2,2}$ using the G gauge.

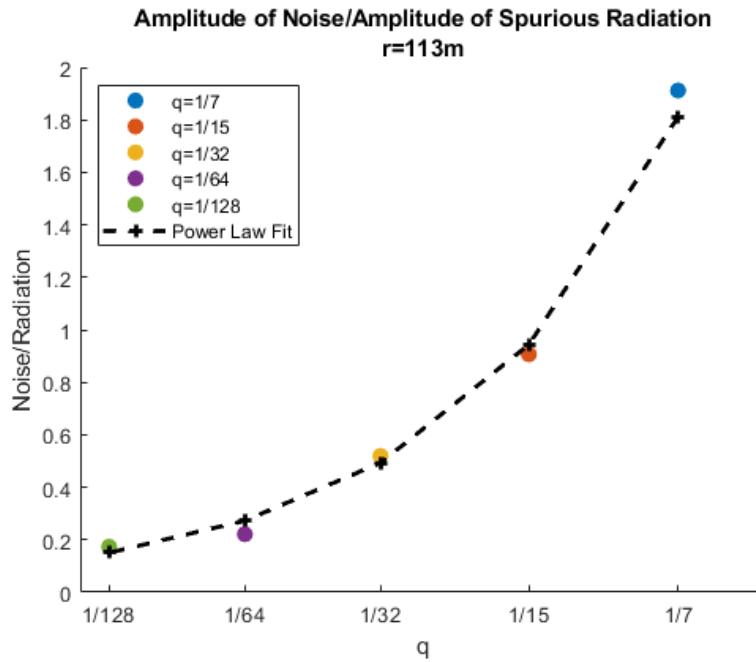


Figure 3.23: The data points show the ratio $\mathcal{N}_{peak}/\mathcal{S}_{peak}$ of $\Psi_4^{2,2}$ extracted at $r = 113m$ for each mass ratio q . The black line is a power law fit to the data $F(q) = 9.9753q^{0.8557}$. Errors are shown in Table 3.8.

Chapter 4

Analytic Analysis of Spacetimes in Generic Transverse Frames.

With the new generation of gravitational wave detectors on the horizon, such as the space-based detector LISA and the constant advancements to the LIGO and VIRGO detectors, it is of interest to develop more accurate, less computationally expensive methods of extracting gravitational wave signals from binary compact object mergers. Typical gravitational wave signals produce long waveforms, especially systems with precession or eccentricity, so the theoretical predictions from the numerical solutions of Einstein's Field Equations must be accurate to an extremely high order to capture as much of the waveform as possible.

In Chapters 2 and 3, we have already studied methods of improving the accuracy of challenging numerical simulations of binary black hole pairs. These improvements are all made to the evolution code - the variable η is calculated at every timestep, and the initial lapse α and shift β are used as initial data for the gauge equations which define the coordinates of the spacetime.

Post-merger, the spacetime can be rotated into a frame that pushes more physical information into the scalar, Ψ_4 , that we use to calculate outgoing gravitational radiation. This, in

4.1. Accurate Extraction of Gravitational Waves: From the Weyl Tensor to the quasi-Kinnersley frame

turn, improves the computation of gravitational wave strain h since

$$\Psi_4 = -\ddot{h}^+ + i\ddot{h}^\times = \ddot{h} \quad (4.0.1)$$

which implies

$$h = - \int_{-\infty}^t \int_{-\infty}^{t'} \Psi_4 dt'' dt'. \quad (4.0.2)$$

This means that if we rotate the spacetime into a frame that encodes more of the physical outgoing gravitational radiation into Ψ_4 , we will be able to extract more accurate gravitational waveforms and therefore improve our post-simulation analysis of BBH systems.

The extraction of gravitational waves in different frames is not new, however, it is mostly done in the asymptotic regime. We are interested primarily in using these frames to study the spacetime in the strong-field regime - very close to and in between the binary. We have a priori knowledge of the spacetime should be as $r \rightarrow \infty$ - it is expected to be Kerr-like in nature [37] - but no information about its classification as $r \rightarrow 0$. This Chapter will develop the necessary framework to rotate a spacetime into a frame with more physical information in Section 4.1 through Section 4.4. In Section 4.6 we will develop and test a new index which helps to classify the strong-field region of the spacetime locally (at each point), bearing in mind the numerical applications. We also introduce the concept of approximately local Petrov types. Then we will study several systems with Brill-Lindquist (head-on collision) initial data. Much of the work in this Chapter is included in an article¹ that has been accepted for publication to Physical Review D.

4.1 Accurate Extraction of Gravitational Waves: From the Weyl Tensor to the quasi-Kinnersley frame

Gravitational radiation in general relativity is defined in regions of the spacetime known as “radiation zones”. Their geometry is characterized by two distinctive length scales

¹Rosato, Nakano, Lousto. Local and Approximate Classification of Spacetimes in the Transverse Frames. *Phys. Rev. D*, accepted 2021. The arXiv version can be found at <https://arxiv.org/pdf/2106.05991.pdf>.

4.1. Accurate Extraction of Gravitational Waves: From the Weyl Tensor to the quasi-Kinnersley frame

1. the average radius of the spacetime's curvature and
2. the wavelength of the gravitational waves.

These scales are distinguishable by very small changes in the curvature caused by the passing of gravitational wave through the spacetime. There are two main approaches to gravitational wave extraction - both based on perturbation theory. The first, the Reggie-Wheeler-Zerilli approach, allows for the direct extraction of gravitational radiation from 3+1 fields. The other, Teukolsky's approach, [105, 106], describes radiation fields near a Kerr black hole. This study will focus on the second approach.

Teukolsky, in 1972, presented separable equations for the radiative parts of electromagnetic and gravitational perturbations on a Kerr background in Boyer-Lindquist coordinates, derived from a formalism introduced by Newman and Penrose in 1962 [107]. This Newman-Penrose formalism uses the Weyl tensor

$$C_{abcd} \tag{4.1.3}$$

which is the trace-free component of the Riemann curvature tensor R_{abcd} , to develop a formalism that re-expresses the 10 independent components of the Weyl tensor in terms of five complex scalars Ψ_0, \dots, Ψ_4 , the Newman-Penrose (Weyl) scalars. In a matter-free spacetime, asymptotically Ψ_0, Ψ_2 and Ψ_4 represent ingoing radiation, the Coulomb field, and outgoing radiation, respectively. Mathematically, they are formed by contraction of the Weyl tensor with an arbitrary (complex) null tetrad $(l^a, n^a, m^a, \bar{m}^a)$. The tetrad itself is formed from combinations of also arbitrary, but orthonormal basis vectors. The Weyl tensor and associated tetrad vectors are contracted in the following way:

$$\Psi_0 = C_{abcd} l^a m^b l^c m^d \tag{4.1.4}$$

$$\Psi_1 = C_{abcd} l^a n^b l^c m^d \tag{4.1.5}$$

$$\Psi_2 = C_{abcd} l^a m^b \bar{m}^c n^d \tag{4.1.6}$$

$$\Psi_3 = C_{abcd} l^a n^b \bar{m}^c n^d \tag{4.1.7}$$

$$\Psi_4 = C_{abcd} n^a \bar{m}^b n^c \bar{m}^d \tag{4.1.8}$$

4.1. Accurate Extraction of Gravitational Waves: From the Weyl Tensor to the quasi-Kinnersley frame

The only constraints on the tetrad are that it must satisfy the relationships $l^a n_a = -1$ and $m^a \bar{m}_a = 1$, and have all other inner products vanishing.

Teukolsky uses this formalism to specify a null tetrad, which differs from the background Kinnersley tetrad [108] (in which the only nonvanishing Weyl scalar is Ψ_2), by leading order perturbations. The Kinnersley tetrad has $\{l^\alpha\}$ and $\{n^\alpha\}$, which are vectors along the two principal null directions (PNDs) [109].

At late times in a binary black hole merger, Teukolsky's perturbed Kinnersley tetrad is expected to have $\Psi_1 = \Psi_3 = 0$, which is the condition that characterizes a transverse frame. The Teukolsky formalism requires classification of a tetrad into a specific transverse frame. There are three possible transverse frames in any generic spacetime and choosing among them is nontrivial.

The transverse frame is used in a number of different analytical applications. For instance, it was used in the Lazarus project [110, 111]. This work constructs Cauchy data for the Teukolsky evolution [110] and then [111] rotates the resultant scalars into the quasi-Kinnersley frame, which allows for the extraction of information about the background Kerr solution and, in turn, the gravitational radiation. We are also interested in using the associated non-quasi-Kinnersley, but still transverse, frames to analyze and classify the spacetime very close to the black holes.

In 2001, the Lazarus project [110] showed that late-time evolutions of a BHB spacetime can be seen as a perturbed Kerr spacetime, and used this to extract information about gravitational radiation. In 2006, the second iteration of this project [111] sought to improve late-time gravitational wave extraction by rotation further of a spacetime into a “quasi-”Kinnersley frame (QKF), and then explored the late-time behavior of a merged BHB system, which should differ only perturbatively from Kerr. The QKF is transverse, which means the Weyl scalars $\Psi_1 = \Psi_3 = 0$, since they are nonphysical in a matter-free spacetime. This means that more physical information is encoded in the gravitational wave scalar Ψ_4 , the ingoing radiation scalar Ψ_0 and the Coulomb field Ψ_2 .

The QKF has since been explored in greater detail in a series of articles by Beetle, Bruni,

4.1. Accurate Extraction of Gravitational Waves: From the Weyl Tensor to the quasi-Kinnersley frame

Burko, and Nerozzi [37], [38], [39], and [40]. The first paper extends the analytic work done in [111] to the numerical regime, by outlining the limits of the quasi-Kinnersley frame, and establishing methodologies for incorporating it into full numerical relativistic simulations.

Beetle et. al. [37] propose the construction of a set of transverse null tetrads that are equivalent under spin-boost and exchange transformations. However, only one frame will be quasi-Kinnersley, and explicit rules for its identification are presented in the paper. We will use their definitions extensively in the coming sections.

The first paper defines the framework for [38] which performs analytic rotations of the five Weyl Scalars Ψ_0, \dots, Ψ_4 using Type I and Type II rotations, and solves for two constant, complex parameters \bar{a} and b necessary to rotate into a quasi-Kinnersley frame (the overbar signifies the complex conjugate of a). The Type I and Type II rotations of the Weyl scalars in the original frame lead to two equations for Ψ_1'' and Ψ_3'' which can be solved for \bar{a} and b (see Eqs. (4.2.18) and (4.2.23)) below. The double apostrophe delineates a doubly transformed scalar. The polynomial Ψ_1'' is sixth order in \bar{a} , but Nerozzi et. al. provide a method of reducing it to fourth order. When the spacetime is perturbatively close to Kerr, namely at late times (post-merger) or at distances far from the binary ($r \rightarrow \infty$), the quasi-Kinnersley frame approximates the background Kinnersley frame. The correct transverse frame is chosen by identifying the eigenvalues of the Weyl tensor (i.e. of Eq. (4.2.11) below) that approach Ψ_2 asymptotically.

The authors go on to discuss how to differentiate between the quasi-Kinnersley frame and other transverse frames, they introduce a new curvature scalar $\xi = \Psi_0\Psi_4$, and finally provide analytic rotations into the QKF of the Weyl scalars in algebraically special spacetimes. Using the Newman-Penrose formalism, the authors provide a fully analytic prescription for constructing the three transverse frames and identifying the one that is quasi-Kinnersley.

Finally, [39] goes further in-depth on the Beetle-Burko radiation scalar $\xi = \Psi_0\Psi_4$, the curvature invariant for general relativistic spacetimes. The scalar measures the total amount of radiation - ingoing, outgoing, and spurious, in a spacetime. The paper applies it to a number of initial data sets describing single black-hole spacetimes. The analysis is done entirely in the

4.2. Analytic Null Rotation into the quasi-Kinnersley Frame

quasi-Kinnersley frame, identified by demanding continuity in Ψ_2 and $\xi \rightarrow 0$ as $r \rightarrow \infty$.

We apply the techniques of [38] to analytic initial data of black hole pairs in order to rotate a particular spacetime into a transverse frame that is quasi-Kinnersley far from the binary, and generically transverse close to them. We will specifically study the strong-field regime of these spacetimes and classify interesting regions into different Petrov types. We will also present a new index \mathcal{D} that, when used in conjunction with the Baker-Campanelli speciality invariant $S = 27J^2/I^3$, will allow us to differentiate between Petrov Type D and II in the strong field regime where there is no a priori knowledge of the spacetime's classification².

This Chapter will proceed as follows: first, we will discuss the analytic method presented by [38] for rotation into the quasi-Kinnersley frame. Then, we will show that the quasi-Kinnersley frame can be used to classify the spacetime close to the black holes, and then discuss where this definition breaks down. Finally, we will construct the \mathcal{D} index and use it, in conjunction with S and a transverse frame (other than the QKF), to successfully classify the strong-field region of a set of black hole binaries that use Brill-Lindquist initial data.

4.2 Analytic Null Rotation into the quasi-Kinnersley Frame

To rotate into the quasi-Kinnersley frame, begin with any arbitrary frame \mathcal{F} characterized by a set of arbitrary null tetrad vectors $(l^a, n^a, m^a, \bar{m}^a)$. From the tetrad vectors, the Weyl scalars in \mathcal{F} can be built up via Eqs. (4.1.4-8). Then, one can write the eigenvalue (λ) equation associated with the Weyl Tensor (as in [109])

$$\frac{1}{2}C_{\alpha\beta\mu\nu}X^{\mu\nu} = \lambda X^{\alpha\beta} \tag{4.2.9}$$

where $C_{\alpha\beta\mu\nu}$ is the Weyl tensor and X is an associated eigenvector. This can be reduced to

$$Q_{ab}r^b = \lambda r_a. \tag{4.2.10}$$

²Full definitions of all six Petrov types can be found in Section 4.2.1

4.2. Analytic Null Rotation into the quasi-Kinnersley Frame

The complex, symmetric matrix Q_{ab} takes the form

$$Q_{ab} = \begin{bmatrix} \Psi_2 - \frac{\Psi_0 + \Psi_4}{2} & \frac{i(\Psi_4 - \Psi_0)}{2} & \Psi_1 - \Psi_3 \\ \frac{i(\Psi_4 - \Psi_0)}{2} & \Psi_2 + \frac{\Psi_0 + \Psi_4}{2} & i(\Psi_1 + \Psi_3) \\ \Psi_1 - \Psi_3 & i(\Psi_1 + \Psi_3) & -2\Psi_2 \end{bmatrix}. \quad (4.2.11)$$

Q_{ab} can also be written in terms of the electric and magnetic parts E_{ab} and B_{ab} of the Weyl Tensor

$$Q_{ab} = E_{ab} - iB_{ab}. \quad (4.2.12)$$

This definition is included to provide some physical motivation for matrix Q_{ab} , but we will use exclusively Eq. (4.2.11) since it is written in terms of the Weyl scalars. For more information on Eq. (4.2.12), or the definitions of E_{ab} and B_{ab} in terms of the Weyl tensor see [43] Chapter 8. In vector notation, this is

$$Q\mathbf{r} = \lambda\mathbf{r}. \quad (4.2.13)$$

The eigenvalues λ of Q are found by setting

$$\det|Q - \lambda I| = 0 \quad (4.2.14)$$

and solving for λ . For a general 4D spacetime, $Q \in \mathbb{C}^{3 \times 3}$, which means that there are 3 complex eigenvalues $\lambda_1, \lambda_2, \lambda_3$. The characteristic polynomial to solve is

$$\lambda^3 - I\lambda + 2J = 0 \quad (4.2.15)$$

where I and J are spacetime invariants which can be written in terms of the Weyl scalars as

$$I = \Psi_4\Psi_0 - 4\Psi_3\Psi_1 + 3\Psi_2^2 \quad (4.2.16)$$

and

$$J = \det \begin{vmatrix} \Psi_4 & \Psi_3 & \Psi_2 \\ \Psi_3 & \Psi_2 & \Psi_1 \\ \Psi_2 & \Psi_1 & \Psi_0 \end{vmatrix}. \quad (4.2.17)$$

All three eigenvalues of Q_{ab} are associated with their own individual transverse frame, in which the Weyl scalars adhere to $\Psi_1 = \Psi_3 = 0$. There will be one eigenvalue (λ_P) considered to be principal and specifically associated with the quasi-Kinnersley frame. Due to the complex nature of the roots of Eq. (4.2.15), choosing the principal eigenvalue is nuanced and nontrivial - continuity must be forced in the strong field region [37]. A discussion on methods of choosing λ_P will proceed in Section 4.3. Once the principal eigenvalue is chosen at every point in the 3D space, it is used to construct the rotation parameter \bar{a} . This is used to transform the Weyl scalars by a Type I rotation:

$$\Psi'_0 \rightarrow \Psi_0 \quad (4.2.18)$$

$$\Psi'_1 \rightarrow \Psi_1 + \bar{a}\Psi_0 \quad (4.2.19)$$

$$\Psi'_2 \rightarrow \Psi_2 + 2\bar{a}\Psi_1 + \bar{a}^2\Psi_0 \quad (4.2.20)$$

$$\Psi'_3 \rightarrow \Psi_3 + 3\bar{a}\Psi_2 + 3\bar{a}^2\Psi_1 + \bar{a}^3\Psi_0 \quad (4.2.21)$$

$$\Psi'_4 \rightarrow \Psi_4 + 4\bar{a}\Psi_3 + 6\bar{a}^2\Psi_2 + 4\bar{a}^3\Psi_1 + \bar{a}^4\Psi_0. \quad (4.2.22)$$

Then, rotation parameter b is constructed from \bar{a} , and a Type II rotation is performed via:

$$\Psi'_0 \rightarrow \Psi_0 + 4b\Psi_1 + 6b^2\Psi_2 + 4b^3\Psi_3 + b^4\Psi_4 \quad (4.2.23)$$

$$\Psi'_1 \rightarrow \Psi_1 + 3b\Psi_2 + 3b^2\Psi_3 + b^3\Psi_4 \quad (4.2.24)$$

$$\Psi'_2 \rightarrow \Psi_2 + 2b\Psi_3 + b^2\Psi_4 \quad (4.2.25)$$

$$\Psi'_3 \rightarrow \Psi_3 + b\Psi_4 \quad (4.2.26)$$

$$\Psi'_4 \rightarrow \Psi_4. \quad (4.2.27)$$

4.2. Analytic Null Rotation into the quasi-Kinnersley Frame

Equivalently the null vectors, l^a, n^a, m^a , can be transformed using \bar{a} and b , and then can be used to reconstruct the quasi-Kinnersley Weyl Scalars Ψ_a^{QK} by contraction with the Weyl tensor. There are equivalent rotations in terms of the tetrad vectors; a Type I rotation:

$$l' \rightarrow l \tag{4.2.28}$$

$$m' \rightarrow m + al \tag{4.2.29}$$

$$\bar{m}' \rightarrow \bar{m} + \bar{a}l \tag{4.2.30}$$

$$n' \rightarrow n + \bar{a}m + a\bar{m} + a\bar{a}l \tag{4.2.31}$$

and a Type II rotation:

$$n' \rightarrow n \tag{4.2.32}$$

$$m' \rightarrow m + bn \tag{4.2.33}$$

$$\bar{m}' \rightarrow \bar{m} + \bar{b}n \tag{4.2.34}$$

$$l' \rightarrow l + \bar{b}m + b\bar{m} + b\bar{b}l. \tag{4.2.35}$$

Both rotation methods require the calculation of complex rotation parameters a and b . An in depth discussion of the rotation will be discussed in Section 4.4.

4.2.1 Petrov Types

We would like to be able to use the transverse-frame Weyl scalars to differentiate between Petrov types of the spacetime. These classifiers provide insight into the dynamics of the spacetime and describe physical properties of the system. There are six Petrov types [112]

1. Petrov Type I: A spacetime in which a tetrad can be chosen so that only Ψ_1 , Ψ_2 , and Ψ_3 are different from 0. There are 4 independent principal null directions (PNDs).
2. Petrov Type II: A spacetime in which a tetrad can be chosen so that only Ψ_2 and Ψ_3 are different from 0. This corresponds to a Coulombic spacetime. There are two coincident PNDs.

3. Petrov Type III: A spacetime in which a tetrad can be chosen so that all scalars except Ψ_3 vanish. There are three coincident PNDs.
4. Petrov Type N: A spacetime in which a tetrad can be chosen so that all scalars except Ψ_4 vanish. There are four coincident PNDs.
5. Petrov Type D: A spacetime in which a tetrad can be chosen to rotate the Weyl scalars so that only Ψ_2 is nonzero. Kerr or Schwarzschild correspond to Type D spacetimes. The PNDs agree in pairs.
6. Petrov Type O: Conformally flat spacetime; all Weyl scalars vanish.

A detailed explanation of the Petrov types can be found in [43] or [113].

The remainder of this Chapter is organized as follows: Section 4.3 will discuss the choice of principal eigenvalue λ_P , then Section 4.4 will discuss how to find rotation parameters \bar{a} and b to rotate general Weyl scalars into a quasi-Kinnersley frame, and Section 4.6 will discuss the results of performing this rotation at each point on a binary with Brill-Lindquist initial data, which is head on collision initial data for two black holes (beginning on the z -axis). Section 4.5 derives a new index \mathcal{D} that differentiates locally between Petrov Types II and D, and applies it to the strong field region of two Brill-Lindquist black hole systems. For the remainder of this Chapter, non-QK Weyl scalars will be written as Ψ_a , and Weyl scalars in the quasi-Kinnersley frame will be written as Ψ_a^{QK} .

4.3 Finding the Principal Eigenvalue

Each eigenvalue of Q_{ab} in Eq. (4.2.11) corresponds to a reference frame from which the Weyl scalars Ψ_a can be computed. One can freely rotate among frames using constants \bar{a} and b , and all such frames constructed using the eigenvalues λ are transverse. One specific frame, the quasi-Kinnersley frame, is associated with an eigenvalue λ_P of Q_{ab} that we will consider to be principal. The identification of the principal eigenvalue is trivial in the wavezone - it needs only to be twice the magnitude of each of the other two eigenvalues (see below [38]). One would like

this principal eigenvalue to be at least C^1 over the whole spacetime, but the invariants used to construct the eigenvalues are complex, and the eigenvalues themselves contain complex cube roots. These roots introduce branch cuts in the eigenvalues unless the principal is *forced* to be continuous at each point in space in either real or imaginary part. This condition requires that λ_P move out of the quasi-Kinnersley frame and into an alternate transverse frame as $r \rightarrow 0$.

Notice that since (4.2.15) is only a cubic equation, there exists a fully analytic solution for the three eigenvalues of Q_{ab} [38]

$$\lambda_1 = -\left(P + \frac{I}{3P}\right) \tag{4.3.36}$$

$$\lambda_2 = -\left(e^{\frac{4\pi i}{3}}P + e^{\frac{2\pi i}{3}}\frac{I}{3P}\right) \tag{4.3.37}$$

$$\lambda_3 = -\left(e^{\frac{2\pi i}{3}}P + e^{\frac{4\pi i}{3}}\frac{I}{3P}\right) \tag{4.3.38}$$

$$\tag{4.3.39}$$

where

$$P = \left(J + \sqrt{J^2 - \left(\frac{I}{3}\right)^3}\right)^{\frac{1}{3}}. \tag{4.3.40}$$

We are now left with the task of choosing which eigenvalue is quasi-Kinnersley at every point. This will correspond with λ_P asymptotically, but it is not necessarily true that $\lambda_P = \lambda_{\text{QK}}$ in the strong-field region. We have already discussed how, asymptotically, λ_P should be twice the magnitude of either of the other eigenvalues [38, 37]. Explicitly, it can be said that as $r \rightarrow \infty$, $\lambda_P = \max_k |\lambda_k|$. However, in the strong-field region, we will show that this definition breaks down. Figure 4.1 shows these eigenvalues for a system that uses analytic Brill-Lindquist initial data, which describes two black holes in a head-on collision from rest, as in Figure 4.2. This system in particular uses two equal mass, nonspinning black holes on the z -axis at $z = \pm 5$. The set up is shown in Figure 4.2. This system was chosen because neither the invariants nor the eigenvalues nor the Weyl scalars have any imaginary components - all are purely real since $P = \frac{I}{3P}$, but this is not the case in general. Figure 4.3 shows the corresponding speciality invariant $S = \frac{27J^2}{I^3}$ on the equatorial plane $\theta = \frac{\pi}{2}$; when $S = 1$, the spacetime is either Petrov

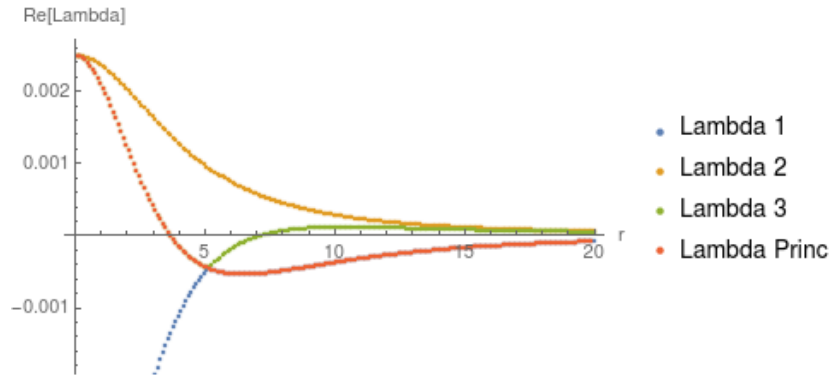


Figure 4.1: Eigenvalues for a BBH system with Brill-Lindquist initial data for $q = 1$ on the equatorial plane $\theta = \pi/2$. The black holes are at $z = \pm 5$. At approximately $r = 5.2$, the principal eigenvalue must be switched from λ_1 so that it remains smooth.

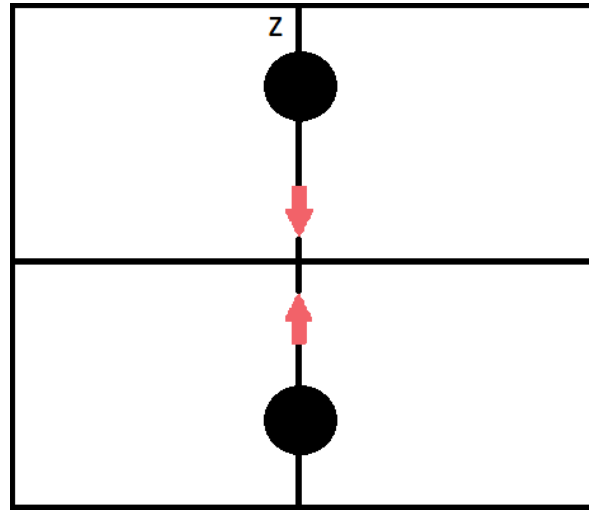


Figure 4.2: The grid set up for our initial data simulation of two equal-mass black holes in a head-on collision.

Type D or Type II.

There are several points of interest in Figures 4.1 and 4.3. We will first discuss the regions where in Fig. 4.3 $S \rightarrow 1$. Notice in Figure 4.1 that as $r \rightarrow \infty$, $\lambda_P = \max_k |\lambda_k| = \lambda_1$. At $r \approx 5.2$, the principal eigenvalue switches branches to maintain continuity. Next, consider the

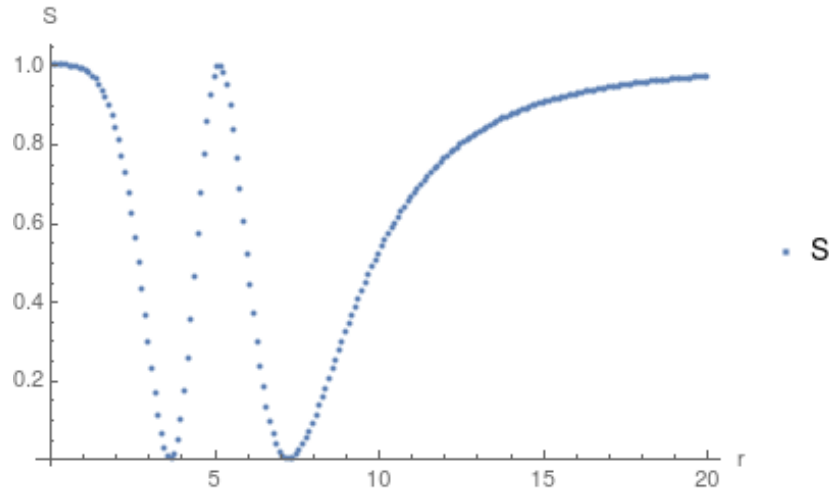


Figure 4.3: S invariant for the $q = 1$, $d = 10$ BL initial data system. At approximately $r = 5.2$, $S = 1$. This corresponds to the location where the principal eigenvalue must be switched from λ_1 .

location where $S = 1$ at $r \approx 5.2m$ between the two points where $S = 0$.

$$S = 1 = \frac{27J^2}{I^3} \quad (4.3.41)$$

$$\implies I = 3J^{\frac{2}{3}} \quad (4.3.42)$$

then, the characteristic polynomial becomes

$$\lambda^3 - 3J^{\frac{2}{3}}\lambda + 2J = 0 \quad (4.3.43)$$

with

$$P = \left(J + \sqrt{J^2 - \left(\frac{3J^{\frac{2}{3}}}{3} \right)^3} \right)^{\frac{1}{3}} \quad (4.3.44)$$

$$= J^{\frac{1}{3}}. \quad (4.3.45)$$

which means the eigenvalues become

$$\lambda_1 = -2J^{\frac{1}{3}}, \quad \lambda_2 = J^{\frac{1}{3}}, \quad \lambda_3 = J^{\frac{1}{3}}$$

Here it is necessary to switch branches to maintain continuity, since, at this point a cusp exists in two of the eigenvalues. This means that λ_P moves out of the transverse frame associated with λ_1 and into the transverse frame associated with λ_3 . We use λ_3 as principal in this region because it allows us to define the QKF continuously over the whole spacetime, even into the strong field regime. Another interesting feature *may* occur at all points in Fig. 4.3 where

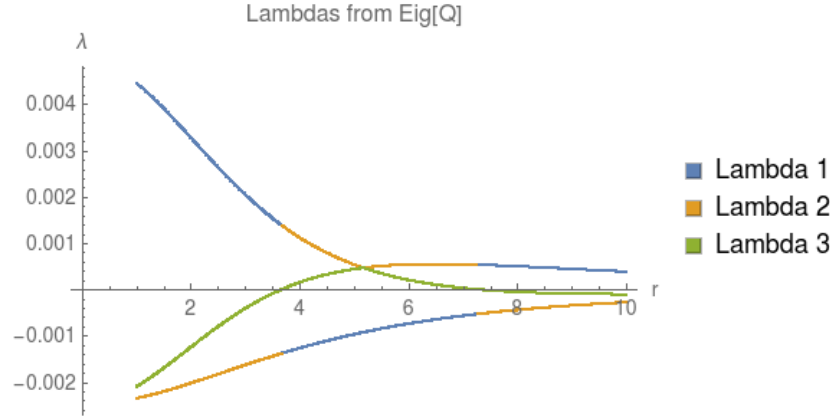


Figure 4.4: Eigenvalues for a BBH system with Brill-Lindquist initial data for $q = 1$ at $\theta = \pi/2$, but with forced branch cuts when $J = 0$. The black holes are at $z = \pm 5$. Before determining the principal branch, here it would be necessary to force continuity in the eigenvalues except at the point $r \approx 5.2$.

$S \rightarrow 0$, since by definition it must also be true that $J \rightarrow 0$. These r values correspond with locations where $\lambda_3 = 0$, $\lambda_2, \lambda_1 = \pm\sqrt{I}$. At these points, J changes sign, and between them, a relabeling of which eigenvalue is which might need to occur in order to maintain continuity. This is shown in Figure 4.4.

However, the branch cuts shown are purely a numerical issue, and completely *compiler dependent*. An analytic way of interpreting this begins by writing P as

$$P = (-1)^{1/3} \left[-J - \sqrt{J^2 - \left(\frac{I}{3}\right)^3} \right]^{1/3} \quad (4.3.46)$$

and (-1) has 3-roots of unity:

$$(-1)^{1/3} = \begin{cases} -1 \\ -e^{\frac{2\pi i}{3}} \\ -e^{\frac{4\pi i}{3}} \end{cases} \quad (4.3.47)$$

Choosing the first branch of (4.3.47) means $P = \left[J + \sqrt{J^2 - \left(\frac{I}{3}\right)^3} \right]^{1/3}$, and no relabeling occurs. Now, assume P traverses a circle once, meaning J changes sign one time. Then, P picks up a factor of $e^{2\pi i}$ and

$$P = -e^{\frac{2\pi i}{3}} \left[-J - \sqrt{J^2 - \left(\frac{I}{3}\right)^3} \right]^{1/3} \quad (4.3.48)$$

which relabels

$$\lambda'_3 \rightarrow \lambda_1, \quad \lambda'_2 \rightarrow \lambda_3, \quad \lambda'_1 \rightarrow \lambda_2.$$

The primes indicate a relabeling of the eigenvalues. Then, assume P traverses a circle a second time, and J changes sign again. Then, P picks up another factor of $e^{2\pi i}$ and

$$P = -e^{\frac{-2\pi i}{3}} \left[-J - \sqrt{J^2 - \left(\frac{I}{3}\right)^3} \right]^{1/3} \quad (4.3.49)$$

which relabels

$$\lambda''_3 \rightarrow \lambda_2, \quad \lambda''_2 \rightarrow \lambda_1, \quad \lambda''_1 \rightarrow \lambda_3.$$

Another flip of sign in J rotates the eigenvalues to their original labeling. In practice, the computer handles all of this behind the scenes, but the relabeling is dependent on the language chosen. For all of this work, unless otherwise specified, we use Mathematica which natively handles branch cuts by choosing a continuous branch when it can. We can explicitly force these cuts to appear, as in Figure 4.4, to emphasize that they do in fact occur when $J = 0$. Languages like C do not natively force continuity when doing complex calculations, and therefore these branch cuts will need to be taken into account in numerical simulations. These are not an

issue with the process of rotating into the quasi-Kinnersley frame, but in fact, come from the practical numerical computations themselves.

4.4 Calculation of Rotation Parameters \bar{a} and b

Since, in Section 4.3, we outlined an analytic methodology of choosing λ_P at each point in space for a particular time-slice, we are now ready to rotate the Weyl scalars into a QK frame. This is done by performing a Type I then a Type II rotation on the scalars using rotation parameters \bar{a} and b . The computations in this section are analogous to performing a Type II and then a Type I rotation (Eqs. (4.2.28-35)). To do this, [38] suggests setting up two equations for the two unknowns by rotating both Ψ_1 and Ψ_3 into a transverse frame as follows

$$\Psi_3 + 3\bar{a}\Psi_2 + 3\bar{a}^2\Psi_1 + \bar{a}^3\Psi_0 \tag{4.4.50}$$

$$+ b(\Psi_4 + 4\bar{a}\Psi_3 + 6\bar{a}^2\Psi_2 + 4\bar{a}^3\Psi_1 + \bar{a}^4\Psi_0) = 0 \tag{4.4.51}$$

$$\Psi_1 + \bar{a}\Psi_0 + 3b(\Psi_2 + 2\bar{a}\Psi_1 + \bar{a}^2\Psi_0) \tag{4.4.52}$$

$$+ 3b^2(\Psi_3 + 3\bar{a}\Psi_2 + 3\bar{a}^2\Psi_1 + \bar{a}^3\Psi_0) \tag{4.4.53}$$

$$+ b^3(\Psi_4 + 4\bar{a}\Psi_3 + 6\bar{a}^2\Psi_2 + 4\bar{a}^3\Psi_1 + \bar{a}^4\Psi_0) = 0. \tag{4.4.54}$$

Then b can be written as a function of \bar{a} as follows

$$b = -\frac{\Psi_3 + 3\bar{a}\Psi_2 + 3\bar{a}^2\Psi_1 + \bar{a}^3\Psi_0}{\Psi_4 + 4\bar{a}\Psi_3 + 6\bar{a}^2\Psi_2 + 4\bar{a}^3\Psi_1 + \bar{a}^4\Psi_0} \tag{4.4.55}$$

and all that is necessary to do is to find \bar{a} . Equation (4.4.50) provides a sixth order polynomial to be solved for \bar{a}

$$A1\bar{a}^6 + A2\bar{a}^5 + A3\bar{a}^4 + A4\bar{a}^3 + A5\bar{a}^2 + A6\bar{a} + A7 = 0 \tag{4.4.56}$$

with coefficients

$$A1 = -\Psi_3\Psi_0^2 - 2\Psi_1^3 + 3\Psi_2\Psi_1\Psi_0 \quad (4.4.57)$$

$$A2 = -2\Psi_3\Psi_1\Psi_0 - \Psi_0^2\Psi_4 + 9\Psi_2^2\Psi_0 - 6\Psi_2\Psi_1^2 \quad (4.4.58)$$

$$A3 = -5\Psi_1\Psi_4\Psi_0 - 10\Psi_3\Psi_1^2 + 15\Psi_3\Psi_2\Psi_0 \quad (4.4.59)$$

$$A4 = -10\Psi_4\Psi_1^2 + 10\Psi_3^2\Psi_0 \quad (4.4.60)$$

$$A5 = 5\Psi_3\Psi_0\Psi_4 + 10\Psi_1\Psi_3^2 - 15\Psi_1\Psi_2\Psi_4 \quad (4.4.61)$$

$$A6 = 2\Psi_3\Psi_1\Psi_4 + \Psi_4^2\Psi_0 - 9\Psi_2^2\Psi_4 + 6\Psi_2\Psi_3^2 \quad (4.4.62)$$

$$A7 = \Psi_1\Psi_4^2 + 2\Psi_3^3 - 3\Psi_2\Psi_3\Psi_4 \quad (4.4.63)$$

which can only be solved using numerical methods. Therefore, it is necessary to find which root, of the six, is associated with the quasi-Kinnersley frame. Due to the computational complexity of solving a sixth-order polynomial, Nerozzi et. al. reduce the polynomial order of Eq. (4.4.56) to fourth order.

4.4.1 Reduction to Fourth Order

The authors of [38] begin by rotating an arbitrary tetrad so that n (or l) is a principal null direction and Ψ_4 (Ψ_0) vanishes. We will outline their method here, as its result will be useful to us later on. Begin by performing a Type I transformation on Ψ_4 , and setting it to zero.

$$b^4\Psi_4 + 4b^3\Psi_3 + 6b^2\Psi_2 + 4b\Psi_1 + \Psi_0 = 0. \quad (4.4.64)$$

This can be reduced to a depressed quartic by making the substitution $\hat{z} = \Psi_4 b + \Psi_3$:

$$\hat{z}^4 + 6\hat{H}\hat{z}^2 + 4\hat{G}\hat{z} + \hat{K} = 0. \quad (4.4.65)$$

for

$$\hat{H} = \Psi_4\Psi_2 - \Psi_3^2 \quad (4.4.66)$$

$$\hat{G} = \Psi_4^2\Psi_1 - 3\Psi_4\Psi_3\Psi_2 + 2\Psi_3^3 \quad (4.4.67)$$

$$\hat{K} = \Psi_4^2I - 3\hat{H}^2 \quad (4.4.68)$$

where the variables

$$\hat{\alpha}^2 = 2\Psi_4\lambda_1 - 4\hat{H} \quad (4.4.69)$$

$$\hat{\beta}^2 = 2\Psi_4\lambda_2 - 4\hat{H} \quad (4.4.70)$$

$$\hat{\gamma}^2 = 2\Psi_4\lambda_3 - 4\hat{H} \quad (4.4.71)$$

can be combined so that

$$\hat{\alpha}\hat{\beta}\hat{\gamma} = 4\hat{G}. \quad (4.4.72)$$

Note that unhatted variables are obtained (equivalent to performing an n null vector rotation) by substituting $\Psi_4 \leftrightarrow \Psi_0$ and $\Psi_1 \leftrightarrow \Psi_3$.

Rotating \hat{G} under a Type I transformation will reproduce the sixth order equation for \bar{a} in Eq. (4.4.56). This means that the polynomial can be written in terms of $\hat{\alpha}$, $\hat{\beta}$ and $\hat{\gamma}$.

$$\frac{\hat{\alpha}^2\hat{\beta}^2\hat{\gamma}^2}{16} = \hat{G}^2 \quad (4.4.73)$$

which increases the order of the polynomial from 6 to 12. However, it is now written as the product of three quartic equations. One of these equations, $\hat{\alpha}^2$, is associated with the principal eigenvalue λ_P , and thus the quasi-Kinnersley frame.

Under a Type I rotation, $\hat{\alpha}^2$ has the form

$$\hat{\alpha}^2 = B1\bar{a}^4 + B2\bar{a}^3 + B3\bar{a}^2 + B4\bar{a} + B5 \quad (4.4.74)$$

with coefficients

$$B1 = \lambda_1 \Psi_0 + 2\Psi_1^2 - 2\Psi_0\Psi_2 \quad (4.4.75)$$

$$B2 = 4\lambda_1 \Psi_1 + \Psi_1\Psi_2 - \Psi_0\Psi_3 \quad (4.4.76)$$

$$B3 = 6\lambda_1 \Psi_2 + 6\Psi_2^2 - 4\Psi_1\Psi_3 - 2\Psi_0\Psi_4 \quad (4.4.77)$$

$$B4 = \lambda_1 \Psi_3 + \Psi_2\Psi_3 - \Psi_1\Psi_4 \quad (4.4.78)$$

$$B5 = 2\Psi_3^2 + \Psi_4(\lambda_1 - 2\Psi_2) \quad (4.4.79)$$

Instead of using this quartic directly, the authors go on to use a reduced variable

$$z = \Psi_0\bar{a} + \Psi_1 \quad (4.4.80)$$

to obtain a quartic

$$Q1z^4 + Q2z^3 + Q3z^2 + Q4z + Q5 = 0 \quad (4.4.81)$$

whose coefficients are

$$Q1 = 1 \quad (4.4.82)$$

$$Q2 = \frac{-4G}{\lambda_1\Psi_0 - 2H} \quad (4.4.83)$$

$$Q3 = \frac{6\Psi_0\lambda_1 H + 6H^3 - 2K}{\lambda_1\Psi_0 - 2H} \quad (4.4.84)$$

$$Q4 = \frac{4G(H + \Psi_0\lambda_1)}{\lambda_1\Psi_0 - 2H} \quad (4.4.85)$$

$$Q5 = \frac{-2KH + 2G^2 + \Psi_0\lambda_1 K}{\lambda_1\Psi_0 - 2H} \quad (4.4.86)$$

where

$$G = \Psi_0^2\Psi_3 - 3\Psi_0\Psi_1\Psi_2 + 2\Psi_1^3 \quad (4.4.87)$$

$$H = \Psi_0\Psi_2 - \Psi_1^2 \quad (4.4.88)$$

$$K = \Psi_0^2 I - 3H^2. \quad (4.4.89)$$

This means the sixth-order equation has been successfully reduced to fourth order. Solving the depressed quartic equation (4.4.65) can be done analytically or numerically. In the following sections, the solution is found via Mathematica's built in *Solve* function. While testing, we also employed an analytic method to reduce the quartic to a cubic equation, solved for the roots of the new cubic, and used them to construct the roots of the quartic. This is a standard analytic technique to find quartic equation solutions. Once the roots of the quartic are found, they are used in conjunction with Eqs. (4.2.18) (4.2.23) to rotate the Weyl scalars into the quasi-Kinnerlsey frame.

In the following sections, we will employ both the quasi-Kinnerlsey frame, as well as the other transverse frames corresponding to the roots of β^2 and γ^2 or, equivalently and more simply, the eigenvalues not associated with the QK frame, in order to classify the strong-field region of an analytic spacetime.

4.5 Analytic Classification of the Spacetime

The goal of this project is twofold: first, we would like to be able to use the quasi-Kinnerlsey frame to more accurately extract gravitational waves from a binary black hole system. Second, we would like to be able to locally classify an arbitrary black hole spacetime into its approximate Petrov Type. The speciality invariant S we studied in the earlier part of this chapter was introduced as a way to measure distortions from a Kerr (Petrov Type D) spacetime [114]. However, the invariant does not differentiate between Type D and Type II. For $r \rightarrow \infty$ it is known that typical gravitational wave spacetimes are Type D, but in the strong field region, we have seen that there are regions of algebraic speciality. Here, we introduce an index \mathcal{D} which, if used in conjunction with S , can differentiate between a Type II and a Type D spacetime at points of algebraic speciality.

$$\mathcal{D} = \sqrt{\frac{12}{I}} \left(\Psi_2 - \frac{\Psi_3^2}{\Psi_4} \right) \quad (4.5.90)$$

To derive \mathcal{D} , return to Eqs. (4.4.87-9). The Petrov types can be characterized in terms of these scalars as shown in Table 4.1. The \mathcal{D} index can be derived from the condition in row 2

Table 4.1: Special Petrov types in terms of G , H and K .

| Petrov type | Characteristics |
|-------------|---------------------------------|
| II | $G \neq 0, K - 9H^2 \neq 0$ |
| D | $G = 0, K - 9H^2 = 0, K \neq 0$ |
| III, N, O | $J = 0, I = 0$ |
| N | $G = 0, H = 0$ |
| O | $G = 0, K = 0, H = 0$ |

of Table 4.1, under the transformation $\Psi_0 \leftrightarrow \Psi_4$ and $\Psi_1 \leftrightarrow \Psi_3$;

$$K - 9H^2 = 0 \tag{4.5.91}$$

$$\Psi_4^2 I - 12H^2 = 0 \tag{4.5.92}$$

$$1 - 12H^2/(\Psi_4^2 I) = 1 - 12/I(\Psi_2 - \Psi_3^2/\Psi_4) = 0 \tag{4.5.93}$$

$$1 - \mathcal{D}^2 = 0. \tag{4.5.94}$$

This means that when $\mathcal{D} \rightarrow \pm 1$ in an arbitrary frame that is not QK, the spacetime heads to either Petrov type D and this index will allow us to differentiate between Petrov types II and D for a region of algebraic speciality.

In a quasi-Kinnersley frame, $\mathcal{D}_{QK} = \pm 2$ in a Petrov Type D spacetime. This can be proven as follows

$$\mathcal{D}_{QK} = \sqrt{\frac{12}{I}} \left(\Psi_2'' - \frac{\Psi_3''^2}{\Psi_4''} \right) \tag{4.5.95}$$

$$= \sqrt{\frac{12}{3\Psi_2''^2 - 4\Psi_3''\Psi_1'' + \Psi_4''\Psi_0''}} \left(\Psi_2'' - \frac{\Psi_3''^2}{\Psi_4''} \right) \tag{4.5.96}$$

$$= \sqrt{\frac{12}{3\Psi_2''^2}} (\Psi_2'') \tag{4.5.97}$$

$$= \sqrt{\frac{12}{3}} = \pm 2, \tag{4.5.98}$$

whereas for an arbitrary transverse frame that is not quasi-Kinnersley, $\mathcal{D} = \pm 1$ if a spacetime is Type D.

For a spacetime in which $\Psi_4 = 0$, the equivalent version of the \mathcal{D} index, with $\Psi_0 \neq 0$

can be obtained under the transformations $\Psi_1 \leftrightarrow \Psi_3$ and $\Psi_0 \leftrightarrow \Psi_4$. A symmetrized version can also be obtained by adding the (averaged) corresponding H, G, K with $\Psi_4 \rightarrow \Psi_0$ and $\Psi_3 \rightarrow \Psi_1$ terms. Other expressions can also be obtained by including multiples of G since it is vanishing for a type D spacetime. Those expressions will be equivalent once we choose a transverse frame. Note that while \mathcal{D} is invariant under Type II and Type III (boost) tetrad rotations, it is frame dependent.

4.6 Analytic Results for Brill-Lindquist Initial Data

In order to (1) verify that we are able to successfully rotate a spacetime into a quasi-Kinnersley frame and then (2) classify the strong-field region into different Petrov Types, we have constructed a series of initial data tests on analytic systems of binary black hole pairs. The first tests we performed of this rotation use analytic Brill-Lindquist initial data on an equal-mass binary system. The black holes are located at $z = \pm 2.5, \dots, 7.5$, and start from rest, so have separations $d = 5m, \dots, 15m$ in increments of $1m$. The system we will look at in-depth has $d = 10m$ and $z = \pm 5$.

We also studied a system with mass ratio $q = \frac{1}{3}$. In this system, the large black hole is located at $z = 1.75$ and the small black hole is at $z = -5.25$ with masses $m_1 = 0.75$ and $m_2 = 0.25$ respectively. We will begin by showing in-depth results of the equal mass binary and then will move on to the unequal mass case. For this study, we will use the non-QK frame for classification. The lapse and shift we use are $-N^2 = -(1 - 2m/r)$ and $\beta^i = 0$. The explicit

values of the Weyl scalars in spherical polar coordinates are

$$\Psi_0 = \frac{1}{r^2 N^4 \psi^6} \left\{ -\psi^2 N_{,\theta}^2 + N\psi [-2N_{,\theta} \psi_{,\theta} + \psi(-\cot\theta N_{,\theta} + N_{,\theta\theta})] + N^2 [3\psi_{,\theta}^2 + \psi(\cot\theta \psi_{,\theta} - \psi_{,\theta\theta})] \right\}, \quad (4.6.99)$$

$$\begin{aligned} \Psi_1 = & \frac{1}{2\sqrt{2}r^2 N^2 \psi^6} \left\{ -r\psi^2 N_{,\theta} N_{,r} + N\psi [2r(\psi_{,\theta} N_{,r} + 2N_{,\theta} \psi_{,r}) + \psi(2N_{,\theta} - rN_{,r\theta})] \right. \\ & \left. - 2N^2 [3r\psi_{,\theta} \psi_{,r} + \psi(\psi_{,\theta} - r\psi_{,r\theta})] \right\}, \end{aligned} \quad (4.6.100)$$

$$\begin{aligned} \Psi_2 = & \frac{1}{6r^2 N^2 \psi^6} \left\{ -2\psi^2 N_{,\theta}^2 + 4N\psi N_{,\theta} \psi_{,\theta} + N^2 [-3\psi_{,\theta}^2 + \psi(\cot\theta \psi_{,\theta} + \psi_{,\theta\theta}) + \psi^2(-1 + r^2 N_{,r}^2)] \right. \\ & \left. + rN^3 \psi [-6rN_{,r} \psi_{,r} + \psi(-2N_{,r} + rN_{,rr})] + N^4 [\psi^2 + 6r^2 \psi_{,r}^2 + 2r\psi(\psi_{,r} - r\psi_{,rr})] \right\} \end{aligned} \quad (4.6.101)$$

$$\begin{aligned} \Psi_3 = & \frac{1}{4\sqrt{2}r^2 \psi^6} \left\{ r\psi^2 N_{,\theta} N_{,r} + N\psi [-2r(\psi_{,\theta} N_{,r} + 2N_{,\theta} \psi_{,r}) + \psi(-2N_{,\theta} + rN_{,r\theta})] \right. \\ & \left. + 2N^2 [3r\psi_{,\theta} \psi_{,r} + \psi(\psi_{,\theta} - r\psi_{,r\theta})] \right\}, \end{aligned} \quad (4.6.102)$$

$$\Psi_4 = \frac{1}{4r^2 \psi^6} \left\{ -\psi^2 N_{,\theta}^2 + N\psi [-2N_{,\theta} \psi_{,\theta} + \psi(-\cot\theta N_{,\theta} + N_{,\theta\theta})] + N^2 [3\psi_{,\theta}^2 + \psi(\cot\theta \psi_{,\theta} - \psi_{,\theta\theta})] \right\}, \quad (4.6.103)$$

with conformal factor ψ . They are constructed using the numerical tetrad [43]

$$l^\mu = \frac{1}{\sqrt{2}}(e_0^\mu - e_1^\mu) \quad (4.6.104)$$

$$n^\mu = \frac{1}{\sqrt{2}}(e_0^\mu + e_1^\mu) \quad (4.6.105)$$

$$m^\mu = \frac{1}{\sqrt{2}}(e_2^\mu - ie_3^\mu) \quad (4.6.106)$$

$$\bar{m}^\mu = \frac{1}{\sqrt{2}}(e_2^\mu + ie_3^\mu), \quad (4.6.107)$$

where e_i^μ are orthonormal basis vectors, and then rotated into a transverse frame using the process in Sections 4.2-4.4.

4.6.0.1 Equal Mass $d = 10$ case.

Figure 4.5 shows all three choices for the eigenvalues λ as well as highlights the principal eigenvalue λ_P (in red) that is associated with the quasi-Kinnersley frame. These correspond to analytic initial data for a Brill-Lindquist binary with separation $d = 10m$ and equal masses versus r , and are shown on the symmetry plane $\theta = \pi/2$. Notice first that at $r = 5m$ (which we

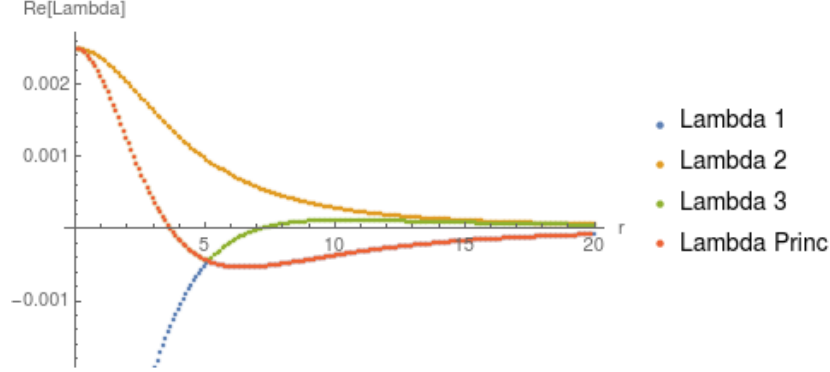


Figure 4.5: Eigenvalues for a BBH system with Brill-Lindquist initial data for $q = 1$ on the symmetry plane $\theta = \pi/2$. The black holes are at $r = \pm 5$ on the z -axis. At approximately $r = 5m$, the principal eigenvalue must be switched from λ_1 so that it remains smooth.

will henceforth refer to as $r = r_{Ring}$) λ_P changes branches from λ_1 to λ_3 . This is done because we can, in fact, demand continuity from our principal eigenvalue [37]. The eigenvalue branch that is quasi-Kinnersley only need be switched when $r = r_{Ring}$, not necessarily whenever $S = 1$, which is true not only at $r = r_{Ring}$, but also asymptotically and between the black holes.

Notice that one could choose λ_2 to be principal everywhere since it is continuous, use this to do the rotation, and transform the Weyl scalars into a transverse frame. Since this eigenvalue does not satisfy $\lambda_P = \max_k |\lambda_k|$ as $r \rightarrow \infty$, the frame that uses λ_2 as principal is transverse, but is not quasi-Kinnersley and therefore asymptotically may not lead to tetrad vectors that are near Kinnersley. It will, however, be of interest to us later on to use these alternative transverse frames to classify the spacetime into different Petrov Types.

When we look just off the symmetry plane (for example, if $\theta = \frac{8\pi}{15}$), the principal eigenvalue remains $\lambda_P = \lambda_1$ for the whole spacetime, which means that the surface $r = r_{Ring}$ is one

dimensional in shape. Figure 4.6 shows this case, with the principal branch in red. We can clearly see that all three eigenvalues, and thus transverse frames, are continuous even in the strong-field region. This means that the points at $(r_{Ring}, \theta_{Ring}) = (r_{Ring}, \pi/2)$ are the

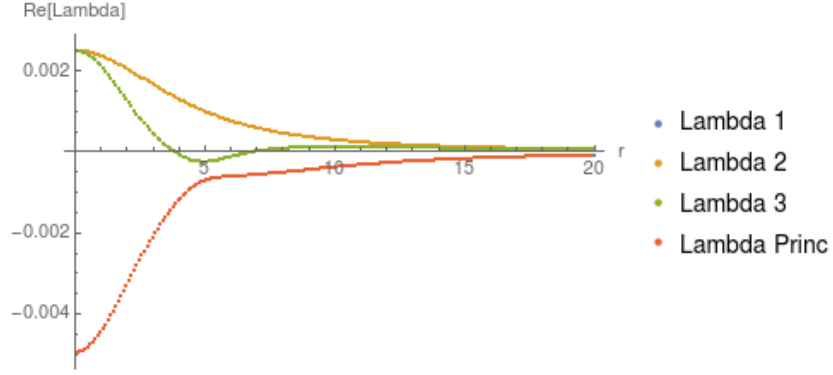


Figure 4.6: Eigenvalues for a BBH system with Brill-Lindquist initial data for $q = 1$ at $\theta = \frac{8\pi}{15}$. The black holes are at $z = \pm 5$. On the whole spacetime, the principal eigenvalue remains λ_1 .

only locations where the eigenvalues have a cusp when $S = 1$. They form a one dimensional ring of points, rather than a three dimensional doughnut shape. This will be studied more in Section 4.6.1.

Moving back to the symmetry plane $\theta = \pi/2$, we have found a principal eigenvalue that is continuous throughout the whole spacetime and can now insert it into Eqs. (4.4.82) to construct the quartic equation (4.4.74). Solving any quartic gives at most four roots a_1, a_2, a_3, a_4 . Of these four solutions, only two are associated with the quasi-Kinnersley frame (two instead of one due to $l \leftrightarrow n$ degeneracy).

To determine which two roots we want, we will introduce the radiation scalar $\xi^{QK} = \Psi_0^{QK} \Psi_4^{QK}$ in the quasi-Kinnersley frame which is used to classify the spacetime in [38] in the far-field region. However, no classification criteria beyond continuity are provided for the strong-field region. Since in the QK frame, both $\Psi_4^{QK}, \Psi_0^{QK} \rightarrow 0$ when $S \rightarrow 1$, it must be true that $\xi \rightarrow 0$ as well. This will be used to help us choose the correct root from a_i .

Figure 4.7 shows $\log|\xi|$ on the equatorial plane for all four transverse frames associated with roots a_1, a_2, a_3, a_4 . The values of ξ for roots a_1 and a_4 and roots a_2 and a_3 (respectively) coincide. Since ξ_2 and ξ_3 head to 0 as $r \rightarrow \infty$ and are both continuous, the roots associated

with the quasi-Kinnersley frame are a_2 and a_3 . Interestingly, at $r = r_{Ring}$, which is where we switch which eigenvalue branch is chosen as principal, ξ_1 and ξ_4 coincide with ξ_2 and ξ_3 (hence the red point at $r = r_{Ring}$ located at about $\xi = 10^{-15}$ on the green curve). This supports the claim that at $r = r_{Ring}$ only one transverse frame exists, since all roots produce the same value of the Weyl scalars at this point. (We will then show that this is characteristic of Petrov Type II spacetimes).

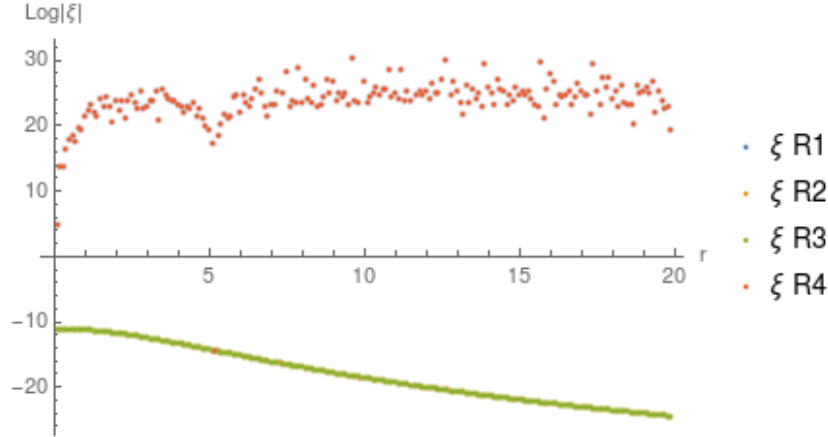


Figure 4.7: A plot of $\log|\xi = \Psi_0^{QK}\Psi_4^{QK}|$ for Ψ_0 and Ψ_4 in all four transverse frames on the plane $\theta = \frac{\pi}{2}$. The scalars ξ_2 and ξ_3 are quasi-Kinnersley since $\xi \rightarrow 0$ as $S \rightarrow 1$ (equivalently, $r \rightarrow \infty$). The red point in the green curve comes from the fact that there is only one transverse frame at that point, so all four values of ξ coincide. This will be discussed in Section 4.6.1.

The disadvantage to this method of root classification is that ξ must be computed for all four roots at each point in the entire spacetime (not just on the symmetry plane, as is shown in Fig. 4.7). This requires both a Type I and Type II rotation of both Ψ_0 and Ψ_4 , and at least a Type I rotation of all other Weyl Scalars. For a small-scale analytic calculation, this is not a problem. For a large scale numerical BBH simulation where this must be done at all points on a 3D grid at every timestep, it could become computationally inefficient.

Even though there are two “correct” choices for the root associated with the quasi-Kinnersley frame, it may be true that Ψ_0 or Ψ_4 do not tend to 0 as $r \rightarrow \infty$. It follows that in order to determine which of the two transverse frames associated with a_2 and a_3 is quasi-Kinnersley, one can look at the values of Ψ_0 and Ψ_4 individually as $r \rightarrow \infty$. This choice can be made by choosing the root that minimizes the magnitude of both Ψ_0 and Ψ_4 for large r . Both a_2 and

4.6. Analytic Results for Brill-Lindquist Initial Data

a_3 produce Ψ_0 that are continuous and head to 0 as $r \rightarrow \infty$. However, there are differences in asymptotic behavior in Ψ_4 : using a_2 , Ψ_4 is continuous and heads to 0 as $r \rightarrow \infty$, but using a_3 , Ψ_4 grows exponentially as $r \rightarrow \infty$. Figure 4.8 show the real parts of Ψ_4 calculated using the roots a_2 and a_3 respectively. Once the correct root is chosen, we can compute the Weyl

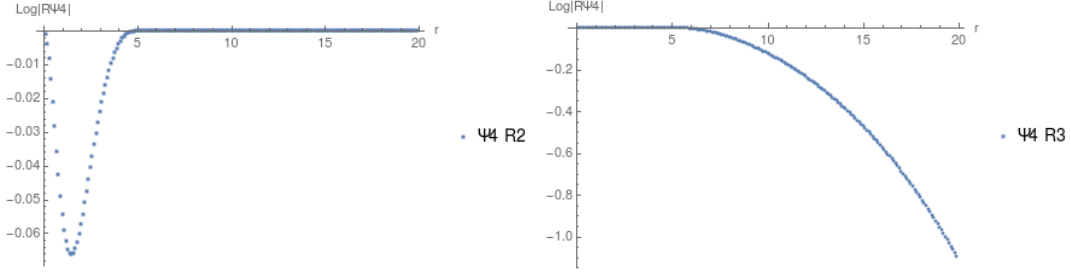


Figure 4.8: The value of Ψ_4 for the two roots a_2 and a_3 (left and right), where $\xi \rightarrow 0$ as $S \rightarrow 1$. For root 2, Ψ_4 has the expected behavior, heading to 0 as $r \rightarrow \infty$, for root 3, Ψ_4 diverges.

scalars in the quasi-Kinnersley frame. Using this construction, first verify that $\Psi_1 = \Psi_3 = 0$ to ensure we have indeed entered a transverse frame (this should be redundant, but is a good sanity check). Figures 4.9 show the three nonzero quasi-Kinnersley frame Weyl scalars on the symmetry plane $\theta = \frac{\pi}{2}$.

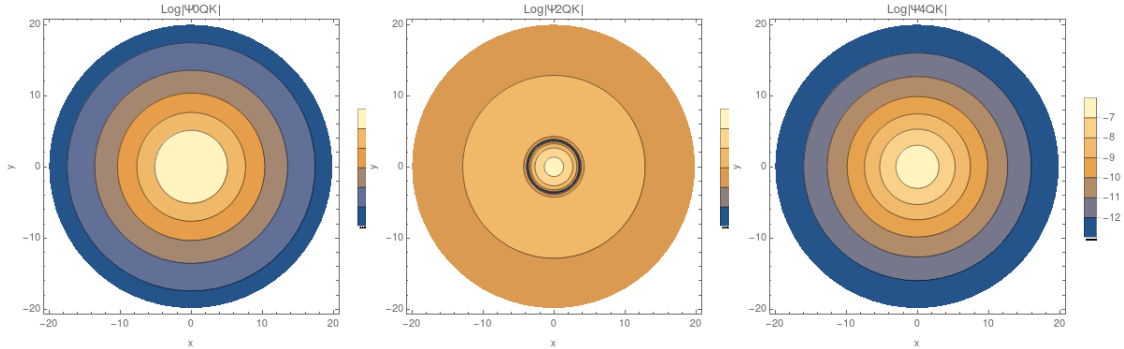


Figure 4.9: The Weyl scalars $\log|\Psi_0^{QK}|$, $\log|\Psi_2^{QK}|$, and $\log|\Psi_4^{QK}|$ shown on the xy -plane for the head-on, equal mass BBH case.

The implementation of this method is not so straightforward. In addition to the choices that need to be made asymptotically, we are attempting to demand continuity in the strong field region as well. This is subject to complex number arithmetic issues, as well as branch changes, among other practical difficulties, especially for binaries that are orbiting or spin-

ning. This is why we have chosen to begin with only analytic results for a head on collision configurations. Future work should be done to extend these analyses to the strong-field region of more complicated systems in order to use it for extraction of gravitational waves.

4.6.1 Study of the location of the ring where $S = 1$

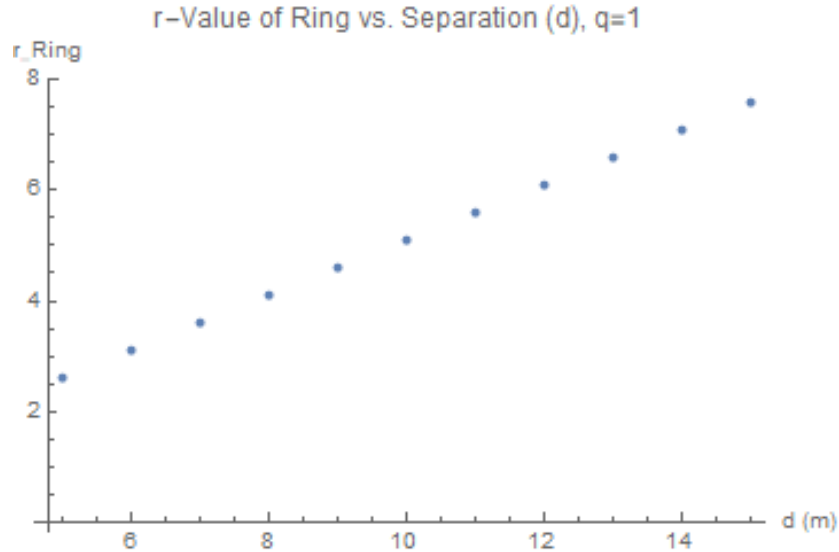


Figure 4.10: The radius of the ring r_{Ring} versus the initial binary separation d of the $q = 1$ Brill-Lindquist system. The ring is always on the equatorial plane, and is always approximately the same distance from the origin on the xy -plane as the singularities are on the z -axis.

In Section 4.6.0.1, we have shown that there is a value of θ , specifically $\theta = \pi/2$, where the eigenvalue branch must be switched. One cannot assume, however, that the location of this ring is the same for all binary separations. Figure 4.10 shows the relationship between r_{Ring} and the binary separation for the $q = 1$ case.

We studied the ring for a number of different separations: $d = 5m, \dots, 10m$ all with $q = 1$ and the center of mass at the origin. All pairs had the ring only on the symmetry plane, at a radius of approximately, but not exactly, $r_{Ring} = d/2$, which corresponds with the location of the binaries on the z -axis. Figure 4.10 shows the radius of the ring versus the binary separation for all ten pairs. The slope of the line connecting the points is exactly 0.5.

4.6.2 Results: Characterization of maxima, minima, and zeros of S and \mathcal{D} .

The goal of our work is to use \mathcal{D} in conjunction with S to do a point-by-point analysis of the approximate Petrov Type of a spacetime, with a specific focus on the strong field region and between the black holes where there is no a priori knowledge of the spacetime's Petrov Type. For this work, consider again the $q = 1$, $d = 10m$ Brill-Lindquist initial data binary.

To begin, look at the invariant S on the xy - and xz -planes (Figure 4.11, left and right respectively). Recall that when $S = 1$, the spacetime is algebraically special. As $r \rightarrow \infty$ we expect the spacetime to be Type D and therefore algebraically special, and in fact, in this region, $S \rightarrow 1$ in both the left- and right-hand plots of Figure 4.11. The xy -plane exhibits algebraic speciality between the black holes in addition to when $r \rightarrow \infty$. Interestingly, but not unexpectedly given our earlier analysis, there is a ring of algebraic speciality at r_{Ring} . This is visible in the xz -plane (right-handed figure) as well - there are two points at $x = \pm r_{Ring}$ where $S = 1$. In fact, on the xz -plane, $S \rightarrow 1$ everywhere except in ellipsoidal regions surrounding the points where $r = r_{Ring}$.

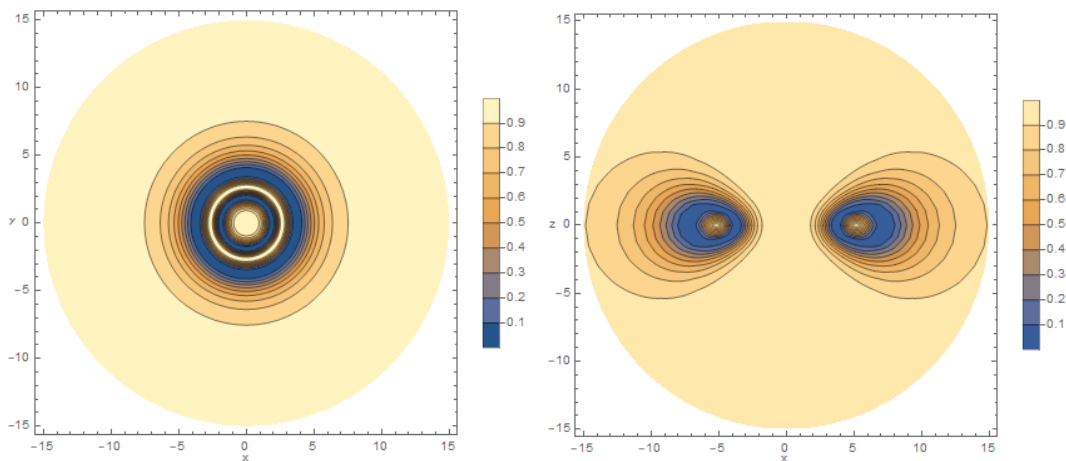


Figure 4.11: The Speciality invariant S on the xy - and xz -planes (left/right) for a $q = 1$ binary with separation $d = 10m$ located on the z -axis. Other than far from the black holes and between the black holes, the only region of algebraic speciality is located in a ring on the x -axis at $r = 5m$.

Where $S \rightarrow 1$, it is known the spacetime is either Type II or Type D [114]. Close to and between the black holes, $S \rightarrow 1$ does not characterize the Petrov Type of the points of the

spacetime since it cannot differentiate between Petrov Type II and a Type D where there is no a priori knowledge of the spacetime's behavior. To remedy this, we propose using the \mathcal{D} index from Eq. (4.5.90) to provide an approximate Petrov characterization of the points in the strong-field region.

Recall Figure 4.5; which shows the eigenvalues of the matrix Q_{ab} for this system on a slice through the equatorial plane at time $t = 0$. The eigenvalues λ_1 and λ_3 have cusps when $S = 1$ at r_{Ring} . This means that the only eigenvalue that exists on this ring of algebraic speciality is λ_2 . This is particularly interesting; it implies that only one transverse frame actually exists here and this frame must *not* be quasi-Kinnersley since λ_2 is not associated with the QK frame. In fact, according to Appendix C of [38], a spacetime with exactly one transverse frame must be Petrov Type II³ and infinitely many transverse frames in a spacetime that is Petrov Type D. This means that we can use \mathcal{D}_{QK} for classification in the far-field region, but at $r = r_{Ring}$ we cannot. The only viable transverse frame, the one that is continuous over the whole spacetime, is associated with λ_2 , which is consistent with the frame being Type II at r_{Ring} . We will call the associated classification index \mathcal{D}_2 . Figure 4.12 shows the corresponding \mathcal{D} index in all three transverse frames - the quasi-Kinnersley frame as well as the other two non-QK transverse frames, and the S -invariant.

At r_{Ring} , $\mathcal{D}_2 = 2$. This means that the points of the spacetime on r_{Ring} should be Type II, and we can prove this as follows

$$\mathcal{D}_2 = \sqrt{\frac{12}{I} \left(\Psi_2'' - \frac{\Psi_3''^2}{\Psi_4''} \right)} \quad (4.6.108)$$

$$= \sqrt{\frac{12}{3\Psi_2''^2 - 4\Psi_3''\Psi_1'' + \Psi_4''\Psi_0''} \left(\Psi_2'' - \frac{\Psi_3''^2}{\Psi_4''} \right)}. \quad (4.6.109)$$

$$(4.6.110)$$

³In Appendix C of [38], there is a typo: $\Psi_4\Psi_0 = \frac{9}{4}$ instead of $\frac{3}{2}$. This makes $\mathcal{D} = 1$ for a Type D spacetime.

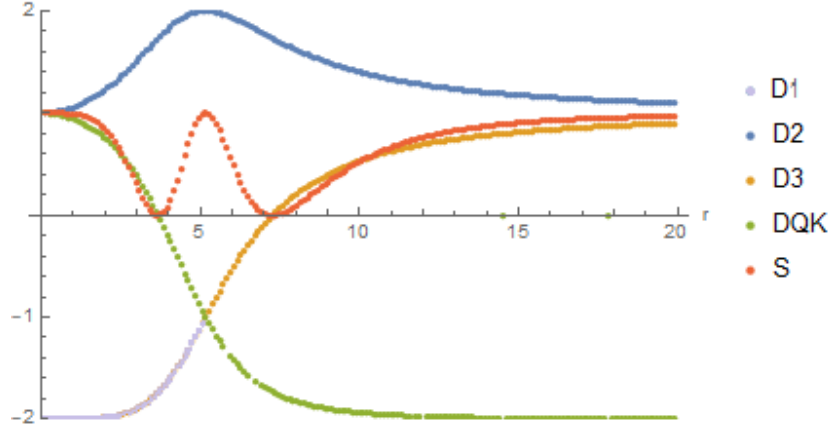


Figure 4.12: \mathcal{D} and S invariants in the quasi-Kinnersley frame for the $q = 1$, $d = 10m$, binary black hole case with Brill-Lindquist initial data on a slice through the symmetry plane $\theta = \frac{\pi}{2}$. The index \mathcal{D} associated with the quasi-Kinnersley frame goes to -2 asymptotically, intersects with \mathcal{D}_3 and then switches branches to be on the branch associated with λ_3 .

We have already seen that $\Psi_4''\Psi_0'' \rightarrow 0$, and since our frame is transverse, $\Psi_3'' = 0$ as well. So,

$$= \sqrt{\frac{12}{3\Psi_2''^2}} (\Psi_2'') \quad (4.6.111)$$

$$= \sqrt{\frac{12}{3}} = \pm 2. \quad (4.6.112)$$

Note that $\Psi_4\Psi_0$ vanishes by Table I of [38] in a Type II spacetime.

Where $r < r_{Ring}$, our QK frame definition requires continuity through $r = r_{Ring}$ in λ_P instead of continuing on the branch $\lambda_P = \lambda_1$. Therefore, between the black holes, where $r = 0m$ and $\mathcal{D} = S = 1$ the spacetime heads to Petrov Type D. Because this switching between frames is done, we would need to shift how we characterize the spacetime when we move past $r = r_{Ring}$ which can easily lead to classification errors, so it is best to use a branch that is natively continuous throughout the whole spacetime. In our Brill-Lindquist system, we have already determined that is the one associated with λ_2 . We can therefore look to \mathcal{D}_2 which, as $r \rightarrow 0$, heads to 1. This is verification that the Petrov Type between the black holes approaches D.

4.6.2.1 Classification of the region where $S = 0$

In Figure 4.12, at approximately $r = 3.68m$ and $7.28m$, $\mathcal{D} = S = 0$. In a spacetime where $S = J = 0$, it can be shown that $\mathcal{D} = \pm\sqrt{3}$ or 0:

$$\begin{aligned}
 \mathcal{D} &= \sqrt{\frac{12}{I} \Psi_2''} \\
 &= \sqrt{\frac{12\Psi_2''^2}{3\Psi_2''^2 + \Psi_0''\Psi_4''}} \\
 J = 0 &\implies \Psi_0''\Psi_4'' = \Psi_2''^2 \\
 &= \sqrt{\frac{12\Psi_2''^2}{3\Psi_2''^2 + \Psi_2''^2}} \\
 &= \sqrt{3}
 \end{aligned}$$

Recall again the plots in Figure 4.11. In both the xy - and xz -planes, there exist regions of the spacetime where $S \rightarrow 0$. Unlike the $S \rightarrow 1$ ring, $S \rightarrow 0$ at two points on $\theta = \pi/2$ ($z = 0$), one to the left of r_{Ring} at $r = 3.68m$ and one to the right at $r = 7.28m$. In fact, $S = 0$ on a ring on the xz -plane itself. The left-hand side of Figure 4.13 shows this ring in Quadrants I and IV of the xz -plane, but the ϕ -symmetry of this system means the ring rotates around the z -axis to form a hollow "doughnut"-shape (right hand side of Figure 4.13). The $S = 0$

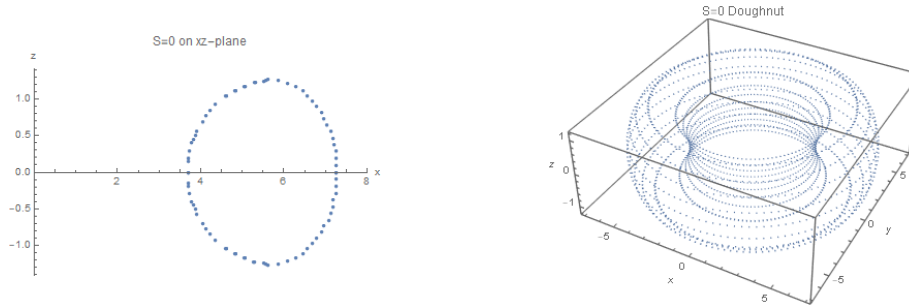


Figure 4.13: The ring of points on the xz -axis where $S = 0$ (left). This ring rotates around the z -axis, forming a hollow "doughnut" of points in space where $S = 0$ (right). As resolution increases, the points will approach a continuous ring on the xz -plane.

doughnut's outer and inner rings have radii of $7.28m$ and $3.68m$ from the origin, respectively, along the x -axis. The doughnut has z -maxima at $(x, z) = (\pm 5.90, 1.25)$ and minima at

$(x, z) = (\pm 5.90, -1.25)$. This region of spacetime surrounds the surface of algebraic speciality located at $r_{Ring} \approx 5.2m$, but is not itself algebraically special since $S = 0$, and is instead a general Type I.

Since we have concluded that $r = 0m$ and $r \rightarrow \infty$ are Type D and r_{Ring} is Type II, we will argue that on this doughnut where $S = 0$, the spacetime is transitioning between Type II and Type D. To investigate this region, we will use the \mathcal{D} index in the transverse frame associated with λ_2 because it is continuous through the point r_{Ring} , rather than the QK frame. This ensures that we are not switching between frames, that all interesting points exist, and reduces the likelihood of classification error. Recall that this means that $\mathcal{D} = 1$ in a Type D spacetime. We have already shown that when $\mathcal{D} = \pm 2$ the spacetime is Type II in Eqs. (4.6.108).

In Figure 4.12, notice that \mathcal{D}_2 is not symmetric around r_{Ring} . Even so, on the left and right hand side at $x = 3.68m$ and $x = 7.28m$ respectively, $\mathcal{D}_2 = 1.73$. Interestingly, this means that the spacetime should be closer to Type II than Type D at these points because a larger value of \mathcal{D}_2 implies a smaller value of $\Psi_4''\Psi_0''$ which leads to $\mathcal{D}_2 \rightarrow -2$.

Table 4.2 shows the r locations of important values on $\theta = \pi/2$. Namely, the location of the ring, and the values of \mathcal{D} and S at important points in different transverse frames (QK, 2, or 3).

4.6.3 Classification off the symmetry plane

If we move off of the symmetry plane $\theta = \pi/2$ to a neighboring region, say the cone $\theta = 8\pi/15$ to be consistent with Figure 4.6, we can use any of the transverse frames for classification since they are all continuous. Figure 4.14 shows the corresponding values of \mathcal{D} and S for the transverse frames associated with the cone $\theta = 8\pi/15$. As $r \rightarrow 0$ and $r \rightarrow \infty$, the two transverse, but not QK, frames, \mathcal{D}_2 and \mathcal{D}_3 go to 1, whereas $\mathcal{D}_{QK} \rightarrow 2$. This is consistent with Type D behavior in these regions. At r_{Ring} , the values of \mathcal{D} do not quite reach 2 (for non-QK) and 1 (for QK), and therefore the spacetime is never exactly Type II, but only Type I in the region between the points where $S = 0$. This is consistent with our findings since (1) $S \neq 1$ in this region, so there is no point of algebraic speciality, and (2) all three transverse

4.6. Analytic Results for Brill-Lindquist Initial Data

| Transverse Frame | S | \mathcal{D} | r/m | Petrov type |
|---------------------------------|------|---------------|----------|-------------|
| 1 QK (1 \rightarrow 3) | 1 | -2 | 0 | D |
| | 0.5 | 0.52 | 2.68 | I |
| | 0 | 0 | 3.8 | I |
| | 0.5 | -1.41 | 4.9 | I |
| | 1 | -1 | 5.05 | II |
| | 0.5 | -1.41 | 5.1 | I |
| | 0.32 | -1.5 | 6.27 | I |
| | 0 | -1.73 | 7.20 | I |
| | 0.5 | -1.93 | 9.88 | I |
| | 1 | -2 | ∞ | D |
| 2 | 1 | 1 | 0 | D |
| | 0.5 | 1.41 | 2.68 | I |
| | 0.31 | 1.5 | 2.97 | I |
| | 0 | 1.73 | 3.8 | I |
| | 0.5 | 1.91 | 4.9 | I |
| | 1 | 2 | 5.05 | II |
| | 0.5 | 1.91 | 5.1 | I |
| | 0 | 1.73 | 7.2 | I |
| | 0.31 | 1.5 | 8.97 | I |
| | 0.5 | 1.41 | 9.88 | I |
| 1 | 1 | ∞ | D | |
| 3 | 1 | 1 | 0 | D |
| | 0.5 | -1.93 | 2.68 | I |
| | 0 | -1.73 | 3.80 | I |
| | 0.32 | -1.5 | 4.26 | I |
| | 0.5 | -1.42 | 4.9 | I |
| | 1 | -1 | 5.05 | II |
| | 0.5 | -1.42 | 5.1 | I |
| | 0 | 0 | 7.2 | I |
| | 0.5 | 0.52 | 9.88 | I |
| | 1 | 1 | ∞ | D |

Table 4.2: Summary of the values of the scalars S and \mathcal{D} at different r -locations in different Transverse frames (QK, 2, and 3) and the associated Petrov type for the $q = 1$ Brill-Lindquist binary on $\theta = \pi/2$. We are using the transverse frame 2 for classification. When $\mathcal{D} = \pm 1.73$ and $S = 0$ the spacetime is Petrov type I, but is closer to Petrov type II than Petrov type D. When $\mathcal{D} = \pm 1.5$, the spacetime is halfway between Petrov types II and D.

frames exist - that cannot be the case in a Type II spacetime.

From these studies, we can draw the conclusion that between the points where $S = 0$ (namely, around $r = r_{Ring}$, the spacetime is actually closer to Type II than it is to Type D and is exactly Type II only on the one dimensional ring at $\theta = \pi/2$.

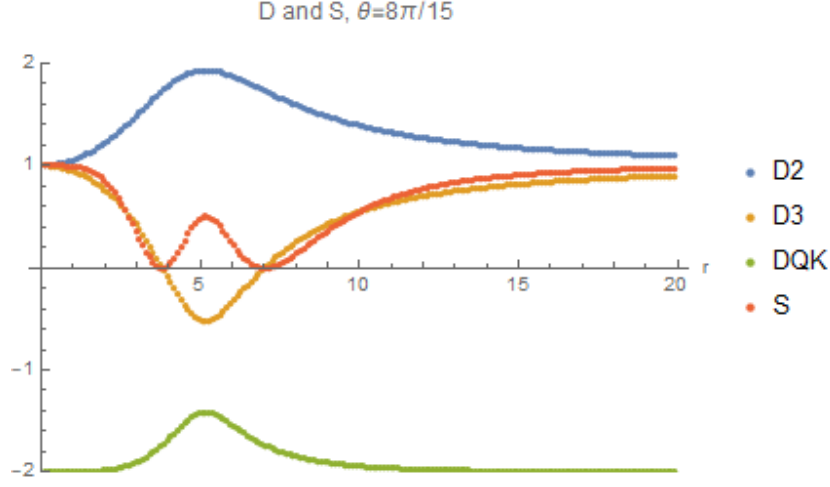


Figure 4.14: D-ality and S invariants in the quasi-Kinnersley frame for the $q = 1$, $D = 10m$, binary black hole case with Brill-Lindquist initial data on a slice through cone $\theta = \frac{8\pi}{15}$.

4.7 Classification Results: Unequal Mass Binary Study

To generalize our results from Section 4.6, we studied a spacetime with an unequal mass binary whose mass ratio is $q = 1/3$. This system also has analytic Brill-Lindquist initial data with $d = 7m$ separated black holes and $r_p = 1.75m$ and $r_m = -5.25m$ with the center of mass located on the origin of coordinates.

In particular, we are interested in (1) the value of r_{Ring} , studied in Section 4.7.1, (2) the Petrov classification using the \mathcal{D} index, studied in Section 4.7.2, and (3) the location of the doughnut $S = 0$, studied in Section 4.7.3.

4.7.1 The Surface r_{Ring}

Let us consider the system with BL initial data with mass ratio $q = 1/3$ and varying separations $d = 5m, 7m, 9m, 11m$. The black holes have masses $3m_1 = 0.75 = m_2$ and are located at respective distances of $r_1 = -d/(1+q)$ and $r_2 = dq/(1+q)$ on the z -axis so that the center of mass is always located at the origin. We are looking to find the one dimensional surface characterized by some $(r_{Ring}, \theta_{Ring})$. We know that, if it exists, the circle occurs at some region where $|S - 1| = 0$. This will also be the location that, in order to maintain continuity in the eigenvalues λ of the associated matrices Q_{ab} , the eigenvalue branch must be flipped.

4.7. Classification Results: Unequal Mass Binary Study

In our implementation, we used that as our criteria for selecting the appropriate (r, θ) pair to define the location of $(r_{Ring}, \theta_{Ring})$.

Figure 4.15 shows the radius of the ring versus the binary separation for all four pairs. In fact, we found the ring is located on a cone at $\theta_{Ring} = 19\pi/15$ and is the same for all separations d , which means that it is determined by the mass ratio of the black holes. The

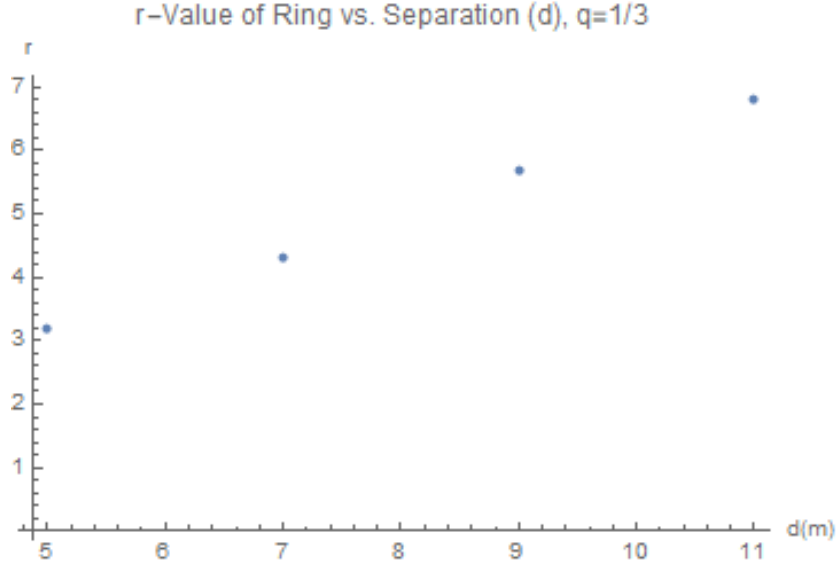


Figure 4.15: The radius of the ring r_{Ring} versus the initial binary separation d of the $q = 1/3$ Brill-Lindquist system. The ring always occurs near $\theta \approx 19\pi/15$ (shown here). There is a distinctly linear relationship between r_{Ring} for each binary and the binary's separation.

takeaway from this analysis should be that r_{Ring} has a linear relationship with respect to the separation d between the black holes whereas θ_{Ring} is independent of separation, and is instead solely a function of mass-ratio q .

4.7.2 Classifying the Spacetime

We would like to generalize the classification results we saw in our study of the $q = 1$ binary in Section 4.5 by extending that work to the case of the $q = 1/3$ binary (and hence infer about other qs). This, again, will be done with the use of the index \mathcal{D} in conjunction with the Baker-Campanelli speciality invariant S . Figure 4.16 shows the S -invariant on the xy - and xz -planes in the left and right panels, respectively. Note the change in color scale between the

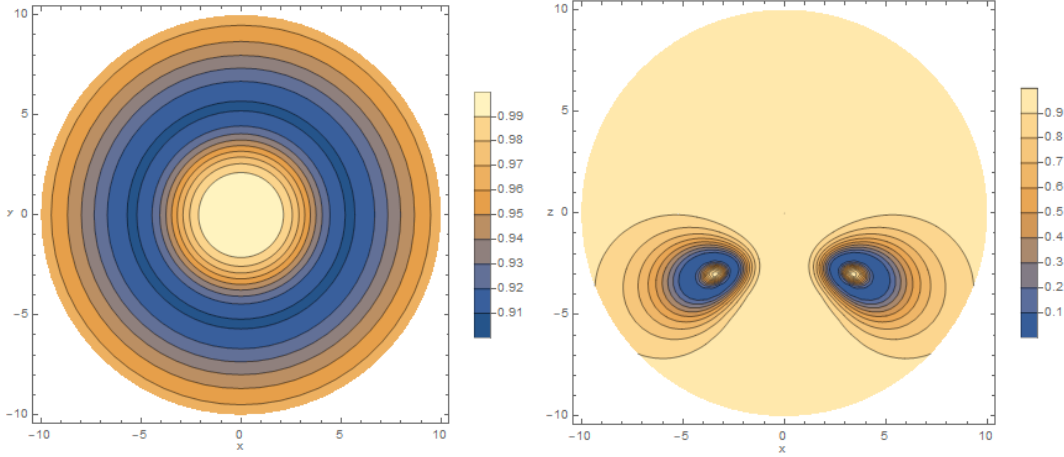


Figure 4.16: The Speciality invariant S on the xy - and xz -planes (left/right) for a $q = 1/3$ binary with separation $d = 7m$ located on the z -axis. Other than far from the black holes and between the black holes, the only region of algebraic speciality is located in a ring with radii in the centers of the “eyes” in the right hand plot. The coordinates of the ring are $(r_{Ring}, \theta_{Ring}) \approx (4.6, 19\pi/15)$

two figures. The xy -plane, Figure 4.16 (a), is symmetric on both axes due to ϕ -symmetry, and has the property that $S = 1$ both between the black holes as well as asymptotically. It drops to $S \approx 0.9$ on a ring that corresponds to where the “eyes” cross the x -axis in Figure 4.16 (b). On the xz -plane, the blue ellipsoidal regions are where $S = 0$. When rotated around the z -axis they become “doughnut-like” in shape, which corresponds with what we saw in Figure 4.11 (b). The value of S at points asymptotically and between the black holes is 1, indicating a region of algebraic speciality over the whole spacetime except near the doughnut. There also exist points where $S = 1$ inside of the doughnut at $(r_{Ring}, \theta_{Ring}) \approx (4.6, 19\pi/15)$ which, when rotated around the z -axis, these form the ring of algebraic speciality - and consequently the location where two of the three eigenvalues λ cease to exist. We expect this ring is Type II, and seek to show that in what follows.

Figure 4.17 shows the values of \mathcal{D} in the quasi-Kinnersley frame as well as in the two other transverse frames overlaid with S . All are shown on the cone $\theta_{Ring} \approx 19\pi/15$. Analogously to Figure 4.12, \mathcal{D}_3 and \mathcal{D}_{QK} cross at r_{Ring} , so forcing continuity means we have to switch frames when crossing r_{Ring} . Furthermore, the frames themselves do not exist at the point of crossing, and only one transverse frame, associated with \mathcal{D}_2 exists and is equal to $+2$. This

means that at the point r_{Ring} the spacetime is of Petrov Type II, which is consistent with our results for the $q = 1$ case. Far away from, as well as between the black holes, $\mathcal{D}_2 = S = 1$ which indicates that the spacetime is of Petrov Type D in these regions.

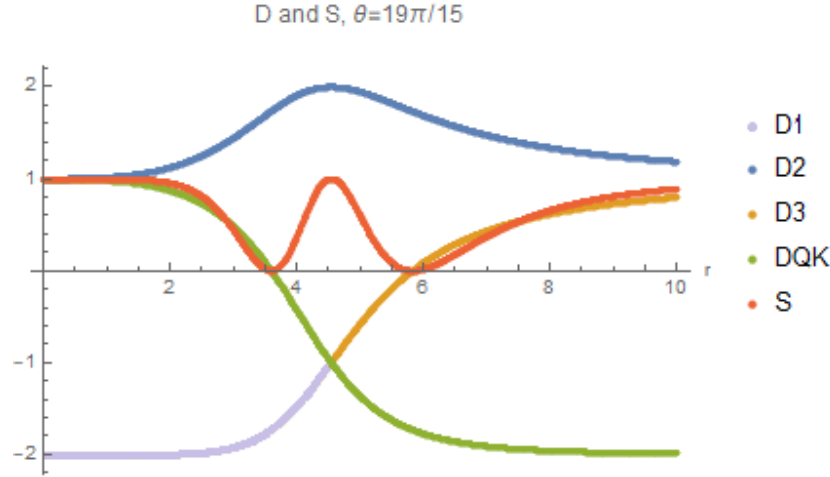


Figure 4.17: D-ality and S invariants in the quasi-Kinnersley frame for the $q = 1/3$, $d = 7m$, binary black hole case with Brill-Lindquist initial data on the conical slice $\theta = \frac{19\pi}{15}$.

4.7.3 Location of Doughnut $S = 0$

Now that our classification results from the $q = 1$ case are confirmed for a $q = 1/3$ binary, we can look at the region that we expect is Petrov Type I. The “doughnut” where $S = 0$ exists in this unequal mass case, as well as in the equal mass binary. The ellipsoid shown in

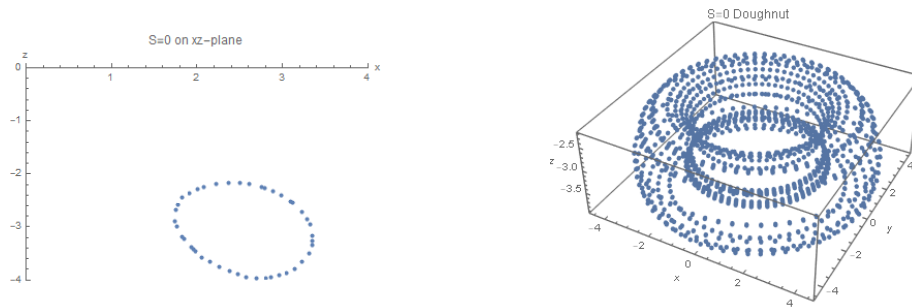


Figure 4.18: The location of the doughnut $S = 0$ on the xz -plane for the $q = 1/3$, $d = 7m$ separated Brill-Lindquist system (left). Because of ϕ -symmetry, the ellipsoid shown is rotated around the z -axis forming a hollow doughnut where $S = 0$ (right).

Figure 4.18 outlines the region where $S = 0$ on the xz -plane (left side) and, when rotated

around the z -axis, will form the “doughnut” shape (right side). Interestingly, on the bounds of this region, $\mathcal{D}_2 = -1.73$, which is the same as in the equal mass case (results shown in Table 4.2). This is a good indication that \mathcal{D} and S on θ_{Ring} have a consistent relationship among different mass-ratios. We can hence safely say that the interior of the doughnut is approximately of Petrov Type I, transitioning to Type II at r_{Ring} .

Table 4.3 shows the r locations of important values on the cone $\theta = 19\pi/15$ - namely the approximate location of the ring and the values of \mathcal{D} and S at important points in different transverse frames (QK, 2, or 3).

| Transverse Frame | S | \mathcal{D} | r | Petrov Type |
|------------------------|-----|---------------|----------|-------------|
| 1 | 1 | -2 | 0 | D |
| | 0 | -1.73 | 3.8 | I |
| | 1 | -1 | 4.9 | II |
| | 0 | -1.73 | 5.8 | I |
| | 1 | -2 | ∞ | D |
| QK (1 \rightarrow 3) | 1 | 1 | 0 | D |
| | 0 | 1.73 | 3.8 | I |
| | 1 | 2 | 4.9 | II |
| | 0 | 1.73 | 5.8 | I |
| | 1 | 1 | ∞ | D |
| 2 | 1 | 1 | 0 | D |
| | 0 | 0 | 3.8 | I |
| | 1 | -1 | 4.9 | II |
| | 0 | 0 | 5.8 | I |
| | 1 | 1 | ∞ | D |
| 3 | 1 | 1 | 0 | D |
| | 0 | 0 | 3.8 | I |
| | 1 | -1 | 4.9 | II |
| | 0 | 0 | 5.8 | I |
| | 1 | 1 | ∞ | D |

Table 4.3: Summary of the values of the scalars S and \mathcal{D} at different r - locations in different Transverse frames (QK, 2, and 3) and the associated Petrov Type for the $q = 1$ Brill-Lindquist binary on $\theta = 19\pi/15$. Note that for $r \leq r_{Ring}$, frames QK and 3 flip places when $S = 1$ at r_{Ring} .

4.8 Numerical Results: Weyl Scalars

In the previous sections, all our computations were done analytically in Mathematica. For practical numerical simulations, the quasi-Kinnersley frame rotation should be reproduced in C (or FORTRAN) in order to be used in conjunction with the existing TwoPunctures thorn. This means we need to explicitly solve for the analytic roots of the quartic (Eq. (4.4.74)), so that

we have control over which roots are chosen at which points. We find them by first reducing Eq. (4.4.74) to a depressed quartic, and then to a cubic whose roots we can use to reconstruct the roots to the quartic. This is a standard technique for solving a quartic equation, known as Euler's method [115], but for consistency, we will provide our steps explicitly below:

- Construct a depressed quartic of the form $y^4 + Py^2 + Qy + R = 0$ by making the substitution $x = y - \frac{b}{4a}$ where

$$P = \frac{c}{a} - \frac{3b^2}{8a^2} \tag{4.8.113}$$

$$Q = \frac{d}{a} - \frac{bc}{2a^2} + \frac{b^3}{8a^3} \tag{4.8.114}$$

$$R = \frac{e}{a} - \frac{bd}{4a^2} + \frac{cb^2}{16a^3} - \frac{3b^4}{356a^4} \tag{4.8.115}$$

- Solve the cubic equation

$$z^3 + 2Pz^2 + (P^2 - 4R)z - Q^2 = 0 \tag{4.8.116}$$

$$\implies Az^3 + Bz^2 + Cz + D = 0 \tag{4.8.117}$$

for roots z_1, z_2, z_3 .

- Construct $D_0 = B^2 - 3AC$ and $D_1 = 2B^3 - 9ABC + 27A^2D$.
- Construct $C_0 = \left(\frac{D_1 \pm \sqrt{D_1^2 - 4D_0^3}}{2} \right)^{\frac{1}{3}}$ (the choice between \pm is arbitrary, but must not lead to $C_0 = 0$).
- Construct the roots

$$z_k = \frac{-1}{3A} \left(B + \xi^k C_0 + \frac{D_0}{\xi^k C_0} \right) \tag{4.8.118}$$

where $k = (0, 1, 2)$ and $\xi = \frac{-1 + \sqrt{-3}}{2}$.

- Use those roots to construct the solutions to the depressed quartic

$$y_1 = \frac{1}{2}(\sqrt{z_1} + \sqrt{z_2} + \sqrt{z_3}) \quad (4.8.119)$$

$$y_2 = \frac{1}{2}(\sqrt{z_1} - \sqrt{z_2} - \sqrt{z_3}) \quad (4.8.120)$$

$$y_3 = \frac{1}{2}(-\sqrt{z_1} + \sqrt{z_2} - \sqrt{z_3}) \quad (4.8.121)$$

$$y_4 = \frac{1}{2}(-\sqrt{z_1} - \sqrt{z_2} + \sqrt{z_3}) \quad (4.8.122)$$

and then choose signs of the square roots such that $\sqrt{z_1}\sqrt{z_2}\sqrt{z_3} = -Q$.

Using these roots, we are able to construct Weyl scalars for a $q = 1$, $d = 10m$ binary with Brill Lindquist initial data whose nonvanishing parts are shown in Figures 4.19-4.21. They are in the QK frame, so $\Psi_1 = \Psi_3 = 0$, and calculated using numerical initial data generated by the TwoPunctures thorn.

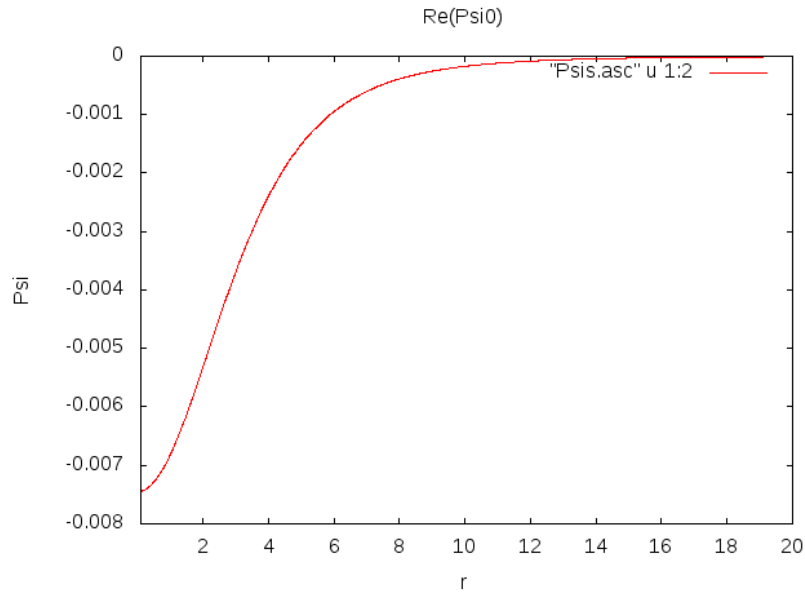


Figure 4.19: Real part of Ψ_0 for a $q = 1$, $d = 10m$ binary with Brill Lindquist initial data in the QK frame calculated using numerical initial data generated by the TwoPunctures thorn.

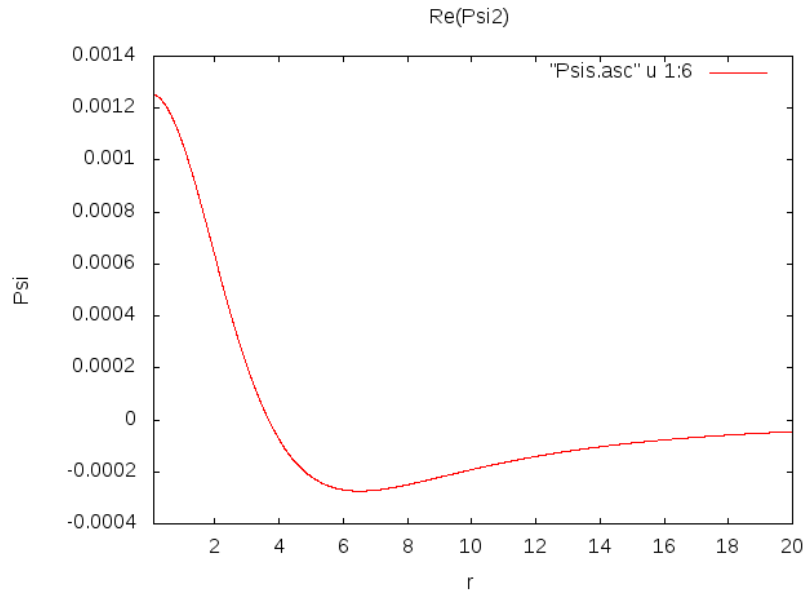


Figure 4.20: Real part of Ψ_2 for a $q = 1$, $d = 10m$ binary with Brill Lindquist initial data in the QK frame calculated using numerical initial data generated by the TwoPunctures thorn.

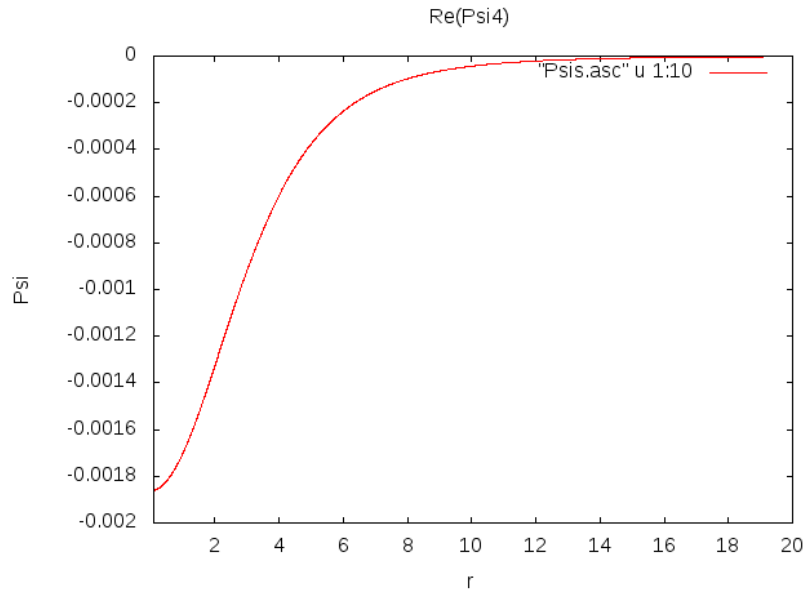


Figure 4.21: Real part of Ψ_4 for a $q = 1$, $d = 10m$ binary with Brill Lindquist initial data in the QK frame calculated using numerical initial data generated by the TwoPunctures thorn.

4.9 Future Work: Extension to Full Numerical Simulation

We have shown that it is possible to successfully rotate the initial data of a nonspinning, equal mass, head on binary into a quasi-Kinnersley frame. We have also used a transverse, but not quasi-Kinnersley frame, to classify interesting points in a Brill Lindquist spacetime into appropriate Petrov Types. Finally, we have included this into the TwoPunctures thorn and shown that it works for this equal-mass case.

Once the rotation is successfully completed on the initial data of a binary with orbital momentum, this work can be extended to full numerical simulations. It would be useful to have the transverse frame rotation implemented and tested for full numerical simulations, for both classification and gravitational wave extraction. We expect gravitational waves extracted in the quasi-Kinnersley frame can be extracted closer to the black holes with the same or higher accuracy as those extracted using our typical numerical tetrad. Using full numerical simulations in transverse frames, we can analyze and classify a dynamical spacetime rather than just the initial setup. The \mathcal{D} index can be used, in conjunction with the S invariant to characterize parts of the spacetime that were previously ambiguously defined, where $S = 1$ as Type D or Type II, and where $S \neq 1$ as Type I.

Chapter 5

Conclusion and Future Work

The first detection of gravitational waves on September 14, 2015 helped to generate renewed interest in the field of numerical relativity. It has become increasingly accessible to newcomers in the field, as well as new programs at different universities, there has been more collaboration among groups, and a newfound popular-science interest in black holes. With these exciting developments comes opportunities for significant advancement in the field. Over the past decade, there has been a push for more accurate simulations of binary black hole mergers for lower computational cost to increase the number of numerical simulations that can be compared with detections. LIGO/Virgo are now detecting binary black hole pairs regularly, and as the detectors' sensitivity increases, the likelihood of detecting a binary with a high mass-ratio increases. With third generation ground-based gravitational wave detectors and LISA, these detections will become reality.

Numerical relativists have studied binaries with many different configurations, but regions of the parameter space that are very challenging to simulate are fairly unexplored. RIT has been able to successfully evolve a $q = 1/128$ binary through merger and ringdown [22], but at significant computational cost. The steep computational resource requirement means that simulation accuracy is absolutely crucial. Methods of accuracy improvement have been proposed such as using quantities of the binary (mass, angular/linear momentum) that are calculated on the horizon instead of from gravitational waves radiated to infinity [65] [67].

These quantities can be used in a series of formulae that use the parameters of the binary to calculate specific properties of the remnant and the gravitational wave emission. Using horizon quantities, these fitting formulae can achieve very high accuracy when compared to the actual numerical relativistically calculated remnant quantities - within 0.05% for the mass and 0.03% for the spin, but only to within 5% for the linear momentum.

To this end, in Section 2, we studied different constant values of gauge damping parameter η lead to the most accurate measures of the linear momentum of the horizon with the non-gauge-independent formula (2.1.1). We found that for small values $0.25 \geq m\eta \leq 0.5$ the horizon linear momentum is a reliable measure and can compete with the measurement at \mathcal{I}^+ of the radiated momentum carried by the gravitational waves.

We studied these different gauges in detail for a nonspinning $q = 1/3$ binary and verified the results using $q = 1/2$ and $q = 1/5$ as control cases, as well as for a $q = 1$ spinning case, and therefore expect these conclusions to be able to be generalized to different configurations. One could extend this study by applying our findings to simulations where the computation of recoil is important, including precessing binaries.

In Chapter 3 we studied a variable η proposed first in Chapter 2 on different binary configurations, with a focus on small mass-ratio pairs. We performed an in-depth study on $q = 1/15$ and $q = 1/32$ binaries, with confirmation studies on $q = 1/7$ and $q = 1/64$, as well as applied our variable η to the $q = 1/128$ binary. We found that, in general, a constant choice for η can be used, even for small mass-ratios, provided enough resolution is given on the time axis. In binaries such as $q = 1/15$, where we typically choose a Courant factor of $1/3$, we are instead required to use $1/4$. This increase in computational cost, while not prohibitive, is unappealing. We chose to analyze physical parameters to determine the benefits of using different gauges, since gauge-dependent measures of accuracy such as constraint violations cannot be reliably used here.

Overall, we found that using the variable η gauge G, made up of two superposed Gaussians, performs as good as or better than our traditional choice for small mass ratios LZ or a constant value. In the smaller mass-ratio binary $q = 1/32$, we found that using $\eta = 2/m$ produced

oscillations in the dominant mode of the gravitational wave strain during the inspiral, which were damped by using G. This G gauge also has the benefit of damping very high frequency noise early on in the waveforms, and during inspiral, as well as better maintained horizon quantities, when compared with the gauge we typically use for small mass-ratio binaries (LZ). Both the variable η s: G and LZ, introduced oscillations to the strain during the ringdown phase, so it was proposed that a more accurate choice would be a gauge that is variable pre-merger, and then constant post-merger. To this end, we introduced η_{G2} which is a modified version of our original η_G that damps some peaks in η that appear when the black holes are close together. In conjunction with modified lapse and zero shift, we recommend a variable η (either G or G2) to be used because of its robustness when handling both small and comparable mass ratio binaries.

Some improvements to BBH simulations can be made to equations that dictate the coordinates, like the gauge improvements presented in Chapters 2 and 3, but it is also helpful to find improved methods of analyzing the output of the simulation. Chapter 4 presents a more accurate frame in which to study the spacetime, as well as a new method of classifying the approximate Petrov Type of the spacetime. These improvements allow us to have a better idea of the behavior of the spacetime in the strong-field region - most interestingly near the black holes and in a region where the spacetime is approximately algebraically special. Where previously, we could not differentiate between Type II and Type D in this region.

There is much work to be done here still. In this thesis, we looked at these systems from the perspective of analytic initial data and “moved” the black holes towards each other using different separations d , but it would be very interesting to see how the spacetime develops during a full head-on (or orbiting) evolution of the binary in both a QK frame and an arbitrary transverse frame.

Improving the evolution of BBH mergers is very important if we are to keep pushing the boundaries on black hole mass-ratio and spin. These types of binaries are of particular interest for third generation gravitational wave detectors [91] and for the space-based mission LISA [92] since they have long inspiral periods. Small mass ratio simulations reaching

100:1 have been achieved with the moving puncture approach [7, 93] and numerical convergence has been proven, and another sequence of nonspinning binaries with mass ratios $q = m_1/m_2 = 1/32, 1/64, 1/128$ has been studied in [22]. However, these simulations should be considered proof of principle. In order to become practical for production purposes, they need improvements, such as the ones presented here, in both computational efficiency and accuracy of the numerical techniques.

The analytic spacetime analysis we present in Chapter 4 is interesting from a theoretical perspective. It provides us with more insight into the spacetime itself and unique ways to analyze the strong-field region of the BBH system and its merger product. This region, since such strong gravitational fields are present, is not particularly well studied and methods need to be developed to accurately analyze what happens near the black holes themselves.

This thesis sought to improve current numerical relativistic techniques from a numeric perspective, and improve analysis of spacetimes from an analytic perspective. Together, these studies provide a way of studying and understanding all parts of a binary black hole system from initial data all the way through merger.

Appendix A

Remnant Fitting:

A convenient method of calculating remnant fits in conjunction with the RIT catalog

Improvements on the breakthrough in 2005 has made simulating binary black hole and binary compact object mergers more widely accessible. As a consequence, the parameter space of binaries that have been simulated through merger has begun to fill. The more finely discretized parameter space has sparked interest in modeling quantities associated with the remnant, such as mass, spin, and kick, based on parameters of the initial binary. As more waveforms are produced, constraints on the fitting functions are tightened, and the accuracy of such models increases.

First attempts at such models were inspired by Post-Newtonian formulas. However, due to the complicated nature of PN terms, a more simplistic approach was desired. Boyle et. al. [116] were the first to use basic symmetry arguments to develop a mapping from the initial mass and angular momentum of the binary to the final mass, spin, and kick of the remnant. They apply their symmetry arguments to a well-chosen Taylor series expansion to construct their remnant

formulae. In this work, the mass ratio of the binary is used as a weight, in conjunction with the binary’s angular momentum. The formulae provided give a fairly accurate approximation of the final remnant quantities, although improvements can always be made.

In [117], Taylor series formulae for the mass and spin for non-precessing binaries were developed based on Post-Newtonian inspired variables. Recoil velocity formulae were included in [117] and precessing binaries were included in [32]. RIT’s research group, in [1], provides a catalog of 36 non-precessing black hole binaries, which are used to develop models for the mass, spin, and kick of the remnant. These quantities are defined as functions of the mass difference and spins of the initial black holes and are constructed to very high order. This work also calculated the maximum linear momenta of the remnants for the 36 simulations. In [33], new simulations were included. In addition to assessing the accuracy of the fitting formulae with the new simulations, the authors included a model for the peak luminosity of the gravitational waves based on the parameters of the initial binary.

Included in [2] are 71 new simulations to further refine the remnant formulae coefficients provided in [1]. The models in this work have accuracy is within one half of one percent of the expected value, which is calculated from the radiated quantities extrapolated to infinity, for the mass, spin, and kick, and within 5% for the peak luminosity, when compared to the direct output from numerical relativity simulations.

Subsequent iterations of this methodology sought to further refine the coefficients’ values by including more varied simulations and increasing the size of the catalog. A 2018 paper [3] provided 74 new simulations. This paper also studied the hangup effect of black holes, which is the role of the black holes’ initial parameters in delaying or accelerating the time of merger. This work specifically considered unequal mass non-precessing binaries.

Most recently, RIT put out a catalog of 777 binary black hole waveforms [35] made up of 477 non-precessing binaries as well as 300 precessing binaries. Of course this catalog is built up for the purpose of comparing directly to observational data from gravitational wave detectors. From these simulations, we can also extract information about the merger remnant such as mass, spin, and linear momentum (m_f, α_f, V_f) . Empirical formulas to calculate these

quantities to within 0.03% accuracy for the mass, 0.16% accuracy for the spin, and 0.5% accuracy for the linear momentum have been proposed using polynomial fits. These studies also include generalized fits for the peak frequency of the 2,2-mode $\Omega_{2,2}^{peak}$, peak waveform amplitude $A_{2,2}^{peak}$, and peak luminosity [1, 32, 117, 33, 79, 3]. These formulas are fourth order expansions with 17 (recoil), or 19 (mass, spin, peak luminosity, peak frequency, peak gravitational wave emission) coefficients. The full formulae can be found in [3] but will be reproduced here for completeness.

A.1 Fitting Formulas

In Ref. [1] the fitting formula for the remnant mass M_{rem} was given by,

$$\begin{aligned}
\frac{M_{\text{rem}}}{m} = (4\eta)^2 \{ & M_0 + K_1 \tilde{S}_{\parallel} + K_{2a} \tilde{\Delta}_{\parallel} \delta m + \\
& K_{2b} \tilde{S}_{\parallel}^2 + K_{2c} \tilde{\Delta}_{\parallel}^2 + K_{2d} \delta m^2 + \\
& K_{3a} \tilde{\Delta}_{\parallel} \tilde{S}_{\parallel} \delta m + K_{3b} \tilde{S}_{\parallel} \tilde{\Delta}_{\parallel}^2 + K_{3c} \tilde{S}_{\parallel}^3 + \\
& K_{3d} \tilde{S}_{\parallel} \delta m^2 + K_{4a} \tilde{\Delta}_{\parallel} \tilde{S}_{\parallel}^2 \delta m + \\
& K_{4b} \tilde{\Delta}_{\parallel}^3 \delta m + K_{4c} \tilde{\Delta}_{\parallel}^4 + K_{4d} \tilde{S}_{\parallel}^4 + \\
& K_{4e} \tilde{\Delta}_{\parallel}^2 \tilde{S}_{\parallel}^2 + K_{4f} \delta m^4 + K_{4g} \tilde{\Delta}_{\parallel} \delta m^3 + \\
& K_{4h} \tilde{\Delta}_{\parallel}^2 \delta m^2 + K_{4i} \tilde{S}_{\parallel}^2 \delta m^2 \} + \\
& \left[1 + \eta(\tilde{E}_{\text{ISCO}} + 11) \right] \delta m^6.
\end{aligned} \tag{1.1.1}$$

With all 19 K_i being fitting parameters. As in Ref. [1] the fitting formula for the final spin has the form,

$$\begin{aligned}
\alpha_{\text{rem}} = \frac{S_{\text{rem}}}{M_{\text{rem}}^2} = (4\eta)^2 \{ & L_0 + L_1 \tilde{S}_{\parallel} + \\
& L_{2a} \tilde{\Delta}_{\parallel} \delta m + L_{2b} \tilde{S}_{\parallel}^2 + L_{2c} \tilde{\Delta}_{\parallel}^2 + L_{2d} \delta m^2 + \\
& L_{3a} \tilde{\Delta}_{\parallel} \tilde{S}_{\parallel} \delta m + L_{3b} \tilde{S}_{\parallel} \tilde{\Delta}_{\parallel}^2 + L_{3c} \tilde{S}_{\parallel}^3 + \\
& L_{3d} \tilde{S}_{\parallel} \delta m^2 + L_{4a} \tilde{\Delta}_{\parallel} \tilde{S}_{\parallel}^2 \delta m + L_{4b} \tilde{\Delta}_{\parallel}^3 \delta m + \\
& L_{4c} \tilde{\Delta}_{\parallel}^4 + L_{4d} \tilde{S}_{\parallel}^4 + L_{4e} \tilde{\Delta}_{\parallel}^2 \tilde{S}_{\parallel}^2 + \\
& L_{4f} \delta m^4 + L_{4g} \tilde{\Delta}_{\parallel} \delta m^3 + \\
& L_{4h} \tilde{\Delta}_{\parallel}^2 \delta m^2 + L_{4i} \tilde{S}_{\parallel}^2 \delta m^2 \} + \\
& \tilde{S}_{\parallel} (1 + 8\eta) \delta m^4 + \eta \tilde{J}_{\text{ISCO}} \delta m^6.
\end{aligned} \tag{1.1.2}$$

With 19 L_i fitting parameters. The formulas for the mass and spin impose the particle limit by including ISCO dependencies (see [1, 118] for more information).

The total remnant recoil is modeled using the methods in [1].

$$\begin{aligned}
v_{\perp} = & H\eta^2 \left(\tilde{\Delta}_{\parallel} + H_{2a} \tilde{S}_{\parallel} \delta m + H_{2b} \tilde{\Delta}_{\parallel} \tilde{S}_{\parallel} + H_{3a} \tilde{\Delta}_{\parallel}^2 \delta m \right. \\
& + H_{3b} \tilde{S}_{\parallel}^2 \delta m + H_{3c} \tilde{\Delta}_{\parallel} \tilde{S}_{\parallel}^2 + H_{3d} \tilde{\Delta}_{\parallel}^3 \\
& + H_{3e} \tilde{\Delta}_{\parallel} \delta m^2 + H_{4a} \tilde{S}_{\parallel} \tilde{\Delta}_{\parallel}^2 \delta m + H_{4b} \tilde{S}_{\parallel}^3 \delta m \\
& + H_{4c} \tilde{S}_{\parallel} \delta m^3 + H_{4d} \tilde{\Delta}_{\parallel} \tilde{S}_{\parallel} \delta m^2 \\
& \left. + H_{4e} \tilde{\Delta}_{\parallel} \tilde{S}_{\parallel}^3 + H_{4f} \tilde{S}_{\parallel} \tilde{\Delta}_{\parallel}^3 \right), \\
\xi = & a + b \tilde{S}_{\parallel} + c \delta m \tilde{\Delta}_{\parallel}
\end{aligned} \tag{1.1.3}$$

$$v_m = \eta^2 \delta m (A + B \delta m^2 + C \delta m^4). \tag{1.1.4}$$

where ξ measures the angle between the “unequal mass” and “spin” contributions to the recoil velocity in the orbital plane, and according to Ref. [79] we have $A = -8712 \text{ km/s}$, and $B = -6516 \text{ km/s}$ and $C = 3907 \text{ km/s}$. These are then used in

$$\vec{V}_{\text{recoil}}(q, \vec{\alpha}_i) = v_m \hat{e}_1 + v_{\perp} (\cos(\xi) \hat{e}_1 + \sin(\xi) \hat{e}_2), \tag{1.1.5}$$

which has \hat{e}_1, \hat{e}_2 are orthogonal unit vectors in the orbital plane.

In [33] the fitting formula for peak luminosity was proposed

$$\begin{aligned}
L_{\text{peak}} = (4\eta)^2 \{ & N_0 + N_1 \tilde{S}_{\parallel} + N_{2a} \tilde{\Delta}_{\parallel} \delta m + N_{2b} \tilde{S}_{\parallel}^2 + \\
& N_{2c} \tilde{\Delta}_{\parallel}^2 + N_{2d} \delta m^2 + N_{3a} \tilde{\Delta}_{\parallel} \tilde{S}_{\parallel} \delta m + \\
& N_{3b} \tilde{S}_{\parallel} \tilde{\Delta}_{\parallel}^2 + N_{3c} \tilde{S}_{\parallel}^3 + \\
& N_{3d} \tilde{S}_{\parallel} \delta m^2 + N_{4a} \tilde{\Delta}_{\parallel} \tilde{S}_{\parallel}^2 \delta m + \\
& N_{4b} \tilde{\Delta}_{\parallel}^3 \delta m + N_{4c} \tilde{\Delta}_{\parallel}^4 + N_{4d} \tilde{S}_{\parallel}^4 + \\
& N_{4e} \tilde{\Delta}_{\parallel}^2 \tilde{S}_{\parallel}^2 + N_{4f} \delta m^4 + N_{4g} \tilde{\Delta}_{\parallel} \delta m^3 + \\
& N_{4h} \tilde{\Delta}_{\parallel}^2 \delta m^2 + N_{4i} \tilde{S}_{\parallel}^2 \delta m^2 \}. \tag{1.1.6}
\end{aligned}$$

Note that the radiated power in the particle limit scales as η^2 (See Ref. [119], Eq. (16) and (20); evaluated at the ISCO for its peak value).

The peak gravitational wave strain amplitude can be modeled as in [3], for aligned spin binaries, by

$$\begin{aligned}
(r/m)h_{22}^{\text{peak}} = (4\eta) \{ & A_0 + A_1 \tilde{S}_{\parallel} + A_{2a} \tilde{\Delta}_{\parallel} \delta m + \\
& A_{2b} \tilde{S}_{\parallel}^2 + A_{2c} \tilde{\Delta}_{\parallel}^2 + A_{2d} \delta m^2 + \\
& A_{3a} \tilde{\Delta}_{\parallel} \tilde{S}_{\parallel} \delta m + A_{3b} \tilde{S}_{\parallel} \tilde{\Delta}_{\parallel}^2 + A_{3c} \tilde{S}_{\parallel}^3 + \\
& A_{3d} \tilde{S}_{\parallel} \delta m^2 + A_{4a} \tilde{\Delta}_{\parallel} \tilde{S}_{\parallel}^2 \delta m + \\
& A_{4b} \tilde{\Delta}_{\parallel}^3 \delta m + A_{4c} \tilde{\Delta}_{\parallel}^4 + A_{4d} \tilde{S}_{\parallel}^4 + \\
& A_{4e} \tilde{\Delta}_{\parallel}^2 \tilde{S}_{\parallel}^2 + A_{4f} \delta m^4 + A_{4g} \tilde{\Delta}_{\parallel} \delta m^3 + \\
& A_{4h} \tilde{\Delta}_{\parallel}^2 \delta m^2 + A_{4i} \tilde{S}_{\parallel}^2 \delta m^2 \}. \tag{1.1.7}
\end{aligned}$$

with all A_i fitting parameters. Similarly, expressions provided for peak frequency for nonspin-

ning binaries provided in [79] were generalized in [3] to

$$\begin{aligned}
m\omega_{22}^{\text{peak}} = & \left\{ W_0 + W_1 \tilde{S}_{\parallel} + W_{2a} \tilde{\Delta}_{\parallel} \delta m + \right. \\
& W_{2b} \tilde{S}_{\parallel}^2 + W_{2c} \tilde{\Delta}_{\parallel}^2 + W_{2d} \delta m^2 + \\
& W_{3a} \tilde{\Delta}_{\parallel} \tilde{S}_{\parallel} \delta m + W_{3b} \tilde{S}_{\parallel} \tilde{\Delta}_{\parallel}^2 + W_{3c} \tilde{S}_{\parallel}^3 + \\
& W_{3d} \tilde{S}_{\parallel} \delta m^2 + W_{4a} \tilde{\Delta}_{\parallel} \tilde{S}_{\parallel}^2 \delta m + \\
& W_{4b} \tilde{\Delta}_{\parallel}^3 \delta m + W_{4c} \tilde{\Delta}_{\parallel}^4 + W_{4d} \tilde{S}_{\parallel}^4 + \\
& W_{4e} \tilde{\Delta}_{\parallel}^2 \tilde{S}_{\parallel}^2 + W_{4f} \delta m^4 + W_{4g} \tilde{\Delta}_{\parallel} \delta m^3 + \\
& \left. W_{4h} \tilde{\Delta}_{\parallel}^2 \delta m^2 + W_{4i} \tilde{S}_{\parallel}^2 \delta m^2 \right\} \tag{1.1.8}
\end{aligned}$$

with all W_i fitting parameters. More information on the performance of these formulas can be found in [3] and references thereof.

A.2 Program for Generalized Fitting Coefficients

With the release of each new iteration of RIT's catalog, it would be useful to be able to quickly output all the coefficients for the fits to include with the full catalog release. We would also like to be able to pull a specific set of simulations from the catalog (say, aligned spins), and produce fitting formulae specific to that subset of cases.

We have created a set of scripts that do just that. They require the catalog data to be in-hand, but once it is, can first extract the relevant simulations from the catalog, then make extensive use of code written by Dr. James Healy, which performs the actual fits, and finally outputs them into text files that can be easily transferred and used in various applications.

The main piece of the code is a bash script that parses the catalog based on different options. The script can be run with the following command:

```
./generateRunList.sh a A q Q 1 p T n
```

with options

- a: All simulations with aligned spins.

- A: All simulations with anti-aligned spins.
- s All simulations with mass ratio $q < 1/10$.
- q: All simulations with unequal mass ratio.
- 1: All equal-mass simulations.
- p: All precessing simulations.
- T: All simulations.
- n: All non-spinning simulations.
- no options: Defaults to "best_list.txt" which is a list of simulations that give coefficients associated with [3].

This script generates a file "run_list_out.txt" which is the list of simulations that is the union of all options. The other file, "run_list_int.txt" is a file that contains the intersection of all options, and will be empty if, for example, options a and A are chosen since there are no simulations which have both aligned spins and anti-aligned spins.

The user then runs

```
runPrivateCatalog.sh run\_list\*.txt
```

which calls several subscripts:

1. make_data_file.sh: for all files in your list of runs, it calls Jim Healy's script "print_final_state.perl" which gathers all data necessary for performing the fits from each run's Metadata file. This is put into a text file called "df".
2. parseData.py: which reads the data from "df" and then writes it to directories

```
Spin, Mass, Kick, Am22, Om22, PLum
```

for use in the fitting script.

3. `mkdirs.sh`: creates necessary subdirectories in each of the six directories from the previous step for data/figure output (DAT/PNG respectively). For example, `Spin>DAT` and `Spin>PNG`
4. The final line is a matlab command that calls ‘`callscript.m`’ in the terminal.
 - “`callscript.m`” calls Dr. Jim Healy’s set of fitting scripts for each of the six remnant formulas with a specific set of initial data that works for each case. If necessary, each formula is run repeatedly until a the variation between subsequent iterations drops below a tolerance, or for a fixed number of iterations.

The output is collected into subdirectories DAT for easy use and any figures are stored in the PNG subdirectory, for example `Spin>DAT>*.asc` contains the data and `Spin>PNG>*.png` contains the figures.

A.3 Run on Aligned-Spin only Binaries

As an example we will compute the fitting coefficients for the fitting formulae when only the 186 aligned-spin binaries are chosen. Table A.1 gives the coefficients for Eqs. (1.1.1) and (1.1.2). Table A.2 gives the coefficients for Eqs. (1.1.3) and (1.1.6). Table A.3 gives the coefficients for Eqs. (1.1.7) and (1.1.8).

To measure the goodness of the fits, we will use them to recompute the known values of remnant mass, spin, kick, and peak luminosity, peak amplitude, and peak frequency of the gravitational wave and compare them to data. Figures A.1- A.6 show these results for the 477 aligned spin runs in the top panels and the log of the residuals in the bottom panels. Overall, the fits generated using our coefficients show good agreement with the outputted data for all simulations.

| | | | |
|-----|------------------------------|-----|------------------------------|
| M0 | $0.95168588 \pm 0.00001123$ | L0 | $0.68681869 \pm 0.00000556$ |
| K1 | $-0.05157442 \pm 0.00005534$ | L1 | $0.61540145 \pm 0.00004189$ |
| K2a | $-0.00494573 \pm 0.00013159$ | L2a | $-0.14750539 \pm 0.00018362$ |
| K2b | $-0.06071780 \pm 0.00015093$ | L2b | $-0.11411091 \pm 0.00005944$ |
| K2c | $-0.00122411 \pm 0.00005339$ | L2c | $-0.00412194 \pm 0.00004156$ |
| K2d | $1.99456701 \pm 0.00017056$ | L2d | $0.80155973 \pm 0.00014449$ |
| K3a | $-0.00718707 \pm 0.00137593$ | L3a | $-0.06246567 \pm 0.00014994$ |
| K3b | $-0.00515254 \pm 0.00033257$ | L3b | $-0.01320338 \pm 0.00027624$ |
| K3c | $-0.11386952 \pm 0.00045410$ | L3c | $-0.08326776 \pm 0.00025636$ |
| K3d | $0.00749896 \pm 0.00067505$ | L3d | $1.53431358 \pm 0.00093854$ |
| K4a | $-0.04958630 \pm 0.00180684$ | L4a | $-0.05705237 \pm 0.00167054$ |
| K4b | $0.00053360 \pm 0.00030777$ | L4b | $-0.00262570 \pm 0.00047047$ |
| K4c | $0.00000670 \pm 0.00000077$ | L4c | $-0.00046736 \pm 0.00003218$ |
| K4d | $-0.14403831 \pm 0.00081503$ | L4d | $-0.05805254 \pm 0.00074401$ |
| K4e | $-0.01354250 \pm 0.00136846$ | L4e | $-0.00061581 \pm 0.00003539$ |
| K4f | $2.97970458 \pm 0.00042614$ | L4f | $0.94853491 \pm 0.00037299$ |
| K4g | $-0.00589503 \pm 0.00104667$ | L4g | $-0.12144283 \pm 0.00054422$ |
| K4h | $0.00448195 \pm 0.00034878$ | L4h | $-0.00349776 \pm 0.00029782$ |
| K4i | $0.07634813 \pm 0.00204839$ | L4i | $-0.07666742 \pm 0.00156035$ |

Table A.1: Table of fitting parameters for mass and spin formulae using only aligned spin binaries.

| | | | |
|-----|----------------------------------|-----|-------------------------------|
| H | $7558.04066901 \pm 200.55472673$ | P0 | $0.00100582 \pm 0.00017362$ |
| H2a | $-2.06826567 \pm 0.01979304$ | P1 | $0.00090869 \pm 0.00058136$ |
| H2b | $-0.64752284 \pm 0.00574375$ | P2a | $-0.00002188 \pm 0.00019420$ |
| H3a | $-0.13045427 \pm 0.02785753$ | P2b | $0.00120091 \pm 0.00169321b$ |
| H3b | $0.12609249 \pm 0.07885353$ | P2c | $0.00004962 \pm 0.00035766$ |
| H3c | $-1.76030567 \pm 0.02556123$ | P2d | $-0.00034773 \pm 0.00139493$ |
| H3d | $-0.02346497 \pm 0.00366556$ | P3a | $0.00046358 \pm 0.00507424$ |
| H3e | $-1.15704123 \pm 0.08684921$ | P3b | $0.00013847 \pm 0.00148325$ |
| H4a | $-0.76951362 \pm 0.09074279$ | P3c | $0.00145053 \pm 0.00411024$ |
| H4b | $-0.57451531 \pm 0.05732186$ | P3d | $-0.00056374 \pm 0.00218745$ |
| H4c | $0.50243640 \pm 0.15256858$ | P4a | $0.00106563 \pm 0.00723171$ |
| H4d | $2.37749576 \pm 0.13104749$ | P4b | $-0.00008133 \pm 0.00049388$ |
| H4e | $-1.33516490 \pm 0.06107957$ | P4c | $-0.00000029 \pm 0.000004117$ |
| H4f | $0.16093566 \pm 0.02970174$ | P4d | $0.00066939 \pm 0.00728816$ |
| aa | $2.42041777 \pm 0.00688169$ | P4e | $0.00009949 \pm 0.001222700$ |
| bb | $1.68714236 \pm 0.01849701$ | P4f | $0.00019742 \pm 0.00210712$ |
| cc | $0.66888956 \pm 0.03677792$ | P4g | $-0.00006484 \pm 0.00086665$ |
| | | P4h | $0.00016965 \pm 0.00178448$ |
| | | P4i | $-0.00083487 \pm 0.00508529$ |

Table A.2: Table of fitting parameters for recoil (in Km/s) and peak luminosity formulae using only aligned spin binaries.

| | | | |
|-----|------------------------------|-----|------------------------------|
| A1 | $-0.00281019 \pm 0.00010337$ | W1 | $0.14362223 \pm 0.00001913$ |
| A2a | $0.00292364 \pm 0.00005788$ | W2a | $0.00485530 \pm 0.00004060$ |
| A2b | $0.00733798 \pm 0.00013015$ | W2b | $0.07503231 \pm 0.00016237$ |
| A2c | $-0.00037101 \pm 0.00003190$ | W2c | $0.00176503 \pm 0.00002066$ |
| A3a | $0.02683710 \pm 0.00106601$ | W3a | $-0.06417348 \pm 0.00025740$ |
| A3b | $0.01799817 \pm 0.00033511$ | W3b | $0.04288594 \pm 0.00010840$ |
| A3c | $0.03384736 \pm 0.00064514$ | W3c | $0.08917775 \pm 0.00009411$ |
| A3d | $0.04631301 \pm 0.00057743$ | W3d | $-0.07856534 \pm 0.00019233$ |
| A4a | $0.07210901 \pm 0.00167853$ | W4a | $0.00923800 \pm 0.00018100$ |
| A4b | $0.00151506 \pm 0.00017390$ | W4b | $0.05179638 \pm 0.00022259$ |
| A4c | $0.00213403 \pm 0.00005764$ | W4c | $-0.00327501 \pm 0.00004273$ |
| A4d | $0.05288653 \pm 0.00070580$ | W4d | $0.15498216 \pm 0.00075424$ |
| A4e | $-0.01506572 \pm 0.00092618$ | W4e | $-0.04188317 \pm 0.00038937$ |
| A4g | $0.00181752 \pm 0.00039222$ | W4g | $-0.01231470 \pm 0.00017606$ |
| A4h | $0.00387155 \pm 0.00061244$ | W4h | $-0.06555392 \pm 0.00008528$ |
| A4i | $-0.01987491 \pm 0.00060695$ | W4i | $-0.07559977 \pm 0.00034319$ |

Table A.3: Table of fitting parameters for peak amplitude and peak frequency formulae using only aligned spin binaries.

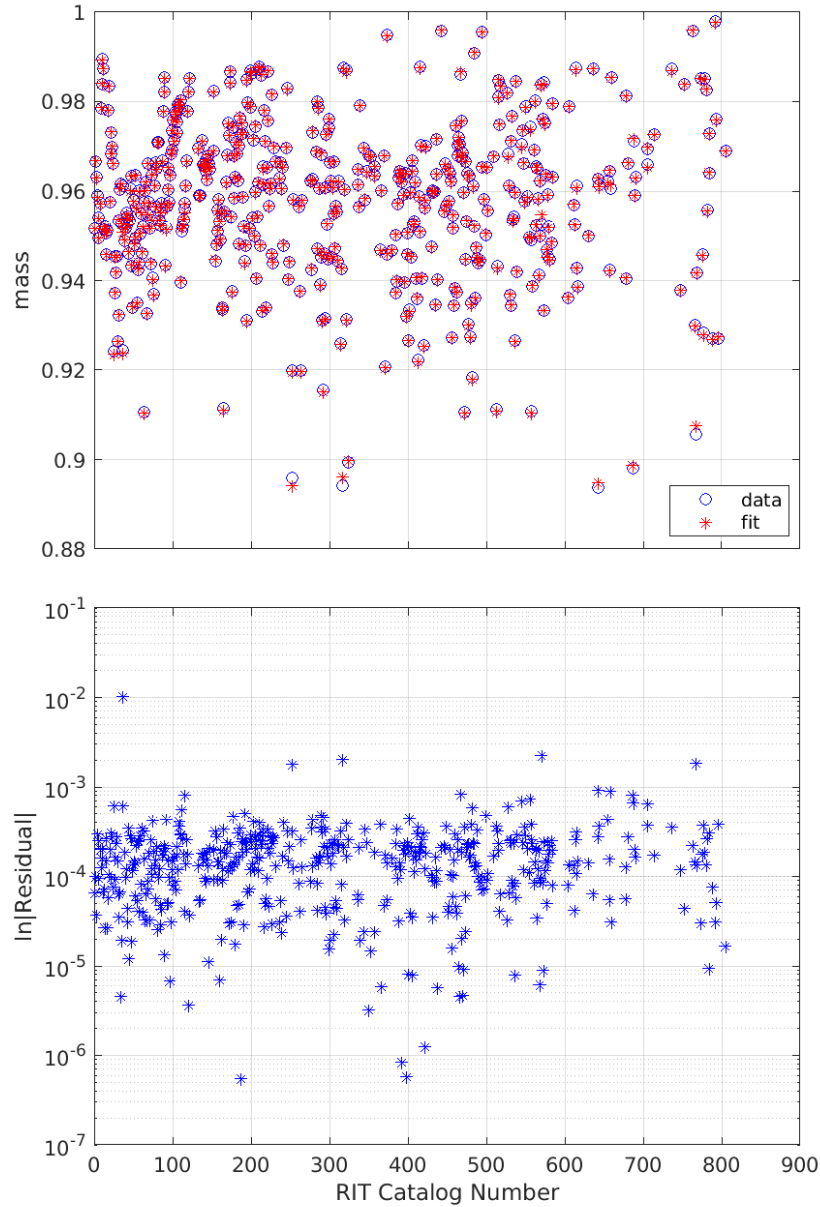


Figure A.1: (Top) Known values of remnant horizon mass for all 477 aligned spin runs (blue circles) and reproduced values using the fitting formula (red cross). (Bottom) Natural log of residuals between fits and data points.

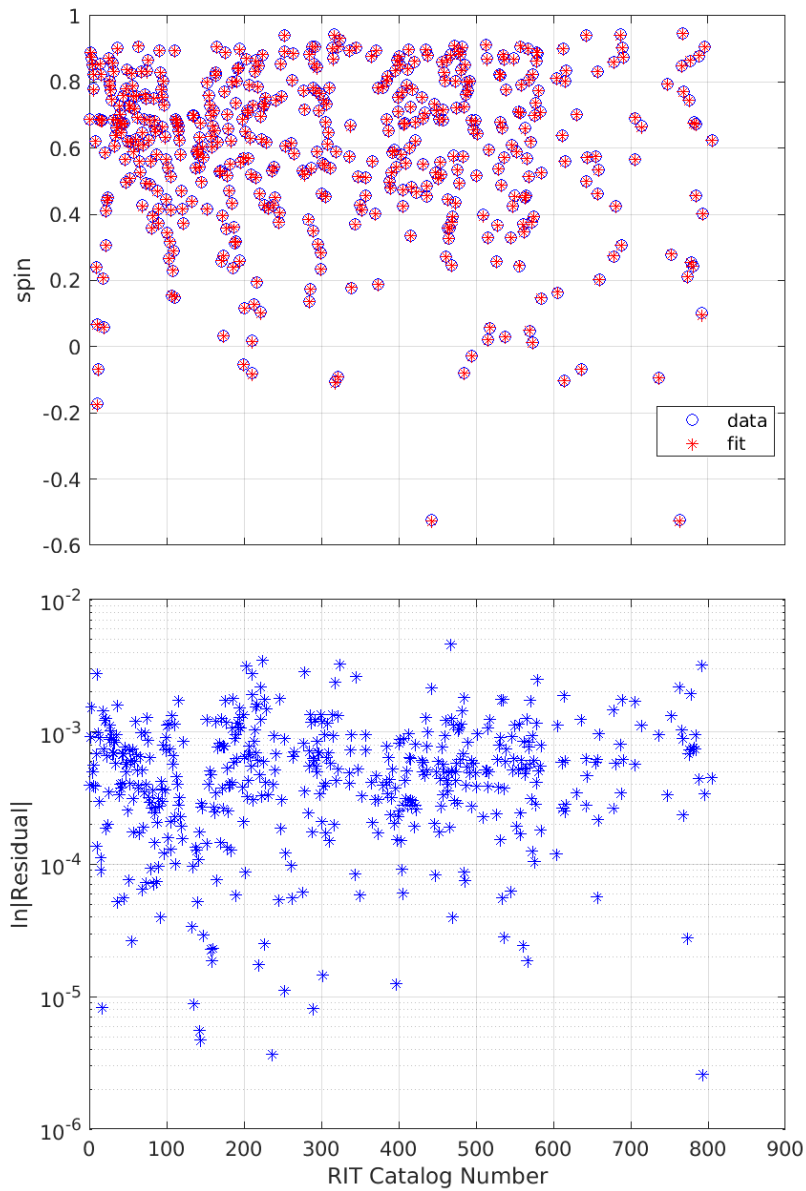


Figure A.2: (Top) Known values of remnant horizon spin for all 477 aligned spin runs (blue circles) and reproduced values using the fitting formula (red cross). (Bottom) Natural log of residuals between fits and data points.

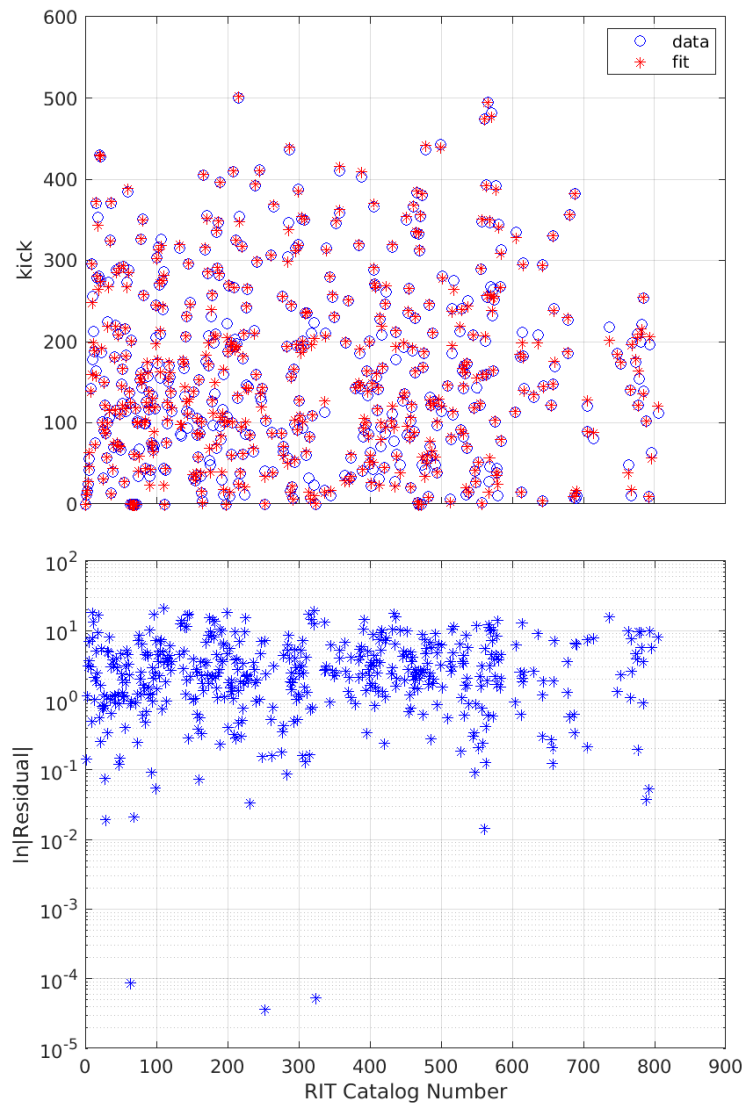


Figure A.3: (Top) Known values of remnant horizon recoil velocity for all 477 aligned spin runs (blue circles) and reproduced values using the fitting formula (red cross). (Bottom) Natural log of residuals between fits and data points.

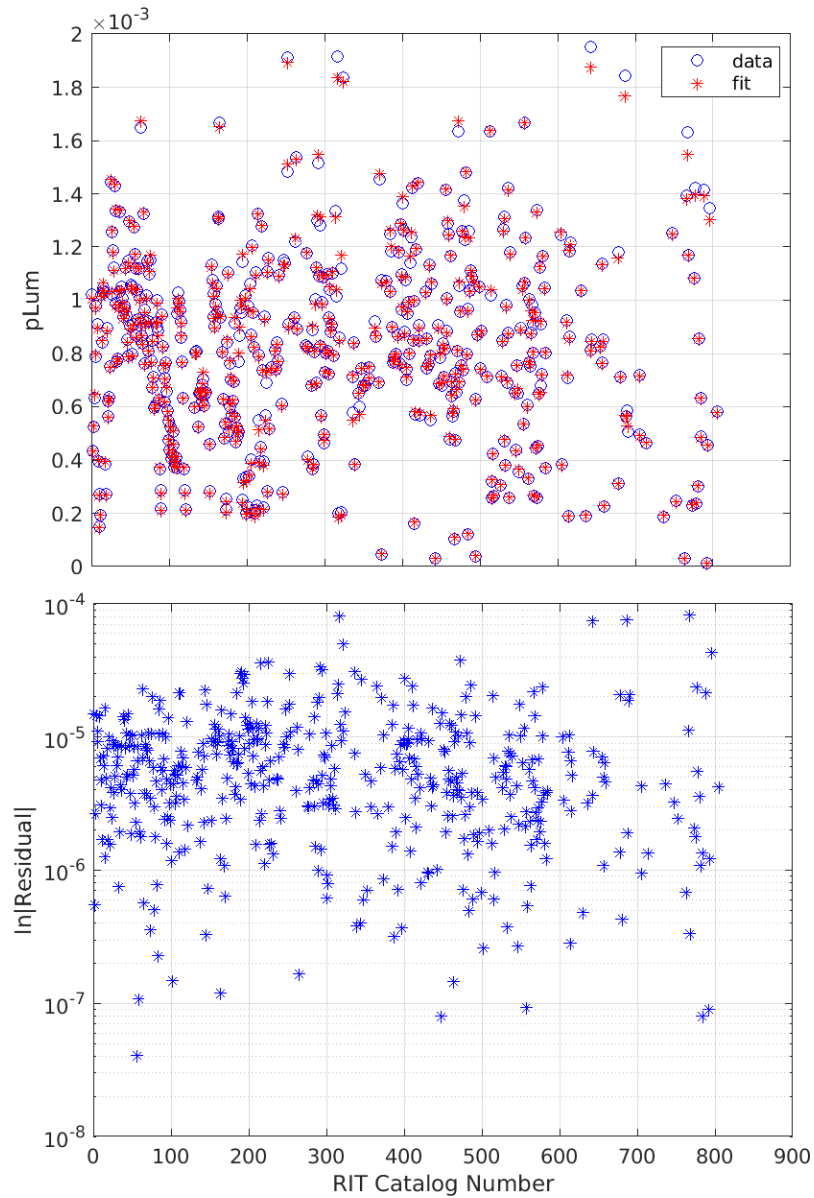


Figure A.4: (Top) Known values of peak luminosity for all 477 aligned spin runs (blue circles) and reproduced values using the fitting formula (red cross). (Bottom) Natural log of residuals between fits and data points.

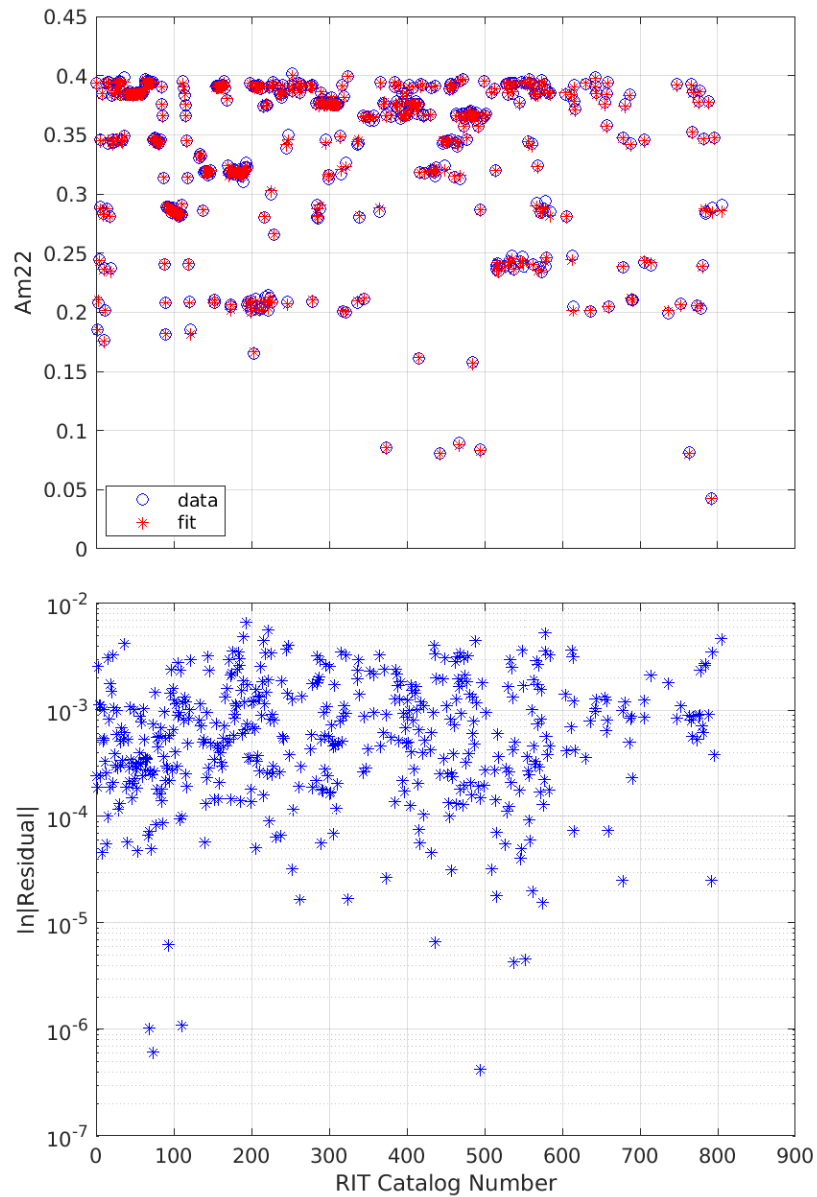


Figure A.5: (Top) Known values of gravitational wave amplitude for all 477 aligned spin runs (blue circles) and reproduced values using the fitting formula (red cross). (Bottom) Natural log of residuals between fits and data points.

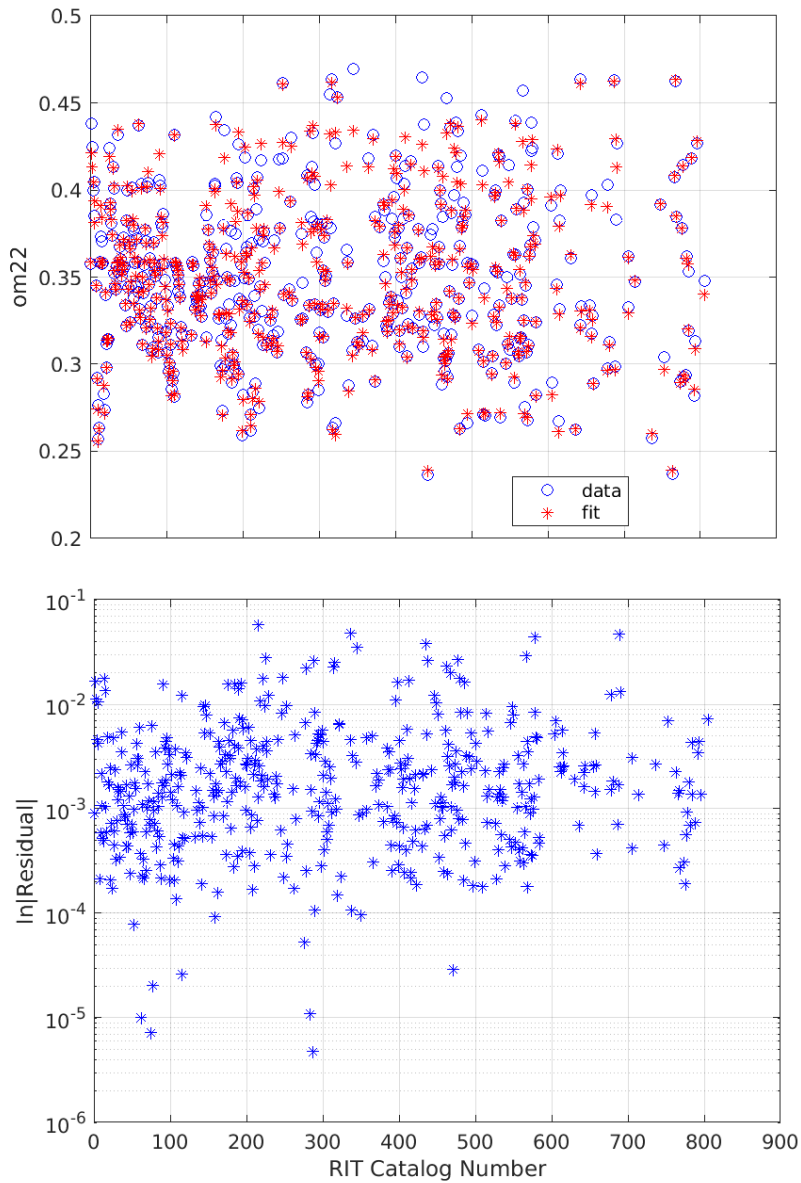


Figure A.6: (Top) Known values of gravitational wave frequency for all 477 aligned spin runs (blue circles) and reproduced values using the fitting formula (red cross). (Bottom) Natural log of residuals between fits and data points.

Bibliography

- [1] James Healy, Carlos O. Lousto, and Yosef Zlochower. Remnant mass, spin, and recoil from spin aligned black-hole binaries. *Phys. Rev.*, D90(10):104004, 2014. (document), 1.2, 1.3.4, 2.2.1, 3.2, A, A.1, A.1, A.1
- [2] James Healy, Carlos O. Lousto, Yosef Zlochower, and Manuela Campanelli. The RIT binary black hole simulations catalog. *Class. Quant. Grav.*, 34(22):224001, 2017. (document), 1.2, 2.4, 2.4, 3.4.1, 3.5, A
- [3] James Healy and Carlos O. Lousto. Hangup effect in unequal mass binary black hole mergers and further studies of their gravitational radiation and remnant properties. *Phys. Rev.*, D97(8):084002, 2018. (document), 1.2, 1.3.4, 2.1, A, A.1, A.1, A.1, A.2
- [4] James J Kolata. The ligo project. In *Neutron Stars, Black Holes and Gravitational Waves*, 2053-2571, pages 8–1 to 8–5. Morgan & Claypool Publishers, 2019. (document), 1.1
- [5] B.P. Abbott et al. Observation of Gravitational Waves from a Binary Black Hole Merger. *Phys. Rev. Lett.*, 116(6):061102, 2016. (document), 1.1, 1.1.1, 1.1.2, 1.2
- [6] Thomas W. Baumgarte and Stuart L. Shapiro. *Numerical Relativity: Solving Einstein's Equations on the Computer*. Cambridge university Press, Cambridge, 2010. (document), 1.3, 1.3.3, 1.3.3

-
- [7] Carlos O. Lousto and Yosef Zlochower. Orbital Evolution of Extreme-Mass-Ratio Black-Hole Binaries with Numerical Relativity. *Phys. Rev. Lett.*, 106:041101, 2011. (document), 2.5.2, 3.1, 3.3.1.1, 3.3.3, 3.6, 3.5, 5
- [8] Manuela Campanelli, C. O. Lousto, P. Marronetti, and Y. Zlochower. Accurate evolutions of orbiting black-hole binaries without excision. *Phys. Rev. Lett.*, 96:111101, 2006. (document), 1.1.2, 1.3.2, 1.3.3, 1.3.4, 2.2, 2.2.1, 2.5, 3.1, 3.2, 3.2, 3.6, 3.5
- [9] B. P. Abbott et al. Directly comparing GW150914 with numerical solutions of Einstein’s equations for binary black hole coalescence. *Phys. Rev.*, D94:064035, 2016. 1.1.1, 2.1
- [10] B. P. Abbott et al. Properties of the Binary Black Hole Merger GW150914. *Phys. Rev. Lett.*, 116(24):241102, 2016. 1.1.1
- [11] B. P. Abbott et al. Binary Black Hole Mergers in the first Advanced LIGO Observing Run. *Phys. Rev.*, X6(4):041015, 2016. 1.1.1, 1.1.2
- [12] Benjamin P. Abbott et al. GW170814: A three-detector observation of gravitational waves from a binary black hole coalescence. *Phys. Rev. Lett.*, 2017. [Phys. Rev. Lett.119,141101(2017)]. 1.1.1
- [13] B. P. Abbott et al. GWTC-1: A Gravitational-Wave Transient Catalog of Compact Binary Mergers Observed by LIGO and Virgo during the First and Second Observing Runs. *Phys. Rev.*, X9(3):031040, 2019. 1.1.1, 2.1
- [14] B. P. Abbott et al. Tests of General Relativity with the Binary Black Hole Signals from the LIGO-Virgo Catalog GWTC-1. *Phys. Rev.*, D100(10):104036, 2019. 1.1.1, 2.1
- [15] K. Danzmann *et al.* Lisa – laser interferometer space antenna, pre-phase a report. Technical Report MPQ 233, Max-Planck-Institut für Quantenoptic, 1998. 1.1.1
- [16] K. Danzmann and A. Rudiger. Lisa technology - concept, status, prospects. *Class. Quant. Grav.*, 20:S1–S9, 2003. 1.1.1

- [17] Walter Del Pozzo, Alberto Sesana, and Antoine Klein. Stellar binary black holes in the LISA band: a new class of standard sirens. *Mon. Not. Roy. Astron. Soc.*, 475(3):3485–3492, 2018. 1.1.1
- [18] S. Dwyer. Advanced LIGO status. *J. Phys. Conf. Ser.*, 610(1):012013, 2015. 1.1.1
- [19] K. Danzmann, P. Bender, A. Brillet, I. Ciufolini A.M. Cruise, C. Cutler, F. Fidecaro, W.M. Folkner, J. Hough, P. McNamara, M. Peterseim, D. Robertson, M. Rodrigues, A. Rüdiger, M. Sandford, G. Schäfer, R. Schilling, B. Schutz, C. Speake, R.T. Stebbins, T. Sumner, P. Touboul, J.-Y. Vinet, S. Vitale, H. Ward, and W. Winkler. Lisa pre-phase a report. *Max-Planck-Institut für Quantenoptik, Report MPQ*, 233, 1998. 1.1.1
- [20] Leor Barack and Curt Cutler. Lisa capture sources: Approximate waveforms, signal-to-noise ratios, and parameter estimation accuracy. *Phys. Rev.*, D69:082005, 2004. 1.1.1
- [21] Heather Audley et al. Laser Interferometer Space Antenna. 2017. 1.1.1, 1.1.2
- [22] Carlos O. Lousto and James Healy. Exploring the small mass ratio binary black hole merger via Zeno’s dichotomy approach. *Phys. Rev. Lett.*, 125(19):191102, 2020. 1.1.1, 1.2, 3.1, 3.4.4, 3.4.4, 3.5, 5
- [23] Frans Pretorius. Evolution of binary black hole spacetimes. *Phys. Rev. Lett.*, 95:121101, 2005. 1.1.2, 1.3.4, 3.1
- [24] John G. Baker, Joan Centrella, Dae-Il Choi, Michael Koppitz, and James van Meter. Gravitational wave extraction from an inspiraling configuration of merging black holes. *Phys. Rev. Lett.*, 96:111102, 2006. 1.1.2, 1.3.4, 2.2, 2.5, 3.1, 3.5
- [25] Geoffrey Lovelace et al. Modeling the source of GW150914 with targeted numerical-relativity simulations. *Class. Quant. Grav.*, 33(24):244002, 2016. 1.1.2, 2.1
- [26] M. Dominik, K. Belczynski, C. Fryer, D. E. Holz, E. Berti, T. Bulik, I. Mandel, and R. O’Shaughnessy. Double Compact Objects. II. Cosmological Merger Rates. *Astrophys. J.*, 779:72, December 2013. 1.1.2

- [27] M. Dominik, E. Berti, R. O’Shaughnessy, I. Mandel, K. Belczynski, C. Fryer, D. E. Holz, T. Bulik, and F. Pannarale. Double Compact Objects III: Gravitational-wave Detection Rates. *Astrophys. J.*, 806:263, June 2015. 1.1.2
- [28] C. L. Rodriguez, M. Morscher, B. Pattabiraman, S. Chatterjee, C.-J. Haster, and F. A. Rasio. Binary Black Hole Mergers from Globular Clusters: Implications for Advanced LIGO. *Physical Review Letters*, 115(5):051101, July 2015. 1.1.2
- [29] M. Morscher, B. Pattabiraman, C. Rodriguez, F. A. Rasio, and S. Umbreit. The Dynamical Evolution of Stellar Black Holes in Globular Clusters. *Astrophys. J.*, 800:9, February 2015. 1.1.2
- [30] Richard O’Shaughnessy, C. Kim, V. Kalogera, and K. Belczynski. Constraining population synthesis models via empirical binary compact object merger and supernovae rates. *Astrophys. J.*, 672:479, 2008. 1.1.2
- [31] Manuela Campanelli, Carlos O. Lousto, Hiroyuki Nakano, and Yosef Zlochower. Comparison of Numerical and Post-Newtonian Waveforms for Generic Precessing Black-Hole Binaries. *Phys. Rev.*, D79:084010, 2009. 1.2
- [32] Yosef Zlochower and Carlos O. Lousto. Modeling the remnant mass, spin, and recoil from unequal-mass, precessing black-hole binaries: The Intermediate Mass Ratio Regime. *Phys. Rev.*, D92:024022, 2015. 1.2, A
- [33] James Healy and Carlos O. Lousto. Remnant of binary black-hole mergers: New simulations and peak luminosity studies. *Phys. Rev.*, D95(2):024037, 2017. 1.2, 2.2.1, 3.2, A, A.1
- [34] James Healy, Carlos O. Lousto, Jacob Lange, Richard O’Shaughnessy, Yosef Zlochower, and Manuela Campanelli. The second RIT binary black hole simulations catalog and its application to gravitational waves parameter estimation. *Phys. Rev.*, D100(2):024021, 2019. 1.2, 2.1, 2.4, 2.4, 3.1, 3.4.1, 3.5

- [35] James Healy and Carlos O. Lousto. Third RIT binary black hole simulations catalog. *Phys. Rev. D*, 102(10):104018, 2020. 1.2, 3.1, 3.4.1, 3.5, A
- [36] Ian Ruchlin, James Healy, Carlos O. Lousto, and Yosef Zlochower. Puncture Initial Data for Black-Hole Binaries with High Spins and High Boosts. *Phys. Rev.*, D95(2):024033, 2017. 1.2, 3.5
- [37] C Beetle, M Bruni, L M Burko, and A Nerozzi. Towards a wave-extraction method for numerical relativity. I. Foundations and initial-value formulation. *Phys. Rev. D*, 72:024013, 2005. 1.2, 4, 4.1, 4.2, 4.3, 4.6.0.1
- [38] Andrea Nerozzi, Christopher Beetle, Marco Bruni, Lior M. Burko, and Denis Pollney. Towards wave extraction in numerical relativity: The quasi-kinnersley frame. *Phys. Rev.*, D72:024014, 2005. 1.2, 4.1, 4.3, 4.3, 4.4, 4.4.1, 4.6.0.1, 4.6.2, 3, 4.6.2
- [39] Lior M. Burko, Thomas W. Baumgarte, and Christopher Beetle. Towards a novel wave-extraction method for numerical relativity: III. Analytical examples for the Beetle-Burko radiation scalar. *Phys. Rev. D*, 73:024002, 2005. 1.2, 4.1
- [40] Andrea Nerozzi, Marco Bruni, Virginia Re, and Lior M. Burko. Towards a wave-extraction method for numerical relativity. IV: Testing the quasi-Kinnersley method in the Bondi-Sachs framework. *Phys. Rev.*, D73:044020, 2006. 1.2, 4.1
- [41] Vitor Cardoso, Leonardo Gualtieri, Carlos Herdeiro, Ulrich Sperhak, Paul M Chesler, Luis Lehner, Seong Chan Park, Harvey S Reall, Carlos F Sopuerta (section coordinators), Daniela Alic, Oscar J C Dias, Roberto Emparan, Valeria Ferrari, Steven B Giddings, Mahdi Godazgar, Ruth Gregory, Veronika E Hubeny, Akihiro Ishibashi, Greg Landsberg, Carlos O Lousto, David Mateos, Vicki Moeller, Hirotada Okawa, Paolo Pani, M Andy Parker, Frans Pretorius, Masaru Shibata, Hajime Sotani, Toby Wiseman, Helvi Witek, Nicolas Yunes, and Miguel Zilhão. NR/HEP: roadmap for the future. *Class. Quant. Grav.*, 29:244001, 2012. 1.2

- [42] Sean M. Carroll. *Spacetime and geometry: An introduction to general relativity*. Addison-Wesley, 2004. 1.3.1
- [43] Miguel Alcubierre. *Introduction to 3+1 Numerical Relativity*. Oxford University Press, Oxford, U.K., 2008. 1.3.1, 1.3.3, 4.2, 4.2.1, 4.6
- [44] Miguel Alcubierre, Bernd Brügmann, Peter Diener, Michael Koppitz, Denis Pollney, Edward Seidel, and Ryoji Takahashi. Gauge conditions for long-term numerical black hole evolutions without excision. *Phys. Rev.*, D67:084023, 2003. 1.3.2, 2.2, 3.2
- [45] R. Arnowitt, S. Deser, and C. W. Misner. Energy and the Criteria for Radiation in General Relativity. *Phys. Rev.*, 118:1100–1104, 1960. 1.3.2
- [46] Richard L. Arnowitt, Stanley Deser, and Charles W. Misner. The Dynamics of general relativity. *Gen.Rel.Grav.*, 40:1997–2027, 2008. 1.3.2
- [47] Takashi Nakamura, Ken-ichi Oohara, and Y. Kojima. General relativistic collapse to black holes and gravitational waves from black holes. *Prog. Theor. Phys. Suppl.*, 90:1–218, 1987. 1.3.2, 2.2
- [48] M. Shibata and Takashi Nakamura. Evolution of three-dimensional gravitational waves: Harmonic slicing case. *Phys. Rev.*, D52:5428, 1995. 1.3.2, 1.3.3, 2.2
- [49] T. W. Baumgarte and S. L. Shapiro. Numerical integration of Einstein’s field equations. *Phys. Rev.*, D59:024007, 1998. 1.3.2, 2.2
- [50] L. E. Kidder, M. A. Scheel, and S. A. Teukolsky. Extending the lifetime of 3D black hole computations with a new hyperbolic system of evolution equations. *Phys. Rev. D*, 64:064017, 2001. 1.3.3
- [51] Masaru Shibata and Takashi Nakamura. Evolution of three-dimensional gravitational waves: Harmonic slicing case. *Phys. Rev.*, D52:5428–5444, 1995. 1.3.3
- [52] Thomas W. Baumgarte and Stuart L. Shapiro. On the numerical integration of Einstein’s field equations. *Phys. Rev.*, D59:024007, 1999. 1.3.3

- [53] Jeffrey M. Bowen and James W. York, Jr. Time asymmetric initial data for black holes and black hole collisions. *Phys. Rev.*, D21:2047–2056, 1980. 1.3.3
- [54] Carlos O. Lousto and James Healy. Kicking gravitational wave detectors with recoiling black holes. *Phys. Rev.*, D100(10):104039, 2019. 2.1, 2.2.1, 3.2
- [55] A. Sesana, M. Volonteri, and F. Haardt. LISA detection of massive black hole binaries: imprint of seed populations and of extreme recoils. *Class. Quant. Grav.*, 26:094033, 2009. 2.1
- [56] Davide Gerosa and Christopher J. Moore. Black hole kicks as new gravitational wave observables. *Phys. Rev. Lett.*, 117(1):011101, 2016. 2.1
- [57] J. Healy et al. Targeted numerical simulations of binary black holes for GW170104. *Phys. Rev.*, D97(6):064027, 2018. 2.1
- [58] James Healy, Carlos O. Lousto, Jacob Lange, and Richard O’Shaughnessy. Application of the third RIT binary black hole simulations catalog to parameter estimation of gravitational waves signals from the LIGO-Virgo O1/O2 observational runs. *Phys. Rev. D*, 102(12):124053, 2020. 2.1, 3.5
- [59] B. P. Abbott et al. Tests of general relativity with GW150914. *Phys. Rev. Lett.*, 116(22):221101, 2016. 2.1
- [60] F. Echeverría. Gravitational-wave measurements of mass and angular momentum of a black hole. *Phys. Rev. D*, 40:3194, 1989. 2.1
- [61] Emanuele Berti, Vitor Cardoso, and Clifford M. Will. On gravitational-wave spectroscopy of massive black holes with the space interferometer LISA. *Phys. Rev.*, D73:064030, 2006. 2.1
- [62] Emanuele Berti, Vitor Cardoso, and Andrei O. Starinets. Quasinormal modes of black holes and black branes. *Class. Quant. Grav.*, 26:163001, 2009. 2.1

- [63] Olaf Dreyer, Badri Krishnan, Deirdre Shoemaker, and Erik Schnetter. Introduction to isolated horizons in numerical relativity. *Phys. Rev.*, D67:024018, 2003. 2.1, 2.4, 3.4.2
- [64] Sergio Dain, Carlos O. Lousto, and Yosef Zlochower. Extra-Large Remnant Recoil Velocities and Spins from Near-Extremal-Bowen-York-Spin Black-Hole Binaries. *Phys. Rev.*, D78:024039, 2008. 2.1
- [65] Badri Krishnan, Carlos O. Lousto, and Yosef Zlochower. Quasi-Local Linear Momentum in Black-Hole Binaries. *Phys. Rev.*, D76:081501, 2007. 2.1, 2.1, 2.3, 2.3, 2.5.2, 3.2, 3.3.3, 3.4.2, 5
- [66] James R. van Meter, John G. Baker, Michael Koppitz, and Dae-Il Choi. How to move a black hole without excision: gauge conditions for the numerical evolution of a moving puncture. *Phys. Rev.*, D73:124011, 2006. 2.1, 2.2, 2.5
- [67] James Healy, Carlos O. Lousto, and Nicole Rosato. Adapted gauge to a quasilocal measure of the black holes recoil. *Phys. Rev. D*, 102(2):024040, 2020. 2.1, 3.1, 3.2, 3.3.3, 3.4.1, 3.4.2, 3.4.3, 3.4.4, 5
- [68] Carlos O. Lousto and Yosef Zlochower. Further insight into gravitational recoil. *Phys. Rev.*, D77:044028, 2008. 2.2, 3.2
- [69] Marcus Ansorg, Bernd Brügmann, and Wolfgang Tichy. A single-domain spectral method for black hole puncture data. *Phys. Rev.*, D70:064011, 2004. 2.2.1, 3.2
- [70] Y. Zlochower, J. G. Baker, Manuela Campanelli, and C. O. Lousto. Accurate black hole evolutions by fourth-order numerical relativity. *Phys. Rev.*, D72:024021, 2005. 2.2.1, 2.5.2, 3.2
- [71] Erik Schnetter, Scott H. Hawley, and Ian Hawke. Evolutions in 3D numerical relativity using fixed mesh refinement. *Class. Quant. Grav.*, 21(6):1465–1488, 21 March 2004. 2.2.1, 3.2
- [72] carpet - adaptive mesh refinement for the cactus framework:
<https://carpetcode.org>. 2.2.1

- [73] Jonathan Thornburg. A fast apparent-horizon finder for 3-dimensional Cartesian grids in numerical relativity. *Class. Quant. Grav.*, 21(2):743–766, 21 January 2004. 2.2.1, 3.2
- [74] Olaf Dreyer, Badri Krishnan, Deirdre Shoemaker, and Erik Schnetter. Introduction to Isolated Horizons in Numerical Relativity. *Phys. Rev.*, D67:024018, 2003. 2.2.1, 3.2
- [75] Manuela Campanelli, Carlos O. Lousto, Yosef Zlochower, Badri Krishnan, and David Merritt. Spin flips and precession in black-hole-binary mergers. *Phys. Rev.*, D75:064030, 2007. 2.2.1, 2.4, 3.2
- [76] M. Campanelli and C. O. Lousto. Second order gauge invariant gravitational perturbations of a Kerr black hole. *Phys. Rev.*, D59:124022, 1999. 2.2.1, 3.2
- [77] Carlos O. Lousto and Yosef Zlochower. A practical formula for the radiated angular momentum. *Phys. Rev.*, D76:041502(R), 2007. 2.2.1, 3.2
- [78] Hiroyuki Nakano, James Healy, Carlos O. Lousto, and Yosef Zlochower. Perturbative extraction of gravitational waveforms generated with Numerical Relativity. *Phys. Rev.*, D91(10):104022, 2015. 2.2.1, 3.2
- [79] James Healy, Carlos O. Lousto, and Yosef Zlochower. Nonspinning binary black hole merger scenario revisited. *Phys. Rev.*, D96(2):024031, 2017. 2.2.1, 3.2, A, A.1, A.1
- [80] Yosef Zlochower, James Healy, Carlos O. Lousto, and Ian Ruchlin. Evolutions of Nearly Maximally Spinning Black Hole Binaries Using the Moving Puncture Approach. *Phys. Rev.*, D96(4):044002, 2017. 2.2.1, 3.2, 3.5
- [81] James Healy, Carlos O. Lousto, Ian Ruchlin, and Yosef Zlochower. Evolutions of unequal mass, highly spinning black hole binaries. *Phys. Rev.*, D97(10):104026, 2018. 2.2.1, 3.2, 3.5
- [82] Manuela Campanelli and Carlos O. Lousto. Second order gauge invariant gravitational perturbations of a Kerr black hole. *Phys. Rev.*, D59:124022, 1999. 2.4

- [83] Carsten Gundlach and Jose M. Martin-Garcia. Well-posedness of formulations of the einstein equations with dynamical lapse and shift conditions. *Phys. Rev.*, D74:024016, 2006. 2.5
- [84] Doreen Müller and Bernd Brügmann. Toward a dynamical shift condition for unequal mass black hole binary simulations. *Class. Quant. Grav.*, 27:114008, 2010. 2.5.2, 3.3.3
- [85] Doreen Müller, Jason Grigsby, and Bernd Brügmann. Dynamical shift condition for unequal mass black hole binaries. *Phys. Rev.*, D82:064004, 2010. 2.5.2
- [86] Erik Schnetter. Time Step Size Limitation Introduced by the BSSN Gamma Driver. *Class. Quant. Grav.*, 27:167001, 2010. 2.5.2, 3.3.3
- [87] Daniela Alic, Luciano Rezzolla, Ian Hinder, and Philipp Mosta. Dynamical damping terms for symmetry-seeking shift conditions. *Class. Quant. Grav.*, 27:245023, 2010. 2.5.2, 3.3.3
- [88] Laura Bernard, Luc Blanchet, Guillaume Faye, and Tanguy Marchand. Center-of-Mass Equations of Motion and Conserved Integrals of Compact Binary Systems at the Fourth Post-Newtonian Order. *Phys. Rev.*, D97(4):044037, 2018. 2.5.2
- [89] Michael Boyle et al. The SXS Collaboration catalog of binary black hole simulations. *Class. Quant. Grav.*, 36(19):195006, 2019. 3.1
- [90] Karan Jani, James Healy, James A. Clark, Lionel London, Pablo Laguna, and Deirdre Shoemaker. Georgia Tech Catalog of Gravitational Waveforms. *Class. Quant. Grav.*, 33(20):204001, 2016. 3.1
- [91] Michael Pürrer and Carl-Johan Haster. Ready for what lies ahead? – Gravitational waveform accuracy requirements for future ground based detectors. *Phys. Rev. Res.*, 2(2):023151, 2020. 3.1, 5
- [92] Jonathan R. Gair, Stanislav Babak, Alberto Sesana, Pau Amaro-Seoane, Enrico Barausse, Christopher P.L. Berry, Emanuele Berti, and Carlos Sopuerta. Prospects for

- observing extreme-mass-ratio inspirals with LISA. *J. Phys. Conf. Ser.*, 840(1):012021, 2017. 3.1, 5
- [93] Ulrich Sperhake, Vitor Cardoso, Christian D. Ott, Erik Schnetter, and Helvi Witek. Extreme black hole simulations: collisions of unequal mass black holes and the point particle limit. *Phys. Rev.*, D84:084038, 2011. 3.1, 5
- [94] Carlos O. Lousto and Yosef Zlochower. Foundations of multiple black hole evolutions. *Phys. Rev.*, D77:024034, 2008. 3.1
- [95] Yosef Zlochower, Marcelo Ponce, and Carlos O. Lousto. Accuracy Issues for Numerical Waveforms. *Phys. Rev.*, D86:104056, 2012. 3.1, 3.5
- [96] Zachariah B. Etienne, John G. Baker, Vasileios Paschalidis, Bernard J. Kelly, and Stuart L. Shapiro. Improved Moving Puncture Gauge Conditions for Compact Binary Evolutions. *Phys. Rev.*, D90(6):064032, 2014. 3.1, 3.4.1
- [97] Mark Hannam, Sascha Husa, Frank Ohme, Bernd Bruegmann, and Niall O’Murchadha. Wormholes and trumpets: the Schwarzschild spacetime for the moving-puncture generation. *Phys. Rev.*, D78:064020, 2008. 3.2.1
- [98] Bernd Brügmann. Schwarzschild black hole as moving puncture in isotropic coordinates. *Gen. Rel. Grav.*, 41:2131–2151, 2009. 3.2.1.1, 3.2.1.1, 3.2.1.2, 3.2.1.2, 3.2.1.2
- [99] Marcus Thierfelder, Sebastiano Bernuzzi, David Hilditch, Bernd Bruegmann, and Luciano Rezzolla. The trumpet solution from spherical gravitational collapse with puncture gauges. *Phys. Rev.*, D83:064022, 2011. 3.2.1.1, 3.2.1.2
- [100] Kyle Slinker, Charles R. Evans, and Mark Hannam. Trumpet Initial Data for Boosted Black Holes. *Phys. Rev.*, D98(4):044014, 2018. 3.3.1
- [101] Kenneth A. Dennison, Thomas W. Baumgarte, and Pedro J. Montero. Trumpet Slices in Kerr Spacetimes. *Phys. Rev. Lett.*, 113(26):261101, 2014. 3.3.1

- [102] Pedro Marronetti, Wolfgang Tichy, Bernd Brügmann, Jose Gonzalez, and Ulrich Sperhake. High-spin binary black hole mergers. *Phys. Rev.*, D77:064010, 2008. 3.3.1.1, 3.3.3
- [103] Carlos O. Lousto, Hiroyuki Nakano, Yosef Zlochower, and Manuela Campanelli. Intermediate Mass Ratio Black Hole Binaries: Numerical Relativity meets Perturbation Theory. *Phys. Rev. Lett.*, 104:211101, 2010. 3.3.3
- [104] Doreen Müller, Jason Grigsby, and Bernd Brügmann. Dynamical shift condition for unequal mass black hole binaries. *Phys. Rev.*, D82:064004, 2010. 3.3.3, 3.3.3, 3.3.3, 3.3.3
- [105] Saul A. Teukolsky. Perturbations of a rotating black hole. 1. Fundamental equations for gravitational electromagnetic and neutrino field perturbations. *Astrophys. J.*, 185:635–647, 1973. 4.1
- [106] S. A. Teukolsky. Perturbations of a rotating black hole. I. fundamental equations for gravitational, electromagnetic, and neutrino-field perturbations. *Astrophys. J.*, 185:635–647, 1973. 4.1
- [107] E. Newman and R. Penrose. An approach to gravitational radiation by a method of spin coefficients. *J. Math. Phys.*, 3:566, 1962. 4.1
- [108] W Kinnersley. Type D vacuum metrics. *J. Math. Phys.*, 10:1195–1203, 1969. 4.1
- [109] M. MacCallum D. Kramer, H. Stephani and E. Herlt. *Exact Solutions of Einstein's Field Equations*. Cambridge University Press, Cambridge, 1980. 4.1, 4.2
- [110] John G. Baker, Manuela Campanelli, and Carlos O. Lousto. The Lazarus project: A Pragmatic approach to binary black hole evolutions. *Phys. Rev.*, D65:044001, 2002. 4.1
- [111] Manuela Campanelli, Bernard J. Kelly, and Carlos O. Lousto. The Lazarus Project II: Space-like extraction with the Quasi-Kinnersley tetrad. *Phys. Rev.*, D73:064005, 2006. 4.1
- [112] A. Z. Petrov. *Einstein Spaces*. Pergamon Press, Oxford, 1969. 4.2.1

-
- [113] H. Stephani, D. Kramer, M. MacCallum, C. Hoenselaers, and E. Herlt. *Exact solutions to Einstein's field equations*. Cambridge, UK: Univ. Pr., 2003. 2nd Edition. 701 P. 4.2.1
- [114] John G. Baker and Manuela Campanelli. Making use of geometrical invariants in black hole collisions. *Phys. Rev.*, D62:127501, 2000. 4.5, 4.6.2
- [115] Leonhard Euler. *Of a new method of resolving equations of the fourth degree*. Springer-Verlag, 1765. 4.8
- [116] Michael Boyle et al. High-accuracy comparison of numerical relativity simulations with post-Newtonian expansions. *Phys. Rev.*, D76:124038, 2007. A
- [117] Carlos O. Lousto and Yosef Zlochower. Black hole binary remnant mass and spin: A new phenomenological formula. *Phys. Rev.*, D89:104052, 2014. A
- [118] Amos Ori and Kip S. Thorne. The transition from inspiral to plunge for a compact body in a circular equatorial orbit around a massive, spinning black hole. *Phys. Rev.*, D62:124022, 2000. A.1
- [119] Ryuichi Fujita. Gravitational Waves from a Particle in Circular Orbits around a Rotating Black Hole to the 11th Post-Newtonian Order. *PTEP*, 2015(3):033E01, 2015. A.1